

CENTER FOR SPACE RESEARCH
THE UNIVERSITY OF TEXAS AT AUSTIN AUSTIN, TEXAS

EARTH RADIATION PRESSURE EFFECTS ON SATELLITES

by

Philip C. Knocke

Center for Space Research

The University of Texas at Austin

May 1989

EARTH RADIATION PRESSURE EFFECTS ON SATELLITES

Philip Charles Knocke, Ph.D.
The University of Texas at Austin, 1989

The unprecedented accuracy of modern laser range measurements and the stringent demands of precision orbit determination have led to the development of increasingly complex force models. The discovery of anomalous motions of the LAGEOS satellite has spurred interest in various esoteric force effects, including the radiation pressure imparted by the energy flux of the Earth. This topic is investigated in terms of orbit perturbations, effects in the presence of real data, and influence on the estimation of parameters.

Two related Earth radiation pressure models are examined. The nominal model assumes the Earth is a completely diffuse reflector and emitter of radiant energy. Satellite radiance data are used for the first time to devise an advanced model which realistically characterizes the directional and diurnal variations in the reflected component of Earth radiation pressure.

Various characteristics of the Earth radiation pressure force are examined, including variation over an orbit, variation with altitude, and the relative importance of the shortwave (reflected) and longwave (infrared) components. Albedo

parameters are estimated from observations of a constellation of geodetic satellites. Consider analyses indicate the correlations between Earth radiation parameters and estimated parameters, including gravity coefficients.

Neither the diffuse nor the advanced Earth radiation pressure models can explain the observed mean secular decrease in the semimajor axis of LAGEOS, or any significant portion of the periodic excursions about this mean. Analyses of GEOS-1 and GEOS-2 data are used to verify the hypothesis that Earth radiation pressure can generate significant along-track accelerations on high eccentricity satellites passing through the Earth's shadow.

The advanced model usually engenders smaller orbit perturbations than the diffuse model, due to the diurnal variation in albedo. Some evidence exists to suggest that the advanced model may be somewhat more separable from competing nonconservative forces than the diffuse model.

TABLE OF CONTENTS

Acknowledgements	iv
Abstract	viii
List of Symbols	xiv
1. INTRODUCTION	1
1.1 Introduction	1
1.2 Solar Radiation, Earth Radiation, and Albedo	6
2. THE DIFFUSE EARTH RADIATION PRESSURE MODEL	10
2.1 The Force Model	10
2.1.1 Satellite-intercepted Flux in terms of Radiances	10
2.1.2 Shortwave Radiance in terms of Albedo: Lambert's Law .	13
2.1.3 Longwave Radiance in terms of Emissivity	17
2.1.4 Diffuse Earth Radiation Pressure Acceleration on a Spherical Satellite	19
2.1.4.1 The Satellite Model: Lochry's Radiation Augmentation Factor	19
2.1.4.2 The Total Acceleration due to all Earth Elements	22
2.1.5 Implementation In UTOPIA	24

2.1.5.1	Determination of the Earth Segment Areas	24
2.2	The Earth Radiation Model	28
2.3	The Partial Derivatives of the Acceleration	30
2.4	Conclusions	33
3.	ORBITAL EFFECTS OF DIFFUSE EARTH RADIATION	41
3.1	Values of the Earth Radiation Constants	41
3.2	Character of Diffuse Earth Radiation Pressure	43
3.2.1	Variation with Altitude	43
3.2.2	Variation over an Orbit	46
3.2.3	Earth Radiation Pressure and High Eccentricity Orbits . .	48
3.3	Orbital Effects of Diffuse Earth Radiation	49
3.3.1	A Comparison of Shortwave and Longwave Radiation Effects	49
3.3.2	Effects of Diffuse Earth Radiation on the Orbit Elements of LAGEOS	51
3.3.3	Earth Radiation Effects on other Satellites	54
3.3.3.1	Diffuse Earth Radiation Pressure and GEOS-1 .	56
3.3.3.2	Diffuse Earth Radiation Pressure and GEOS-2 .	61
3.4	Diffuse Earth Radiation Pressure and the Estimation of Parameters .	62
3.4.1	Estimation of Albedo Parameters from Satellite Orbit Observations	62
3.4.1.1	The LAGEOS-Only Solution	65

3.4.1.2	The Multi-Satellite Solution	68
3.4.2	Sensitivity Analysis of Earth Radiation Pressure	72
3.5	Effects of Longitudinal Variations in Albedo	76
3.6	Conclusions	81
4.	THE ADVANCED EARTH RADIATION PRESSURE MODEL	111
4.1	Introduction	111
4.2	Anisotropy and Diurnal Variations in Shortwave Earth Radiation .	112
4.3	The Advanced Earth Radiation Force Model	118
4.3.1	Satellite Data Supporting the Force Model	118
4.3.2	Mathematical Formulation of the Force Model	120
4.3.2.1	The Anisotropic Reflectance Model	120
4.3.2.2	The Diurnally Varying Albedo Model	125
5.	ORBITAL EFFECTS OF ANISOTROPIC AND TIME VARIANT SHORTWAVE EARTH RADIATION PRESSURE	163
5.1	Character of Nondiffuse and Time Variant Shortwave Earth Radiation Pressure	163
5.1.1	The Nature of an Unbiased Advanced Earth Radiation Model	163
5.1.2	The Flux Function	166
5.1.3	Variation over an Orbit and the Number of Earth Segments	169
5.1.4	Advanced Vs. Diffuse Models: Trajectory Comparisons	171

5.2 Orbital Effects on LAGEOS	173
5.3 Orbital Effects on GEOS-1	176
6. CONCLUSIONS	199
6.1 Diffuse Earth Radiation Pressure	199
6.2 Anisotropic and Diurnally Varying Earth Radiation Pressure . . .	201
6.3 Recommendations for Further Study	203
APPENDIX A: EARTH RADIATION PRESSURE ALGORITHM . . .	206
BIBLIOGRAPHY	211

LIST OF SYMBOLS

a	=	albedo
a_s	=	fraction of incident flux reflected by the satellite
\vec{a}	=	acceleration
A'	=	projected attenuated area of Earth element dA
A_c	=	cross sectional area of satellite
b_s	=	fraction of incident flux reemitted by the satellite
c	=	speed of light
dA	=	area of Earth element
e	=	emissivity
E_s	=	solar irradiance (Watts m ⁻²)
h	=	altitude
j	=	subscript referring to the jth Earth element
JD	=	Julian date of interest
L	=	radiance (Watts m ⁻² steradian ⁻¹)
M	=	exitance (Watts m ⁻²)
P_n	=	nth degree Legendre polynomial
r	=	distance from Earth element to satellite
\hat{r}	=	unit vector pointing from Earth element to satellite
r_{EARTH}	=	Earth-Sun distance
R	=	reflection law effectiveness coefficient

R_E	=	radius of the Earth
α	=	view angle
η_R	=	solar radiation satellite reflectivity
η_E	=	Earth radiation satellite reflectivity
θ_S	=	solar zenith angle
ξ	=	emission law effectiveness coefficient
ϕ	=	equatorial latitude
Φ	=	radiant flux (Watts)
ψ	=	azimuth angle
ω	=	frequency of periodic Earth radiation coefficients
Ω	=	solid angle (steradians)

CHAPTER 1

INTRODUCTION

1.1 *Introduction*

In its most general sense, radiation pressure refers to the momentum imparted to a body due to the impact, absorption, and re-emission of photons. The study of this subject easily predates the advent of artificial satellites, e.g. *Poynting* [1903], but the genesis of the space age has elevated this topic to a new level of relevance. Solar radiation pressure is a significant perturbative force on many satellites, and has even been suggested as a propulsive agent [*Garwin*, 1958]. The analysis of solar radiation pressure continues to this day, and a host of results and models have been presented pursuant to a better understanding of this force.

For terrestrial satellites, a natural extension of this study is the investigation of Earth radiation pressure. The Earth constitutes the next largest source of radiant energy for such bodies. For both solar and terrestrial radiation pressure, momentum is transmitted to a satellite by virtue of its interaction with intercepted photons. Special complications arise in the evaluation of Earth radiation pressure, however, in part because its source is an extended body located at a finite distance from the spacecraft. Terrestrial radiation pressure also possesses significant variations associated with the reflective and emissive properties of the Earth, the position of the Sun, and the position of the satellite. Earth radiation pressure,

unlike its solar counterpart, involves fluxes from two wavebands, the shortwave (reflected) and the longwave (emitted), each of which possesses distinct characteristics. Reflected radiation varies in a substantial and complex manner over the course of an orbit, as the satellite is exposed to lit and unlit portions of the Earth. Total longwave radiation, however, is nearly invariant from daylight to darkness [McCarthy and Martin, 1977; Barlier *et al.* 1986]. It is clear that the accurate determination of the radiation pressure due to the Earth's radiant flux involves complications not found in the representation of solar radiation pressure.

Terrestrial radiation pressure, as a phenomenon and as a modeling challenge, has been examined with varying degrees of rigor and interest, for more than 25 years. Early investigators often employed numerous simplifying assumptions which made the problem analytically tractable, but left significant questions unanswered. For example, in Wyatt [1962], only the radial component of Earth radiation pressure is considered. Levin [1962] assumes that the radiation reflected from an illuminated element of the Earth is independent of the solar position, and Sehnal [1963] assumes the Sun lies in the orbit plane. In general, these various assumptions are employed in order to simplify the surface integrals associated with the mechanics of radiative transfer from a three dimensional, partially illuminated body, i.e. the Earth. First Baker [1966], and later Lochry [1966], and Lautmann [1977a, 1977b] solve this "integral problem" through a clever choice of coordinate systems, but in all cases the resulting expressions are not well disposed to either parameterization or flexibility in the representation of the albedo and longwave emissivity. Many of these analytical and quasi-analytical models tend towards a certain inflexibility which precludes their utilization on a wide range of satellite

orbits and situations. *Smith* [1970] summarizes the drawbacks of purely analytical formalisms in the general treatment of Earth radiation pressure.

In the course of their studies, various investigators have predicted that the magnitude of the Earth radiation pressure should be approximately equal to 10% to 25% of the direct solar radiation pressure magnitude for most satellites [*Wyatt*, 1962; *Lochry*, 1966; *Sehnal*, 1969]. Measurements by accelerometers aboard drag make-up satellites like CACTUS tend to verify these estimates, and provide empirical evidence for the physical existence and orbital influence of the Earth radiation pressure [e.g. *Barlier et al.*, 1977]. At altitudes between 200 and 300 km, however, the magnitude of Earth radiation pressure can be 35% of the direct solar pressure. (See Section 3.2.)

A useful body of work exists relating observations of balloon satellites to Earth radiation pressure (e.g. *Fea* [1970]; *Zerbini* [1979]). From an analysis of Echo-1 and PAGEOS-1 data, *Prior* [1970] suggests that Earth radiation pressure is capable of being aliased into certain gravitational terms and density estimates. *Slowey* [1974], in an analysis of Dash-2 observations, illustrates the insufficiency of Earth radiation pressure models which use only a single, global value of the albedo.

A relatively recent renaissance in the examination of Earth radiation pressure has been occasioned by the advent of high precision laser ranging observations of geodetic satellites. In particular, analyses of such data indicate that the semimajor axis of the geodetic Earth satellite LAGEOS undergoes an unexplained mean secular decrease of approximately 1.1 mm/day, once all conventional force effects are taken into account [*Smith and Dunn*, 1980]. Large and complex periodic variations of

the semimajor axis about this mean secular decrease are also present. Various force effects, including Earth radiation pressure, have been proposed to explain this anomalous behavior. (See, for example, *Rubincam* [1980], and *Barlier et al.* [1986].) *Anselmo et al.* [1983] use a model which furnishes transverse impulses as the satellite passes over the terminator, to argue that diffuse Earth radiation pressure can account for the anomalous behavior of LAGEOS. *Rubincam and Weiss* [1985], provide an elegant analytical representation of the shortwave Earth radiation pressure through the use of a spherical harmonic model of albedo and an innovative treatment of the terminator. Their results, however, indicate that diffuse Earth radiation pressure cannot explain the "LAGEOS problem."

It has been suggested that the residual secular or periodic variations in the semimajor axis of LAGEOS may be driven by fluctuations in Earth radiation pressure arising from diurnal variations in albedo or the directional (anisotropic) nature of reflected sunlight. An early treatment of the effects of specular reflection can be found in *Wyatt* [1962]. *Morgan* [1984] attributes the deceleration to the effects of a morning-evening difference in albedo, coupled with specular reflection. *Barlier et al.* [1986] contend that anisotropic reflected radiation creates an along-track acceleration with the same periodicities as the drag-like agent, but of too small a magnitude. Analyses of CACTUS data indicate that anisotropic Earth radiation pressure is too small to account for the drag-like force on LAGEOS [*Walch*, 1984]. *Rubincam et al.* [1987] use an extreme model, in which Earth's northern hemisphere is assumed purely diffuse, and the southern hemisphere is assumed to reflect highly anisotropically, to argue that directional reflectance cannot explain the residual deceleration on LAGEOS.

As part of an ongoing effort to understand the responsible mechanism or

mechanisms driving this effect, and in the broader context of improving force models for precision orbit determination and enhancing the accurate estimation of geophysical parameters, an Earth radiation pressure model has been developed for the University of Texas orbit determination program (UTOPIA). The method for calculating the Earth radiation pressure is based on a numerical approach devised by *McCarthy and Martin [1977]*. This representation was chosen because of its generality, simplicity, and flexibility. As mentioned earlier, the other available models all tend to be either too inaccurate, incomplete, or inflexible to embrace the wide domain of satellite orbits and circumstances encountered in the field of precise orbit determination and geodetic research. Even the model proposed by *Rubincam and Weiss [1985]* is restricted primarily to low eccentricity satellites, a purely zonal albedo distribution, and diffuse radiation mechanics.

In the course of this dissertation, a purely diffuse earth radiation model is described and analyzed, as well as a more complex model which provides a realistic representation of anisotropic reflection and the diurnal variation in albedo. The advanced model is based on analyses of satellite radiometer measurements. For both representations, the orbital effects of Earth radiation pressure are explored, along with the influence of this force on the recovery of various estimated parameters. Although the LAGEOS anomaly provided the initial impetus for this study, the effects of Earth radiation pressure on other satellites are examined as well. The course of this study has established that satellites in highly eccentric orbits possess an unusually high sensitivity to this force. This conclusion is supported by analyses of tracking data obtained for the satellites GEOS-1 and GEOS-2.

It should be noted that *Rubincam* [1988] attributes the greater portion of the secular change in LAGEOS' semimajor axis to a thermal inertia force whose source is longwave Earth radiation. If this conclusion is sustained, then the secular part of the LAGEOS anomaly may be in large part solved. The source or sources of the large periodic variations about this mean are still uncertain.

1.2 *Solar Radiation, Earth Radiation, and Albedo*

A proper analysis of Earth radiation pressure requires some mention of the important radiative interactions between the Sun and the Earth. This is particularly useful in the understanding of albedo, which has a rigorous definition but an unfortunate affinity for loose usage.

Figure 1.1 shows the spectral irradiance of the Sun, and illustrates the extent of the solar radiation waveband. The Sun radiates in a portion of the ultraviolet, across the entire visible waveband, and in the near infrared. This involves all electromagnetic radiation with wavelengths between approximately 0.2 and 4.0 μm . In the following discussion, electromagnetic radiation emanating across this band, whether from the Sun, Earth, or any radiative source, is referred to as "broadband shortwave" radiation, or simply shortwave radiation.

When solar radiation encounters the Earth-atmosphere system, some percentage of this flux is immediately reflected and scattered as shortwave radiation. It is the radiative flux across the full extent of the shortwave band, and not merely the visible flux, which defines classical albedo. Specifically, the albedo of a surface is the ratio of the total broadband shortwave flux emanating from the

element in all directions, to the total broadband shortwave flux incident on the surface. (See Section 2.1.2 for a more complete definition.) It should be remembered that Earth albedo is primarily a measure of electromagnetic radiation in the visible and near infrared. To sufficient accuracy, the Earth radiates very little in the ultraviolet.

Not all the incident solar energy is reflected. The balance is absorbed and re-emitted in delayed fashion as longwave infrared radiation between $4 \mu\text{m}$ and $50 \mu\text{m}$ [Barlier *et al.*, 1978]. This is the "heat radiation" or emitted radiation of the Earth, and is considered separately from the near infrared constituent of the reflected radiation.

As mentioned earlier, a region of the Earth's surface gives rise to shortwave radiation only when it is in sunlight. This reflected flux exhibits considerable variation over the course of a day, due to the changing angle of solar incidence, and other properties of the Earth-atmosphere system. The longwave radiation is "on" even in darkness, and displays little diurnal variation, due to the large thermal inertia of the Earth.

The "terrestrial sphere" defined by the Earth-atmosphere system is certainly not homogeneous in composition or time-invariant in its qualities, and reacts to incident solar energy in a complex and not always intuitive fashion. In general, its properties vary according to season, geography, cloud cover, atmospheric composition, and surface type. The difficulty of the situation is alluded to in Levin [1962]. Fortunately, however, it is possible to utilize recent satellite radiometer measurements in a very direct and effective manner to characterize many of these phenomena, including diurnal variations in albedo and directional, or anisotropic reflection. Satellite radiometers measure the flux directly, as it wells from the

Earth-atmosphere system, and therefore as it impinges directly on any exo-atmospheric bodies.

Because the ultimate source of the Earth's radiant energy is the Sun, it is important to understand the nature of any variations in incident solar flux. The "solar constant" is often used to describe the total radiant output of the Sun. It is defined as the total radiant flux density of the Sun at one astronomical unit [Suits, 1975]. The term "solar constant" is advisedly used; recent analyses place the variation in this quantity at less than 0.1% [Willson and Hudson, 1988]. The solar constant is sometimes confused with the "local" solar irradiance, i.e. the solar flux density at a point in space corresponding to the location of the Earth at the time of interest. The latter quantity varies as the Earth-Sun distance changes, due to Earth's orbital eccentricity.

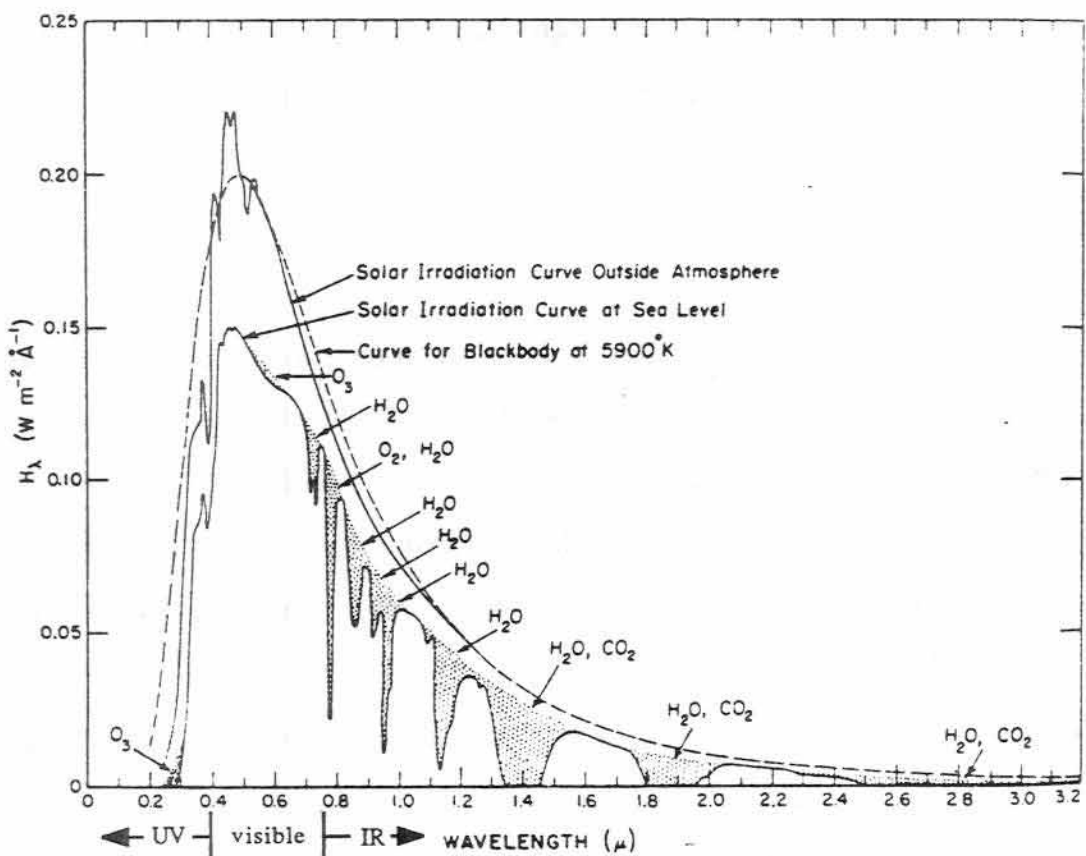


Fig. 1.1
The Solar Spectrum
(Source, *Gast* [1965])

CHAPTER 2

THE DIFFUSE EARTH RADIATION PRESSURE MODEL

2.1 *The Force Model*

The calculation of the diffuse Earth radiation pressure force on a satellite is based on the model by *McCarthy and Martin* [1977], in which the portion of the Earth's surface "visible" to the satellite is first divided into discrete segments. (See Figure 2.1.) The incremental acceleration due to diffuse shortwave and longwave radiation from each segment is calculated using Lambert's law of diffuse radiation, assuming that each segment may be approximated as a plane surface tangent to the center of the segment. It is also assumed that the satellite may be approximated as a sphere with constant cross-sectional area. The incremental accelerations are summed vectorially to obtain the aggregate effect. Details of this implementation are described in following sections, and an algorithmic summary of the calculations appears in Appendix A. Substantial elements of this representation were first described in *Knocke and Ries* [1987], and *Knocke, Ries, and Tapley* [1988].

2.1.1 *Satellite-intercepted Flux in terms of Radiances*

Consider the influence of a single Earth element. In the following discussion, an Earth "element" or "segment" refers to a reflecting/emitting surface with the same

planetary albedo and longwave emissivity as the Earth-atmosphere system at that point. (Planetary albedo refers to the albedo of the Earth-atmosphere system as seen from space.) To sufficient accuracy, this surface may be considered to be located at the surface of a spherical Earth with radius equal to the mean radius of the true Earth. Also, it is assumed that the influence of a given Earth segment may be approximated by the radiation interactions associated with a planar segment of equal surface area, tangent to the center of the Earth segment. This assumption tends to become more accurate as the number of segments per visible Earth area increases.

Suppose that a planar Earth element of area dA has a certain radiance L , which may be due to reflected radiation or longwave radiation. Radiance is chosen from among the myriad measures of electromagnetic radiation because it is the quantity most nearly measured directly by satellite radiometers. Radiance is defined as follows [Suits, 1975]:

$$L = \frac{d\Phi}{d\Omega \ dA \cos \alpha} \quad (2-1)$$

where L = radiance ($\text{Watts m}^{-2} \text{ sr}^{-1}$),

$d\Phi$ = portion of the total flux (Watts) radiated by Earth element dA
which is intercepted by A_i ,

$d\Omega$ = solid angle $= A_i / r^2$ (steradians),

r = distance from Earth element dA to intercepting element A_i ,

A_i = area which intercepts the flux, projected along the line from dA
to A_i ,

α = viewing angle (see Figure 2.2), the angle between the normal to
 dA and the line to A_i

Thus, the flux intercepted by A_i is:

$$\begin{aligned} d\Phi &= L d\Omega dA \cos \alpha \\ &= L \frac{A_i}{r^2} dA \cos \alpha \end{aligned} \quad (2-2)$$

Consider now the flux which must be intercepted by a spherical satellite of radius R_s . Consider also a portion of the satellite surface ΔA_s , whose normal makes an angle α_s with the line from dA to ΔA_s , as shown in Figure 2.3. The flux intercepted by ΔA_s is:

$$\Delta(d\Phi) = L \frac{\Delta A_s}{r^2} \cos \alpha_s dA \cos \alpha. \quad (2-3)$$

(It is assumed that $r \gg R_s$.) It can be shown, after integrating over the satellite hemisphere which faces dA , that the total flux from dA intercepted by the satellite is:

$$d\Phi = L \frac{A_c}{r^2} dA \cos \alpha, \quad (2-4)$$

where $A_c = \pi R_s^2$, the cross sectional area of the satellite. This result, in fact, applies to any satellite of cross sectional area A_c , and need not be restricted to spherical satellites.

Recall that radiance is a wavelength-dependent quantity, and that the Earth radiates in two spectral bands, the shortwave and the longwave. Thus, to sufficient accuracy, the total satellite-intercepted flux due to a single Earth element dA may be expressed as follows:

$$\begin{aligned} d\Phi_{TOT} &= d\Phi_{SW} + d\Phi_{LW} \\ d\Phi_{TOT} &= (L_{SW} + L_{LW}) \frac{A_c}{r^2} dA \cos\alpha \end{aligned} \quad (2-5)$$

where L_{SW} = total broadband shortwave radiance of dA ,
 L_{LW} = longwave radiance of dA .

2.1.2 Shortwave Radiance in terms of Albedo: Lambert's Law

The above expressions are fairly general representations of the satellite-intercepted radiation fluxes in terms of radiances. Consider now the shortwave flux, and its relation to classical albedo.

The albedo a of element dA is defined as follows:

$$a = \frac{\Phi_{OUT_H}}{\Phi_{IN}}, \quad (2-6)$$

where Φ_{OUT_H} = total shortwave flux out of dA (i.e. the flux in the wavelengths from $0.2 \mu m$ to $4 \mu m$ intercepted by a hemisphere centered at dA and arcing above it. See Figure 2.2.)

Φ_{IN} = total solar flux ($0.2 \mu m$ to $4 \mu m$) incident on dA .

Referring to Equation (2-2), the total hemispherical shortwave flux out of dA is:

$$\begin{aligned}
 \Phi_{\text{OUT}_H} &= \int_{\text{hem.}} d\Phi_{\text{SW}} \\
 &= \int_{\text{hem.}} L_{\text{SW}} dA \cos\alpha \frac{A_i}{r^2} \\
 \Phi_{\text{OUT}_H} &= dA \int_{\text{hem.}} L_{\text{SW}} \cos\alpha \frac{r d\alpha r \sin\alpha d\psi}{r^2} \\
 &= dA \int_{\psi=0}^{2\pi} \int_{\alpha=0}^{\frac{\pi}{2}} L_{\text{SW}} \sin\alpha \cos\alpha d\alpha d\psi. \tag{2-7}
 \end{aligned}$$

where $\int_{\text{hem.}}$ = integration over the hemisphere,
 ψ = azimuth angle of A_i , (See Figure 2.2.)

In order to proceed from this point, one must know how the radiance L_{SW} varies with the view angle α and the azimuth ψ . In general, this is a function of surface properties, but it is known that all reflecting surfaces exhibit characteristics situated between two extremes. One extreme is defined by specular (mirrorlike) reflection, where L_{SW} is strongly dependent on the orientation angles. At the other extremity is purely diffuse reflection, also known as isotropic reflection, in which the radiance is constant for all values of α and ψ . Most surfaces exist somewhere between these limits, and must be described in terms of more complicated bidirectional reflectance laws.

Many investigators state that if one were to consider the Earth-atmosphere system as a combination of purely specular components and purely diffuse components, the specular shortwave flux would amount to 1% to 10% of the diffuse shortwave flux [Wyatt, 1962; Baker, 1966; Sehnal, 1970]. This makes

intuitive sense, as the only sources of true specular reflection on the Earth should be calm bodies of water such as lakes. Also, satellite radiance measurements reveal that all Earth "surface" elements (e.g. snow, ice, cloud, and ocean) behave more or less diffusely at low solar zenith angles, and anisotropically only at high solar zenith angles [Taylor and Stowe, 1984]. Because the illumination of an element varies as the cosine of the solar zenith angle, one might conclude that any portion of the Earth-atmosphere system is likely to behave quite diffusely during periods of high illumination, and become anisotropic only during intervals of low illumination, when the Earth radiation pressure is small in any event. All this lends some weight to the argument that Earth radiation pressure may be calculated to acceptable accuracy using a diffuse Earth model. (See Chapters 4 and 5 for an analysis of the effects of anisotropy on Earth radiation pressure.)

On the strength of these arguments, it is assumed, in accordance with *McCarthy and Martin, [1977]* that shortwave Earth radiation may be modeled as purely diffuse. Section (2.1.3) deals with the longwave component, which also is assumed to be purely diffuse. Thus, the Earth-atmosphere system qualifies as a Lambertian surface (purely diffuse reflector and emitter) and may be described via Lambert's law:

$$L(\alpha, \psi) = L, \text{ a constant.}$$

Equation (2-7) may now be integrated, as follows:

$$\Phi_{\text{OUT}_H} = L_{\text{SW}} dA \int_{\psi=0}^{2\pi} \int_{\alpha=0}^{\frac{\pi}{2}} \sin\alpha \cos\alpha d\alpha d\psi \\ = \pi L_{\text{SW}} dA \quad (2-8)$$

The flux exiting dA has been defined. In order to relate albedo and shortwave radiance through Equation (2-6), the total solar flux incident on the surface must also be evaluated. The total amount of solar flux incident on a (planar) Earth element is:

$$\Phi_{\text{IN}} = E_S \cos\theta_S dA \quad (2-9)$$

where Φ_{IN} = solar flux incident on dA ,
 E_S = local solar irradiance (Watts m^{-2}),
 θ_S = solar zenith angle,
 dA = area of Earth element.

Both θ_S and dA are illustrated in Figure 2.2. Recall that E_S is the total radiant flux density of the Sun at 1 A.U. If the Sun is assumed to be an isotropic source, the total solar flux is related to E_S as follows:

$$E_S = \frac{\Phi_{\text{SUN}}}{4\pi r_{\text{EARTH}}^2} \quad (2-10)$$

where Φ_{SUN} = total solar flux,
 r_{EARTH} = Earth-Sun distance.

(Note that $4\pi r_{\text{EARTH}}^2$ is the area of a spherical surface of radius r_{EARTH} which intercepts all of the solar flux.)

Combining Equations (2-6), (2-8), and (2-9) yields the following expression for the albedo of a diffusely reflecting surface in terms of its radiance:

$$a = \frac{\pi L_{SW}}{E_S \cos\theta_S}.$$

Thus,

$$L_{SW} = \frac{a E_S \cos\theta_S}{\pi}. \quad (2-11)$$

2.1.3 Longwave Radiance in terms of Emissivity

Emissivity is used to characterize the longwave infrared flux in the UTOPIA model of Earth radiation pressure. The emissivity of an Earth element dA is defined as follows:

$$e = \frac{M_{LW}}{M_B} \quad (2-12)$$

where e = emissivity (dimensionless),

M_{LW} = longwave exitance of dA (Watts m $^{-2}$),

M_B = exitance of dA , assuming the Earth is an ideal black body (perfect absorber) which re-emits all the incident solar radiation isotropically (Watts/m $^{-2}$).

Exitance is defined as follows [Suits, 1975]:

$$M = \frac{\Phi}{A}$$

where Φ = total flux exiting a surface A .

Thus,

$$\begin{aligned}
 M_B &= \frac{\text{earth-intercepted solar flux}}{\text{total surface area of the earth}}, \\
 &= \frac{E_S \pi R_E^2}{4\pi R_E^2}, \\
 M_B &= \frac{E_S}{4} \quad (2-13)
 \end{aligned}$$

where R_E = radius of the Earth. Now M_{LW} must be converted into radiance. Assuming dA is a diffuse emitter:

$$\begin{aligned}
 M_{LW} &= \frac{\Phi_{LW}}{dA} \\
 &= \frac{dA \int_{\psi=0}^{2\pi} \int_{\alpha=0}^{\frac{\pi}{2}} L_{LW} \sin\alpha \cos\alpha d\alpha d\psi}{dA} \\
 M_{LW} &= \pi L_{LW} \\
 L_{LW} &= \frac{M_{LW}}{\pi} \quad (2-14)
 \end{aligned}$$

Thus,

$$L_{LW} = \frac{e M_B}{\pi} \quad (2-15)$$

where $M_B = E_S / 4$.

As with the reflected flux, the emitted flux is assumed to be diffuse. For most bodies, and especially for the Earth, this assumption is quite good. The

nature of the Earth-emitted flux is that of "delayed" (and therefore nearly isotropic) thermal reradiation of the incident flux.

2.1.4 Diffuse Earth Radiation Pressure Acceleration on a Spherical Satellite

Combining Equations (2-5), (2-11), and (2-15) yields the following expression for the total diffuse flux intercepted by a satellite with cross sectional area A_c , located at a distance r from a radiating element dA possessing albedo a and emissivity e :

$$d\Phi_{TOT} = (a E_S \cos\theta_S + e M_B) \frac{A_c}{\pi r^2} \cos\alpha dA. \quad (2-16)$$

Recall that: E_S = local solar irradiance,

$$M_B = E_S / 4,$$

$$\alpha = \text{view angle}.$$

Dividing the flux by the cross sectional area and the speed of light c produces a quantity commonly referred to as the "radiation pressure":

$$dp = \frac{d\Phi_{TOT}}{c A_c} \quad (2-17)$$

This quantity is introduced primarily as a computational convenience, and as a point of reference to the works of other investigators.

2.1.4.1 The Satellite Model: Lochry's Radiation Augmentation Factor

The total force engendered by the satellite-intercepted radiant flux has three

primary components. The first constituent is the "black body" force, i.e. the force which the body would experience if it were a perfect absorber. This force always points in the direction of the incident flux, regardless of the geometry of the intercepting body, or its reflective and emissive properties. The second component is the force arising from reflected flux. In general, this force is not directed along the line of incident flux. (For example, in the case of diffuse reflection from a planar surface, the reflected flux force is directed normal to the surface.) The third constituent of the total radiation pressure acceleration is that due to absorbed radiation re-emitted from the satellite by thermal means. As with the reflected flux, the dynamical influence of emitted radiation is dependent on the directional properties of the flux and the geometry of the body.

In the context of modeling the dynamic effect of these radiation phenomena, Lochry defines a useful "augmentation factor" K [Lochry, 1966]:

$$K = 1 + a_s R + b_s \xi$$

where the unity term refers to the "black body" force mentioned above, and

- a_s = fraction of the total incident flux reflected by the satellite,
- R = reflection law effectiveness coefficient,
- b_s = fraction of the total incident flux emitted by the satellite,
- ξ = emission law effectiveness coefficient.

R and ξ are functions of the body's reflection and emission laws (e.g. specular or diffuse), geometry, and orientation. Often, the portion of the augmentation factor not associated with the black body term is combined into a single parameter η and referred to under the misnomer of "satellite reflectivity". Hence:

$$K = 1 + \eta_E ,$$

where

$$\eta_E = a_S R + b_S \xi ,$$

and where η_E is the (combined reflective and emissive) "satellite reflectivity" for the Earth radiation calculations.

The primary utility of the augmentation factor lies in describing the dynamical effect of radiation pressure on a sphere, a flat plate oriented normal to the flux, or any other configuration in which the resultant radiation pressure acceleration is along the line of incident flux. (For a given Earth element, as illustrated in Figure 2.2, the line of incident flux is defined by the vector \hat{r} .) In this context, an "effectiveness coefficient" is a measure of the efficiency with which satellite-reflected or -emitted flux generates thrust along the element-satellite line. For example, a specularly reflecting flat plate normal to the incident flux has a reflection effectiveness measure of $R = 1$. This indicates that all of the reflected flux is bounced back towards the source. According to Lochry, a diffusely reflecting sphere has a reflection law effectiveness of $R = 4/9$. The emission law effectiveness coefficient is simpler to characterize. If the satellite reradiates energy "promptly", i.e. before the occurrence of substantive heat transfer, then the emissions are diffuse, with dynamical effects identical to those of diffusely *reflected* flux. If the intercepting body is a perfect conductor, then the emitted radiation is "delayed" isotropic reradiation. Because the body emanates equally in all directions, the net dynamic effect is zero, and $\xi = 0$. Thus [Lochry, 1966]:

$$0 \leq \xi \leq R_d ,$$

where R_d is the reflection law effectiveness coefficient for a properly configured

diffusely reflecting body. In this instance, "properly configured" means any combination of body geometry and orientation such that the net radiation pressure acceleration lies along the line of incident flux.

The range of K may be deduced from the above considerations, and by assuming, reasonably, that all the incident energy is either reflected or emitted (i.e. $a_s + b_s = 1$). Thence:

$$1 \leq K \leq 2 ,$$

where unity refers to the case of total absorption, and $K=2$ corresponds to the case of a flat, perfect reflector oriented normal to the incident flux ($\alpha = 1, R = 1$).

In sum, the acceleration experienced by a properly configured satellite of mass m , due to diffuse shortwave and longwave radiation emanating from a single Earth element is:

$$d\vec{a} = K dp \frac{A_c}{m} \hat{r}, \quad (2-18)$$

where dp = radiation pressure (Equation 2-17). Finally:

$$d\vec{a} = K (a E_s \cos \theta_s + e M_B) \frac{A_c \cos \alpha dA}{m c \pi r^2} \hat{r}, \quad (2-19)$$

where \hat{r} is the unit vector pointing from the Earth element to the satellite.

2.1.4.2 The Total Acceleration due to all Earth Elements

A rigorous evaluation of the total effect of Earth radiation pressure due to flux from the entire "effective" area of the Earth (defined as a "cap" whose apex is located at the subsatellite point and includes all points on the Earth in direct line of

sight to the satellite) requires the integration of Equation (2-19) over this "effective cap". As suggested earlier, analytical evaluation of such an integral always requires the specification of an albedo/emissivity model, and usually involves various coordinate transformations as well, as in *Lochry* [1966]. This reduces the generality of the result, because any change in the albedo/emissivity model induces significant alterations in the final form of the expressions. To avoid these difficulties, McCarthy and Martin replace the integration with a simple summation over a small number of discrete Earth elements.

Thus, the total acceleration on a spherical satellite of constant cross sectional area and invariant reflective and emissive properties, due to diffuse radiation from all "effective" Earth elements, may be approximated as follows:

$$\vec{a} = \sum_{j=1}^N d\vec{a}_j, \quad (2-20)$$

where

$$d\vec{a}_j = \frac{K}{c\pi} \left[(\tau a E_s \cos \theta_s + e M_B) \frac{A_C}{m} \frac{dA \cos \alpha}{r^2} \hat{r} \right]_j \quad (2-21)$$

- and
- | | | |
|-----------|---|--|
| N | = | total number of Earth elements, |
| j | = | subscript referring to the jth Earth element, |
| τ | = | 0 if the center of element j is in darkness,
1 if the center of element j is in daylight, |
| \hat{r} | = | unit vector pointing from the center of the jth Earth
element to the satellite, |
| A_C | = | cross sectional area of satellite. |

Note that if the center of an Earth element is in darkness, the shortwave (reflected)

flux is set to zero, while the longwave flux continues to act on the satellite.

It is clear that the calculations in Equations (2-20) and (2-21) must be performed in a manner which tends to approximate the analytical integration as closely as possible. This topic is discussed in Section 2.1.5.1.

It would appear that Equations (2-20) and (2-21) are not very general with regard to satellite properties. However, even for geometrically complex satellites of high reflectivity, it is likely that a major portion of the Earth radiation influence can be described by the "black body" term alone ($K = 1$). Recall that this force is always directed along the element-satellite line, and, except for cross sectional area, is independent of satellite configuration. Any Earth radiation pressure forces not acting along the element-satellite line are primarily due to reflection (many satellites emit nearly isotropically in the infrared) the effect of which is scaled by a factor, a_s , usually much less than unity. For example, the solar radiation reflectivities used in UTOPIA for GEOS-1, LAGEOS, and Starlette are 0.1, 0.13, and 0.12, respectively. SEASAT, with a reflectivity of 0.5, represents an extreme and somewhat pathological case. It is clear that any forces connected with reflected flux will generally be much less than the "black body" influence. Thus, a reasonable approximation to the Earth radiation pressure acceleration on a non-spherical satellite would be represented by Equations (2-20) and (2-21), in which the cross sectional area varies with the direction from which it is viewed.

2.1.5 *Implementation in UTOPIA*

2.1.5.1 *Determination of the Earth Segment Areas*

In order to perform the summation in Equation (2-20) such that the result approximates an analytical integration of Equation (2-19), McCarthy and Martin divide the Earth's effective cap into segments which have equal projected areas. The UTOPIA version expands on this concept by organizing the effective cap into segments which have equal projected, *attenuated* areas [Knocke and Ries, 1987]. The projected, attenuated area is defined as the element area dA multiplied by the cosine of the view angle and divided by π times the square of the element-satellite distance, i.e.:

$$A' = \frac{dA_j \cos\alpha_j}{\pi r_j^2} \quad (2-22)$$

where A' is the projected, attenuated area of dA_j . By thus defining a weighting factor which is the same for all Earth elements, several mathematical operations are saved for each evaluation of Equation (2-21).

Consider a differential strip of the Earth's surface, defined by a given value of ζ and a given value of r . (See Figure 2.4.) This differential strip is located somewhere on the effective cap, the limits of which are defined by angle ζ_M , where

$$\zeta_M = \sin^{-1} \frac{R_E}{r_s}, \quad (2-23)$$

and R_E = radius of the Earth,

r_s = distance from the center of the Earth to the satellite.

The area of the differential strip, projected along the line to the satellite, is: .

$$\begin{aligned} dS \cos \alpha &= (r d\zeta) (2 \pi r \sin \zeta) \\ &= 2\pi r^2 \sin \zeta d\zeta \end{aligned}$$

Integrating between limits ζ_{i-1} and ζ_i defines a "ring" of finite size. (See Figure

A.1, Appendix A.) If this ring is divided into N_{S_i} units, one obtains the following expression for the attenuated, projected area of an arbitrary Earth element j :

$$A' = \frac{\int_{\zeta_{i-1}}^{\zeta_i} 2\pi r^2 \sin \zeta d\zeta}{N_{S_i} \pi r^2}$$

$$A' = \frac{2}{N_{S_i}} (\cos \zeta_{i-1} - \cos \zeta_i) \quad (2-24)$$

where N_{S_i} = number of segments in ring,

ζ_{i-1}, ζ_i = limits of ring.

The projected, attenuated area of the subsatellite cap is determined by substituting the following into Equation (2-24): $\zeta_{i-1} = \zeta_0 = 0$, $\zeta_i = \zeta_1$, $N_{S_1} = 1$. Thence:

$$A' = 2 (1 - \cos \zeta_1). \quad (2-25)$$

Because A' is the same for all segments, the total projected, attenuated area of the entire effective cap is:

$$A'_{EC} = N 2 (1 - \cos \zeta_1) \quad (2-26)$$

where N is the total number of segments. This quantity may also be derived from Equation (2-25), in which the entire effective cap is treated as a single subsatellite segment. In this case, $\zeta_1 = \zeta_M$, and

$$A'_{EC} = 2 (1 - \cos \zeta_M). \quad (2-27)$$

Equating expressions (2-26) and (2-27) produces the following equation for ζ_1 :

$$\cos \zeta_1 = \frac{N - 1 + \cos \zeta_M}{N}, \quad (2-28)$$

where ζ_M is defined in Equation (2-23).

Consider a configuration in which the entire effective cap is subdivided into n_{ring} rings, plus a central cap. In this case,

$$\zeta_M = \zeta_{n_{ring} + 1},$$

and ζ_1 may be determined from Equation (2-28). The remaining angles $\zeta_2, \zeta_3, \dots, \zeta_{n_{ring}}$ must also be calculated, in order to determine the location of all the Earth elements. If the first ring contains 6 elements and each succeeding ring contains 6 more elements than the previous ring, the following recursion holds:

$$\text{for } i = 2, \dots, n_{ring}: \quad k = k + 6(i-1),$$

$$\cos(\zeta_i) = k \cos(\zeta_1) - k + 1.$$

The nominal diffuse configuration in UTOPIA uses two rings, each subdivided as described above. The first ring has six elements, and the second has 12 elements, for a total of 19 elements, including the central cap. Tests of the model indicate that increasing the total number of elements beyond this point does not significantly affect the resulting magnitude.

Knowledge of the ζ_i permits the calculation of the vector from the Earth's center to a given Earth surface segment, and thence the vector pointing from the segment to the satellite, i.e. \hat{r} . This specifies the direction of the incremental acceleration $d\vec{a}$. The means by which this is accomplished, along with an algorithmic overview of the Earth radiation model, is included in Appendix A.

In summary, then, the UTOPIA version of Equation (2-21) is:

$$d\vec{a}_j = K A' \frac{A_c}{m c} [(\tau a E_S \cos \theta_{S_j} + e M_B) \hat{r}]_j. \quad (2-29)$$

where $A' = 2(1 - \cos \zeta_1)$,

$$\cos \zeta_1 = \frac{N - 1 + \cos \zeta_M}{N},$$

$$\zeta_M = \sin^{-1}(R_E / r_s).$$

Equation (2-29), summed over the active elements, is intended to be an accurate approximation of Equation (2-19), integrated analytically. In the limiting case of constant albedo, constant emissivity, and uniform illumination, an analytical integration of (2-19) is possible. For this case, the UTOPIA model and the analytical integration produce comparable magnitude estimates [Knocke and Ries, 1987].

2.2 *The Earth Radiation Model*

The force model described above is completely independent of the geographical and temporal distribution of the albedo and emissivity of the Earth. In their Earth radiation model, McCarthy and Martin define an Earth-fixed set of blocks which covers the surface of the Earth. Each block possesses its own value of albedo and infrared emission. This arrangement has the advantage of including both longitudinal and latitudinal variations in the radiation of the terrestrial sphere. However, as McCarthy and Martin themselves admit, the table lookups are cumbersome, and arrangements must be made to smooth out the effects of the discontinuities at block boundaries. Also, the satellite-derived values used by McCarthy and Martin appear to be annual averages; aside from the very small seasonal variation in the local solar irradiance, no attempt is made to include a time

dependent Earth radiation model. A more suitable device would be a minimally parameterized analytical approximation of the seasonal and positional distribution of the Earth's radiation. This is the goal of the UTOPIA Earth radiation modeling effort.

Satellite data indicate that the albedo and emissivity of the terrestrial sphere display strong variations in latitude, and somewhat weaker longitudinal dependencies [Lochry, 1966]. In addition, it is likely that the Earth's rotation tends to average out any long period orbital effects engendered by longitudinal variations in Earth radiation. On the basis of these arguments, many investigators [Wyatt, 1962; Lochry, 1966; Lautmann, 1977b], use albedo and emissivity models which are exclusively latitude dependent. Also, note that the most efficient general analytical representation of the Earth radiation is probably a spherical harmonic expansion similar to that used in defining the gravity potential of the Earth. For these reasons, the nominal UTOPIA model uses a purely zonal representation of the geographical distribution of Earth radiation. The nominal UTOPIA inputs include no explicit provision for tesseral and sectorial Earth radiation parameters, although there is no reason why these terms could not be embraced with a minimum of difficulty. A relatively simple modification was required for the calculation of the 4 x 4 albedo field discussed in Section 3.5.

Analyses of Earth radiation budgets by *Stephens et al.*, [1981] suggest that the albedo and emissivity may be modeled adequately using zeroeth, first and second degree zonal harmonics only, where the first zonal coefficient is periodic with a period of 365.25 days. Figures 2.5, 2.6, 2.7, and 2.8 show Stephen's seasonal averages and least squares fits for each season, using a second degree

zonal model [Knocke and Ries, 1987]. The model appears to be good enough to simulate both the latitudinal variation in Earth radiation and the seasonally dependent latitudinal asymmetry. The fit could be improved with a higher order model, particularly near the equator.

In summary, the nominal albedo and emissivity models may be represented as follows:

$$a = a_0 + a_1 P_1(\sin\phi) + a_2 P_2(\sin\phi), \quad (2-30)$$

$$e = e_0 + e_1 P_1(\sin\phi) + e_2 P_2(\sin\phi), \quad (2-31)$$

$$\text{where } a_1 = c_0 + c_1 \cos(\omega(JD - t_0)) + c_2 \sin(\omega(JD - t_0)), \quad (2-32)$$

$$e_1 = k_0 + k_1 \cos(\omega(JD - t_0)) + k_2 \sin(\omega(JD - t_0)), \quad (2-33)$$

$P_n(\sin\phi)$ = nth degree Legendre polynomial with argument $\sin\phi$,

ϕ = latitude of the point of interest on the Earth,

JD = Julian date of interest,

t_0 = epoch of the periodic terms,

ω = frequency of the periodic terms (period = 365.25 days).

The albedo and emissivity parameters for this model are $a_0, c_0, c_1, c_2, a_2, e_0, k_0, k_1, k_2, e_2$. Note that the time dependent nature of the albedo and emissivity parameters is limited to purely seasonal effects.

2.3 The Partial Derivatives of the Acceleration

The diffuse Earth radiation pressure model has been developed in the context of parameter estimation and orbit determination tasks. In order to permit the estimation of the Earth radiation parameters, the partial derivatives of the Earth

radiation acceleration with respect to η_E and also with respect to the albedo and emissivity coefficients are calculated as part of the UTOPIA implementation. The determination of these partials is formally trivial, since the Earth radiation parameters appear as explicit linear multiplicative factors through Equations (2-21), (2-30), (2-31), (2-32), and (2-33). For example, the partial with respect to η_E is:

$$\frac{\partial \vec{a}}{\partial \eta_E} = A' \frac{A_C}{m c} \sum_{j=1}^N [(\tau a E_S \cos \theta_{Sj} + e M_B) \hat{f}]_j.$$

This is easily derived from Equations (2-20) and (2-29), where $K = 1 + \eta_E$. The exact partials with respect to the Earth radiation parameters are accumulated along with the incremental accelerations themselves.

In the analytical formalism of the linear estimation problem, the partial derivatives of the total satellite acceleration, including the contribution of Earth radiation pressure, with respect to the satellite position and velocity are required for the estimation of initial conditions [Tapley *et al.*, 1985]. In this regard, it should be noted that the acceleration due to Earth radiation is not dependent on the satellite's velocity, making this portion of the partial derivative identically zero. Obviously, the Earth radiation force is dependent on the satellite's position. However, the satellite's initial conditions are so weakly affected by Earth radiation pressure that the contribution of the Earth radiation partial with respect to the satellite's position is minuscule. This fact, combined with the gruesome algebraic complexities of an exact representation, and an attendant computational overhead potentially as large as that associated with the calculation of the force itself, has led to the development of an approximate partial. For the purpose of calculating this partial derivative, the albedo and emissivity are assumed not to vary with satellite

position. Only a single Earth surface element, consisting of the entire effective cap, is utilized. In this case, the (approximate) acceleration due to Earth radiation pressure may be expressed as follows:

$$\vec{a} = A' B C \hat{r}_S,$$

where A' = projected, attenuated area of the effective cap,

$$B = \tau a E_S \cos \theta_S + e M_B \quad [\text{Equation (2-21)}]$$

$$C = (1+\eta_E) A_C / m$$

\hat{r}_S = unit vector to the satellite.

The partial with respect to satellite position is, therefore:

$$\frac{\partial \vec{a}}{\partial \vec{r}_S} = C \left\{ B \hat{r}_S \frac{\partial A'}{\partial \vec{r}_S} + A' \hat{r}_S \frac{\partial B}{\partial \vec{r}_S} + A' B \frac{\partial \hat{r}_S}{\partial \vec{r}_S} \right\}.$$

The explicit dependence of A' on the satellite position is determined in the following manner:

$$A' = 2(1-\cos \zeta_M) = 2 \left(1 - \frac{\sqrt{r_S^2 - R_E^2}}{r_S} \right).$$

The quantity B is dependent on the satellite position through the cosine of the solar zenith angle, as follows:

$$\cos \theta_S = \hat{r}_S^T \hat{r}_{\text{sun}},$$

where \hat{r}_{sun} = the unit vector pointing towards the Sun,

T = matrix transpose operator.

It can be shown that the partial derivative of the approximate acceleration with respect to the satellite position vector is:

$$\frac{\partial \vec{a}}{\partial \vec{r}_S} = (1+\eta_E) \frac{A_C}{m} \left\{ \begin{array}{l} \frac{-2R_E^2}{r_S^2 \sqrt{r_S^2 - R_E^2}} [\tau a E_S \cos \theta_S + e M_B] \hat{r}_S \hat{r}_S^T \\ + A' \tau a E_S \hat{r}_S \hat{r}_{\text{sun}}^T \left(\frac{[I] - \hat{r}_S \hat{r}_S^T}{r_S} \right) \\ + A' [\tau a E_S \cos \theta_S + e M_B] \left(\frac{[I] - \hat{r}_S \hat{r}_S^T}{r_S} \right) \end{array} \right\} \quad (2-34)$$

where $[I]$ = the Identity matrix.

This equation, although approximate, is complete, requiring no summation over the effective elements. The values for a , e , and θ_S used in the above equation are those determined for the subsatellite cap during the nominal calculation of the Earth radiation pressure. As mentioned earlier, the influence of this partial derivative is negligible.

2.4 Conclusions

The model and implementation described in this chapter represent an effective, efficient, and extremely flexible representation of the major characteristics of diffuse Earth radiation pressure. It includes a number of improvements to the original model proposed by McCarthy and Martin, but retains the desirable qualities of that seminal effort. In addition, as the following chapters will illustrate, it provides a useful foundation for advanced work in the area of Earth radiation pressure modeling.

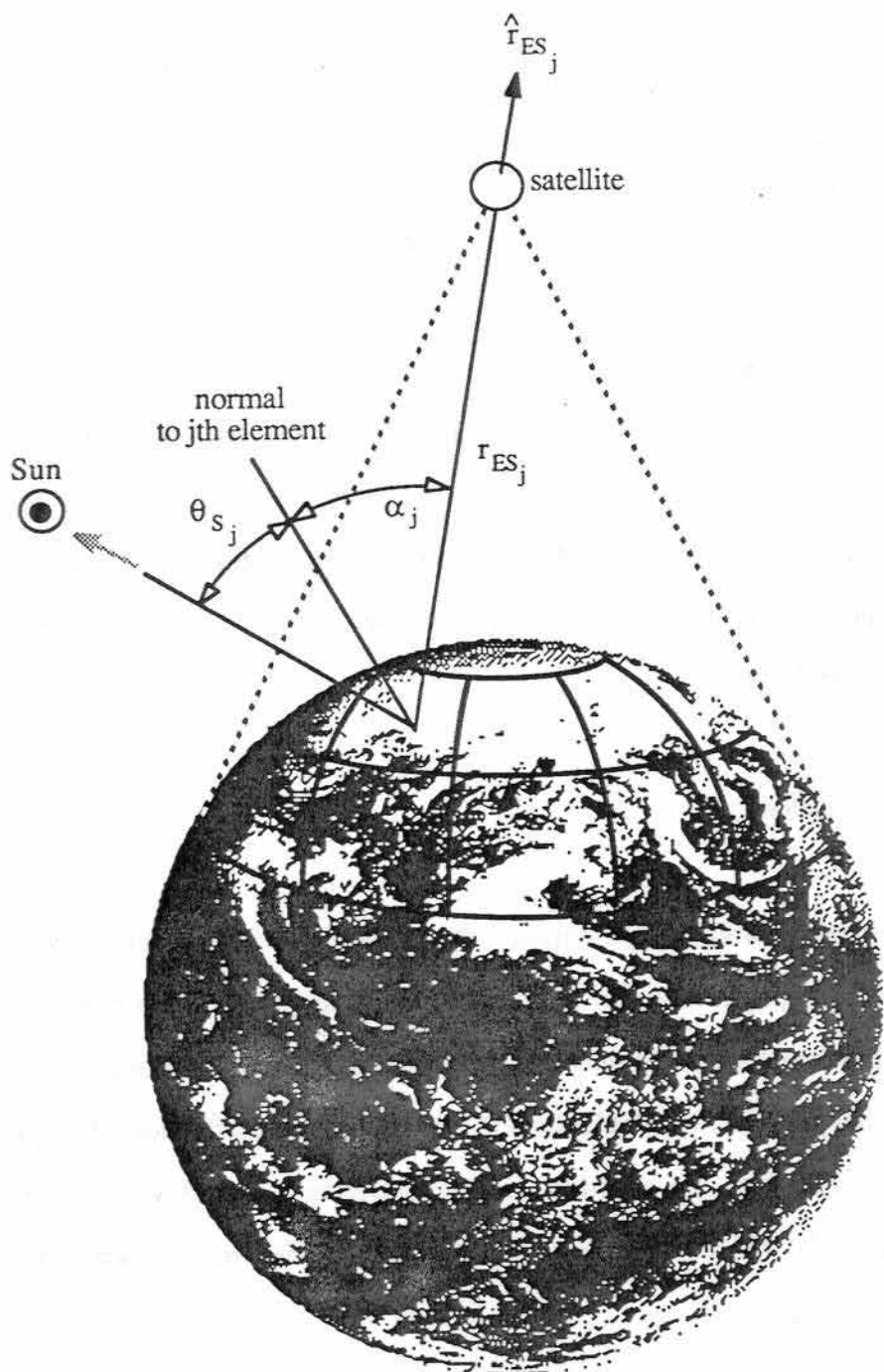


Fig. 2.1

The Earth Radiation Pressure Model

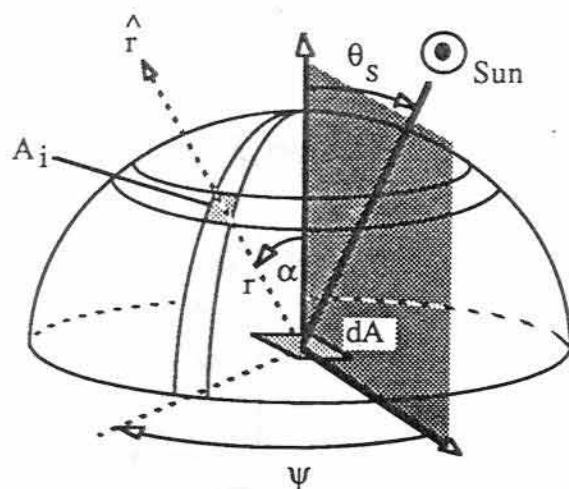


Fig. 2.2

Radiance Geometry

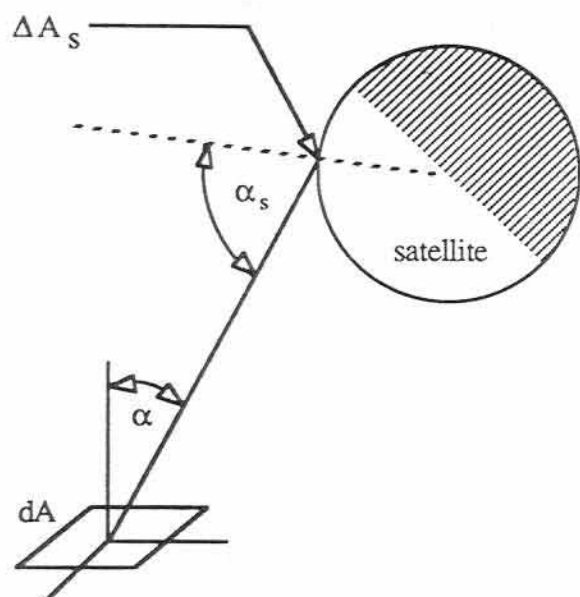


Fig. 2.3

Satellite Intercepting Flux from a Planar Element

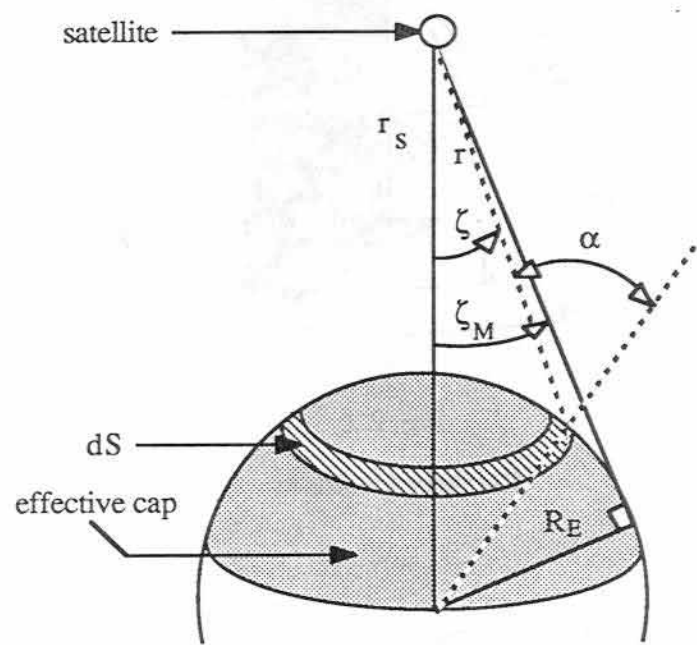


Fig. 2.4
Calculation of the Projected, Attenuated Area

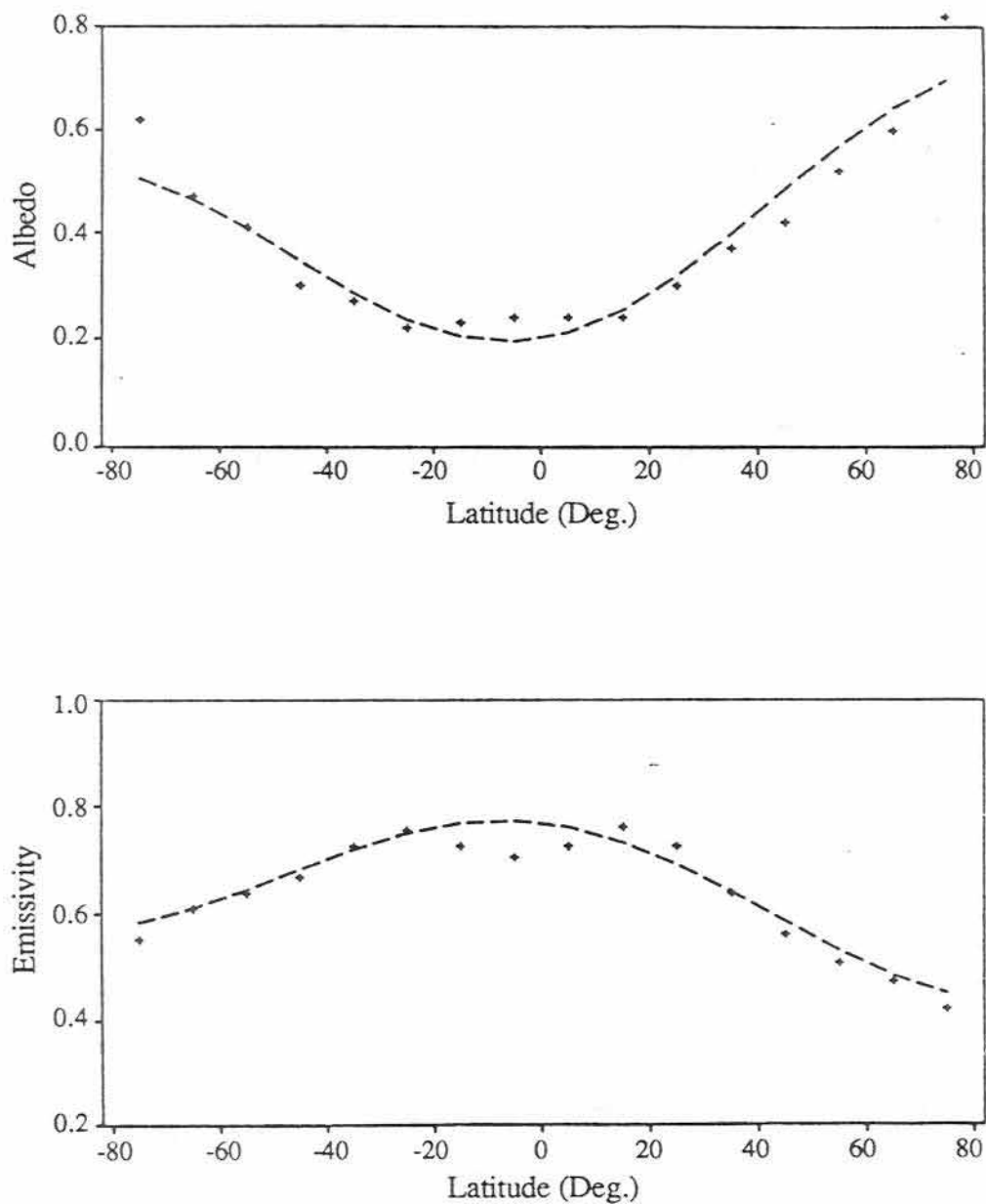


Fig. 2.5

Earth Radiation Data and Model: Winter

(Source, *Knocke and Ries [1987]*)

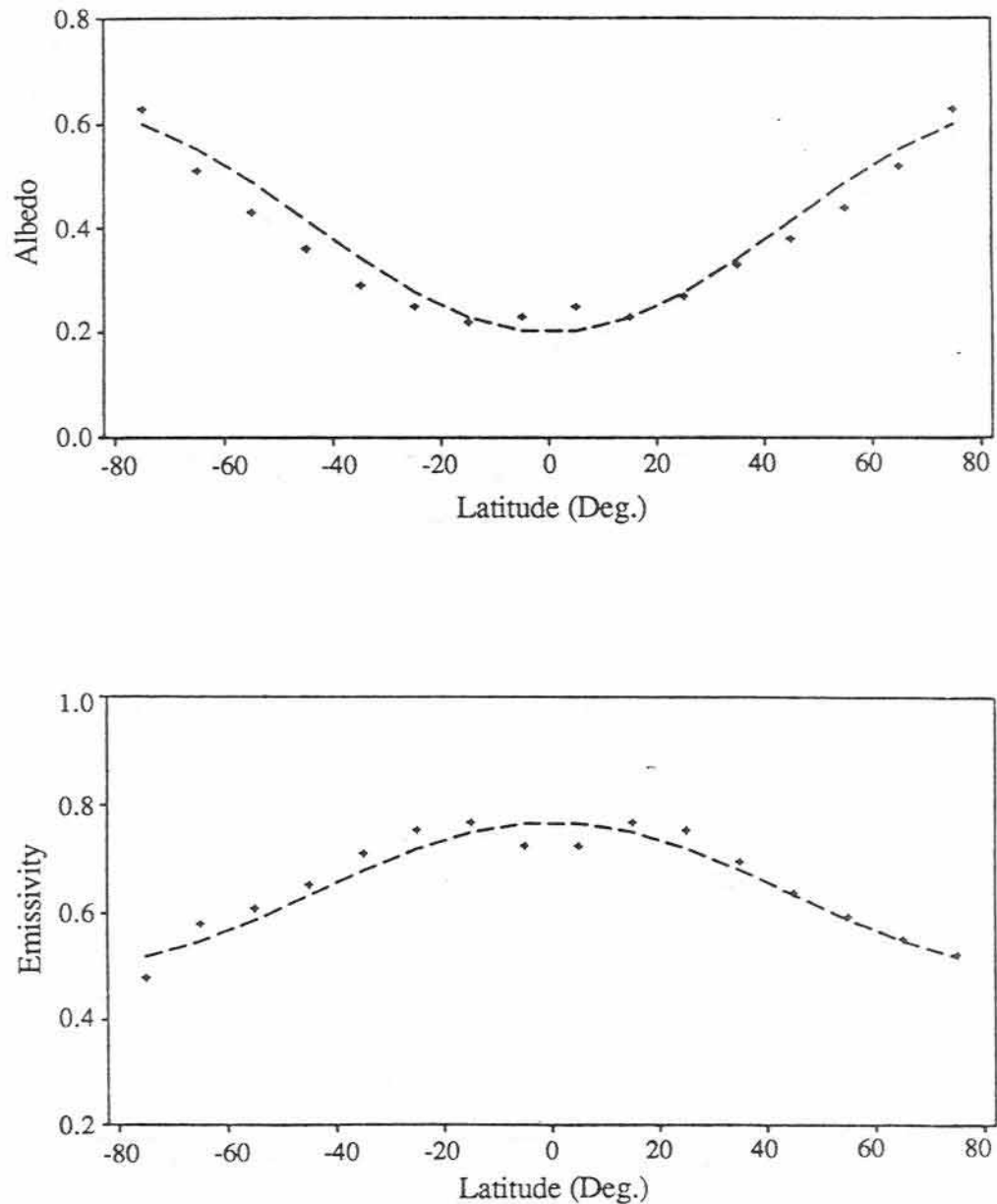


Fig. 2.6
Earth Radiation Data and Model: Spring
(Source, Knocke and Ries [1987])

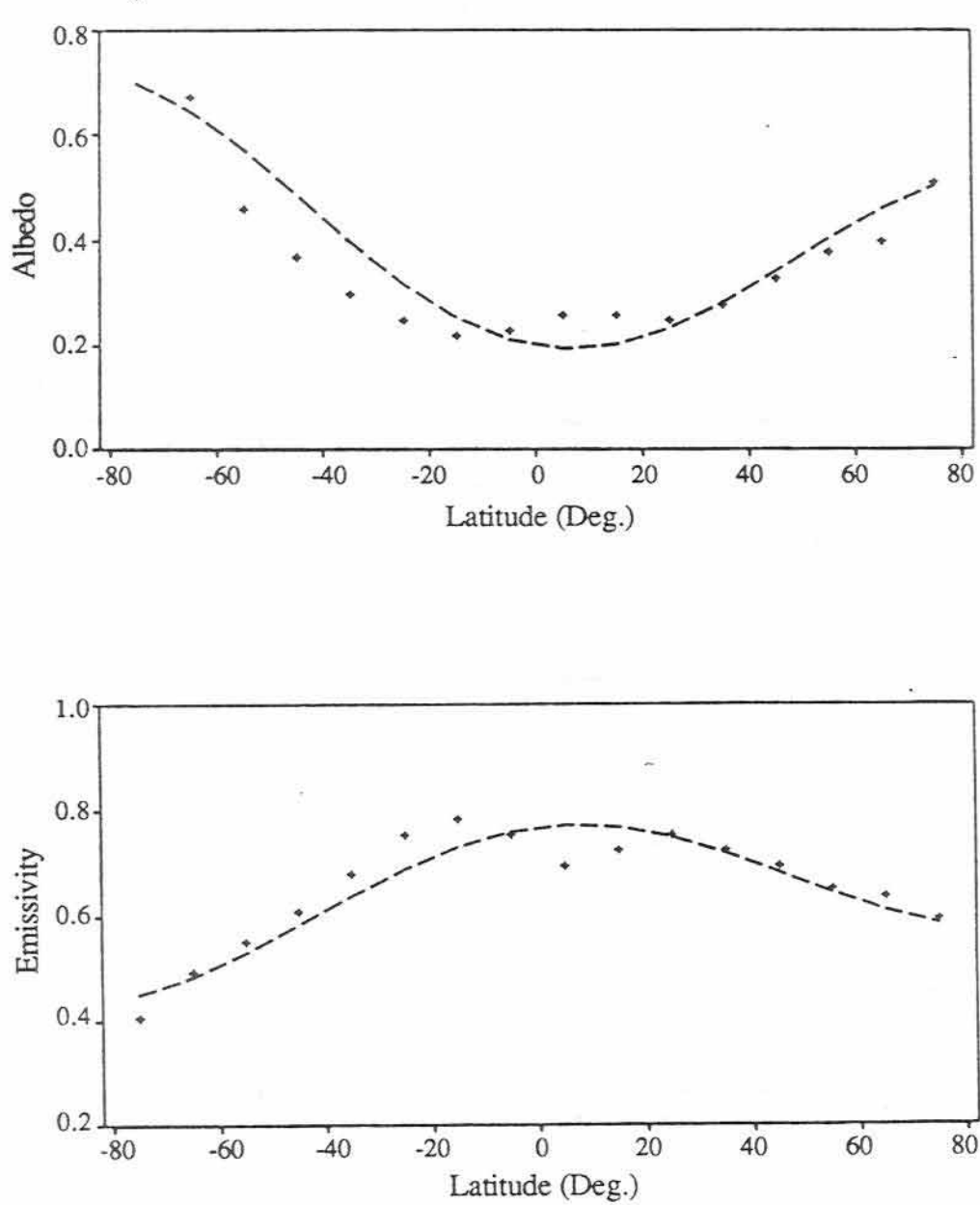


Fig. 2.7

Earth Radiation Data and Model: Summer

(Source, *Knocke and Ries [1987]*)

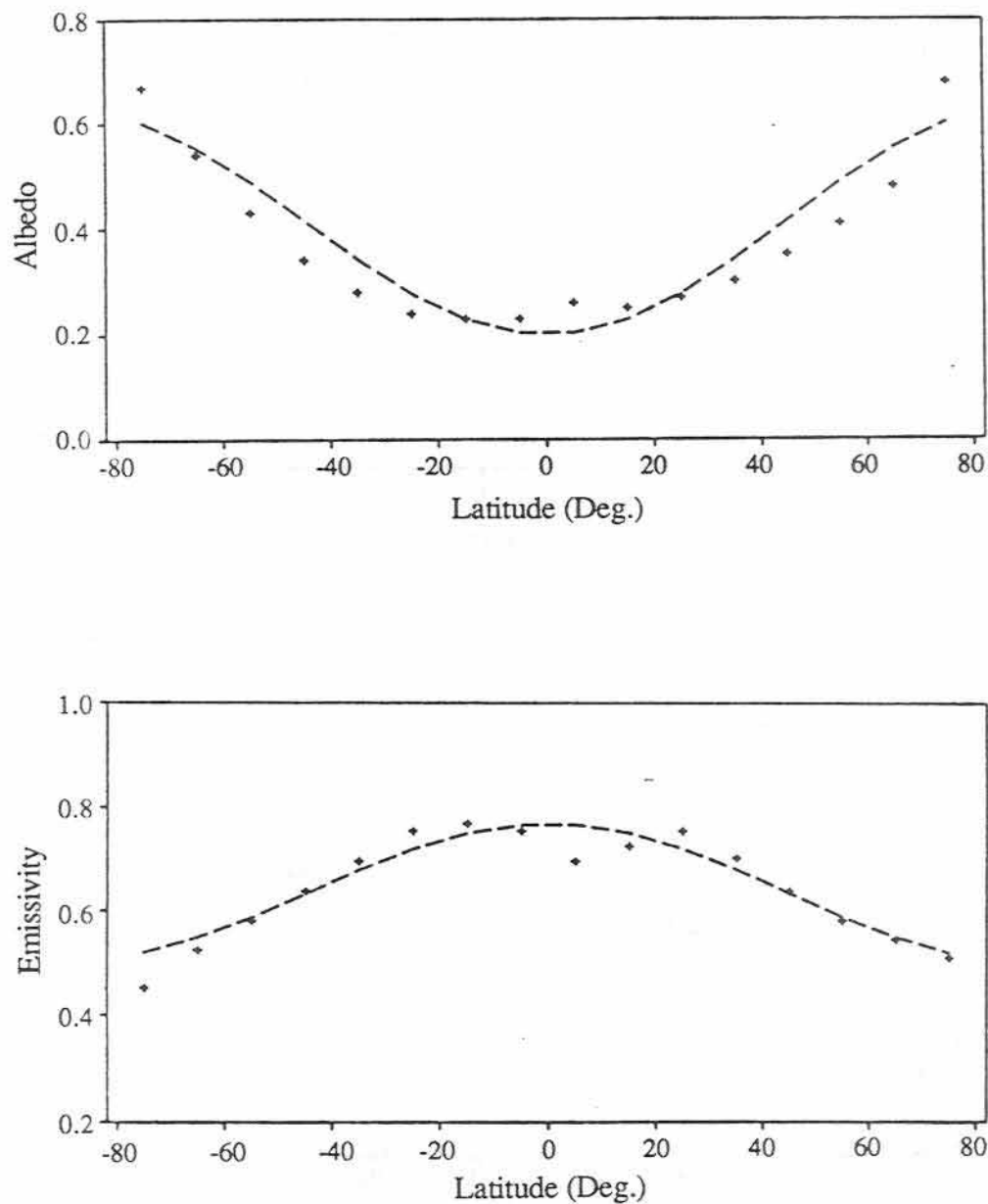


Fig. 2.8

Earth Radiation Data and Model: Fall

(Source, Knocke and Ries [1987])

CHAPTER 3

ORBITAL EFFECTS OF DIFFUSE EARTH RADIATION

3.1 *Values of the Earth Radiation Constants*

In order to evaluate the effects of Earth radiation pressure on the trajectories of LAGEOS and other satellites, various constants in the force model and the Earth radiation model must be adopted or determined. As mentioned earlier, this study uses 19 Earth segments to subdivide the effective cap. The solar irradiance, divided by the speed of light is calculated as follows [Willson, 1978]:

$$\frac{E_S}{c} = \frac{4.5605(10^{-6})}{r_{\text{EARTH}}^2} \quad (\text{Joules m}^{-3}), \quad (3-1)$$

where r_{EARTH} is the Sun-Earth distance in astronomical units. The Earth radiation parameters described in Section 2.2 are obtained from least squares fits of Stephens' seasonal averages [Stephens *et al.*, 1981]. The values used in this study are [Knocke and Ries, 1987]:

$a_0 = 0.34$	$e_0 = 0.68$
$c_0 = 0.$	$k_0 = 0.$
$c_1 = 0.1$	$k_1 = -0.07$
$c_2 = 0.$	$k_2 = 0.$
$a_2 = 0.29$	$e_2 = -0.18.$

(The epoch value t_0 is December 22, 1981.)

The remaining values required in the Earth radiation pressure calculations are all satellite specific. The reflective properties of the satellites herein considered are all reasonably well known from studies of the direct solar radiation pressure. The satellite emissive properties, which are usually very poorly known, are extrapolated from the reflective properties. The values of η_E chosen for this study are all equal to the nominal solar satellite reflectivity η_R . The tacit assumption in this choice is that the satellite reflects and emits Earth radiation in a manner similar to its interaction with solar radiation. This is reasonable, as the ultimate origin of Earth radiation is incident solar energy. The use of solar reflectivity to calculate the Earth radiation augmentation factor is particularly apropos in another sense, as η_R is obtained entirely from the orbital effects of solar radiation pressure, and is therefore devoid of the dubious qualities of laboratory measurements.

The satellites examined in this study include the geodetic satellites LAGEOS (launched by the National Aeronautics and Space Administration (NASA) in 1978), Starlette (Centre Nationale d'Etudes Spatiale (CNES), 1975), GEOS-1 (NASA, 1965), GEOS-2 (NASA, 1968), GEOS-3 (NASA, 1975), and AJISAI (National Space Development Agency of Japan, 1985), the oceanographic satellite SEASAT (NASA, 1975), and the joint NASA/CNES TOPEX/POSEIDON oceanographic satellite scheduled for launch in 1991. The following table indicates the nominal orbital parameters, area to mass ratios, and Earth radiation augmentation factors for each of these satellites, listed in order of ascending altitude.

TABLE 3.1
SATELLITE PROPERTIES

	altitude [km]	a [km]	e	i [deg.]	A_C/m [m ² kg. ⁻¹]	η_E
SEASAT	786.	7164.	.0007	108.0	.012	.5
GEOS-3	842.	7220.	.001	115.0	.004	.1
Starlette	953.	7331.	.02	49.8	.001	.12
GEOS-2	1324.	7703.	.03	105.9	.006	.29
TOPEX	1334.	7712.	.0015	63.4	.009	.2
AJISAI	1492.	7870.	.0006	50.1	.005	.15
GEOS-1	1690.*	8077.	.07	59.4	.007	.29
LAGEOS	5893.	12271.	.004	109.7	.0007	.13

* perigee altitude = 1101 km, apogee altitude = 2278 km

3.2 *Character of Diffuse Earth Radiation Pressure*

3.2.1 *Variation with altitude*

The interesting question arises of the exact manner in which Earth radiation pressure varies with altitude. An examination of this topic is instructive, both from the perspective of distinguishing this force from other nonconservative forces, and as a rule of thumb for predicting the relative importance of this effect. At first glance, it might appear that Earth radiation pressure obeys a strict inverse square

dependency on altitude, as suggested by Equation (2-21). It should be remembered, however, that the force exerted on a satellite due to Earth emanations is the aggregate effect of all "active" Earth segments, i.e. those Earth elements in direct line-of-sight to the satellite. As the altitude increases, this "visible cap" increases (asymptotically approaching one half of the terrestrial sphere) thus compensating in some measure for the inverse square attenuation. The cosine terms in (2-21), which are associated with illumination levels and viewing angles, vary both with altitude and position on the visible cap, thus further complicating the picture. It would seem, in any case, that the magnitude of this force should fall off according to a power law somewhat less severe than r^{-2} .

In this regard, consider a generalized, spherical satellite possessing an area-to-mass ratio of 0.01, and a reflectivity of 0.1. For the purposes of illustration, this satellite is placed directly over the subsolar point, and the total Earth radiation pressure magnitude is calculated for altitudes between 200 km and 6000 km. Also determined are the solar radiation pressure and the drag force at these altitudes. The results are shown in Figures 3.1.

Figure 3.1a is a semilog plot of drag, solar radiation pressure, and Earth radiation pressure acceleration magnitudes versus altitude. As expected, the magnitude of the solar radiation pressure is invariant with altitude, and the drag displays a characteristic exponential decay. Drag predominates over radiation pressure, both direct and reflected, at altitudes below 400 km, while radiation pressure from both sources easily surpasses drag above 800 km. In the neighborhood of 600 km, all three forces share the same order of magnitude, but it is important to keep in mind the very considerable difference in the characteristic

directions of each of these forces. As will be demonstrated later in this section, the Earth radiation vector is largely radial; drag is primarily tangential, and solar radiation lies along the Sun-satellite line.

Figure 3.1b is a linear plot of acceleration vs. altitude for the given hypothetical satellite configuration in the neighborhood of 10^{-8} m s^{-2} . Above 400 km, the change in Earth radiation pressure with altitude might best be described as a very gradual exponential decay. The best fit of Figure 3.1b is the following:

$$|\vec{a}| = 1.935(10^{-8}) e^{-0.00021 h}, \quad (3-2)$$

where h is the altitude in Kilometers. As expected, this represents a much more gradual decay than inverse square attenuation. Indiscriminate use of the inverse square law to extrapolate Earth radiation calculations to higher altitudes could easily cause an underestimation of this force of several orders of magnitude. For example, a very simple inverse square model of Earth radiation pressure leads *Sehnal* [1974] to conclude that shortwave Earth radiation pressure would not exceed drag in magnitude until an altitude of 1200 km is achieved.

Not shown in Figure 3.1b is the behavior of this force at the relatively uninteresting region below 200 km. The pressure force reaches a maximum at about 300 km, and then decreases rapidly to zero at zero altitude. This somewhat counterintuitive behavior is almost certainly due to the rapid shrinkage of the visible cap at very low altitudes.

The unusual dependence of Earth radiation pressure on altitude indicates that this force should be separable from gravity forces and other effects, given a data set consisting of high accuracy range observations of many satellites at various altitudes, or through observations of a single highly eccentric satellite. These topics

are addressed in forthcoming sections.

3.2.2 Variation over an orbit

Due to the considerable changes in illumination as the satellite progresses in its orbit, the Earth radiation pressure acceleration undergoes large variations in both direction and magnitude. For the purposes of this study, it is useful to follow a particular satellite, in this case LAGEOS, as it traverses a single revolution about the Earth.

Figure 3.2 shows the magnitudes of the Earth radiation accelerations over a single orbit of LAGEOS, for an orbit plane which is perpendicular to the plane of the terminator, at a time when the Sun lies on the equator. This orbital orientation exposes the satellite to maximum shadowing by the Earth. Note that the maximum magnitude of the Earth radiation acceleration is on the order of $10^{-10} \text{ m s}^{-2}$, which is about ten percent of the solar radiation acceleration on LAGEOS. This is in agreement with the results summarized in Figure 3.1.

As indicated by Figure 3.2, the shortwave constituent of the Earth radiation pressure goes to zero in Earth's shadow. Note that the satellite's passage into darkness produces a continuous variation in the Earth radiation pressure, due to the smoothly varying number of illuminated Earth segments. This contrasts with the more rapid variations in the solar radiation pressure during daylight-darkness transitions.

Figure 3.3 breaks the total Earth radiation acceleration experienced during this orbit into components in the radial, transverse, and normal directions. Note the

predominance of the radial component, and the antisymmetric nature of the transverse component. Note also that the magnitude of the largest positive transverse acceleration is approximately equal to that of the greatest negative transverse acceleration. Given the assumption of diffuse terrestrial reflection and the nearly constant altitude of the satellite, the only variations in this quantity must arise solely from latitudinal variations in the Earth radiation parameters.

Figure 3.4 demonstrates the variation in diffuse Earth radiation pressure for a noneclipsing orbit. The shortwave Earth radiation acceleration never goes to zero in this case, but decreases to a low level on the poorly illuminated side of the Earth. The associated radial, transverse, and normal components are illustrated in Figure 3.5.

It is evident that the shortwave portion of the Earth radiation acceleration undergoes significant variations over a single orbit. The longwave component is much less variable. Figures 3.2 and 3.4 clearly indicate that the signature of the total Earth radiation acceleration (magnitude) is essentially the same as that of the shortwave portion alone, biased by a nearly constant longwave term. Also, because the longwave component is essentially independent of diurnal effects, the acceleration due to longwave emissions is nearly radial. It would seem, therefore, that the influence of the longwave emitted radiation would be almost indistinguishable from a small change in the gravitational constant of the Earth, for low eccentricity orbits. As a consequence, one would expect the shortwave component to have a greater orbital effect than the longwave component, in spite of the comparable magnitudes of their accelerations. The orbital influence of these components is explored in subsequent sections.

3.2.3 Earth Radiation Pressure and High Eccentricity Orbits

Satellites possessing highly eccentric orbits are of particular interest in the study of Earth radiation pressure, due to the large variations in altitude experienced in the course of their orbits. In addition, in this class of satellite, the along-track acceleration is significantly affected by the projection of the very large radial acceleration component in the tangential direction. GEOS-1 has the largest eccentricity of the satellites cited in Table 3.1, and is examined in some detail.

In the case of high eccentricity orbits, it is instructive to examine the substantial difference between the tangential acceleration and the transverse acceleration. Figure 3.6 illustrates the discrepancy between these two components during a single orbit of GEOS-1, during which the satellite experiences deep eclipse. For this orbit, the average along track acceleration due to all Earth radiation pressure is $7.6 (10^{-11}) \text{ m s}^{-2}$, as compared to the average *transverse* acceleration of $5.5 (10^{-12}) \text{ m s}^{-2}$. The average tangential acceleration is more than an order of magnitude larger than the transverse because of the projection of the sizeable radial acceleration in the along-track direction. The average force over an orbit is nonzero because the eclipse causes an imbalance in the accelerations. As the maximum drag on this satellite is only $(10^{-11}) \text{ m s}^{-2}$, it is clear that the along track component of Earth radiation pressure *during eclipse* tends to supercede the drag force in importance. It is important to remember that the magnitude and direction of the average Earth radiation tangential acceleration depends on the exact nature of the eclipse event (e.g. a North-South eclipse versus a South-North eclipse passage), and the perigee location.

During noneclipse orbits, the average tangential acceleration is much smaller, and somewhat more commensurate with the average transverse acceleration. Figure 3.7 shows the Earth radiation along track and transverse force components in a noneclipsing orbit. The one-rev. average tangential acceleration is $-4.3 (10^{-12}) \text{ m s}^{-2}$, and the one-rev. average transverse acceleration is $-1.5 (10^{-12}) \text{ m s}^{-2}$.

3.3 Orbital Effects of Diffuse Earth Radiation

3.3.1 A Comparison of Shortwave and Longwave Radiation Effects

In order to determine the orbital influences of the various Earth radiation components on LAGEOS and other satellites, the trajectory comparison option in UTOPIA has been used. A typical comparison run begins with the generation of a reference trajectory calculated with a given force model. A comparison trajectory obtained with a different force model is generated also. The two trajectories may be differenced in order to determine the pure effect of Earth radiation pressure. Alternatively, the reference trajectory may be treated as a set of perfect observations for the comparison orbit, which is then fit to the reference orbit in a least squares sense. In general, the user may specify any set of estimated parameters to achieve the fit, but the only parameters estimated in this portion of the study are the initial conditions (position and velocity). The number in the "total effect" column of the following table represents the RMS of the radial differences between a reference trajectory generated with the Earth radiation pressure "turned on" and a comparison trajectory with Earth radiation ignored. The result is an estimate of the "cost" in

radial orbit error of ignoring Earth radiation pressure, after the removal of all effects which are removable via estimation of the initial conditions. For LAGEOS, the Earth radiation effect over 365 days is on the order of 0.4 meters in radial RMS. The estimation of additional dynamical parameters removes most of this effect, but at the cost of small errors in the estimated parameters.

The table below displays the significant difference between the orbital effects of Earth's shortwave and longwave emanations.

TABLE 3.2
COMPARISON OF SHORTWAVE AND LONGWAVE EFFECTS
Trajectory Comparison, Estimating Initial Conditions

	arc [days]	Shortwave Only Radial Difference [meters]	Longwave Only Radial Difference [meters]	Total Effect Radial Difference [meters]
Starlette	30.	.10	.008	.11
TOPEX	10.	.26	.034	.23
LAGEOS	365.	.40	.026	.42

For three different satellites the evidence is clear that the longwave emitted component by itself accounts for only ten percent or so of the total orbital influence of Earth radiation. The broadband shortwave (reflected) flux of the Earth accounts for almost all of the Earth radiation effects, with the exception of perturbations in the longitude of the ascending node. This topic is explored in the following section.

3.3.2 Effects of Diffuse Earth Radiation Pressure on the Orbit Elements of LAGEOS

The question remains of the long term influence of Earth radiation pressure on LAGEOS' orbit, and in particular, its influence on LAGEOS' semimajor axis. If Earth radiation is in fact responsible for the unmodeled secular decrease in the semimajor axis of LAGEOS, a trajectory comparison run configured to quantify the effects of 100% error in Earth radiation pressure should reveal a net change of approximately 0.4 meter in the semimajor axis over a one year arc. A trajectory comparison of this type would also establish the nature of perturbations on the other orbit elements.

Figures 3.8 through 3.11 are plots of changes in the semimajor axis, eccentricity, inclination, and argument of perigee of LAGEOS for a 365 day arc in which the nominal trajectory is generated with Earth radiation pressure activated, and the comparison trajectory is generated with Earth radiation pressure absent from the force model. Figure 3.12 shows the perturbation in the node due to Earth radiation pressure for a 1100 day trajectory comparison. Figures 3.8 through 3.12 indicate the trajectory differences when no fitting is employed.

If Earth radiation pressure is the sole agent of the observed secular decrease, then Figure 3.8 should display a linear trend in the residual semimajor axis, with a maximum value of 0.4 meter occurring at the end of the 365 day arc. Instead, the envelope of the semimajor axis residuals undergoes a *periodic* fluctuation with a mean near zero, no significant secular trend, and a maximum difference of 0.02 meter. It is evident that the mysterious behavior of LAGEOS cannot be explained in

terms of the diffuse Earth emanations modeled. This result is in agreement with *Rubincam and Weiss [1985]*.

Frequency analyses of a 2100 day arc reveal the important periodicities in the semimajor axis perturbations. Figure 3.13 shows that the largest peaks for the diffuse model occur near 296 days and 509 days. It seems likely that these peaks are associated with the LAGEOS' node rate with respect to the Sun. LAGEOS' node makes one full revolution with respect to the Sun in 560 days. Note in Figure 3.13 that the 509 day peak is quite broad, indicating problems accurately recovering this period.

As Figures 3.9 through 3.11 suggest, the eccentricity, inclination, and argument of perigee all suffer small, long period fluctuations due to Earth radiation pressure. Only the longitude of the ascending node displays a secular tendency, as indicated in the 1100 day trajectory comparison of Figure 3.12. The node is perturbed by the diffuse model at a rate which varies between approximately $-0.3(10^{-3})$ arcsecond/year and $-5(10^{-3})$ arcsecond/year. This variability is extremely long period, greater than 1100 days, and is probably due to the effect of orbital and solar geometry on the shortwave component. The shortwave component causes the node to either increase or decrease, depending on the geometry of the orbit, whereas longwave Earth radiation causes a uniform decrease in the node. Just as the attractive gravity force, in conjunction with an oblateness (J_2) term causes LAGEOS' node to increase, the repulsive longwave radiation pressure in conjunction with an oblateness (e_2) term causes the node to decrease. The following table compares some UTOPIA estimates with various published results.

TABLE 3.3
EFFECT OF DIFFUSE EARTH RADIATION PRESSURE ON
THE NODE OF LAGEOS
Various 365 Day Arcs: Direct Trajectory Comparisons

	arc	$\Delta\Omega [10^{-3} \text{ arcsec}]$ Shortwave Only	$\Delta\Omega [10^{-3} \text{ arcsec}]$ Longwave Only
UTOPIA model	1980	+2.1	-2.4
	1982	-3.0	-2.4
<i>Rubincam and Weiss</i> [1985]		+0.57	
<i>Sehnal</i> [1981]			-36.8

The UTOPIA model predicts a variable influence due to the shortwave component, while the analytical model described in *Rubincam and Weiss* [1985] indicates the presence of a uniform secular increase due to the shortwave component. One might imagine that the UTOPIA results, over a sufficiently long time interval, could average to a small number on the order of the value cited in *Rubincam and Weiss*. Part of the discrepancy also may be due to LAGEOS' eccentricity, which is assumed to be zero in *Rubincam and Weiss*. A dependence on the argument of perigee might also explain the long period nature of the variability in the node rate. In addition, the influence of the longwave Earth radiation pressure is smaller, by about one order of magnitude, than that predicted by the analytical model in *Sehnal*, [1981].

The node rate is small in any event. In comparison, the general relativistic effect of Earth's angular momentum induces a secular decrease in the LAGEOS node of approximately $30(10^{-3})$ arcsecond per year [*Ciufolini*, 1986]. Nevertheless, if the node rate is required to accuracies of several milliarcseconds per

year, special attention must be paid to the correct characterization of both the longwave and shortwave components.

3.3.3 *Earth Radiation Effects on other Satellites*

Table 3.4 shows the orbital effects of Earth radiation on the satellites described in Table 3.1. The column labeled "percent shadow" indicates the percentage of time the satellite of interest is in Earth shadow, and is intended to give some indication of the lighting conditions during the arc. Just as before, the orbital effects are quantified using a trajectory comparison run in which the nominal trajectory has Earth radiation activated and the comparison orbit has Earth radiation turned off.

Note the disproportionately large RMS values for GEOS-1, which has the most eccentric orbit. (Over the course of an orbit, GEOS-1's altitude varies by 1177 km, while GEOS-2's altitude fluctuates by 485 km, and Starlette's altitude varies by only 293 km.) Even when drag and solar reflectivity are adjusted, there remains a sizeable residual effect on GEOS-1's trajectory due to Earth radiation pressure. GEOS-2 and Starlette also display this phenomenon, somewhat less dramatically. All this lends support to the theory, expressed in Section 3.2.3, that high eccentricity satellites tend to exhibit a particularly high degree of sensitivity to Earth radiation pressure. Analyses of GEOS-1 and GEOS-2 data are included in subsequent sections.

The TOPEX entries are intended to explore divers characteristics of the Earth radiation force model. For instance, for a ten day arc, a sizeable change in the

TABLE 3.4
DIFFUSE EARTH RADIATION EFFECTS

	eccentricity	arc [D.]	Estimated Parameters	Percent Shadow	Radial RMS [m.]	Transverse RMS [m.]
SEASAT	.0007	30.	IC	33.	1.5	4.0
		30.	IC, C_D , η_R	33.	.066	.39
GEOS-3	.001	30.	IC	31.	.39	.91
		30.	IC, C_D , η_R	31.	.063	.14
Starlette	.02	30.	IC	32.	.11	4.03
		30.	IC, C_D , η_R	32.	.01	.15
GEOS-2	.03	30.	IC	26.	.92	30.3
		30.	IC, C_D , η_R	26.	.09	.45
TOPEX ^c	.0015	10.	IC	29.	.30	.63
		10.	IC	1.4	.23	.52
		10.	IC, C_D , η_R	1.4	.021	.042
TOPEX ^v	.0015	10.	IC	1.4	.30	.90
		10.	IC, C_D , η_R	1.4	.020	.14
AJISAI	.0006	30.	IC	15.	.35	.70
		30.	IC, C_D , η_R	15.	.03	.08
GEOS-1	.07	30.	IC	10.	1.8	34.2
		30.	IC, C_D , η_R	10.	1.4	3.7
Lageos	.004	365.	IC	7.	.42	8.4
		365.	IC, C_T^* , η_R	7.	.40	3.95

c: constant cross sectional area = 12 m².

v: variable cross sectional area (see Figure 3.14).

* C_T : along track drag coefficient.

lighting conditions engenders very little difference in the Earth radiation orbital effect. The influence of variable geometry is also examined. In Table 3.4, the superscript "c" refers to a satellite model in which the cross sectional area is assumed constant. The superscript "v" refers to an approximation of the variable geometry modification mentioned at the end of Section 2.1.4.2, for an early configuration of the TOPEX satellite. In this case, the area projected onto the subsatellite point is used as a rough estimate of the Earth radiation reference area A_{Cj} , and is assumed constant for all Earth elements. (See Figure 3.14.) The use of such a model leads to no significant alteration in the orbital effects due to Earth radiation pressure, for the arc length considered.

3.3.3.1 Diffuse Earth Radiation Pressure and GEOS-1

Recent analyses of GEOS-1 tracking data suggest the presence of unmodeled forces on the satellite. Specifically, the best available data fits include long intervals during which drag coefficient estimates are large and negative [Dah-Ning Yuan, *personal communication*], indicating the presence of positive along track accelerations of the same order as drag. Figure 3.15 shows the estimated drag coefficients during tracking campaigns in 1977 and 1978. Note that the largest negative drag coefficients occur during a period of eclipse, but that the negative C_D values are not confined to shadowing events. The interval possessing the largest measures of negative drag includes the deep eclipse orbit of Figure 3.6. The nonconservative tangential accelerations on GEOS-1, averaged over this orbit, are indicated in the following table, where "positive" is in the direction of motion.

TABLE 3.5
AVERAGE TANGENTIAL ACCELERATIONS ON GEOS-1
DUE TO NONCONSERVATIVE FORCES
(6-27-77)

SOLAR RADIATION PRESSURE	1.7 E-9 m s ⁻² (positive)
ATMOSPHERIC DRAG ($C_D = 3.0$)	1.3 E-10 m s ⁻² (negative)
EARTH RADIATION PRESSURE	8.2 E-11 m s ⁻² (positive)

It is evident that the dominant nonconservative along track acceleration on the satellite in this orbital orientation is the solar radiation pressure. Note, however, that the tangential component of Earth radiation pressure, averaged over this eclipsing orbit, is of the same order as drag, and is in the positive along track direction as well. It is clear that errors in the determination of either solar radiation pressure or Earth radiation pressure may be capable of generating the observed negative C_D values.

One possible source of error in the determination of solar radiation pressure involves variations in the area which intercepts the solar flux. GEOS-1 is a gravity-gradient stabilized satellite, which presents the same surface to the Earth at all times, and thus presents a continually varying cross section to the Sun. Figure 3.16 illustrates the GEOS-1 configuration, the cross sectional area of which varies by less than 20% between the (Earth-pointing) "bottom" and the "side". Note, however, that the side of the satellite is covered with dark solar cells, while the underside is composed of highly reflective retroreflecting elements and beacons. The solar radiation pressure model in UTOPIA includes several variable area

models, but requires a single solar reflectivity parameter η_R . As a result, variations in the surface properties must be simulated by means of "effective areas" which are calculated as follows:

$$(1 + \eta_S) A_S = (1 + \eta_R) A_{S_{\text{eff}}} \quad (3-3)$$

$$(1 + \eta_B) A_B = (1 + \eta_R) A_{B_{\text{eff}}},$$

where η_R = UTOPIA input solar reflectivity

η_S = "side" reflectivity

η_B = "bottom" reflectivity

$A_S, A_{S_{\text{eff}}}$ = true and effective "side" cross sectional areas

$A_B, A_{B_{\text{eff}}}$ = true and effective "bottom" cross sectional areas.

An extreme case, in which the side area is assumed to be 1/10th as reflective as the underside, produces an effective area variation of 34%. Use of this model leads to a small "improvement" in the C_D values, i.e. they are made slightly less negative. Various other area variations have been tested, without significantly affecting the C_D levels.

As mentioned earlier, the Earth radiation pressure on this satellite is also capable of generating sizeable along track accelerations. Analyses indicate that estimating the zeroeth degree albedo parameter a_0 produces a highly salutary effect on the "worst" drag coefficients. In fact, among the various estimated parameters examined in this study, only albedo has a dramatic effect on the extremely large negative C_D values present in the arc starting 6-27-77. Some further improvement is effected when a variable area solar radiation pressure model is added.

Figure 3.17 illustrates the influence of Earth radiation pressure on drag coefficients estimated during a 30 day arc starting June 27, 1977. At the start of the

arc, the orbit of the satellite passes through deep shadow. As the arc progresses, nodal precession causes the orbit to move entirely out of shadow by July 11 (day 14 on the plot). One drag coefficient is estimated for each 3 day interval in the arc. Nominally, a single solar radiation reflectivity is estimated for the entire 30 day trajectory. The largest negative drag coefficients occur when Earth radiation pressure is ignored completely, as depicted by the bottom line in Figure 3.17. When the nominal Earth radiation model is utilized, there is a measurable improvement in the C_D values, in the sense that they are driven towards a more physically reasonable level. Some additional improvement is evident when, in addition, solar radiation reflectivities are estimated every 5 days. This run is characterized by reasonable values of solar reflectivity in the early, eclipsing part of the arc, followed by physically impossible values outside this region. In fact, the solar reflectivities themselves become large and negative towards the end of the arc. As Figure 3.17 indicates, the latter part of this run is also marked by equally unlikely large *positive* C_D estimates.

The most dramatic improvements in the C_D values occur when the zeroeth degree albedo parameter is estimated. The two uppermost lines on Figure 3.17 show the drag coefficients estimating a_0 , with and without the benefit of a 30% solar pressure area variation model. In regions of deep eclipse, estimation of a_0 results in C_D values which are one tenth to one half the size of those estimated without the benefit of Earth radiation pressure. The estimated values of a_0 are extremely high, however, approaching unity in both cases.

It is interesting to note that the impact of Earth radiation pressure decreases smoothly as the satellite's orbit precesses out of shadow. Even when the orbit itself is no longer shadowed, the total Earth radiation pressure is influenced by the unlit

hemisphere. By the time the orbit is well out of shadow, however, the Earth radiation imbalance which caused a significant along track acceleration has disappeared. The latter portion of the arc depicted in Figure 3.17 shows drag coefficients relatively insensitive to Earth radiation pressure.

The motion of the satellite during the arc described above is such that eclipse is traversed from South to North. When the node with respect to the Sun has precessed sufficiently, the eclipse passage is North to South, and the sense of the average tangential Earth radiation acceleration is reversed. In this case, the Earth radiation pressure acceleration, averaged over an orbit, is in the negative along-track direction. The question in this case is whether or not the inclusion of the Earth radiation pressure model, by thus creating an additional drag-like force, might cause the C_D values to become even more negative to compensate.

Figure 3.18 illustrates the effects of Earth radiation pressure during another 30 day arc characterized by large, negative C_D values. Now the eclipse passage is from North to South, and the average tangential Earth radiation acceleration opposes the satellite's motion. It is clear that Earth radiation pressure has a much smaller effect on the drag coefficients in this case, although it might be argued that the average influence is still slightly beneficial, as the C_D estimates are made very slightly less negative. Note also that the maximum negative drag coefficients for this arc are much smaller than those for the South-to-North eclipse. The main import of this experiment is that, even when the Earth radiation pressure produces an average along-track deceleration, the drag coefficients are not made "worse", in the sense of being driven to even more negative values.

The exact origins of the large negative C_D 's for GEOS-1 are still not clear.

As Figure 3.17 indicates, even when an unusually high albedo value is used, many C_D estimates remain at an uncomfortably large negative level. In fact, it would appear that Earth radiation pressure is incapable of driving the drag coefficients to levels above ~ -5 . Also, despite the manifest impact of Earth radiation pressure on the drag coefficients, the orbit fit is not improved by the estimation of albedo parameters. All this suggests that another, or perhaps several other unmodeled or mismodeled mechanisms are at work. It is possible that some mismodeling of the solar radiation pressure plays a part in this, despite the relatively small effect on the C_D 's engendered by various solar pressure configurations. Another promising mechanism is the thermal thrust created by temperature imbalances across the spacecraft surface. (See, for example, *Rubincam* [1987] and *Slabinski* [1988].) Keeping in mind that the GEOS-1 drag problem is unresolved, it remains clear that Earth radiation pressure can affect parameter estimation to a significant degree.

3.3.3.2 Diffuse Earth Radiation Pressure and GEOS-2

As indicated in Table 3.4, the high eccentricity satellite GEOS-2 also displays a marked sensitivity to Earth radiation pressure. This recommends an analysis similar to that performed on GEOS-1. The two GEOS spacecraft are part of the same series, and possess similar properties, in terms of reflectivity and overall geometry. GEOS-2 is slightly heavier than GEOS-1, but operates at a lower altitude, and possesses an orbital eccentricity less than half that of GEOS-1.

Laser range data analyzed for GEOS-2 produce negative drag coefficient estimates in much the same manner as for GEOS-1. Figure 3.19 displays the C_D

estimates and eclipse events for the available data interval. The clear periodic trend in the drag coefficients, once again suggests the presence of a real along track force of unknown origin.

Figure 3.20 illustrates how the GEOS-2 drag coefficient estimates are affected by diffuse Earth radiation pressure. When Earth radiation pressure is activated, the C_D 's are driven towards a more physically appropriate level. Estimation of the zeroeth degree albedo parameter improves the drag coefficient estimates even more, at the expense of a high value for a_0 .

The similarity of these findings to the GEOS-1 results is clear. One must conclude that high eccentricity satellites, in general, are sensitive to diffuse Earth radiation pressure, and that this tendency is demonstrable via analyses of real data. Bodies in highly eccentric orbits which intersect the Earth's shadow experience a net along-track force of significant magnitude, arising from diffuse Earth radiation, which can corrupt the accurate estimation of drag coefficients.

3.4 Diffuse Earth Radiation Pressure and the Estimation of Parameters

3.4.1 Estimation of Albedo Parameters from Satellite Orbit Observations

It has been suggested that Earth radiation pressure might be separable from competing forces, given high accuracy observations of several satellites distributed at various altitudes, or given accurate measurements of a single highly eccentric orbit. Assuming a correct Earth radiation pressure model, it might then be possible to estimate the Earth radiation parameters directly. Aside from the prospect of

verifying and improving the Earth radiation pressure model, such an exercise would also illuminate any tendency of Earth radiation pressure to conceal itself in force effects of similar character, thereby corrupting the estimation of parameters.

The University of Texas's Large Linear System Solver has been used to perform this analysis, which involves the simultaneous estimation of large numbers of global and local parameters. In this context, "global" refers to parameters common to all the satellites, such as albedo parameters and gravity coefficients. "Local" parameters are specific to each satellite, and typically include solar reflectivity and drag coefficients. Data for each satellite are expressed as D-U-Z's, i.e. Square Root Information Matrices (SRIM), and the Givens-Gentleman technique is used to solve the linear system [Tapley *et al.*, 1985]. The multi-satellite solutions are iterated according to an optimal weighting strategy.

The following table indicates the satellites and data examined in this study. Not all the data sets are temporally contiguous. For example, the GEOS-1 data often contain gaps of several months, which explains the irregular arc lengths used. The data sets also vary in quality, depending on data type and how recently the data were gathered. AJISAI and LAGEOS provide data of a higher quality than BE-C and GEOS-1, for example.

TABLE 3.6
DATA USED IN THE MULTISATELLITE ALBEDO STUDY

satellite	altitude (km)	eccen.	incl. (deg.)	data description [local parameters]	data type
GEOS-3	842.	.00	115.0	nine 30 day arcs [for each arc: 1 η_R , 6 C_D 's]	laser
Starlette	953.	.02	49.8	a single 460 day arc [1 η_R , 92 C_D 's]	laser
OSCAR-14	1067.	.00	89.3	a single 92 day arc [6 η_R 's, 92 C_D 's]	doppler
BE-C	1129.	.03	41.2	five arcs, 32 to 38 days in length [1 η_R , 2 day C_D 's]	laser
NOVA-1	1171.	.00	90.0	five 19-day arcs [for each arc: 1 η_R , 3 C_T 's, NOVA station locations]	doppler
GEOS-2	1327.	.03	105.9	six arcs, 15 to 35 days in length [for each arc: 1 η_R , daily C_D 's]	laser
AJISAI	1492.	.00	50.1	four 30 day arcs [for each arc: 1 η_R , 6 C_D 's]	laser
GEOS-1	1690.	.07	59.4	seven arcs, 10 to 51 days in length [for each arc: 1 η_R , 5 day C_D 's]	laser
LAGEOS	5893.	.00	109.7	a single 6.4 year arc [4 η_R 's, 152 C_T 's]	laser

3.4.1.1 *The LAGEOS-Only Solution*

In spite of its relative insensitivity to Earth radiation pressure, LAGEOS remains an interesting subject in the analysis of Earth radiation effects. The LAGEOS tracking data are certainly the most precise available. Also, the extremely low level of drag at LAGEOS altitude and the simple configuration of the satellite make LAGEOS a promising candidate for revealing the presence of small perturbing forces. Finally, the LAGEOS data represent the longest contiguous observation record of any artificial satellite in existence. For these reasons, the genesis of this study is an estimate of Earth radiation parameters using LAGEOS data alone.

In this type of analysis, the parameters available for estimation are strictly limited to the parameters estimated during the generation of the SRIM. The following nominal set of parameters is estimated in this study:

TABLE 3.7
GLOBAL PARAMETERS ESTIMATED IN THE LAGEOS-ONLY SOLUTION:

7X7 Gravity Field, plus LAGEOS Resonance Terms: (8,6), (8,7), (8,8), (9,6), (9,7), (9,8), (14,13)
Tides P1, K1, M2, S2, K2
Earth Gravitational Parameter (μ)
Albedo Parameters

The tides selected represent the minimum subset of important tidal parameters for this spacecraft's orbit. Partial derivatives for the emissivity parameters were not included in the SRIM, and therefore cannot be estimated. Early studies, [John

Ries, *personal communication*] and the nature of the longwave component of Earth radiation pressure, indicate that the emissivity coefficients are difficult to recover from orbital observations of a single low eccentricity satellite.

As expected, the successful estimation of the Earth radiation parameters depends to a large extent on the presence of other estimated parameters. The following table indicates the estimates of various albedo parameters, and the circumstances of the analyses.

TABLE 3.8
RECOVERY OF ALBEDO PARAMETERS FROM LAGEOS DATA

case	estimated parameters	a ₀	c ₀	a ₂	c ₁	c ₂
[1]	7x7 field, tides, μ , η_R 's, C _T 's	0.7	-0.3	0.46		
[2A]	7x7 field, tides, μ , C _T 's	0.33				
[2B]		0.34	0.50	0.29		
[2C]		0.42	0.51	0.65	0.35	-0.07
[3A]	7x7 field, μ , C _T 's	0.33	0.35	0.23		
[3B]		0.34	0.35	0.28	0.13	-0.03
[4]	7x7 field (except J ₅ ,J ₇), μ , C _T 's	0.36	0.31	0.35	0.17	-0.03
[5]	7x7 field (except J ₃ ,J ₅ ,J ₇), μ , C _T 's	0.36	0.002	0.36	0.14	-0.03
[6]	7x7 field (except J ₃ ,J ₅ ,J ₇), C _T 's	0.34	-0.008	0.30	0.14	-0.03
[nominal values:		0.34	0.00	0.29	0.10	0.00]

The parameter C_T is a constant, along-track empirical drag coefficient for LAGEOS. Also, recall that $a_1 = c_0 + c_1 \cos(\omega(JD - t_0)) + c_2 \sin(\omega(JD - t_0))$, from Equation (2-32). It is evident that estimating the 560-day subarc solar reflectivities largely masks the Earth radiation effects. Once the solar reflectivities are frozen, however, the albedo estimates are much more tractable and reasonable. In particular, note that the recovered value of a_0 is almost always within 6% of nominal; the only exception occurs in case 2C when all the albedo parameters are estimated. The Earth's average albedo is therefore quite well determined, and capable of being recovered from accurate orbital observations. The parameter a_2 , which governs the seasonally fixed variation of albedo with latitude, is also well determined. The first degree seasonally varying term c_0 is difficult to estimate however, unless the odd zonal geopotential terms are frozen. The correlation between a_1 and the odd zonals is understandable, given the similarity of their mathematical representations. Freezing the tidal coefficients also allows the periodic albedo terms to seek a more appropriate level.

Table 3.8 shows that the estimation of Earth radiation parameters can be affected by adjusting solar reflectivity, odd degree zonals, or, to a lesser extent, ocean tides. The correlation of the albedo parameters with solar reflectivity is especially troublesome, as η_R is traditionally estimated even during short arcs. Although it is acceptable to freeze the values of η_R for this study, such a technique is difficult to sanction in most cases.

Case 2B is perhaps the most significant in determining whether or not the albedo parameters are estimable from precise orbit observations. It allows adjustment of the largest numbers of parameters, aside from the estimation of solar reflectivities. It is significant that, even during the simultaneous estimation of many

gravity coefficients, tides, the gravitational parameter, and 15 day C_T's, the average albedo is recoverable from precise orbit observations.

3.4.1.2 *The Multi-Satellite Solution*

Estimation of albedo parameters from orbit observations has been shown to be possible, once LAGEOS solar reflectivities are frozen. The question remains of how the solution might be improved by including data from other satellites. In particular, the possibility of improving the estimate of the first degree albedo term presents itself. To this end, the satellite data described in Table 3.6 have been included in the Multi-Satellite Albedo Study (MSAS).

Table 3.9 summarizes the global parameters estimated in this study. The individual gravity terms listed in Part 1 of this table are the important resonant coefficients for the satellites listed in Table 3.6. The indicated ocean tides have been selected for the importance of their perturbations on the satellites in the constellation. In all cases, the reflectivities for LAGEOS are not estimated, although the reflectivities for the other satellites are estimated, apparently without ill effect. The MSAS might be considered a study of how case 2B is perturbed by additional satellite data. The albedo parameters are free to adjust as needed; no a priori variances are specified.

The multi-satellite albedo estimates are indicated in Table 3.10. Note first that the LAGEOS-only solution in Part 1 is nearly the same as that of case 2B, Table 3.8, in spite of the estimation of a larger gravity field and additional tides. In all cases, the a₀ term is easily recovered and its estimate remains stable over a wide

TABLE 3.9
ESTIMATED GLOBAL PARAMETERS: MULTI-SATELLITE ALBEDO STUDY

PART 1: 15 x 15 Gravity Field, plus Resonance Terms: (8,6), (8,7), (8,8),
 (9,6), (9,7), (9,8), (14,13), (16,12), (17,12) through (21,14),
 (27,24), (28,24), (28,27)(34,27), (35,27), (53,41), (54,41)

Tides P1, K1, M2, S2, K2, MM, MF, O1, N2, and S1

Earth Gravitational Parameter (μ)

Albedo Parameters

PART 2: 36 x 36 Gravity Field, plus Resonance Terms: (53,41), (54,41)

Tides P1, K1, M2, S2, K2, MM, MF, O1, N2, and S1

Earth Gravitational Parameter (μ)

Albedo Parameters

TABLE 3.10
MULTI-SATELLITE ALBEDO ESTIMATES

case		a_0	c_0	a_2
nominal values		0.34	0.00	0.29
Part 1: [15 x 15]				
[M0] LAGEOS only		0.34	0.49	0.29
[M1] LAGEOS, Starlette		0.33	0.53	0.28
[M2] LAGEOS, BE-C		0.33	0.43	0.28
[M3] LAGEOS, GEOS-1, GEOS-2, GEOS-3, BE-C, AJISAI		0.35	0.23	0.21
[M4] LAGEOS, GEOS-1, GEOS-2, GEOS-3, BE-C, AJISAI, NOVA-1		0.35	0.16	0.22
[M5] LAGEOS, OSCAR-14, GEOS-1, GEOS-2, GEOS-3, BE-C, AJISAI, NOVA-1		0.35	0.06	0.21
[M6] LAGEOS, Starlette, OSCAR-14, GEOS-1, GEOS-2, GEOS-3, BE-C, AJISAI, NOVA-1		0.34	0.30	0.33
Part 2: [36 x 36]				
[M7] LAGEOS, OSCAR-14, GEOS-1, GEOS-2, GEOS-3, BE-C, AJISAI, NOVA-1		0.34	0.42	0.26
[M8] LAGEOS, Starlette, OSCAR-14, GEOS-1, GEOS-2, GEOS-3, BE-C, AJISAI, NOVA-1		0.33	0.47	0.26

range of data combinations. The a_2 term shows somewhat greater sensitivity to the conditions of the solution, but is also well established. The estimate of c_0 varies considerably, however, depending on the choice of satellite data and the geopotential coefficients estimated. In all cases the formal standard deviations of the albedo coefficients are very low, on the order of (10^{-3}).

Cases M1 and M2 show what can happen to c_0 when a single additional data set is combined with LAGEOS data. The largest perturbations to c_0 are evident during a LAGEOS/Starlette solution and a LAGEOS/BE-C solution. Only Starlette causes an *increase* in c_0 over the LAGEOS-only solution. BE-C satellite data decrease the estimate of c_0 slightly, as shown. All the other satellite data, when combined with LAGEOS singly, produce estimates of c_0 between 0.46 and 0.49. It is clear that the estimate of c_0 cannot be improved with just one additional data set.

Cases M3 through M6 hint at the potential power of geodetic constellations in the estimation of albedo parameters. When the 15×15 field is estimated, the value of c_0 can be brought to reasonable levels with a multi-satellite solution. Case M5 produces good values for all the estimated albedo coefficients; in particular, the estimate of c_0 is dramatically improved over the LAGEOS-only solution. This case seems to be especially well determined in other respects, as well. For example, the estimate of the gravitational parameter μ for this case is quite close to the nominal. Also, when this configuration is run estimating LAGEOS solar reflectivities, the estimated values of the nonperiodic albedo coefficients are: $a_0 = 0.49$, $c_0 = -0.18$, $a_2 = 0.25$. This represents a significant improvement over the estimates indicated in Table 3.8.

Enlarging the estimated gravity field to degree and order 36 pulls the estimates

of c_0 up, to between 0.42 and 0.47. This is about where it is for the LAGEOS-only solution. It is almost impossible for the Earth to possess a value of c_0 this large, however. The high solution confidence suggested by c_0 's formal sigma must be leavened by an understanding of the physical nature of the results.

Any nonzero value for c_0 indicates the presence of a constant offset in the latitudinally averaged albedo distribution of the Earth. A constant bias of some sort is possible, due perhaps to an unequal distribution of large land masses between the hemispheres. Satellite radiometer measurements suggest that any such bias would be small, however. The consistently positive estimates of c_0 in this study point to the possibility that the northern hemisphere is inherently more reflective than the southern hemisphere. Figure 3.21 compares the latitudinal albedo variation for the nominal, M5 and M8 cases. The M8 case, where $c_0 = 0.47$, borders on the physically impossible, while case M5 suggests a more reasonable situation. The intractability of the constant first degree term may be due to errors in the odd degree zonals, and perhaps to aliasing with selected tides. Analyses of the LAGEOS-only solution indicate that the albedo coefficients are weakly correlated with J_3 , and the K1, and K2 tides.

The use of geodetic satellite constellations in recovering albedo parameters must be considered only a qualified success. The mean albedo a_0 and the albedo "oblateness" a_2 are well determined in most cases, when LAGEOS solar reflectivities are frozen. The first degree term appears to be less tractable, although its estimate is clearly affected by the presence of additional satellite data. In spite of the inconclusive nature of these results, the potential utility of geodetic satellite observations in the determination of the Earth's radiation budget has been

demonstrated. The intriguing possibility exists that measurements of satellite motion may eventually reveal the nature of global asymmetries in the Earth's albedo. Finally, this analysis has revealed certain correlations between the albedo parameters and other estimated parameters, and the influence of gravity field size on the recovery of albedo parameters.

3.4.2 Sensitivity Analysis of Earth Radiation Pressure

Having addressed the questions of how Earth radiation pressure affects the motion of a satellite, and how the albedo parameters might be recovered from observing such motion, the next question might be: how does Earth radiation affect the accurate recovery of other parameters? Of particular interest is its impact on estimates of parameters describing the gravity field of the Earth. A sensitivity analysis has been used to quantify the influence on the estimation of gravity parameters due to errors in the Earth radiation pressure parameters. In this, the University of Texas consider analysis program CONAN has been used to analyze the recovery of geopotential coefficients from a 7.7 year LAGEOS long arc.

In consider analysis, the generalized state vector of dynamic and measurement model parameters is partitioned into estimated and "considered" parameters. The consider parameters are treated as constants with uncertain values, to which are assigned a priori standard deviations. The method of weighted least squares, applied to the partitioned state vector, produces a perturbation matrix, which quantifies the error in each estimated parameter due to a one-sigma error in each consider parameter. The perturbation matrix $[\Gamma]$ is defined as follows

[Tapley *et al.*, 1985]:

$$[\Gamma] = [S_{xc}] [\sigma_c], \quad (3-4)$$

where $S_{xc} = \partial \hat{x} / \partial c$, the sensitivity matrix,

\hat{x} = estimated parameter vector,

c = consider parameter vector,

σ_c = vector of consider standard deviations.

In this study the Earth radiation parameters $a_0, c_0, c_1, c_2, a_2, e_0, k_0, k_1, k_2, e_2$ are treated as consider parameters. The following table indicates the assumed consider sigmas for each Earth radiation parameters, derived from early LAGEOS estimation sigmas [John Ries, *personal communication*]. The large sigma given to c_2 is a coding mistake, but does not affect the results, as no gravity coefficient estimates appear to be sensitive to errors in this parameter.

TABLE 3.11
EARTH RADIATION CONSIDER PARAMETER VALUES

a priori	a_0	c_0	c_1	c_2	a_2	e_0	k_0	k_1	k_2	e_2
value	0.34	0.00	0.10	0.00	0.29	0.68	0.00	-0.07	0.00	-0.18
sigma	0.02	0.04	0.03	0.4	0.04	0.2	0.2	0.1	0.03	0.3

In this case, the assigned a priori sigmas are measures of the ability to determine the coefficients. For example, the consider sigma of e_0 is 0.2. This means that e_0 is difficult to estimate, not that the a priori value of e_0 , as obtained from Stephen's model, is likely to be in error by that amount. The actual errors in the albedo coefficients are difficult to quantify, due to possible biases in Stephen's model arising from anisotropic reflection. (See Section 5.1.1.)

Entries in Table 3.12, following, are obtained by dividing the elements of the perturbation matrix by the appropriate standard deviations of the GEM-L2 gravity field [Lerch *et al.*, 1985]. For example, the "normalized" perturbation of gravity coefficient $C_{i,j}$ would be:

$$\Gamma'(C_{i,j}) = \Gamma(C_{i,j}) / \sigma(C_{i,j})_{\text{GEM-L2}},$$

where $\sigma(C_{i,j})_{\text{GEM-L2}}$ = GEM-L2 standard deviation for $C_{i,j}$.

Normalizing the perturbations in this manner illustrates the importance of each coefficient perturbation, relative to its uncertainty. Only the largest perturbations are shown for each run.

Among the estimated parameters listed in Table 3.12 is \dot{C}_T , which refers to the time rate-of-change of the along-track drag coefficient. The LAGEOS periodic drag terms, also estimated, represent an empirical periodic model of the along-track deceleration anomaly. As always, η_R is the solar reflectivity and μ the gravity parameter.

Some sensitivity of the odd zonals to errors in the first degree albedo term is evident in case C1, below. (The reverse scenario is treated in the preceding section, in which errors in the odd zonals are shown to interfere with the accurate estimation of the albedo parameters, in particular the first degree term.) It should be noted, however, that case C1 is overly pessimistic, in the sense that the solution itself is poorly determined. In particular, it is unrealistic to expect observations from a single satellite, even one as well observed as LAGEOS, to resolve all the coefficients in a full 7x7 field. The large values of the perturbations for the odd zonals is due in part to the strong negative correlation which exists among these terms. When a smaller set of gravity coefficients is estimated, as in case C2, the

TABLE 3.12
GRAVITY COEFFICIENT PERTURBATIONS DUE TO ERRORS IN
EARTH RADIATION PARAMETERS
(Normalized by GEML2 standard deviations.)

case	Estimated Parameters									
[C1]	7x7 Gravity field, η_R , μ , C_T , \dot{C}_T , LAGEOS periodic drag terms									
Grav. Coeff.	a_0	$[c_0]$	c_1	$c_2]$	a_2	e_0	$[k_0]$	k_1	$k_2]$	e_2
J_3	14.	203.	200.	<10	<10	<10	-14.	<10	-11.	<10
J_5	-11.	-183.	-179.	<10	<10	<10	13.	<10	10.	<10
J_7	-13.	203.	200.	<10	<10	<10	-14.	10.	-11.	<10
$C_{7,1}$	27.	<10	-10.	<10	-12.	<10	-11.	16.	<10	<10
$S_{7,1}$	<10	<10	<10	<10	<10	-44.	<10	-32.	<10	<10
case	Estimated Parameters									
[C2]	$J_2, J_3, C_{4,1}, S_{4,1}, C_{7,1}, S_{7,1}, \eta_R, \mu, C_T, \dot{C}_T$, LAGEOS periodic drag terms									
Grav. Coeff.	a_0	$[c_0]$	c_1	$c_2]$	a_2	e_0	$[k_0]$	k_1	$k_2]$	e_2
$C_{4,1}$	<1	1.	1.	<1	<1	-2.	<1	<1	<1	<1
$S_{4,1}$	<1	2.	2.	<1	<1	1.	<1	<1	<1	<1
$C_{7,1}$	<1	7.	6.	<1	<1	5.	-3.	3.	-2.	<1
$S_{7,1}$	6.	4.	3.	<1	-1.	-9.	-2.	-3.	-1.	<1

values in the perturbation matrix fall dramatically. In this better determined situation, the correlation between the odd zonal term J_3 and the albedo parameters is no longer evident. Accurate recovery of the order 1 coefficients is still affected by errors in the albedo and emissivity terms, however. This makes sense, as both the albedo and the order 1 terms possess significant daily variations.

In sum, it would appear that the albedo and emissivity coefficients are capable

of affecting the accurate recovery of some gravity coefficients. In particular, the odd degree zonals and the first order terms appear to be correlated with Earth radiation pressure, and may be adversely affected by errors in the Earth radiation pressure model.

3.5 Effects of Longitudinal Variations in Albedo

Thus far, the albedo and emissivity models considered in this study have embodied latitudinal variations only. Two arguments support this implementation, the first being that variations in the Earth radiation parameters show a dominant latitudinal dependency. Also, in the absence of resonance, the rotation of the Earth will average out long period orbital effects of longitudinal signals in albedo and emissivity. Nevertheless, it is difficult to ignore the presence of large scale longitudinal albedo variations, which even the most cursory examination of a globe or satellite photos reveals. Combine this with the known influence of land mass on cloudiness, and seasonal changes in cloud cover and ice mass, and the possibility of large scale long term longitudinal variations in albedo cannot be discounted. It would seem worthwhile, therefore, to examine the influence of a nonzonal albedo model on the orbital effects of various satellites.

When nonzonal terms are included, the albedo is calculated as follows:

$$a = \sum_{n=0}^{\infty} \sum_{m=0}^n P_{nm}(\sin \phi) [a_{c_{nm}} \cos m\lambda + a_{s_{nm}} \cos m\lambda], \quad (3-5)$$

where P_{nm} = Legendre's associated function,

ϕ = geocentric latitude,

$$\begin{aligned}\lambda &= \text{longitude}, \\ a_{c_{nm}} &= \text{cosine coefficient}, \\ a_{s_{nm}} &= \text{sine coefficient}.\end{aligned}$$

This is the general form of the spherical harmonic expansion common in the characterization of the Earth's geopotential [Kaula, 1966]. The coefficients are unnormalized.

The albedo coefficients used for this study are based on a preliminary field developed by Philip Ardanuy and Richard Hucek of Research and Data Systems, Inc. [Ardanuy and Hucek, *personal communication*]. This four by four field represents a deconvolution of NIMBUS-7 wide field-of-view (WFOV) radiometer data for January, 1981, corrected for diurnal variations in albedo. (See Hucek *et al.* [1987] for a description of the deconvolution procedure.) The albedo coefficients in this case are determined by direct radiometer measurements of the Earth, unlike the coefficients in Sehnal [1979], which are inferred from solar sensor data and an assumed model of the Earth's reflectivities and surface type distribution.

A contour map of Ardanuy and Hucek's albedo field is shown in Figure 3.22. The contours clearly illustrate the expected dominance of zonal terms. Also, while the selection of a low degree and order field is motivated primarily by considerations of simplicity and efficiency, it is interesting to note the high degree of correlation between the contours and distributions of land, ocean, and snow-ice areas. Specifically, the oceans are shown as areas of low albedo, while the land masses display somewhat higher reflectivities, especially at northern mid-latitude locations. Such results are consistent with known properties of the terrestrial sphere, in particular the darkness of the oceans and the high planetary albedo

associated with high cloudiness and snow fields during winter in the northern hemisphere. The very high albedo values shown at extreme northern latitudes might be due in some measure to the presence of arctic ice and snow fields, although it is likely that some of the data at these locations are somewhat corrupted by the scattering of direct sunlight into the WFOV radiometer [Ardanuy and Hucek, *personal communication*]. In general, though, the 4 x 4 field appears to produce an albedo distribution which is intuitively "reasonable" for the indicated season. The following table lists Ardanuy and Hucek's albedo coefficients for January, 1981, converted into unnormalized form for use in UTOPIA:

TABLE 3.13
4 x 4 ALBEDO FIELD for January, 1981

n	m	$a_{c_{nm}}$	$a_{s_{nm}}$
0	0	0.367	
1	0	0.108	
2	0	0.361	
3	0	0.049	
4	0	0.158	
1	1	0.00863	0.01921
2	1	-0.00046	0.00577
2	2	-0.00118	-0.00921
3	1	0.00425	0.00034
3	2	-0.00182	0.00295
3	3	0.00083	0.00212
4	1	-0.00696	-0.00426
4	2	-0.00075	0.00351
4	3	0.00077	0.00029
4	4	-0.00019	0.00046

In an effort to simulate some of the expected north-south periodic variations in

albedo, the following 365.25 day periodicity is imposed on the coefficients $a(1,0)$ and $a(3,0)$:

$$a(1,0) = .118 \cos(\omega(JD - t_0)) \quad (3-6)$$

$$a(3,0) = -.026 + .082 \cos(\omega(JD - t_0)), \quad (3-7)$$

where $\omega = 2\pi/365.25$,

JD = Julian date of interest,

t_0 = epoch of the periodic terms (December 22, 1980).

The general form of these equations and in particular the constant term in the expression for $a(3,0)$ are based on Rubincam's periodic expressions for these coefficients [Rubincam, 1985]. Both of these coefficients agree with Ardanuy and Hucek's field at mid-January. Figure 3.23 is a contour map of the Earth's albedo at mid-summer in the northern hemisphere. In this case, the larger albedo values occur in the Southern hemisphere, as expected.

When the 4x4 field is utilized with the diffuse model, the resulting perturbations to the LAGEOS orbit, as determined by trajectory comparisons, are similar in nature and magnitude to the effects given by a purely zonal representation. Figures 3.24 through 3.27 illustrate the direct trajectory differences for semimajor axis, eccentricity, inclination, and argument of perigee. In most respects they are quite close to the plots generated via the second degree zonal model. The node perturbations for a 1100 day trajectory comparison are shown in Figure 3.28. The overall node rate is reduced slightly, due in part to the larger value of a_2 , and to the presence of the fourth degree zonal term.

The 4 x 4 quasi-periodic albedo representation at first appears to increase, slightly, the overall orbital influence of Earth radiation pressure, as illustrated by

Table 3.14. The position difference RMS is larger by approximately 5% when the extended field is used, but this is certainly due to the larger value of a_0 in the 4x4 field. A trajectory comparison run in which the extended field is utilized, but a_0 is reset to the nominal value of 0.34 indicates an RMS 5.6% *smaller* than the nominal second degree zonal results.

TABLE 3.14
COMPARISON OF 4 x 4 ALBEDO FIELD WITH 2 x 0 ALBEDO FIELD
365 Day LAGEOS Arc

MODEL	Estimated Parameters	RMS of fit [m.]
diffuse 2 x 0	IC	8.4
diffuse 2 x 0	IC, C_T , η_R	3.95
diffuse 4 x 4	IC	8.9
diffuse 4 x 4	IC, C_T , η_R	4.13
diffuse 4 x 4 ($a_0 = 0.34$)	IC, C_T , η_R	3.75

It is evident that the introduction of higher degree tesseral and sectorial terms in the albedo representation does not contribute significantly to the orbital perturbations. As expected, the magnitude of the zonal terms is of much greater importance in determining the long term evolution of the orbit of LAGEOS. Thus, an important assumption motivating the choice of a purely zonal albedo representation has been verified.

The possible existence of resonant terms at higher orders cannot be ruled out, although resonance would require commensurability between the orbital period, the Earth's rotation period, and the solar geometry. At the high orders expected to

produce resonance, however, the albedo terms would likely be quite variable. The effects of clouds and shadowing on the planetary albedo of a small portion of the terrestrial sphere would tend to prevent the systematic sensing of a commensurate term.

3.6 Conclusions

The effect of diffuse Earth radiation pressure on low eccentricity satellites manifests itself as small amplitude, long period variations in the semimajor axis, eccentricity, inclination, and argument of perigee. Only the node is affected by a small secular change, which is influenced to like order by both the shortwave and longwave Earth radiation. It has been shown that diffuse Earth radiation pressure cannot be the drag-like agent which is causing the residual change in LAGEOS' semimajor axis.

For satellites in highly eccentric, eclipsing orbits, diffuse Earth radiation pressure can generate non-negligible average along-track accelerations or decelerations. Analyses of real satellite data suggest the importance of an Earth radiation pressure model in the accurate determination of drag coefficients.

The albedo coefficients a_0 and a_2 are capable of being recovered from LAGEOS data, and from a multi-satellite data set, if LAGEOS solar reflectivities are frozen. The constant first degree term c_0 , however, is more difficult to resolve. This study represents the first time that a multi-satellite data set has been used to estimate Earth radiation parameters. Results of the multi-satellite study and covariance analysis have identified the correlations between albedo parameters and

other estimated parameters.

With the exception of perturbations in the node, the orbital perturbation due to longwave radiation amounts to only about ten percent of the total Earth radiation pressure effect. In addition, little enhancement in performance is obtained with the use of a low degree and order nonzonal albedo model. Thus, any significant improvements in the determination of Earth radiation pressure must be directed towards the modeling of the shortwave component. Terrestrial shortwave radiation possesses significant nondiffuse and time-variant properties not addressed in the nominal model. It remains to be seen what real effect these properties have in the context of orbit determination. An advanced Earth radiation model which embraces both directional reflectance and various diurnal albedo variations is described in the following sections.

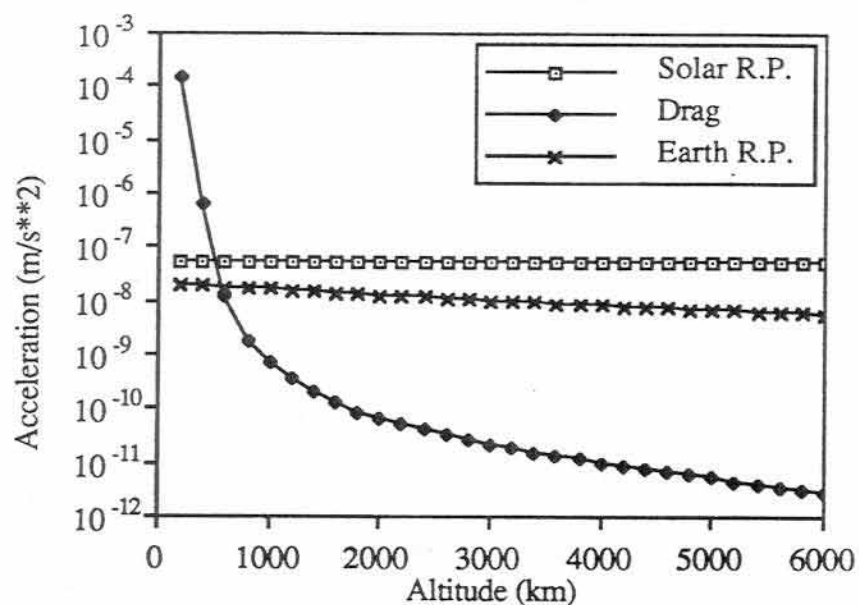


Fig. 3.1(a)

Variation of Earth Radiation Pressure With Altitude: Semilog Plot

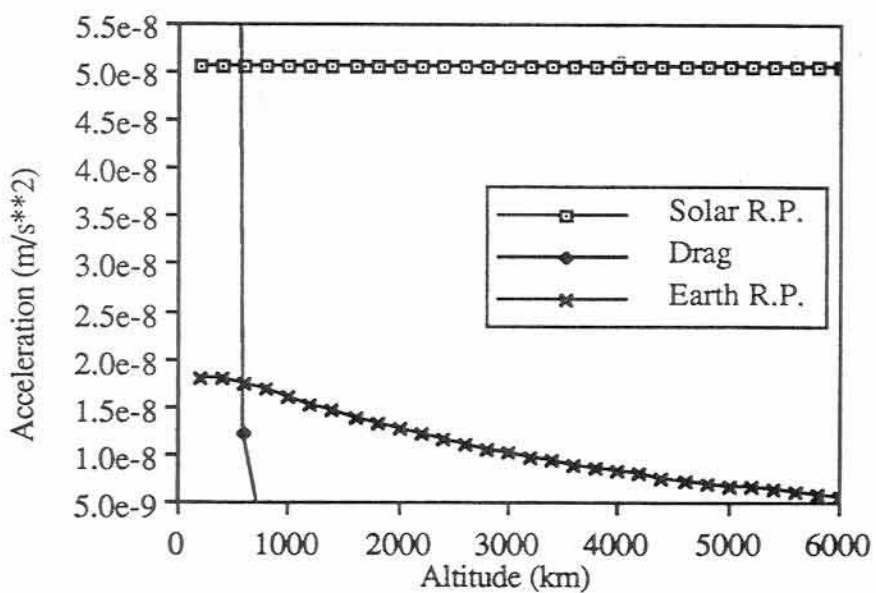


Fig. 3.1(b)

Variation of Earth Radiation Pressure With Altitude: Linear Plot

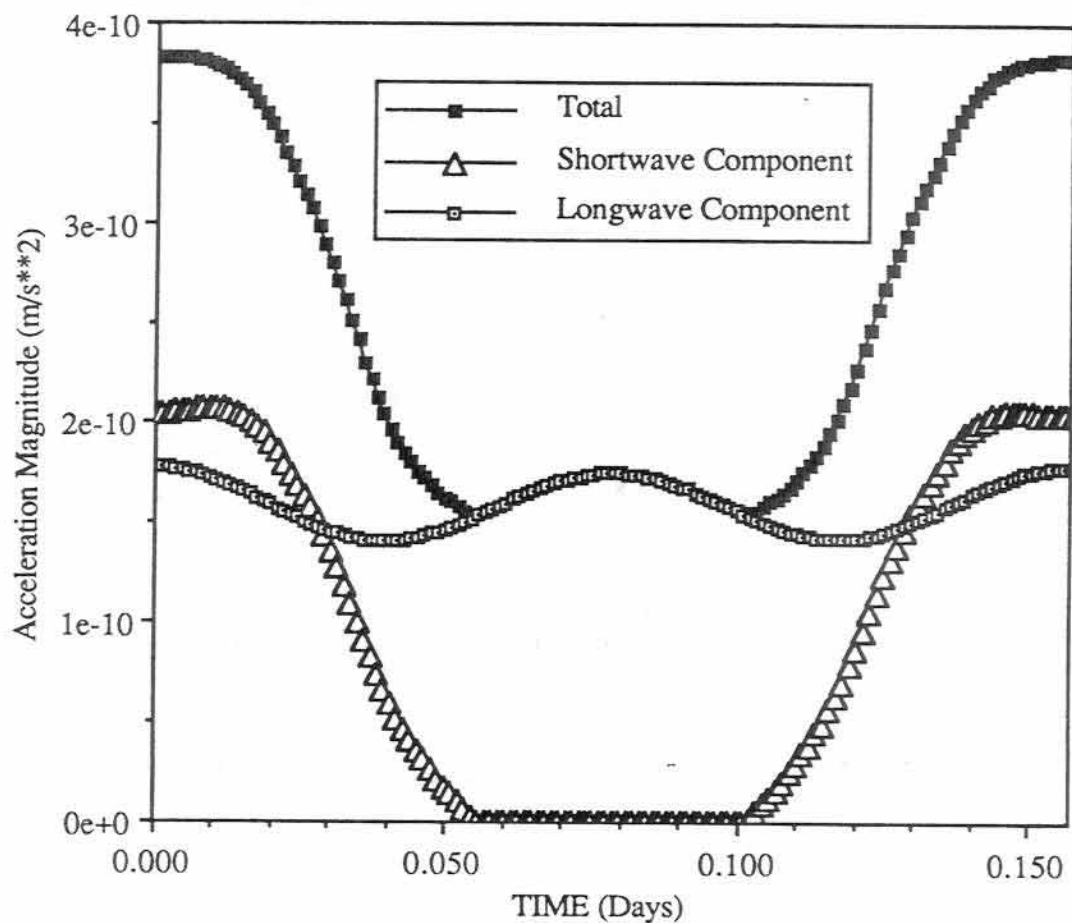


Fig. 3.2

Shortwave and Longwave Components of Earth Radiation Pressure
on LAGEOS: Diffuse Model, Eclipsing Orbit

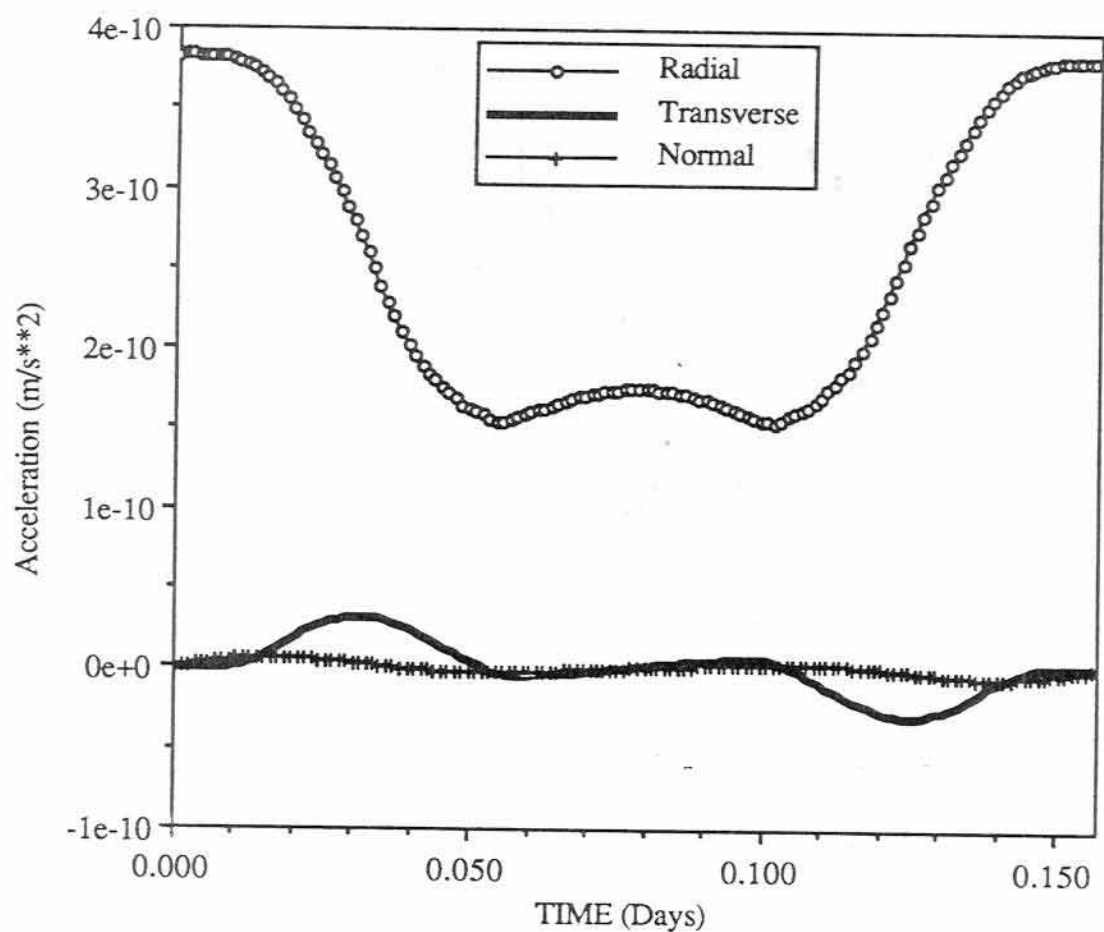


Fig. 3.3
Radial, Transverse, and Normal Earth Radiation Accelerations
on LAGEOS: Diffuse Model, Eclipsing Orbit

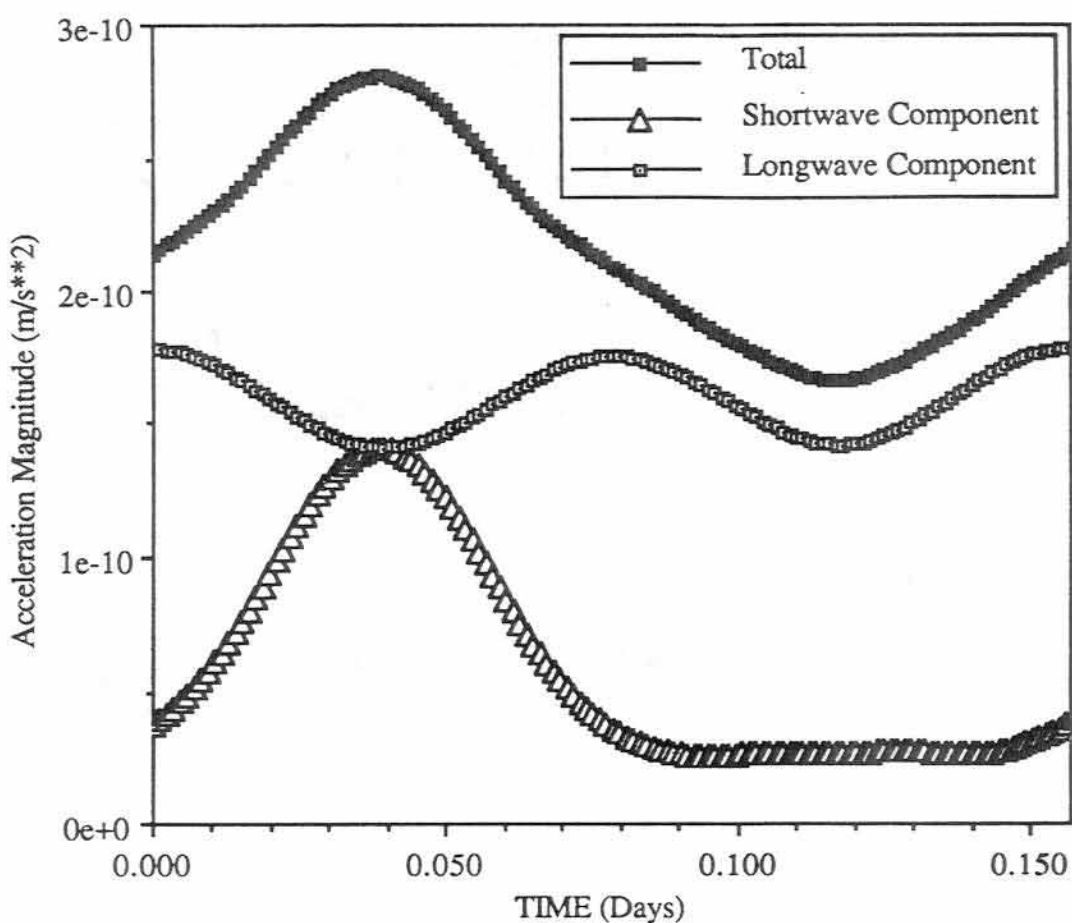


Fig. 3.4

Shortwave and Longwave Components of Earth Radiation Pressure
on LAGEOS: Diffuse Model, Non-eclipsing Orbit

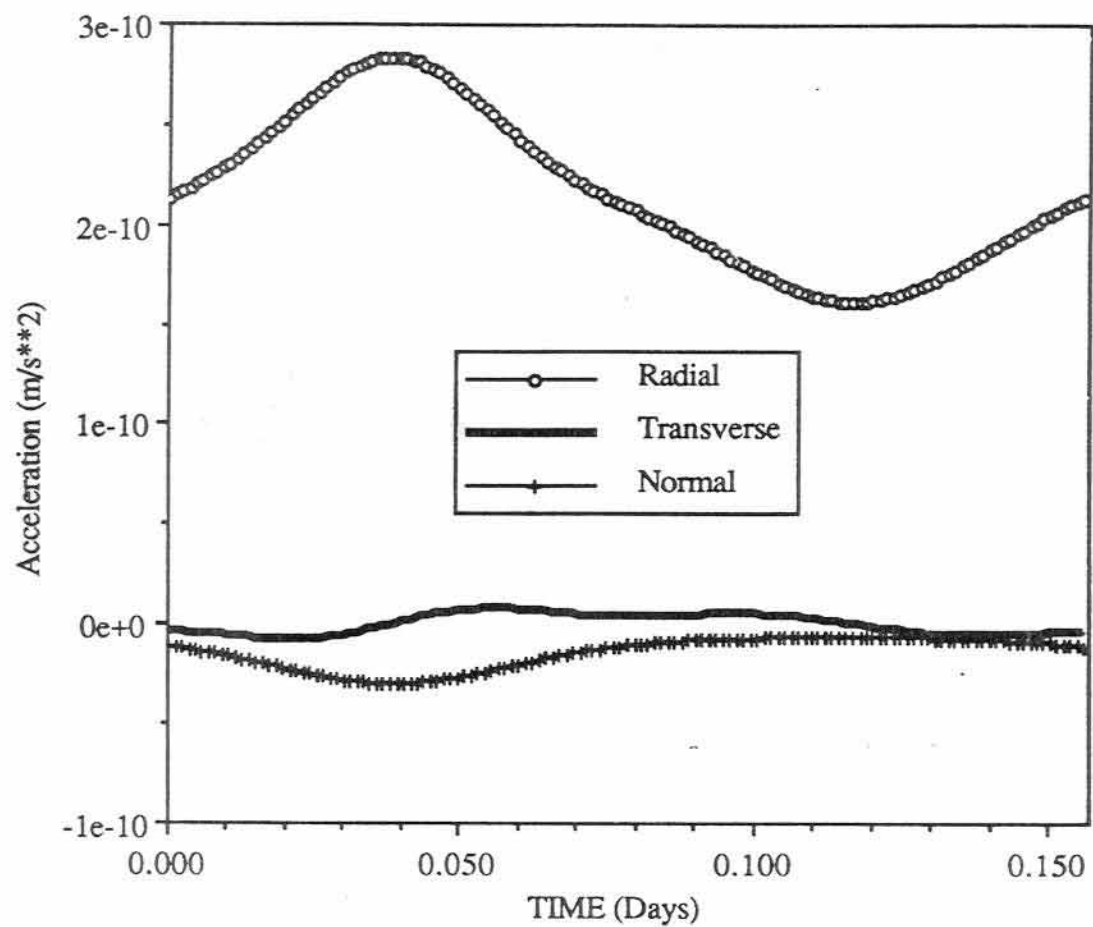


Fig. 3.5
Radial, Transverse, and Normal Earth Radiation Accelerations
on LAGEOS: Diffuse Model, Non-eclipsing Orbit

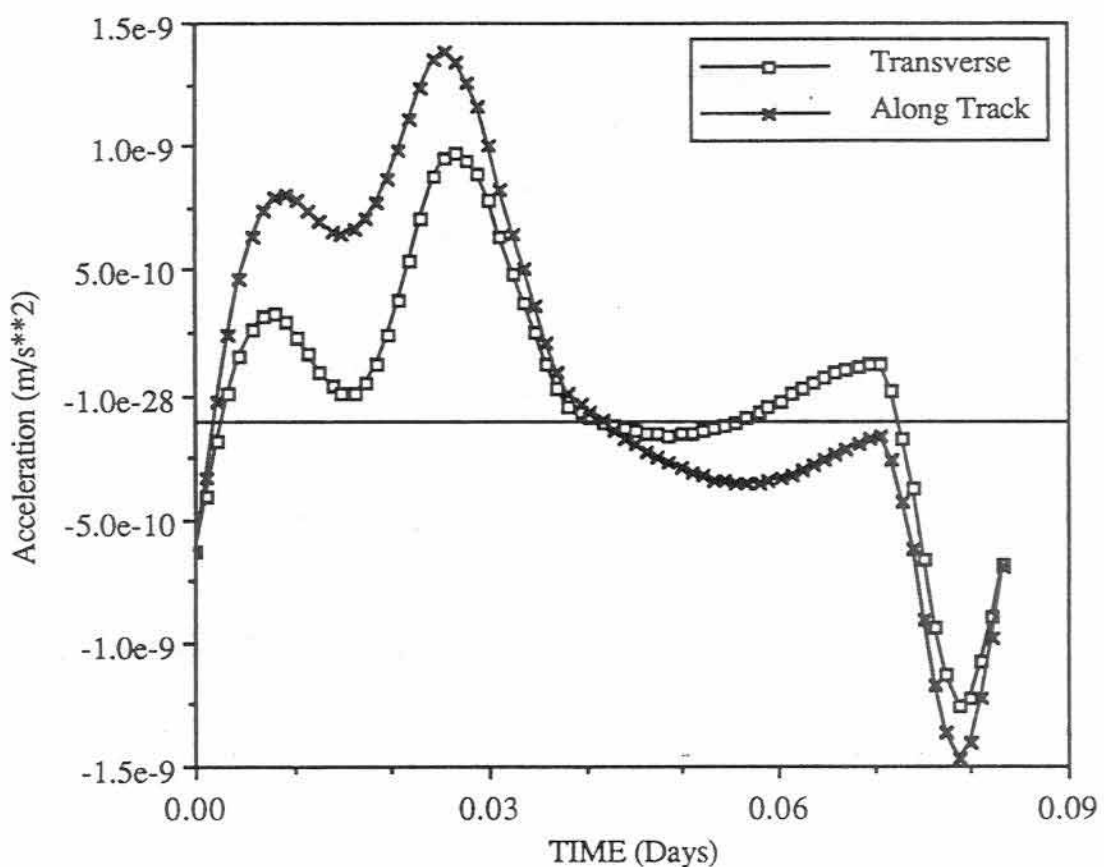


Fig. 3.6
Transverse and Along-Track
Diffuse Earth Radiation Acceleration on GEOS-1
Eclipsing Orbit: 6-27-77

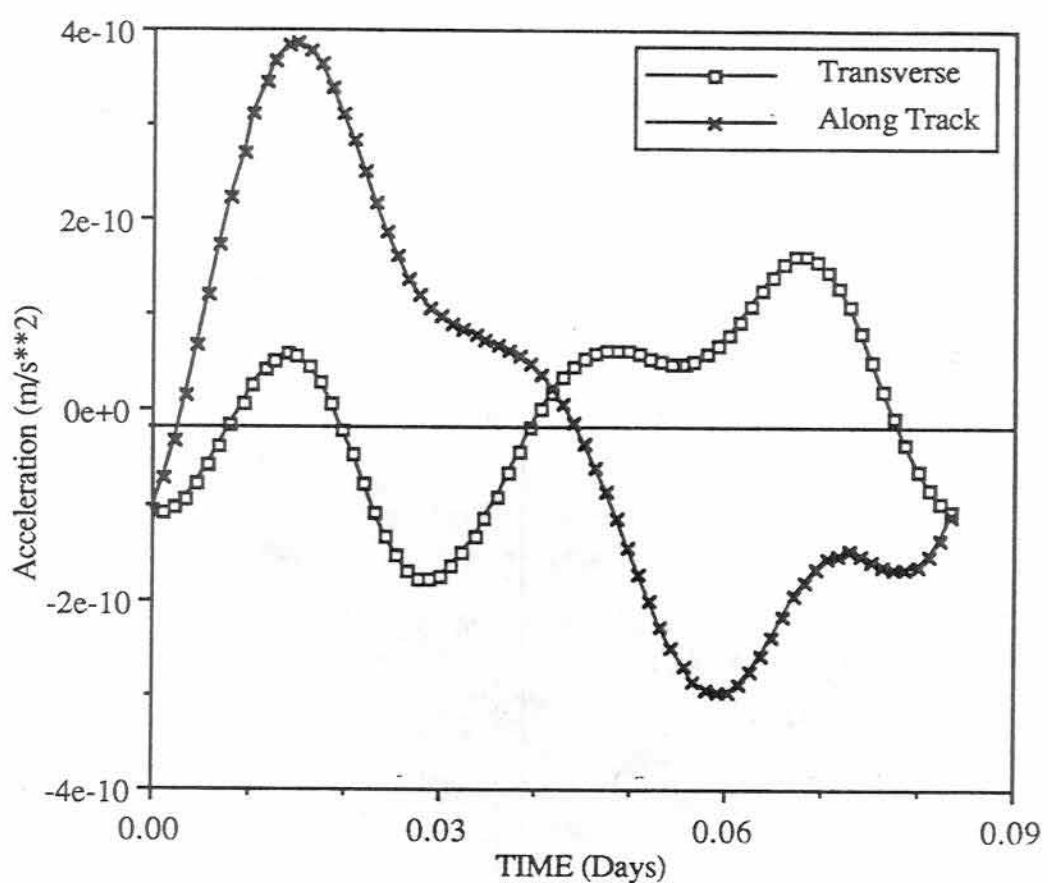


Fig. 3.7
Transverse and Along-Track
Diffuse Earth Radiation Acceleration on GEOS-1
Non-eclipsing Orbit

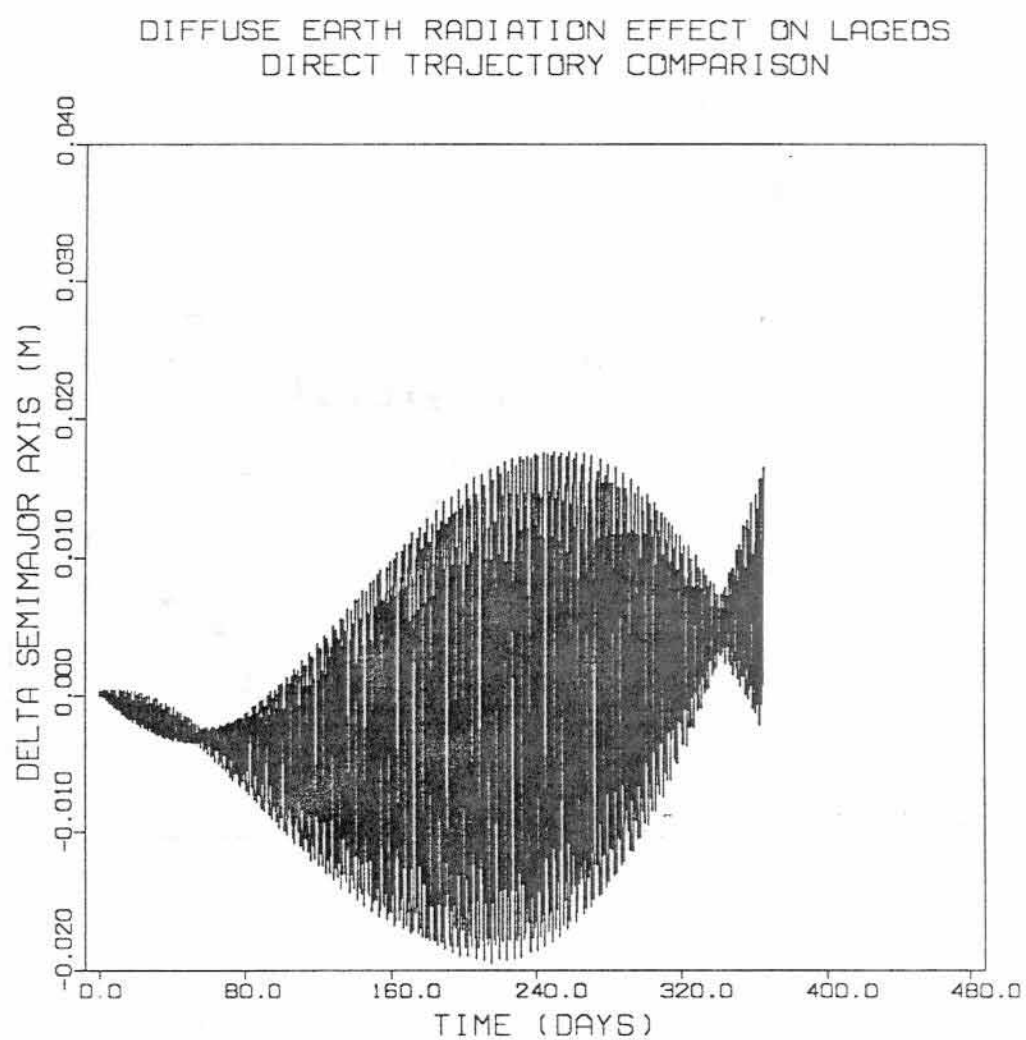


Fig. 3.8
Diffuse Earth Radiation Effect on LAGEOS:
Change in the Semimajor Axis

DIFFUSE EARTH RADIATION EFFECT ON LAGEOS
DIRECT TRAJECTORY COMPARISON

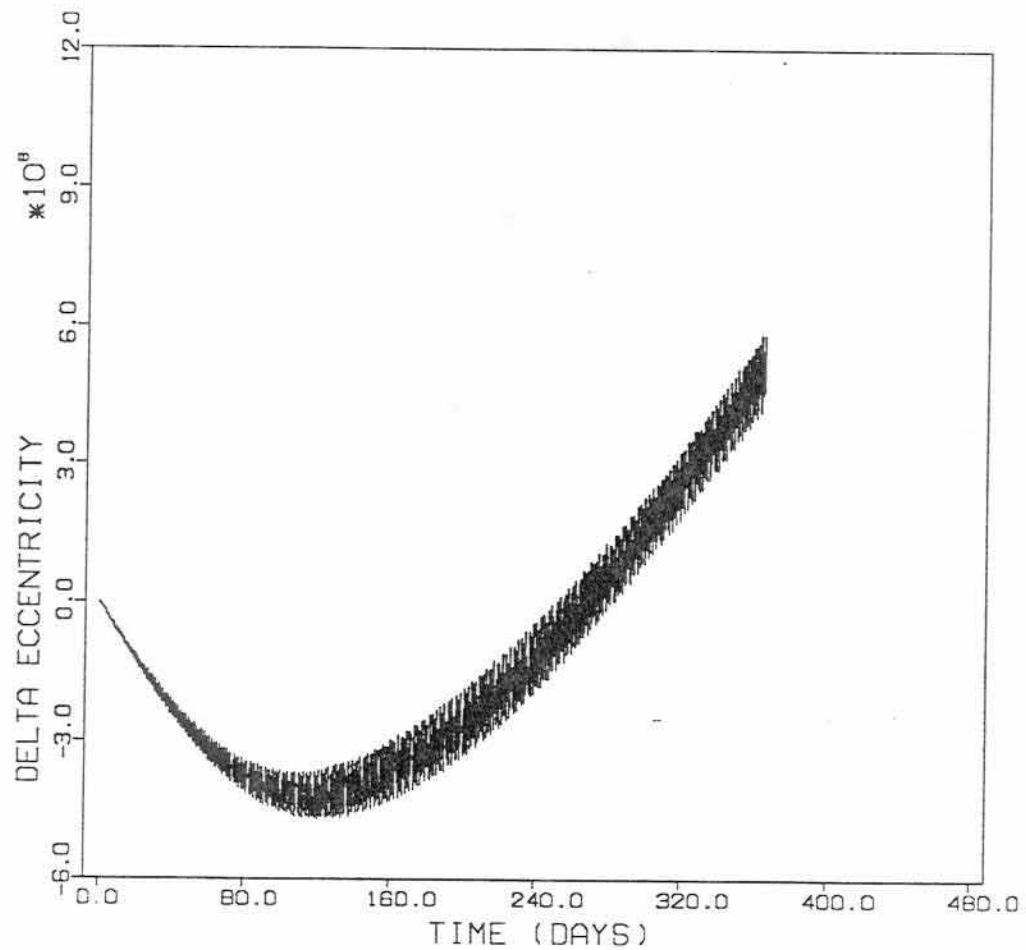


Fig. 3.9

Diffuse Earth Radiation Effect on LAGEOS:
Change in the Eccentricity

DIFFUSE EARTH RADIATION EFFECT ON LAGEOS
DIRECT TRAJECTORY COMPARISON

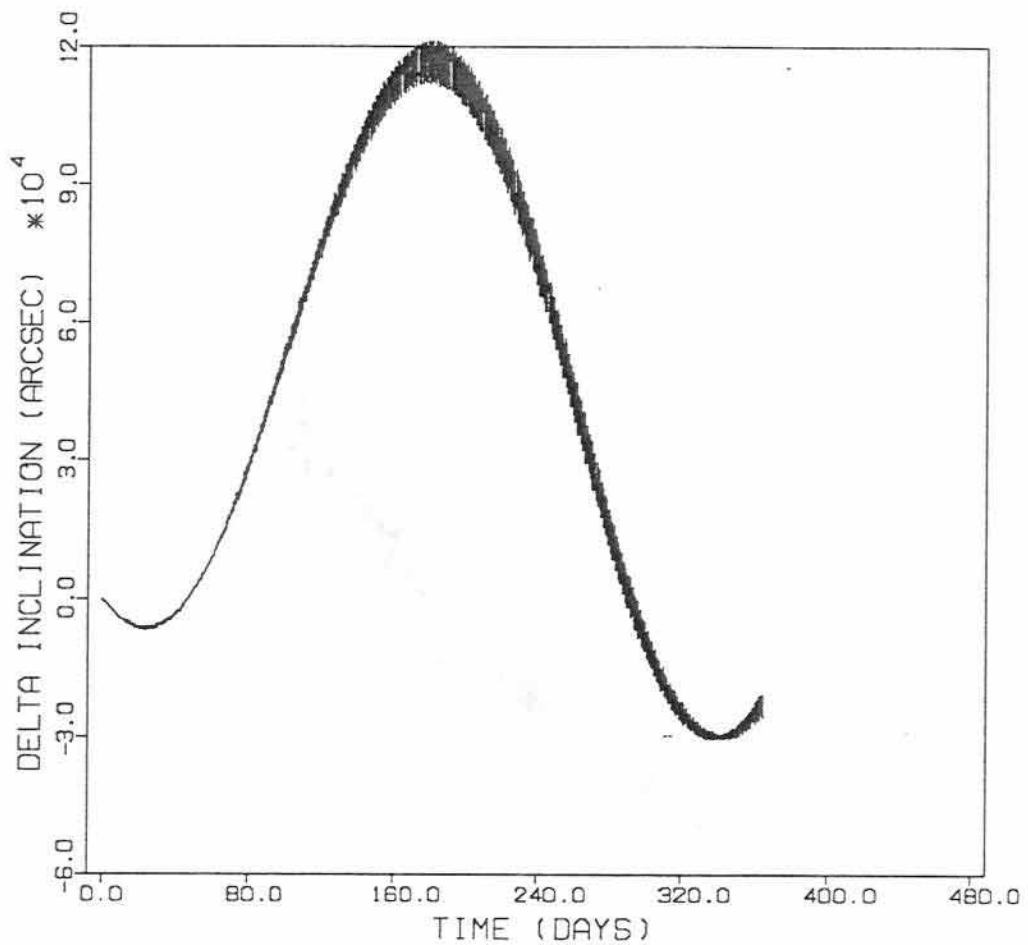


Fig. 3.10
Diffuse Earth Radiation Effect on LAGEOS:
Change in the Inclination

DIFFUSE EARTH RADIATION EFFECT ON LAGEOS
DIRECT TRAJECTORY COMPARISON

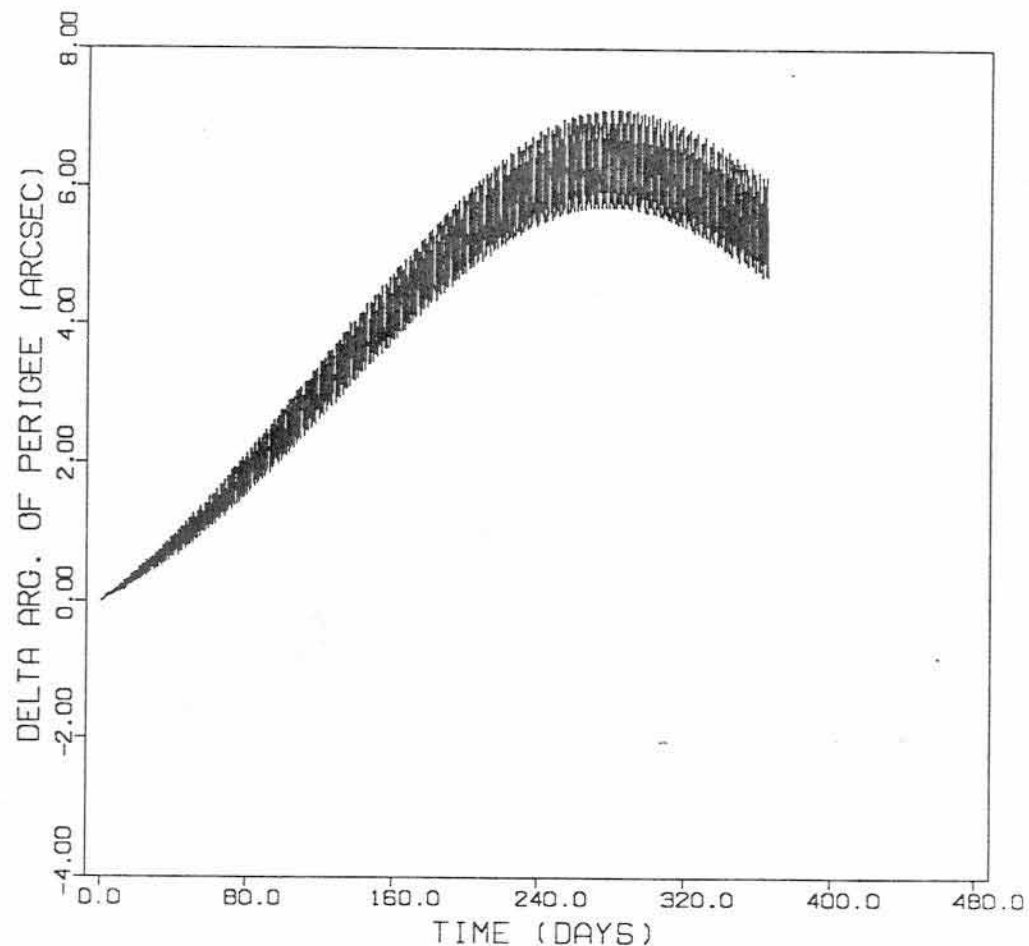


Fig. 3.11

Diffuse Earth Radiation Effect on LAGEOS:

Change in the Argument of Perigee

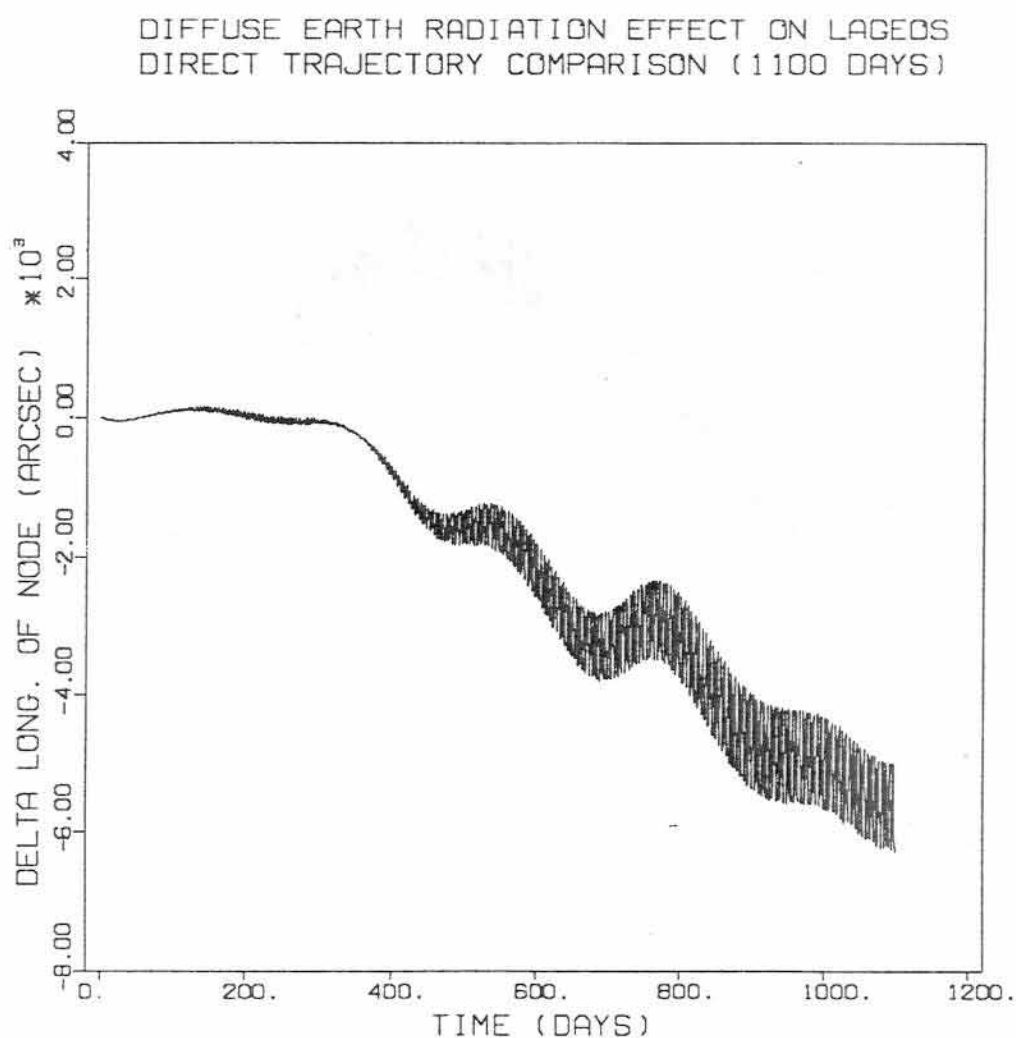


Fig. 3.12
Diffuse Earth Radiation Effect on LAGEOS:
Change in the Node for a 1100 Day Arc

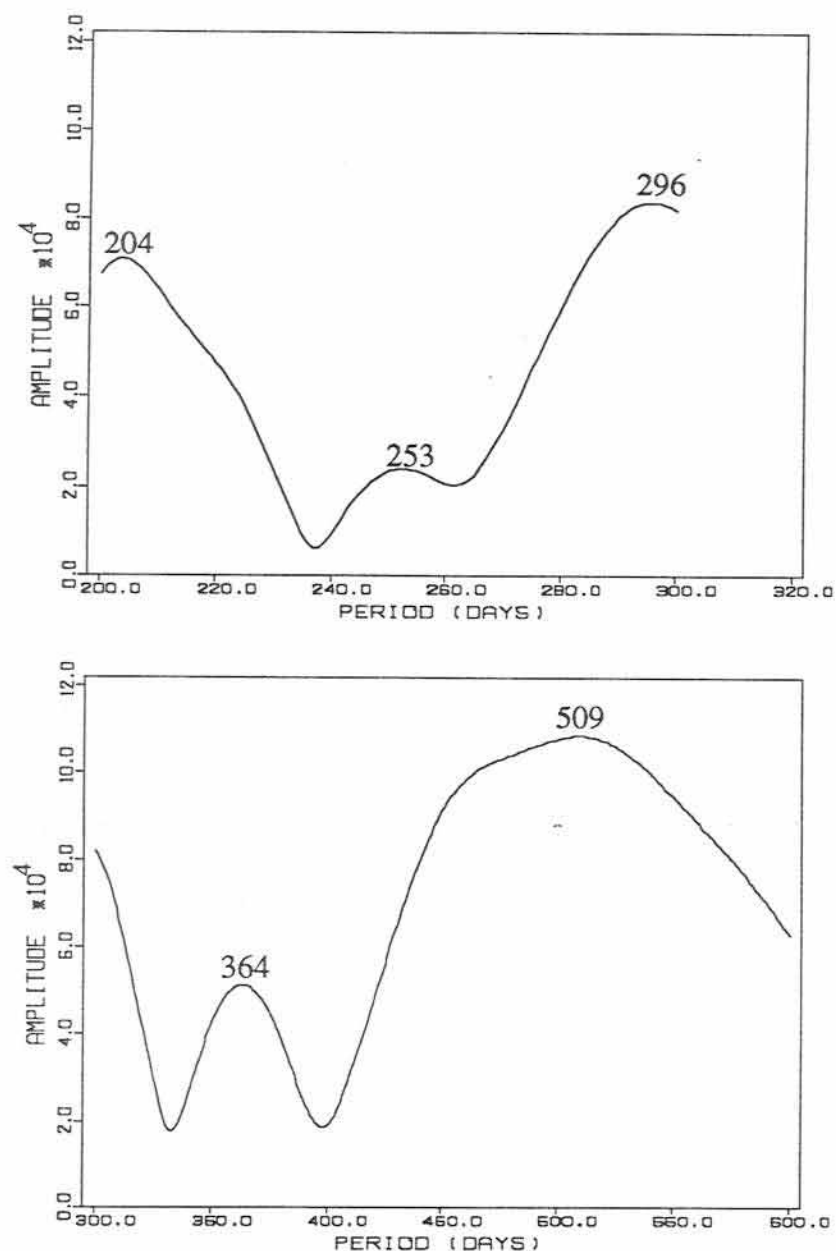


Fig. 3.13

Periodogram of Change in the Semimajor Axis of LAGEOS

2100 Day Trajectory Comparison, Diffuse Model, Estimating IC, C_T, η_R

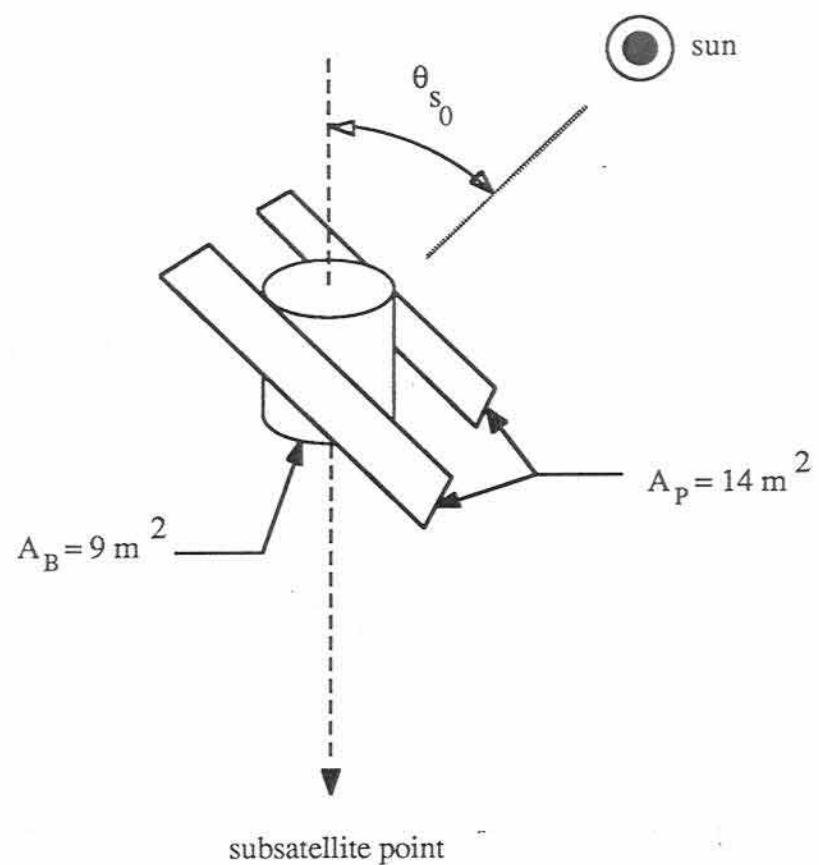


Fig. 3.14
Variable Area Model

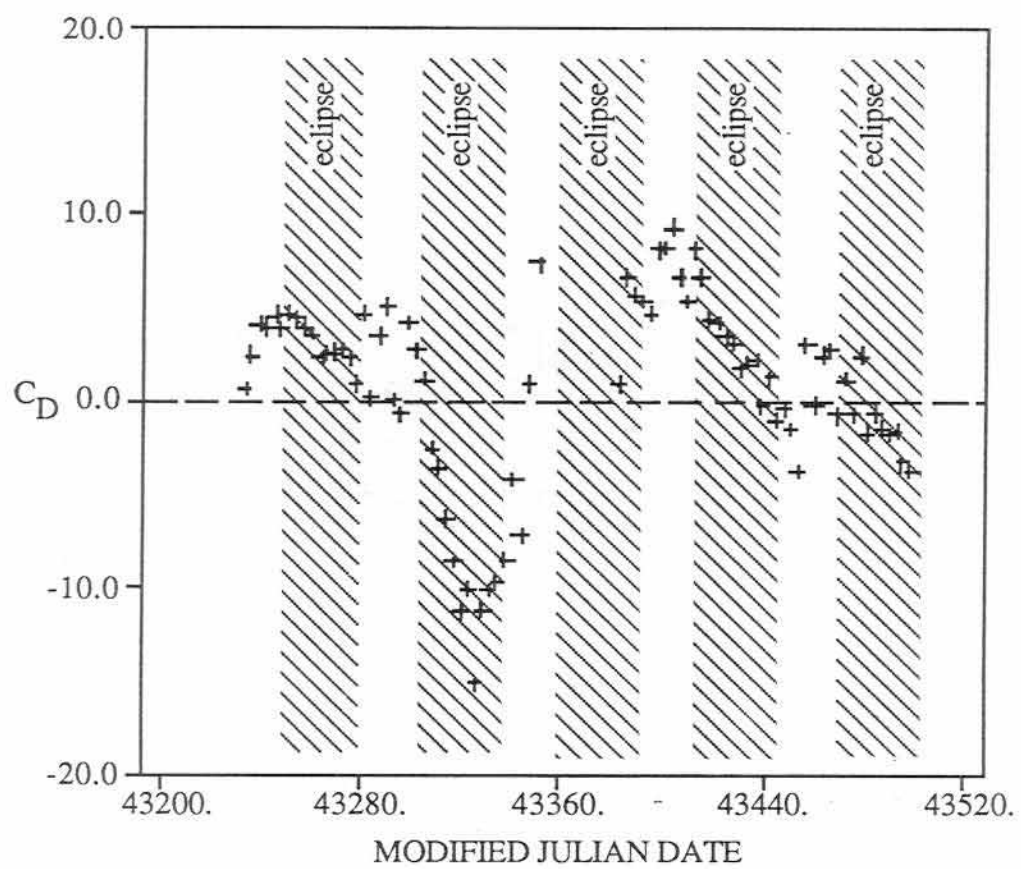
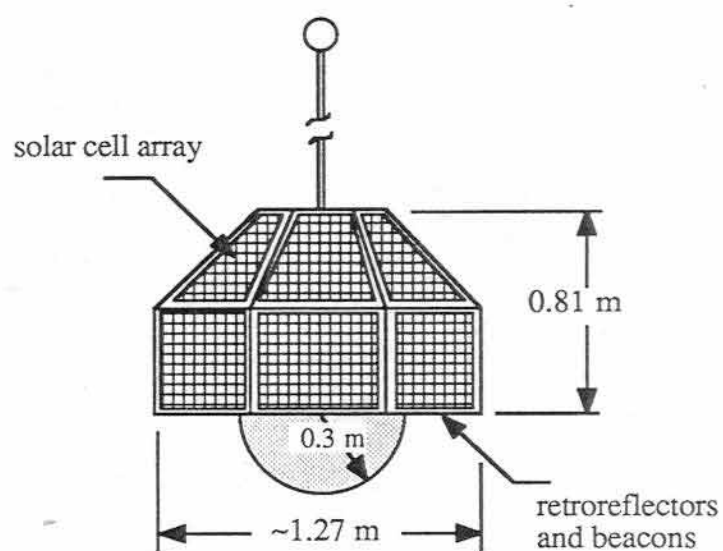


Fig. 3.15
GEOS-1 Drag Coefficients and Eclipse Intervals



$$\begin{aligned} \text{area from below} &= 1.24 \text{ m}^2 \\ \text{area from side} &= 1.02 \text{ m}^2 \end{aligned}$$

mass = 176 kg

gravity gradient stabilized

Fig. 3.16

GEOS-1 Physical Characteristics

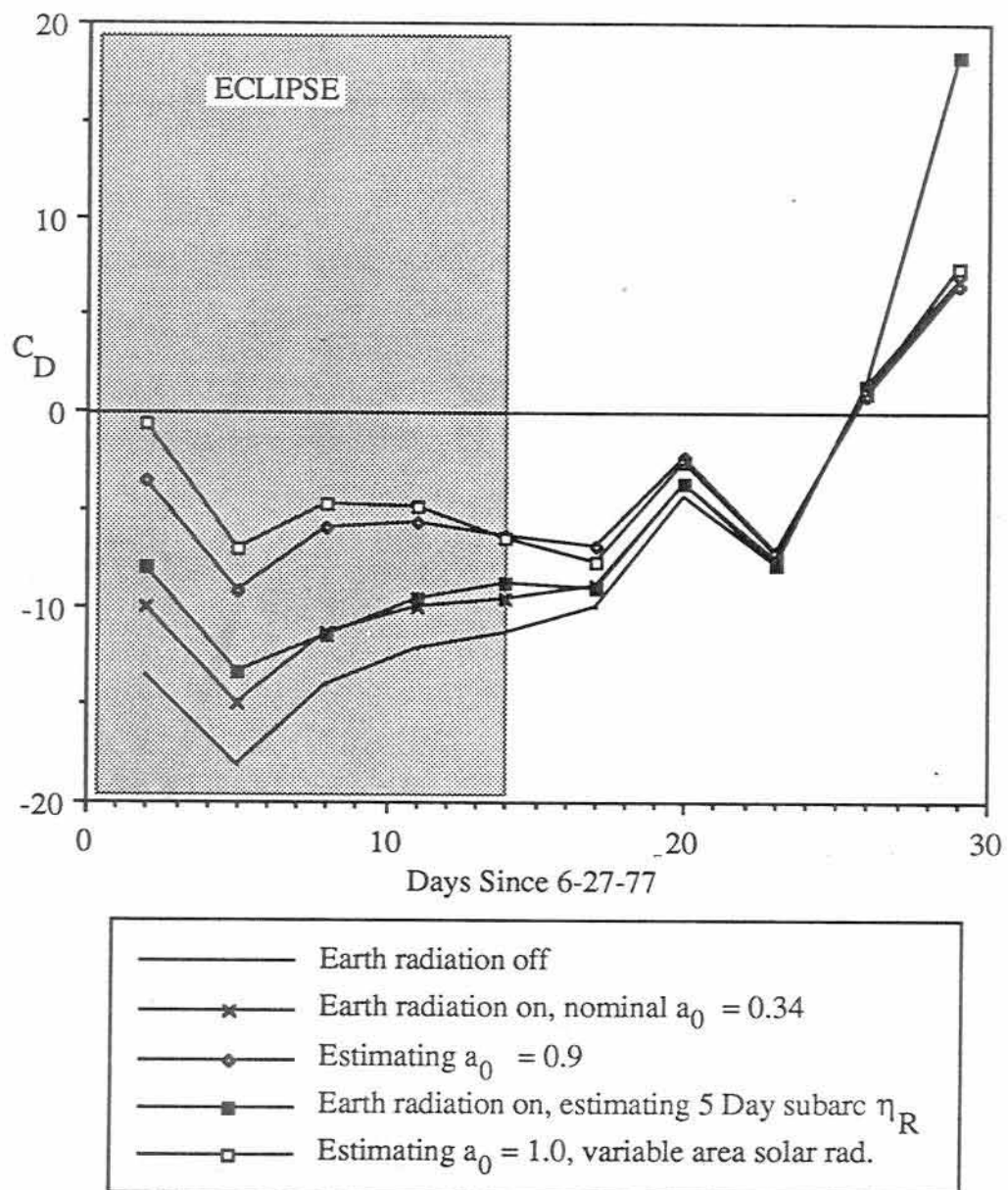


Fig. 3.17

Effects of Earth and Solar Radiation Pressure on GEOS-1 C_D Estimates30 Day Arc Starting 6-27-77, 3-Day C_D Values

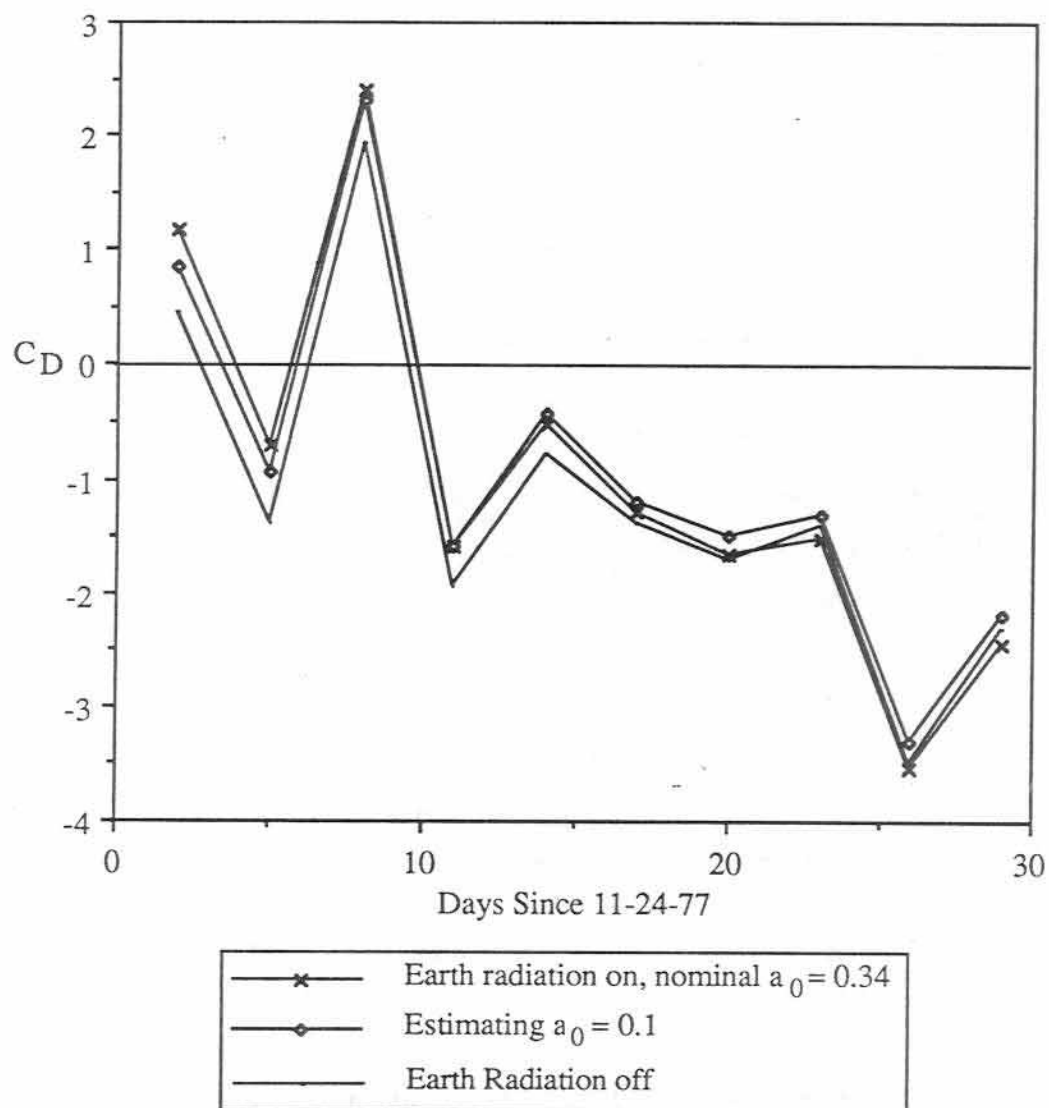


Fig. 3.18

Effects of Earth Radiation Pressure on GEOS-1 C_D Estimates
30 Day Arc Starting 11-14-77, 3-Day C_D Values

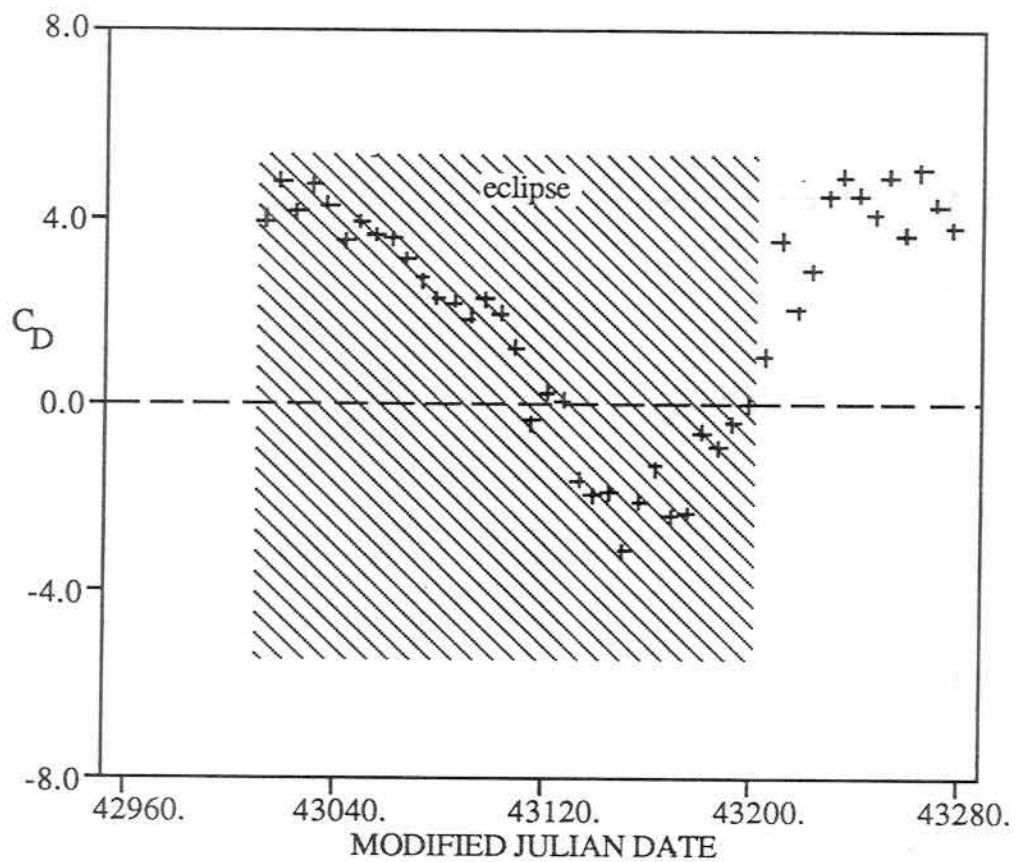


Fig. 3.19
GEOS-2 Drag Coefficients and Eclipse Intervals

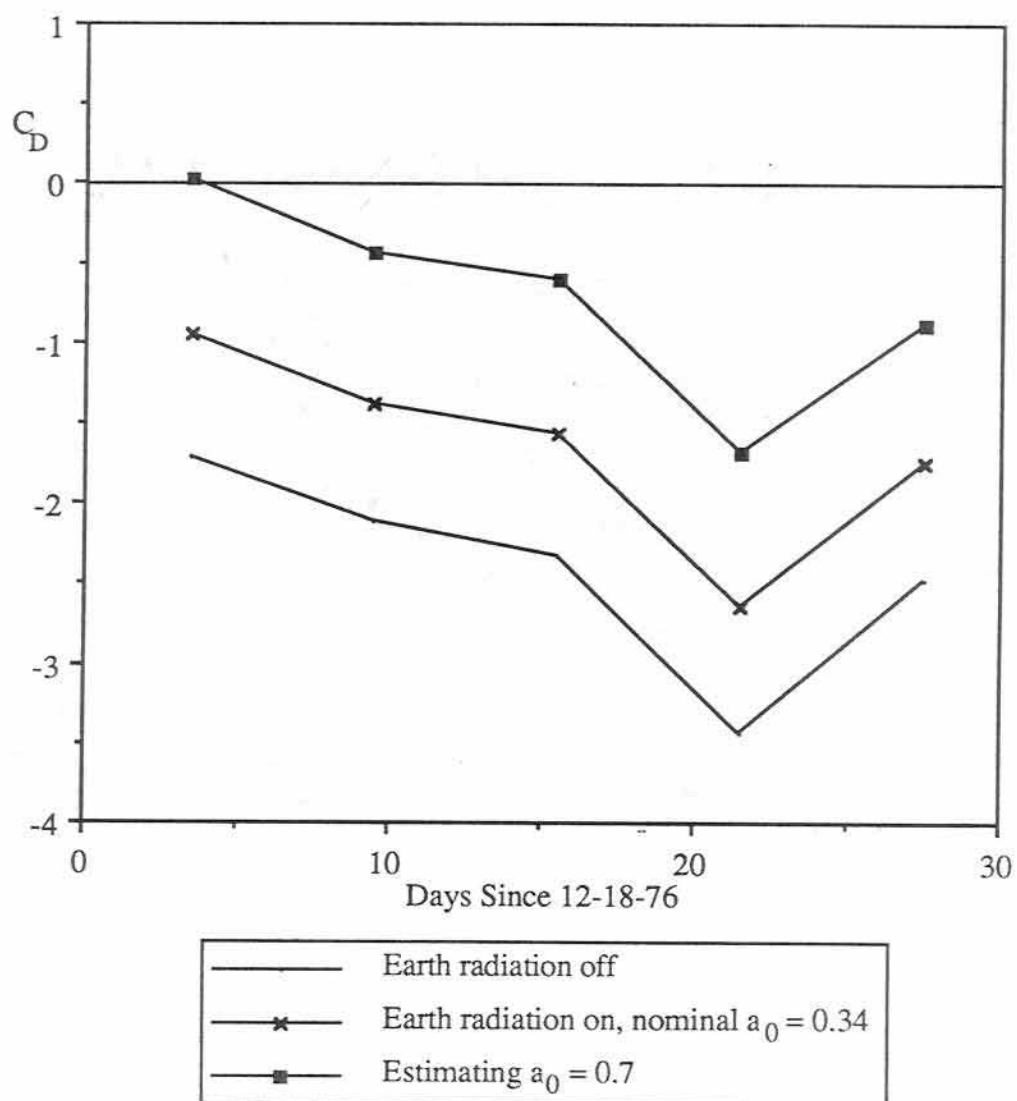


Fig. 3.20
Effects of Earth Radiation Pressure on GEOS-2 C_D Estimates
30 Day Arc Starting 12-18-76, 6-Day C_D Values

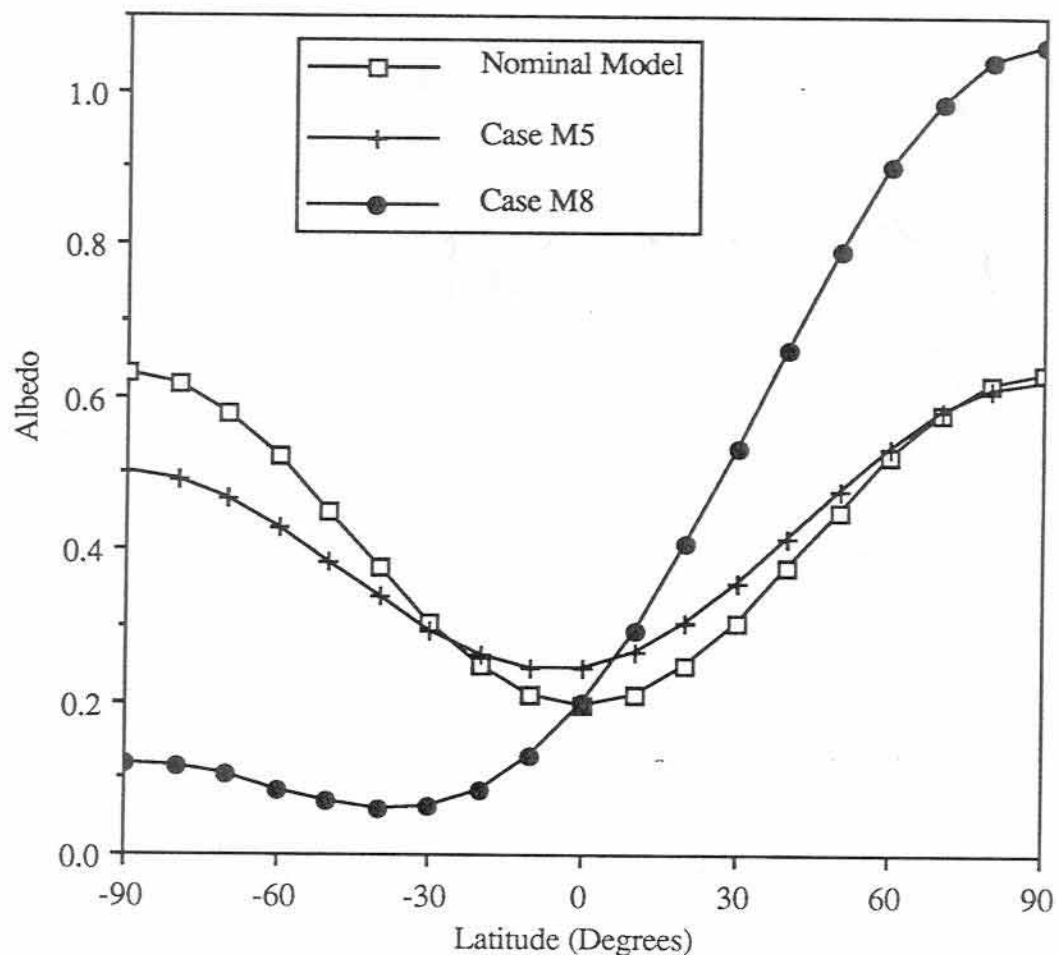


Fig. 3.21

Comparison of Nominal Albedo Model and Multi-Satellite Cases M5 and M8
(Non-periodic Terms Only)

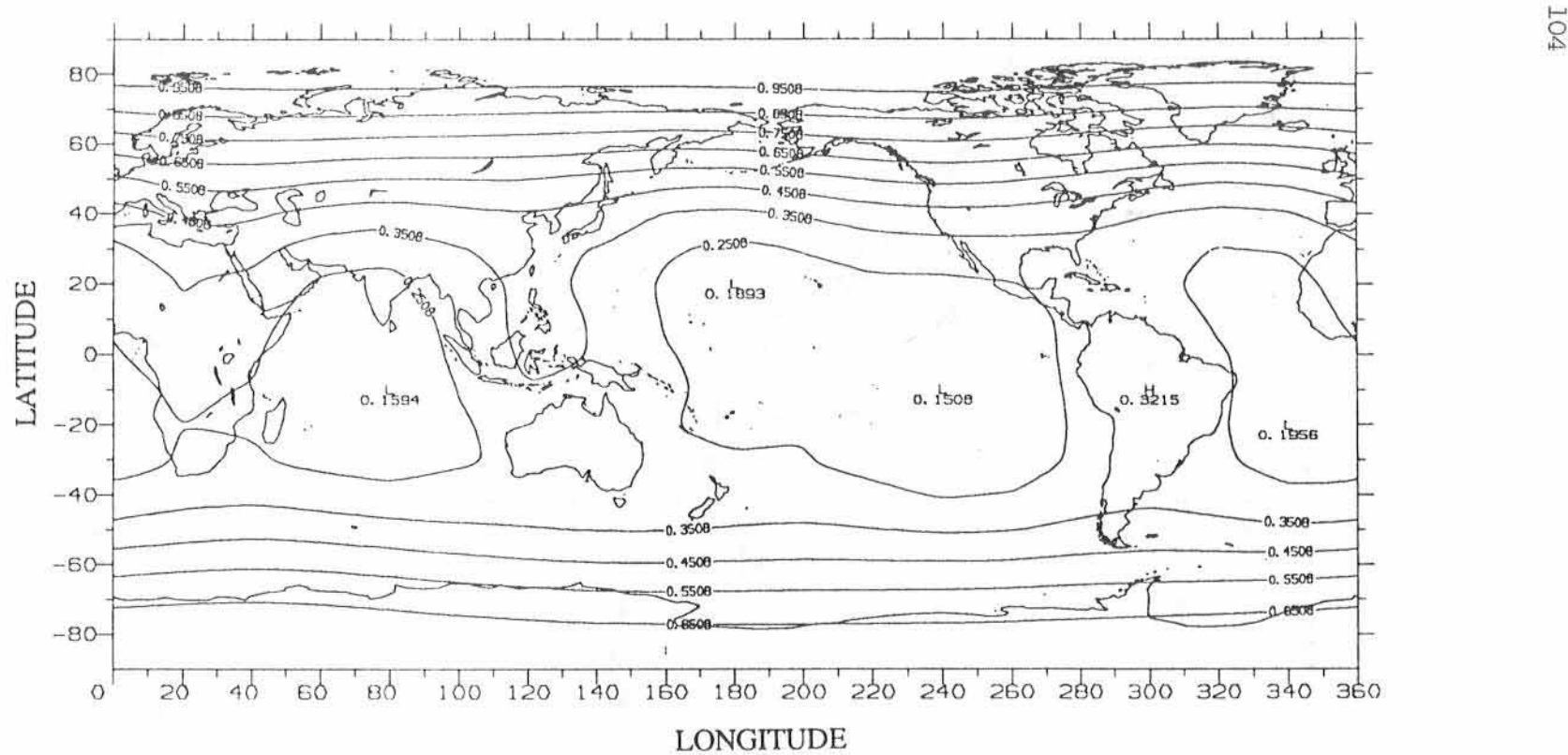


Fig. 3.22

Earth Albedo, 4 x 4 Field, January, 1981

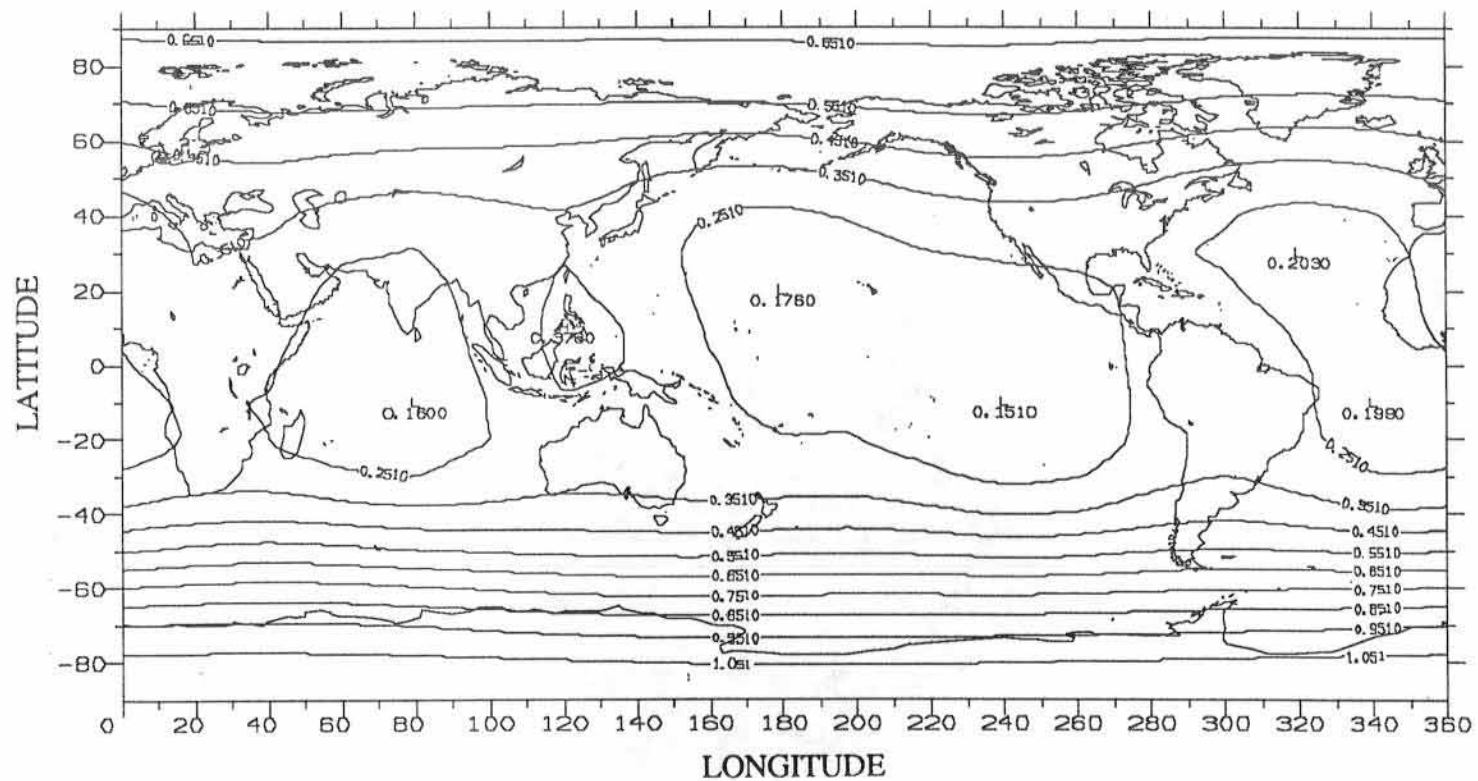


Fig. 3.23
Earth Albedo, 4×4 Field, Summer

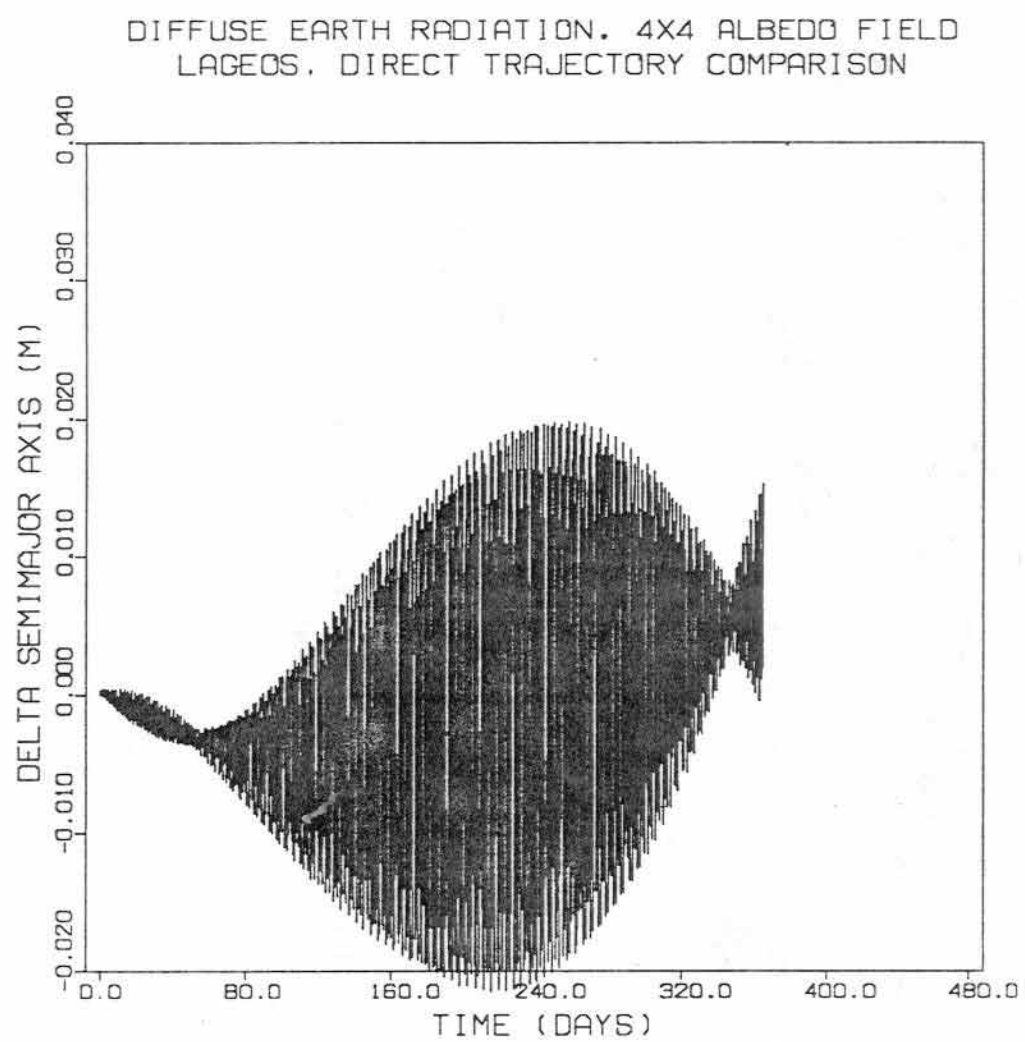


Fig. 3.24

Diffuse Earth Radiation Effect on LAGEOS: 4 x 4 Albedo Field
Change in the Semimajor Axis

DIFFUSE EARTH RADIATION. 4X4 ALBEDO FIELD
LAGEOS, DIRECT TRAJECTORY COMPARISON

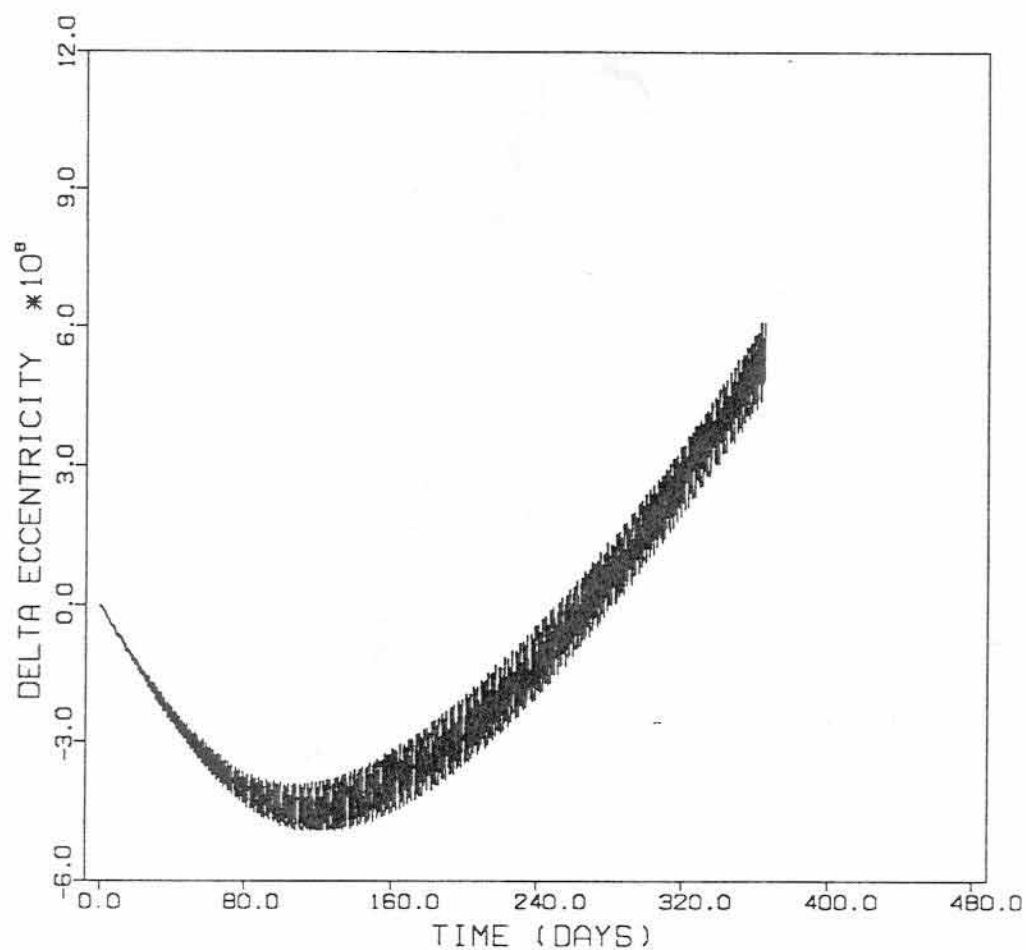


Fig. 3.25

Diffuse Earth Radiation Effect on LAGEOS: 4 x 4 Albedo Field

Change in the Eccentricity

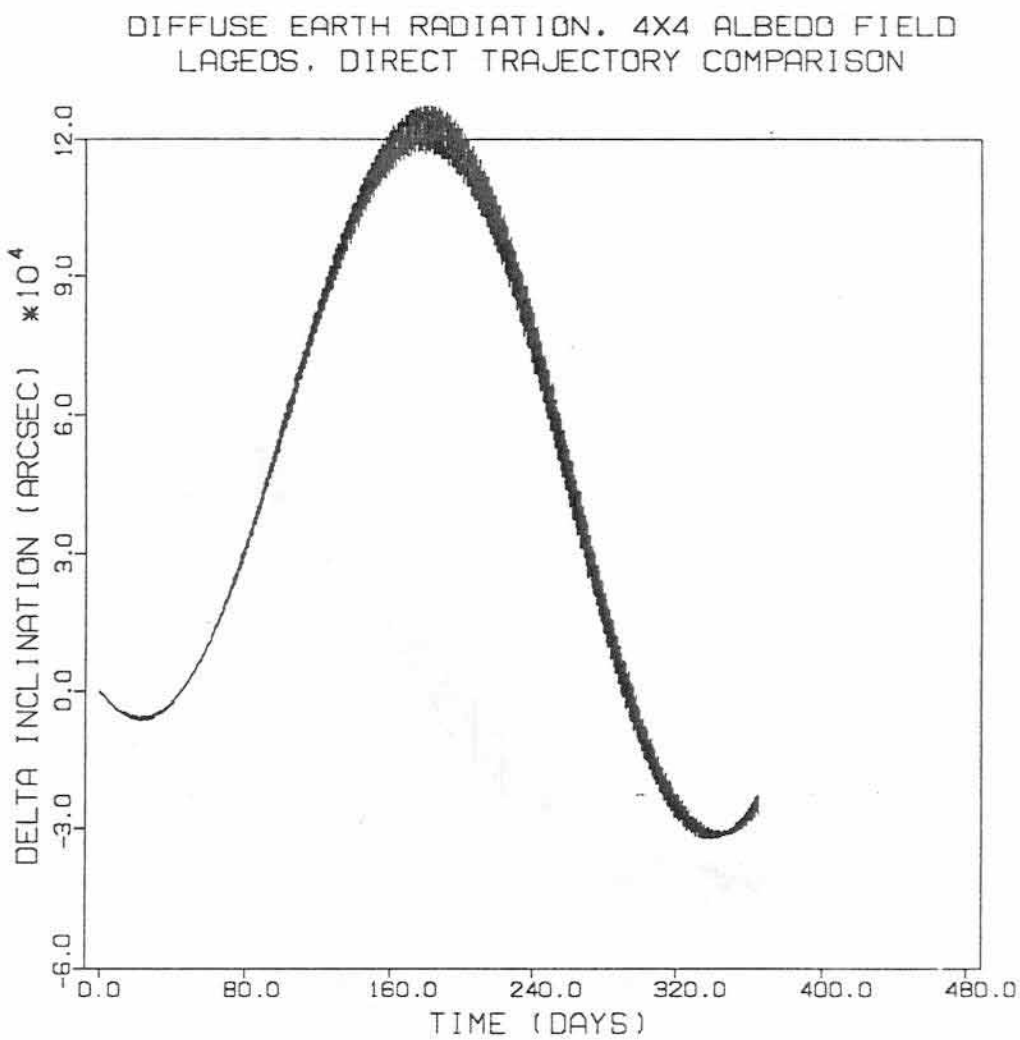


Fig. 3.26

Diffuse Earth Radiation Effect on LAGEOS: 4 x 4 Albedo Field
Change in the Inclination

DIFFUSE EARTH RADIATION. 4X4 ALBEDO FIELD
LAGEOS. DIRECT TRAJECTORY COMPARISON

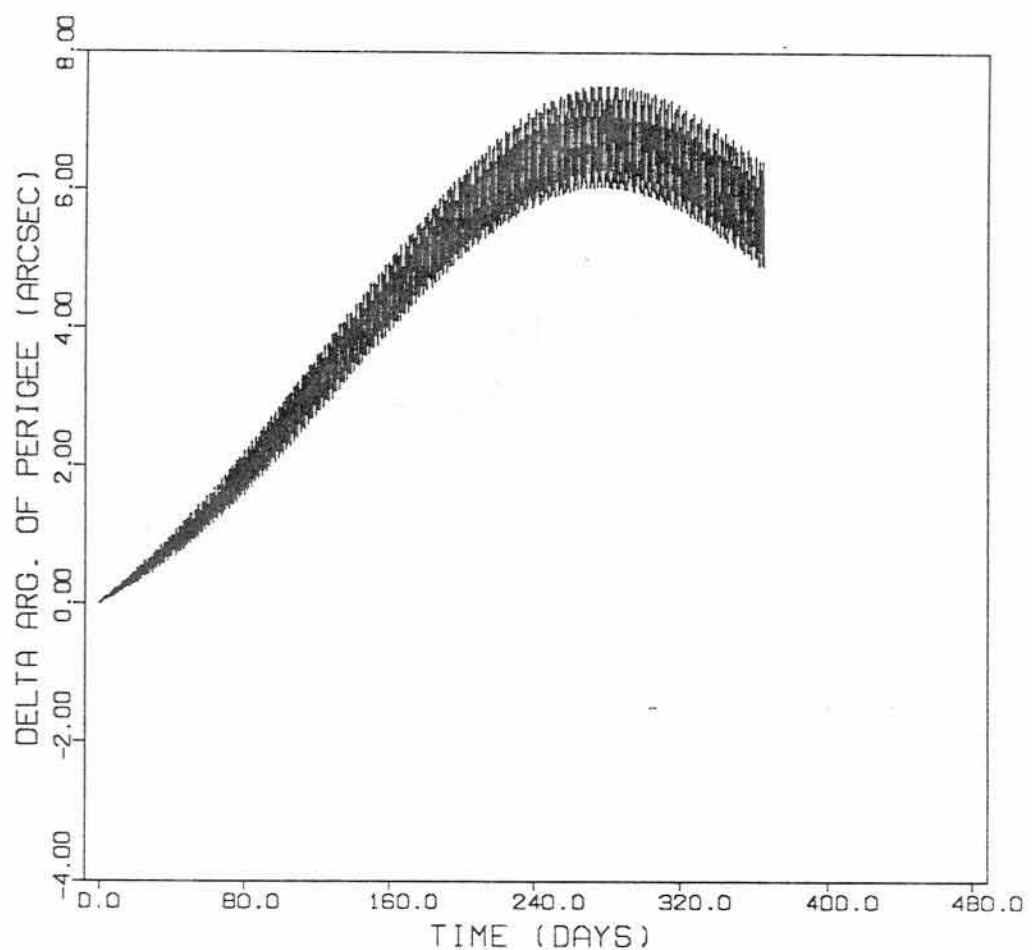


Fig. 3.27
Diffuse Earth Radiation Effect on LAGEOS: 4 x 4 Albedo Field
Change in the Argument of Perigee

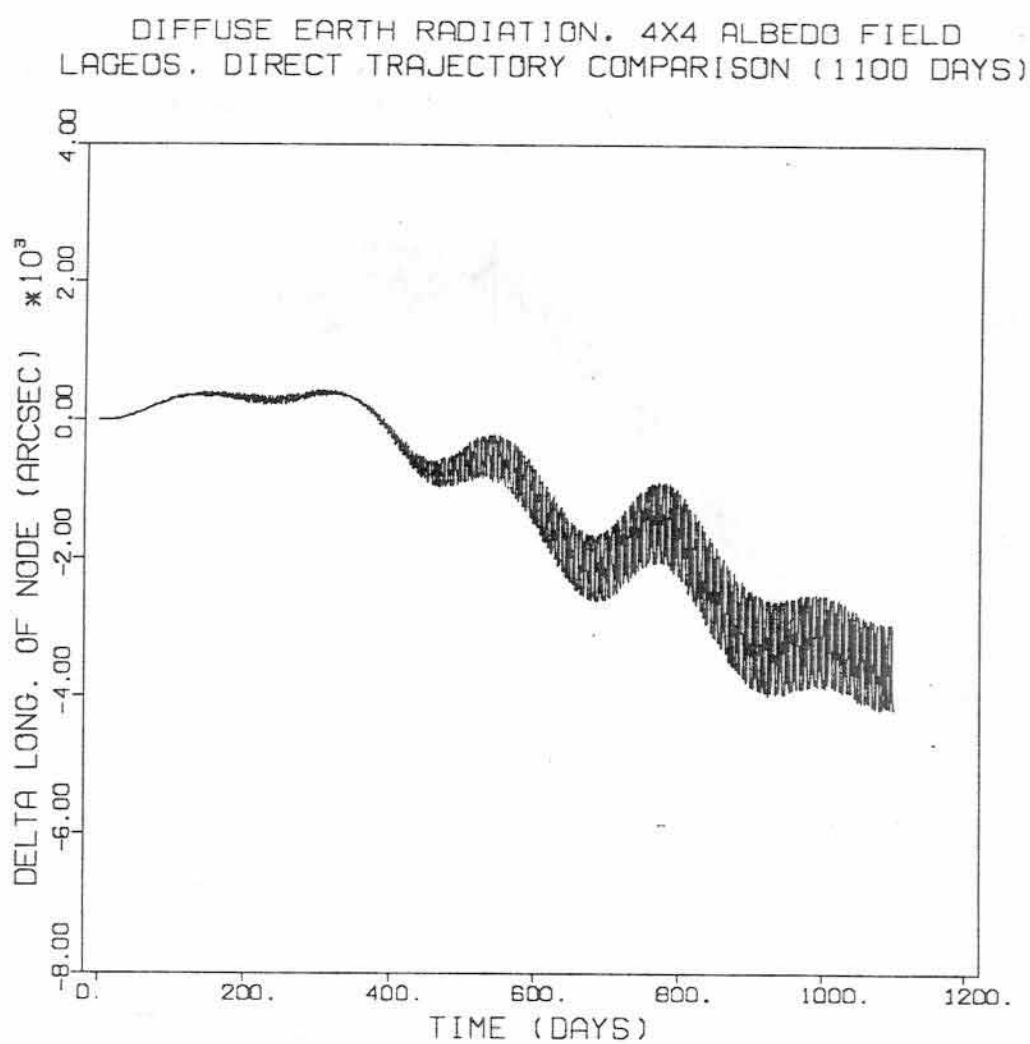


Fig. 3.28

Diffuse Earth Radiation Effect on LAGEOS: 4 x 4 Albedo Field

Change in the Node for a 1100 Day Arc

CHAPTER 4

THE ADVANCED EARTH RADIATION PRESSURE MODEL

4.1 *Introduction*

As mentioned in earlier sections, potentially the most dangerous assumption made in the development of the nominal Earth radiation pressure model is that of diffuse reflection. In reality, the Earth-atmosphere system is a highly complex anisotropic reflector and emitter of radiant energy, due to its exceedingly inhomogeneous composition. A rigorous description of the intricate physical interactions between incident solar energy and the solid, liquid, and gaseous elements of the Earth is a topic beyond the proper province of this work, and would probably be of small use in the modeling of Earth radiation pressure. Instead, it is instructive to consider the Earth-atmosphere system as being composed of many "surface" types, each possessing its own reflective and emissive properties. From this direction the problem may be attacked in a straightforward, accurate and systematic manner, in which recent satellite radiometer measurements can play an important role.

A prominent shortcoming in previous work in this area is the nearly universal reliance on theoretical models of the Earth's anisotropic reflectance. This is the approach taken by several investigators [Wyatt, 1962; Baker, 1966; Morgan, 1984] who rely on largely conjectural estimates of the degree of specular reflection

to address this issue. Only recently have broadband radiance measurements become available for a quantitative study of anisotropy. *Rubincam et al.* [1987] make use of satellite radiometer measurements of the ocean to study the effect on LAGEOS of a hypothetical severe hemispherical asymmetry in the Earth's directional reflectance. The current Advanced Earth Radiation Pressure model includes a global representation of shortwave anisotropy, based on Nimbus-7 radiance measurements.

It has been established that the shortwave component of Earth radiation pressure is by far the dominant constituent in terms of orbital influence. For this reason, and also because the longwave emissions of the Earth are in fact nearly isotropic, the Advanced Earth Radiation Pressure model differs from its diffuse incarnation only in the representation of the shortwave radiation pressure.

Another major assumption pursued in the development of the nominal, or diffuse model is the temporal invariance of albedo, apart from seasonal changes. It is well known that the albedo of Earth surface elements vary considerably in the course of a day [*Pinker and Razgaitis, 1983; Taylor and Stowe, 1984*]. A diurnal model based on Nimbus-7 radiometer measurements is included in the Advanced Earth Radiation Pressure representation.

4.2 Anisotropy and Diurnal Variations in Shortwave Earth Radiation

The development of an anisotropic model suitable for use in orbit determination requires some cognizance of the character of the terrestrial sphere's directional reflectance. Until recently, reliable bi-directional reflectance laws, which

quantify the extent to which a surface element deviates from diffuse reflection, have been difficult to derive from satellite radiance measurements. In particular, before the advent of the broadband radiometers flown aboard Nimbus-6 and Nimbus-7, satellite radiance measurements had been either narrow band, requiring empirical correction to broadband values, or severely limited in coverage [*Stephens et al. 1981*].

The Nimbus-7 data in particular have been analyzed extensively by V. R. Taylor and L. L. Stowe, resulting in a comprehensive atlas of reflectance patterns for various surfaces associated with the Earth-atmosphere system [*Taylor and Stowe, 1984*]. These "uniform surfaces" include clear ocean, clear land, clear snow, clear ice, and clouds of varying composition and altitudes, as observed by the Nimbus-7 satellite. It should be noted that the information in this reference is not corrected for atmospheric scatter, but refers to the actual broadband shortwave radiation of elements of the Earth-atmosphere system as seen from space. Thus, the resulting reflectance maps are particularly well suited for analyses of anisotropy in the context of Earth radiation pressure models. In addition, Taylor and Stowe's analyses provide data on the variation of albedo with solar zenith angle, i.e. the diurnal variation in albedo.

The provenance of the Taylor and Stowe atlas is the Nimbus-7 ERB Sub-Target Radiance Tapes (STRT), which contain radiance values and surface configurations for a total of 272 days during the interval from November 16, 1978 to May 19, 1980 [*Stowe and Fromm, 1983*]. The atlas entries are determined from a 61 day subset of these data. Reflectance factors are obtained by segregating the radiance measurements according to solar zenith angle, surface type, and satellite

view angles, and numerically performing the calculation suggested by Equation (2-7), repeated here for convenience:

$$\Phi_{\text{OUT}_H} = dA \int_{\psi=0}^{2\pi} \int_{\alpha=0}^{\frac{\pi}{2}} L_{\text{SW}}(\alpha, \psi) \sin\alpha \cos\alpha d\alpha d\psi. \quad (2-7)$$

Recall that L_{SW} is the shortwave radiance at a point defined by the satellite view angles α (zenith angle) and ψ (azimuth). The albedo is, therefore:

$$\text{albedo} = \frac{dA}{\Phi_{\text{IN}}} \int_{\psi=0}^{2\pi} \int_{\alpha=0}^{\frac{\pi}{2}} L_{\text{SW}}(\alpha, \psi) \sin\alpha \cos\alpha d\alpha d\psi. \quad (4-1)$$

For a particular range of solar zenith angles, the radiances $L_{\text{SW}}(\alpha, \psi)$ are obtained directly from the radiometer, and the albedo calculated via a numerical approximation of (4-1) [Stowe and Fromm, 1983]. The diffuse radiance is calculated from this albedo value and is divided into the true radiance to obtain the anisotropic factor f :

$$f(\alpha, \psi) = \frac{L_{\text{SW}}(\alpha, \psi)}{L_{\text{SW, diffuse}}}. \quad (4-2)$$

When the anisotropic factor is equal to 1, the surface is reflecting diffusely. If f is less than 1, the true radiance is smaller than that expected of a diffuse surface with the same albedo. Anisotropic factors above 1 indicate a true radiance greater than that predicted by diffuse reflection. It is important to realize that the albedos and anisotropic factors thus obtained are, first, applicable only for the given range of solar zenith angles, and second, completely independent of any assumed form or theory of reflection.

Figures 4.1 and 4.2 show Taylor and Stowe's clear ocean bi-directional reflectance maps for extremely low and extremely high solar zenith angles. Each figure displays two half-maps of the anisotropic factor for clear ocean. It is assumed that the reflectance patterns are symmetric about the plane defined by the Sun, the satellite, and the subsatellite point. This plane also defines the origin of the map, in which the angular axis refers to the satellite azimuth angle, and the radial axis is the satellite zenith angle. (See Figure 2.2.) Each half map corresponds to a particular small range of solar zenith angles.

In Figure 4.1, which pertains to solar zenith angles between 0 (overhead) and approximately 37 degrees, the anisotropic factor never falls below 0.8, and attains its maximum value of 1.5 only in extremely limited areas. Thus, when the Sun is close to overhead (maximum illumination), even the ocean, which is known to be the strongest directional reflector of all the uniform surfaces, never deviates appreciably from isotropy. However, at large solar zenith angles (low illumination levels) the ocean displays the striking and highly organized anisotropic behavior depicted in Figure 4.2. Recall that the Sun is located in the plane of 0 degrees azimuth. At large solar zenith angles the ocean displays very strong "forward" scattering, i.e. the amount of reflected radiation received by a satellite at azimuth angles around 180 degrees is much larger than that predicted by Lambert's Law. Note that the very largest reflectance factors are located at high satellite zenith angles, 180 degrees away from the Sun, during periods characterized by high solar zenith angles. This indicates that the strong forward scatter is due to specular reflection off the water. The back scattered flux is also larger than that indicated by diffuse reflection laws, but is less prominent than forward scattered radiance. There

is also a well organized central region of anisotropic factors smaller than 1.

An examination of the reflectance maps of all the uniform surfaces reveals a conspicuous similarity in their properties. Although the "magnitude" of anisotropy is distinct for each surface type, it would appear that the tendencies described above for the ocean are common to all the terrestrial surfaces. Specifically, all the surface types tend towards diffuse reflection during periods of high illumination (low solar zenith angles) and become strongly anisotropic only near sunrise and sunset (high solar zenith angles). All surface types display the same anisotropic patterns at high solar zenith angles, characterized by strong forward scatter, some backscatter, and depressed central scatter.

It should be noted that the marked similarity in the behavior of these surface types may be due in part to inaccuracies in surface recognition. Surface identification is accomplished through a combination of Nimbus-7 THIR (Temperature-Humidity Infrared Radiometer) measurements, geographical data, and climatological and meteorological data. The authors themselves admit some difficulty in the reliable separation of cloud levels [*Taylor and Stowe, 1984*]. While such considerations are of importance in some contexts, it should be noted that a satellite in Earth orbit will rarely sense radiation pressure from large uncorrupted surface areas. Instead, it will be subjected to fluxes from various surface combinations, e.g. a mergence of land, snow, and cloud. While this suggests that the anisotropy sensed by an Earth orbiting spacecraft should be of a fairly consistent nature, it does present a problem in implementation. Specifically, in order to use Taylor and Stowe's anisotropic atlas, it would be necessary to develop some Earth-fixed map of surface types and abundances, and determine the

anisotropic behavior of mixed scenes. While this is possible in theory, it would probably require global estimates of cloud and snow/ice cover, coupled with a geographic map. While this approach is probably superior to the largely theoretical analyses of previous investigators, it introduces numerous uncertainties which would be difficult to examine or quantify. For example, the behavior of mixed surface types would have to be modeled, as it is likely that a 50% cloudy scene over ocean would not behave like a simple linear combination of oceanic anisotropy and cloud anisotropy.

Taylor and Stowe's atlas also provides information on the diurnal variation in the albedos of the uniform surfaces. In fact, as indicated by Equations (2-11) and (4-1), the albedo must be calculated in order to determine the diffuse radiance $L_{SW\text{diffuse}}$, and hence the anisotropic factor f . Fortunately, diurnal variations in albedo are somewhat easier to characterize than anisotropy. In general, the albedos of terrestrial surfaces increase with solar zenith angle [Raschke *et al.*, 1973; Pinker and Razgaitis, 1983; Taylor and Stowe, 1984]. Taylor and Stowe suggest that snow may be an exception; their analyses show the albedo of this surface decreasing slightly in the range of solar zenith angles from 60 degrees to 80 degrees. Earlier investigations by Raschke *et al.* [1973], using a less extensive Nimbus-3 data set indicate that the albedo of snow increases with solar zenith angle, in accord with the behavior of other uniform Earth surfaces. The diurnal albedo variation for snow is small in either case.

Taylor and Stowe's set of surface-dependent diurnal data suffer the same shortcomings, in terms of implementation, as do their anisotropic maps. Fortunately, a more suitable set of Earth surface anisotropic and diurnal information is available. These data consist of averaged anisotropic factors and albedos for each

18 degree band of geocentric latitude, as functions of solar zenith angle. This data set is described in greater detail in the next section.

4.3 *The Advanced Earth Radiation Force Model*

4.3.1 *Satellite Data Supporting the Force Model*

For reasons already mentioned, the Taylor and Stowe atlas of anisotropic reflectance patterns is not ideally suited to Earth radiation pressure calculations. The *concept* of an anisotropic factor, however, is extremely useful, and particularly conformable to the problem at hand. Suppose the diffuse Earth radiation pressure is known, for example by means of the model described in previous sections, and that a suitable anisotropic factor were at hand. In this case, the anisotropic radiation is easily determined by multiplying the diffuse radiation by the anisotropic factor. The diurnal variation in albedo could be treated in a similar manner. Thus, while Taylor and Stowe's atlas is not perfectly tailored to the problem of calculating Earth radiation pressure, something very much like it is indicated.

The STRT data base which serves as the foundation for the uniform surface atlas has been analyzed by V. Ray Taylor (NOAA) to produce a global anisotropy model [V. Ray Taylor, *personal communication*]. In this analysis, the full 272 day data set has been segregated according to latitude, as opposed to surface type, to produce maps of anisotropic factors for each 18 degree band of geocentric latitude. In a manner similar to *Taylor and Stowe* [1984], anisotropic factors for a given latitude band and solar zenith angle interval are provided for 49 angular "bins"

distributed from 0° to 180° in satellite azimuth, and from 0° to 90° in satellite zenith angle. It is assumed that the factors are symmetric about the plane defined by the Sun, the satellite, and the subsatellite point. It should be noted that these data only pertain to 272 days, distributed somewhat unevenly over the STRT interval, and thus fall somewhat short of a full year's average. In fact, analyses of data evenly distributed over several consecutive years would have been preferable, but are currently unavailable. Another important consideration is the geographical coverage available from the Nimbus-7 data. Nimbus-7 is in a Sun-synchronous orbit, and thus the range of solar zenith angle sensed for a particular latitude band is limited. In particular, large zenith angles are not sensed at latitudes near the equator, because the satellite always crosses the equator at the same local time. Low zenith angles are never sensed at high northern or southern latitudes due to the low declination of the Sun.

Figures 4.3 through 4.5 are contour maps of anisotropic factors pertaining to various solar zenith angles, for the latitude band from 54 degrees to 72 degrees North, using Taylor's data. The coordinate axes are the same as those in Figure 4.1. Not surprisingly, contours of the latitudinally averaged data are similar in shape to the uniform surface maps. Also, there appears to be less variability from one latitude band to the next than there is between the uniform surfaces. Figure 4.3 reveals that, once again, low solar zenith angles are characterized by nearly diffuse behavior. As the solar zenith angle increases, the forward scatter, back scatter and central scatter regions display their familiar characteristics. It is evident that any treatment of Earth radiation pressure due to anisotropic shortwave radiation must model these universal properties.

Determination of the anisotropic factors requires a simultaneous calculation of albedo, in order to determine the diffuse radiance. Taylor's analyses therefore provide latitudinally averaged albedo values as functions of solar zenith angle. This yields valuable information on the variation of albedo with the Sun's zenith distance, a phenomenon commonly referred to as the *diurnal variation in albedo*. It should be noted that this analysis does not return any data on the possible dependence of albedo on solar azimuth.

The large scale properties of albedo diurnal variations for all the latitude bands are roughly congruent with the trends of the uniform surfaces. Figure 4.6 displays the general tendency of the terrestrial sphere to exhibit albedos which increase with solar zenith angle, although a number of local exceptions to this rule are evident for some ranges of the solar zenith angle.

4.3.2 Mathematical Formulation of the Force Model

4.3.2.1 The Anisotropic Reflectance Model

With a suitable data set in hand, the question arises of the proper mathematical form which the anisotropic force model should adopt. *Rubincam et al.* [1987] present a series of equations by which Taylor and Stowe's anisotropic factors may be emulated mathematically. These expressions simulate the oceanic anisotropic factors with reasonable fidelity, but are somewhat unwieldy and underestimate the backscatter slightly. Also, it is unlikely that an Earth orbiting satellite would be sensitive to the manifold detailed contours which this representation is capable of modeling.

A simpler approach is adopted in modeling anisotropy in UTOPIA. As indicated previously, the anisotropic factors display certain uniform characteristics, as functions of satellite view angles and solar zenith angle. In order to model these properties, the anisotropic reflectance maps are first divided into three regions: the "forward" reflected area, the "back" scatter region, and the "center" scatter area. For a given latitude band and solar zenith angle available in the data set, the anisotropic factors are averaged within each of these distinct areas. In this manner, the 49 angular bins of Taylor's data are combined into only three bins.

The three bin model described above is illustrated in Figure 4.7. The central region covers all values of satellite azimuth, for satellite zenith angles from zero to a given value α_c . The forward and back regions cover the satellite zenith angles from α_c to 90 degrees, but are restricted in their azimuth ranges, as shown.

This model must be configured in such a manner as to avoid biasing the shortwave component. That is, the integration of the shortwave radiance over the upwelling hemisphere must be the same whether or not the anisotropic factor is applied. In other words, the *albedo* must be unchanged by the application of the multiplicative reflectance factors. This may be expressed as a single equation in a single unknown, α_c . For a given solar zenith angle, Equation (4-2) returns:

$$L_{SW} = f(\alpha, \psi) L_{SW\text{diffuse}}$$

where L_{SW} = true radiance,

f = anisotropic factor,

$$L_{SW\text{diffuse}} = \text{diffuse radiance} = \frac{a E_S \cos \theta_S}{\pi},$$

and integrating both sides over the upwelling hemisphere,

$$\begin{aligned}
 dA \int_{\psi=0}^{2\pi} \int_{\alpha=0}^{\frac{\pi}{2}} L_{SW} \sin \alpha \cos \alpha d\alpha d\psi = \\
 dA \int_{\psi=0}^{2\pi} \int_{\alpha=0}^{\frac{\pi}{2}} f \frac{a E_S \cos \theta_S}{\pi} \sin \alpha \cos \alpha d\alpha d\psi . \quad (4-3)
 \end{aligned}$$

From Equation (2-7), the left hand side of the above expression is always equal to Φ_{out_H} , the upwelling shortwave flux. Combining Equations (4-3), (2-6), and (2-9), and noting that the albedo a , the solar constant E_S , and the solar zenith angle θ_S are not functions of α and ψ , yields:

$$a E_S \cos \theta_S dA = \frac{a E_S \cos \theta_S}{\pi} dA \int_{\psi=0}^{2\pi} \int_{\alpha=0}^{\frac{\pi}{2}} f \sin \alpha \cos \alpha d\alpha d\psi .$$

Dividing both sides of the equation by $a E_S \cos \theta_S dA$ generates:

$$\frac{dA \int_{\psi=0}^{2\pi} \int_{\alpha=0}^{\frac{\pi}{2}} f \sin \alpha \cos \alpha d\alpha d\psi}{\pi} = 1 . \quad (4-4)$$

Evaluating this integral for the three bin model leads to the following requirement for an unbiased model:

$$J = \frac{1}{2} (1 - \cos 2\alpha_C) f_C + \frac{1}{4} (1 + \cos 2\alpha_C) (f_B + f_F) - 1 = 0 , \quad (4-5)$$

where f_C = "center scatter" reflectance factor,

- f_B = "back scatter" reflectance factor,
 f_F = "forward scatter" reflectance factor.

The value of α_C is chosen to minimize the cost function $|J|$. Fortunately, the search for the best possible choice of α_C is simplified by the coarseness of the raw data. The 49 angular bins in Taylor's data are bounded by satellite zenith angles of 15° , 27° , 39° , 51° , 63° , 75° , and 90° . Thus, the cost function $|J|$ need only be evaluated for these seven values of α_C . An analysis of the reflectance factors for all latitude bands and solar zenith angles yields an optimum value of $\alpha_C = 63$ degrees. Using this configuration, the value of J never exceeds 0.008 and never falls below -0.016, resulting in a nearly unbiased anisotropic model.

Average reflectance factors for each of the characteristic zones (forward, back, and center) are obtained for each range of solar zenith angle and each latitude band. No attempt is made to weight the raw data for this averaging process, aside from taking into account the differing sizes of the 49 angular bins. The few data points which are questionable, being the result of a relatively low number of radiometer measurements, do not materially affect the average anisotropic factors. Plots of these average reflectance factors are shown as functions of solar zenith angle for all ten latitude bands, in Figures 4.8 through 4.17. These plots clearly illustrate the limitations of the Nimbus-7 STRT data set, the most unfortunate being the lack of data for high solar zenith angles in the equatorial regions. Ironically, the equatorial areas are likely to be important in the calculation of Earth radiation pressure, because they are subjected to high levels of illumination at all times of the year. One is struck by the similarity in the behavior of the reflectance factors from one latitude band to the next. The similarity is so strong, in fact, that there appears to be little

point in retaining a separate anisotropic model for each latitude band, especially in view of the sparsity of equatorial data. Note also that the reflectance factors vary smoothly enough so that a low order polynomial fit is a reasonable mode of implementation. With these facts in mind, the average forward and center reflectance factors for each latitude band have been fit to quadratic functions of the solar zenith angle. The average back scatter reflectance factors have been fit to a cubic. As indicated by the data and best fits, shown in Figures 4.18 through 4.20, the forward and central regions are well modeled by this technique. The back scatter shows the most variability from one latitude band to the next. The polynomial fits are only used for solar zenith angles above 15 degrees. Below this "cutoff", the reflectance factors are all set equal to unity. The resulting global reflectance model is shown in Figure 4.21. An evaluation of Equation (4-5) reveals that the global model never biases the shortwave component by more than -1.6%. Values for the polynomial coefficients are listed in the following table.

TABLE 4.1
GLOBAL ANISOTROPY MODEL POLYNOMIAL COEFFICIENTS

$$f = b_0 + b_1 \theta_s + b_2 \theta_s^2 + b_3 \theta_s^3 \quad (\text{solar zenith angle in radians})$$

Zone	b_0	b_1	b_2	b_3
Forward	1.23902086	-1.00038277	1.17197216	
Back	0.84825026	0.91360102	-1.21922084	0.550470538
Center	0.99339291	0.04944551	-0.12775275	

4.3.2.2 The Diurnally Varying Albedo Model

The goal of this modeling effort is a diurnal factor, say $g(\theta_S)$, to which would be multiplied the albedo from the nominal model:

$$a(\theta_S) = g(\theta_S) \bar{a}, \quad (4-6)$$

where \bar{a} = nominal model albedo,

a = true albedo.

It is assumed that the nominal albedo, obtained from *Stephens et al.* [1981], represents an average over the range of solar zenith angles from $\theta_{S_{\min}}$ (the minimum solar zenith distance for that latitude and season) to 90° (sunrise or sunset), i.e.:

$$\bar{a} = \frac{\int_0^{\frac{\pi}{2}} a(\theta_S) d\theta_S}{\frac{\pi}{2} - \theta_{S_{\min}}}, \quad (4-7)$$

where $\theta_{S_{\min}}$ = minimum solar zenith angle = $|\phi - \delta_S|$,

ϕ = latitude,

δ_S = solar declination.

A useful and instructive precursor to the diurnal function $g(\theta_S)$ is an "intermediate diurnal function" $h(\theta_S)$, which defines the relationship between the true albedo a and the albedo when the Sun is directly overhead, as follows:

$$a(\theta_S) = h(\theta_S) \overset{\circ}{a}, \quad (4-8)$$

where $\overset{\circ}{a}$ = albedo at vertical solar incidence. This formulation has the

advantage of depending on a true constant, \bar{a} , instead of the average albedo, which varies with season as the solar declination changes. The concept of an overhead albedo is often something of an abstraction, however, as the Sun never reaches local vertical for latitudes greater than 23.5° North or below 23.5° South. Figure 4.22 shows the intermediate diurnal function for all latitude bands. Overhead albedo values for latitudes which never see the vertical Sun are obtained by extrapolation. It is clear that the diurnal albedo variation fluctuates considerably with latitude, necessitating a distinct diurnal function for each latitude band.

Substituting Equation (4-8) into (4-7):

$$\bar{a} = \frac{\bar{a} \int_{\theta_S = \theta_{S_{\min}}}^{\frac{\pi}{2}} h(\theta_S) d\theta_S}{g(\theta_S)} = \frac{\frac{\pi}{2} - \theta_{S_{\min}}}{\int_{\theta_S = \theta_{S_{\min}}}^{\frac{\pi}{2}} h(\theta_S) d\theta_S}. \quad (4-9)$$

Thus,

$$g(\theta_S) = \frac{\left(\frac{\pi}{2} - \theta_{S_{\min}} \right)}{\int_{\theta_S = \theta_{S_{\min}}}^{\frac{\pi}{2}} h(\theta_S) d\theta_S}. \quad (4-10)$$

By assuming a form for $h(\theta_S)$ and substituting into the above equation, one may obtain the diurnal function $g(\theta_S)$. Note that the average value of g in the interval from $\theta_{S_{\min}}$ to $\pi/2$ is always equal to 1.0, regardless of the nature of the intermediate diurnal function. This ensures an unbiased diurnal model. In this study, the intermediate function h is set equal to unity for "low" solar zenith angles,

i.e. all solar zenith angles below some chosen θ_1 , as shown in Figure 4.23. For solar zenith angles larger than θ_1 , a quadratic form is usually assumed for $h(\theta_S)$. In sum, then:

$$\begin{aligned} \text{for } \theta_S < \theta_1 : \quad h(\theta_S) &= 1.0 \\ \text{for } \theta_S \geq \theta_1 : \quad h(\theta_S) &= d_0 + d_1 \theta_S + d_2 \theta_S^2 \end{aligned}$$

Thence:

$$g(\theta_S) = \frac{[d_0 + d_1 \theta_S + d_2 \theta_S^2] (\frac{\pi}{2} - \theta_{S_{\min}})}{\theta_1 - \theta_{S_{\min}} + (\frac{\pi}{2} - \theta_1) [d_0 + \frac{d_1}{2} (\frac{\pi}{2} + \theta_1) + \frac{d_2}{3} \{(\frac{\pi}{2})^2 + \frac{\pi}{2} \theta_1 + \theta_1^2\}]} \quad (4-11)$$

On occasion, θ_1 may be smaller than $\theta_{S_{\min}}$, in which case θ_1 is replaced by $\theta_{S_{\min}}$ in the above equation.

In the implementation of this strategy, linear diurnal functions are used instead of the quadratic form whenever possible. Also, the "low angle correction" which constrains the function to unity near vertical irradiance, is only necessary at those latitudes which actually "see" the vertical Sun. Figure 4.24 shows the available intermediate diurnal functions for all latitude bands, and the best fit linear function. This "global average" function is used for the equatorial region, between 18 degrees South and 18 degrees North, since the data at these locations are too sparse to afford a reliable local model. Figures 4.25 through 4.32 show the intermediate diurnal functions and their best fit polynomials for all the other latitude bands. In most cases, the quadratic or linear functions chosen are reasonable approximations to the data. The mid-southern latitudes, however, exhibit a somewhat more complex diurnal signal, which is difficult to model. The linear functions chosen never deviate more than approximately 15% from the "true" diurnal behavior. The

following table summarizes the constants used in the latitudinal diurnal model.

TABLE 4.2
INTERMEDIATE DIURNAL FUNCTION
POLYNOMIAL COEFFICIENTS

$$h = d_0 + d_1 \theta_s + d_2 \theta_s^2 \quad (\text{solar zenith angle in radians})$$

Latitude Band	d_0	d_1	d_2	θ_1 (degrees)
72°N to 90°N	0.88	0.602	0.	0.
54°N to 72°N	0.646	1.08	0.	0.
36°N to 54°N	0.978	-0.157	0.755	15.
18°N to 36°N	1.15	-1.05	1.59	15.
0° to 18°N	0.752	0.739	0.	15.
0° to 18°S	0.752	0.739	0.	15.
18°S to 36°S	1.13	-0.745	0.896	15.
36°S to 54°S	0.892	0.430	0.	15.
54°S to 72°S	0.904	0.779	0.	0.
72°S to 90°S	0.986	0.189	0.	0.

In the above table, $\theta_1 = 0$ means that no "low angle" correction is required for the given latitude band.

The difference between the intermediate diurnal function h and the diurnal function g is illustrated in figure 4.33. This figure shows the values of h and g for the equatorial bands, in which the "average" diurnal model is used. The diurnal function g has the same functional dependence on θ_s that h does, as Equation (4-11) indicates. In fact, g is merely equal to h , multiplied by a seasonally-

dependent factor which is always less than unity. The important consideration here is that the presence of the diurnal variation model actually *decreases* the radiance generated at low solar zenith angles. The implications of this development are explored in the next section.

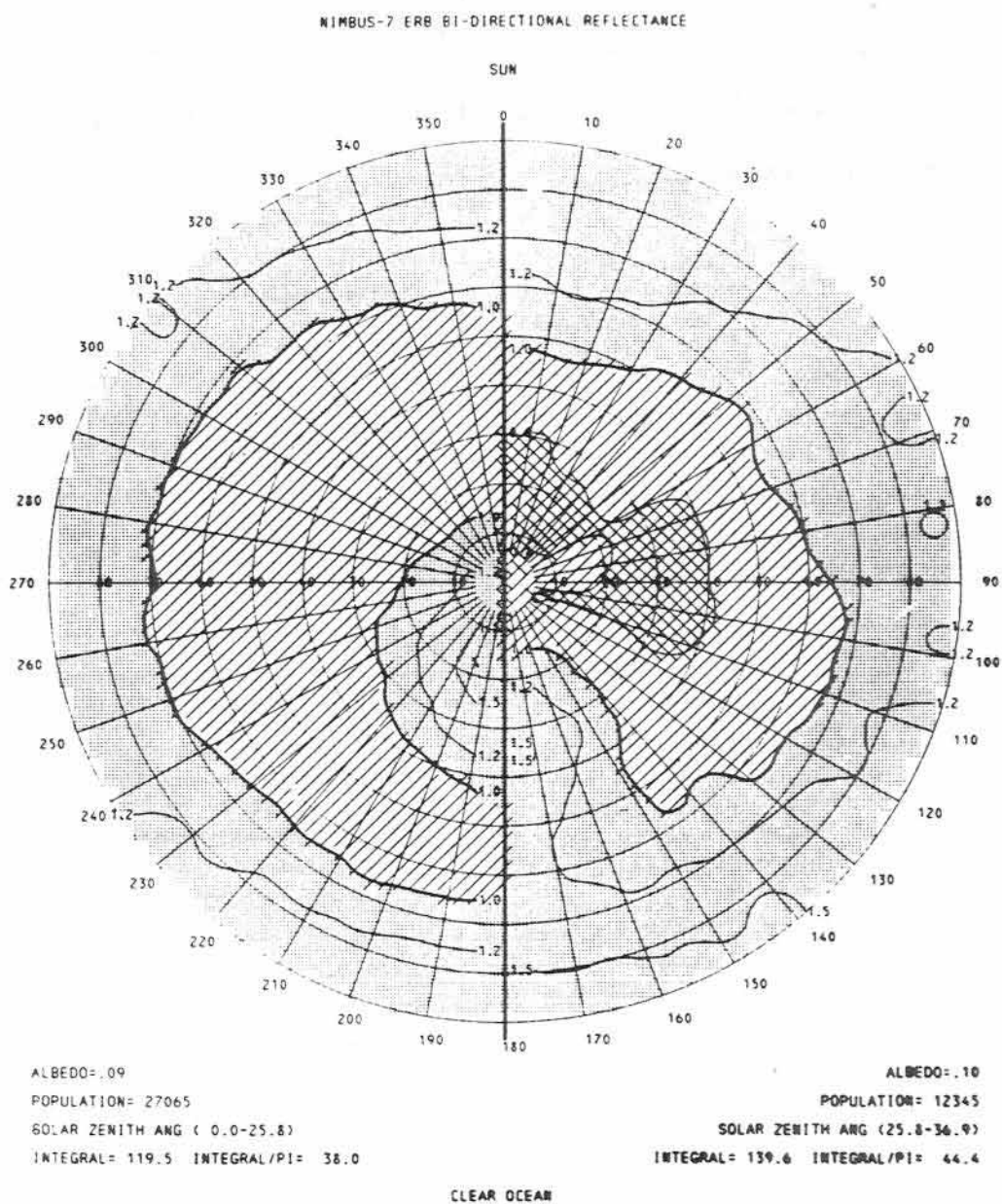


Fig. 4.1

Nimbus-7 Anisotropic Factors for Clear Ocean, Low Solar Zenith Angles,
(Source, *Taylor and Stowe [1984]*)

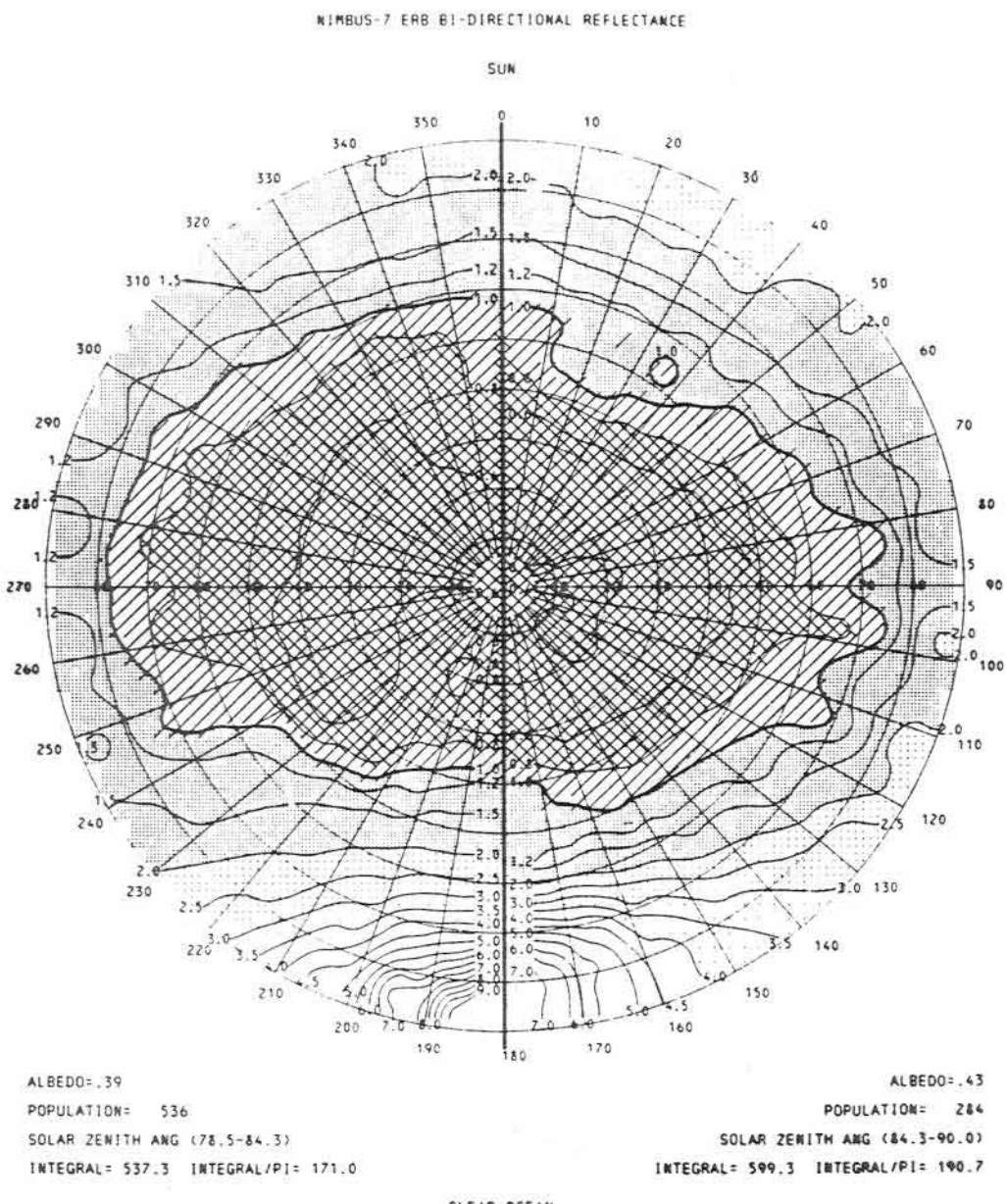


Fig. 4.2

Nimbus-7 Anisotropic Factors for Clear Ocean, High Solar Zenith Angles,

(Source, *Taylor and Stowe [1984]*)

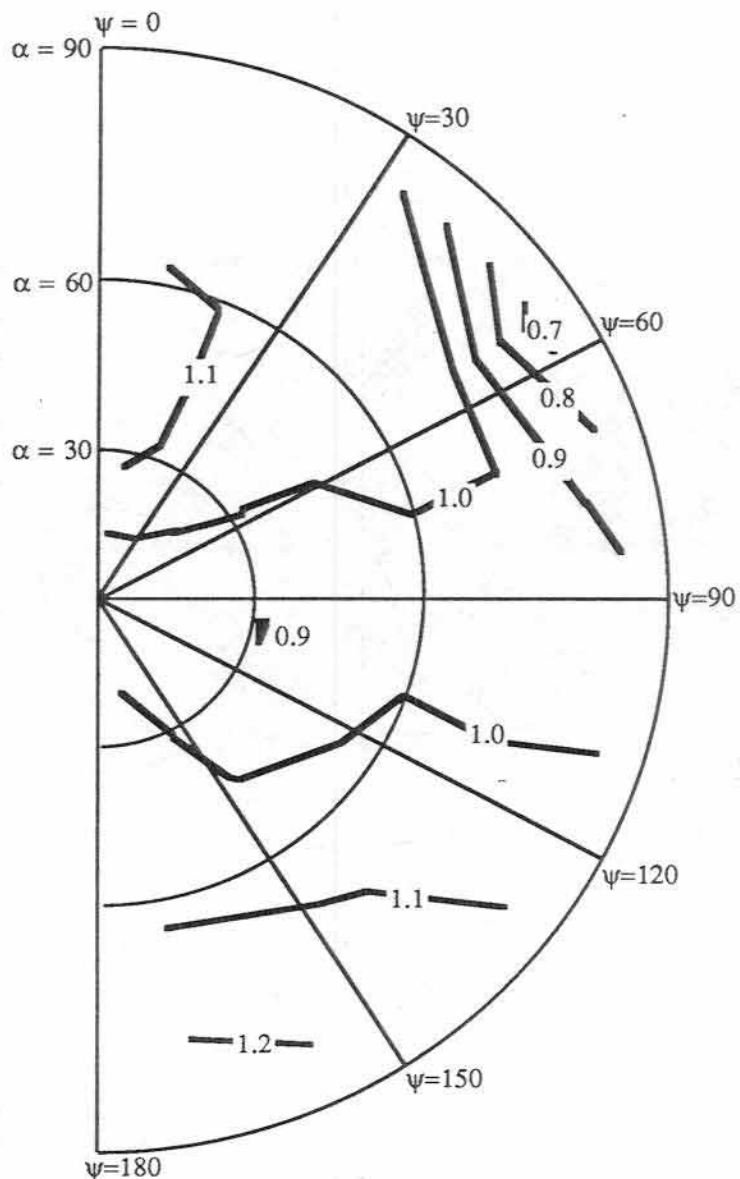


Fig. 4.3
Anisotropic Factors for Latitudes 54° to 72° North
Solar Zenith Angles from 26° to 37°

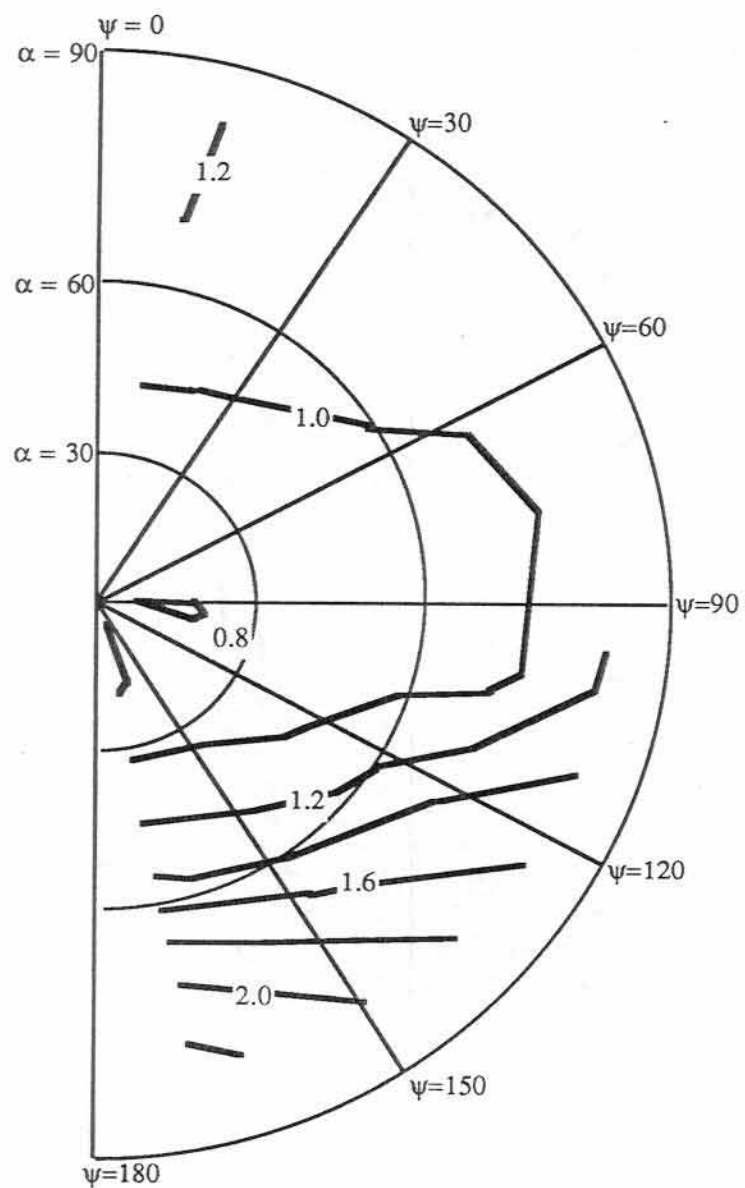


Fig. 4.4
Anistropic Factors for Latitudes 54° to 72° North
Solar Zenith Angles from 60° to 66°

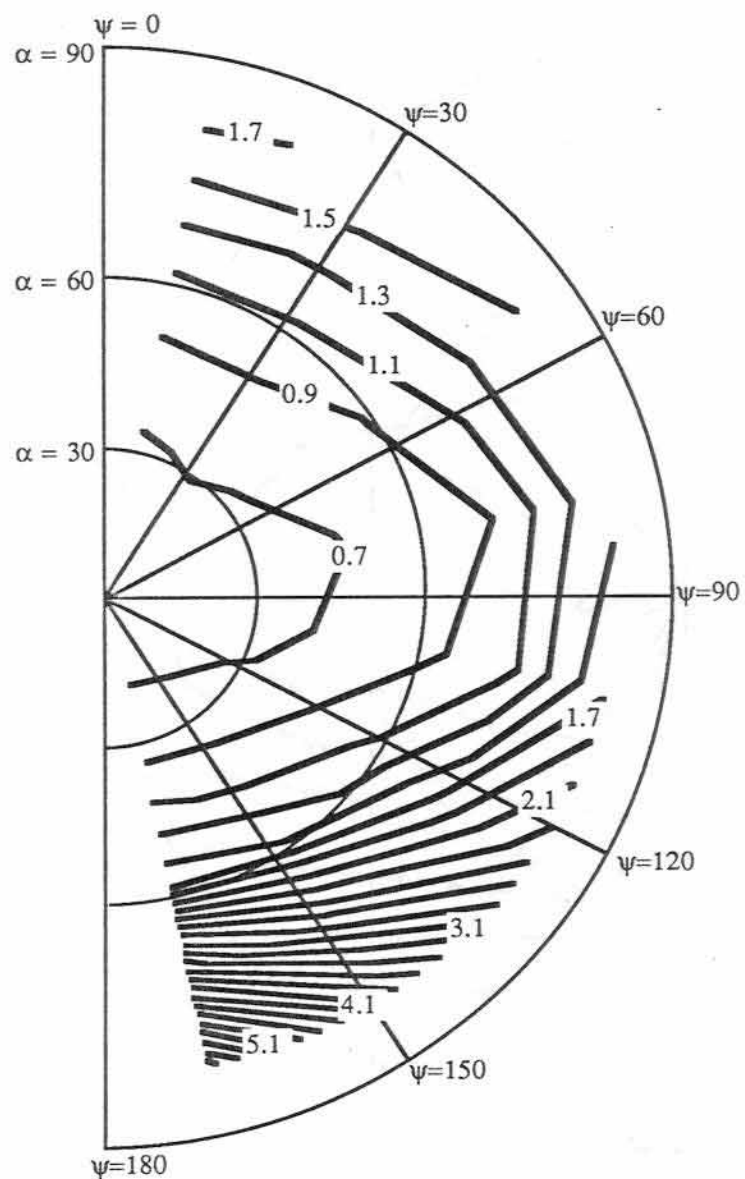


Fig. 4.5
Anisotropic Factors for Latitudes 54° to 72° North
Solar Zenith Angles from 84° to 90°

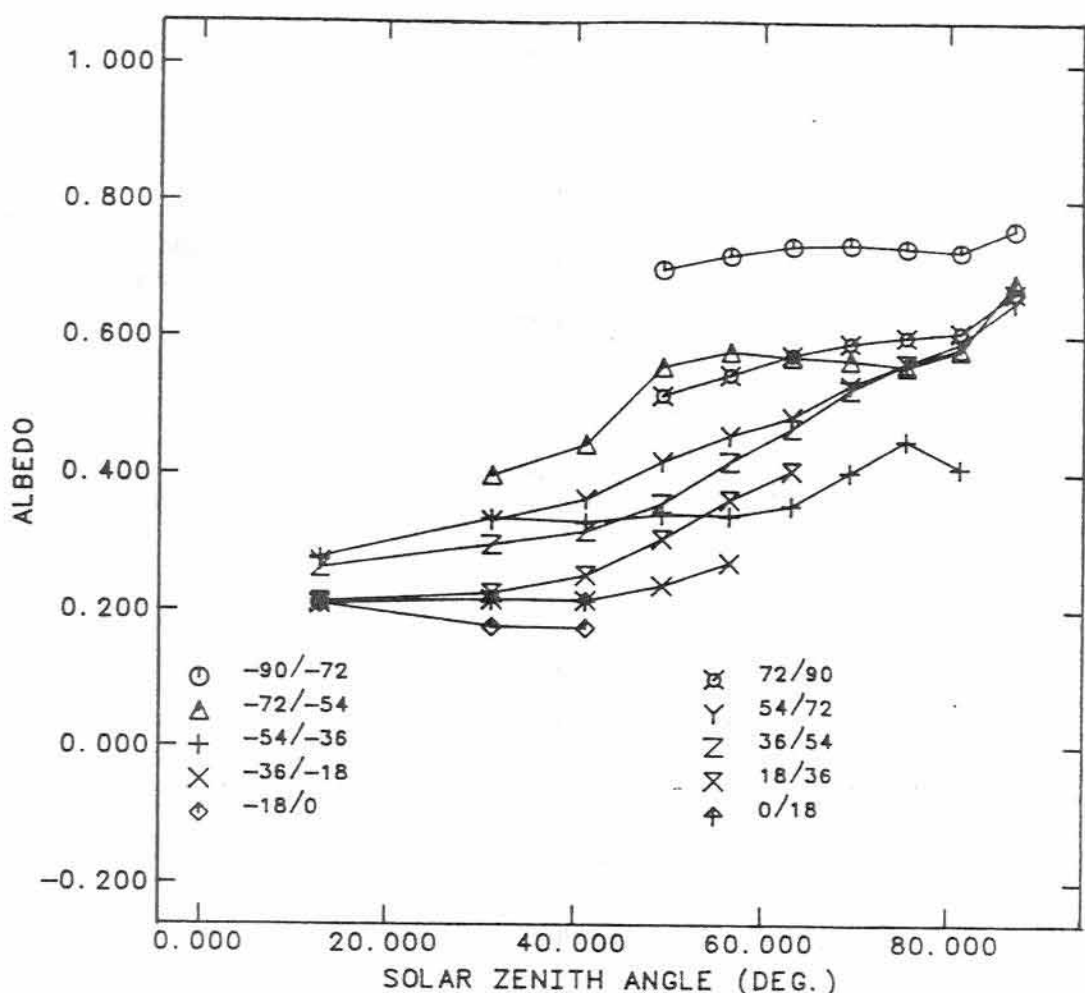


Fig. 4.6
Albedo Vs. Solar Zenith Angle for Each
Latitude Band

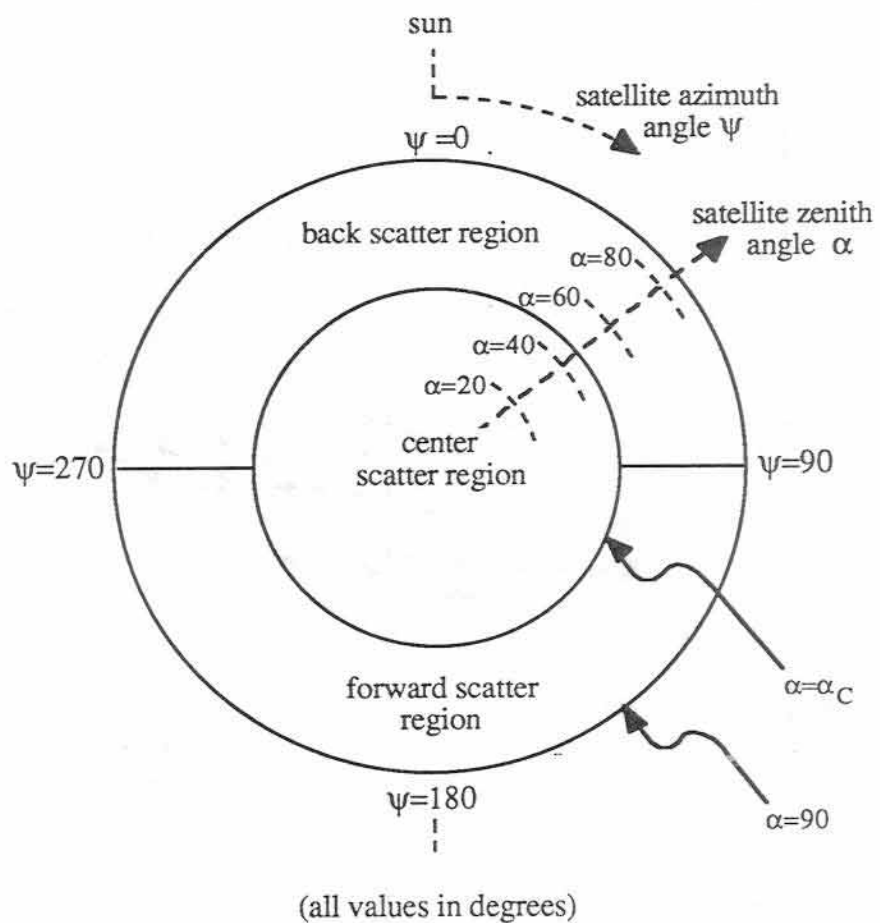


Fig. 4.7
Three Bin Anisotropy Model

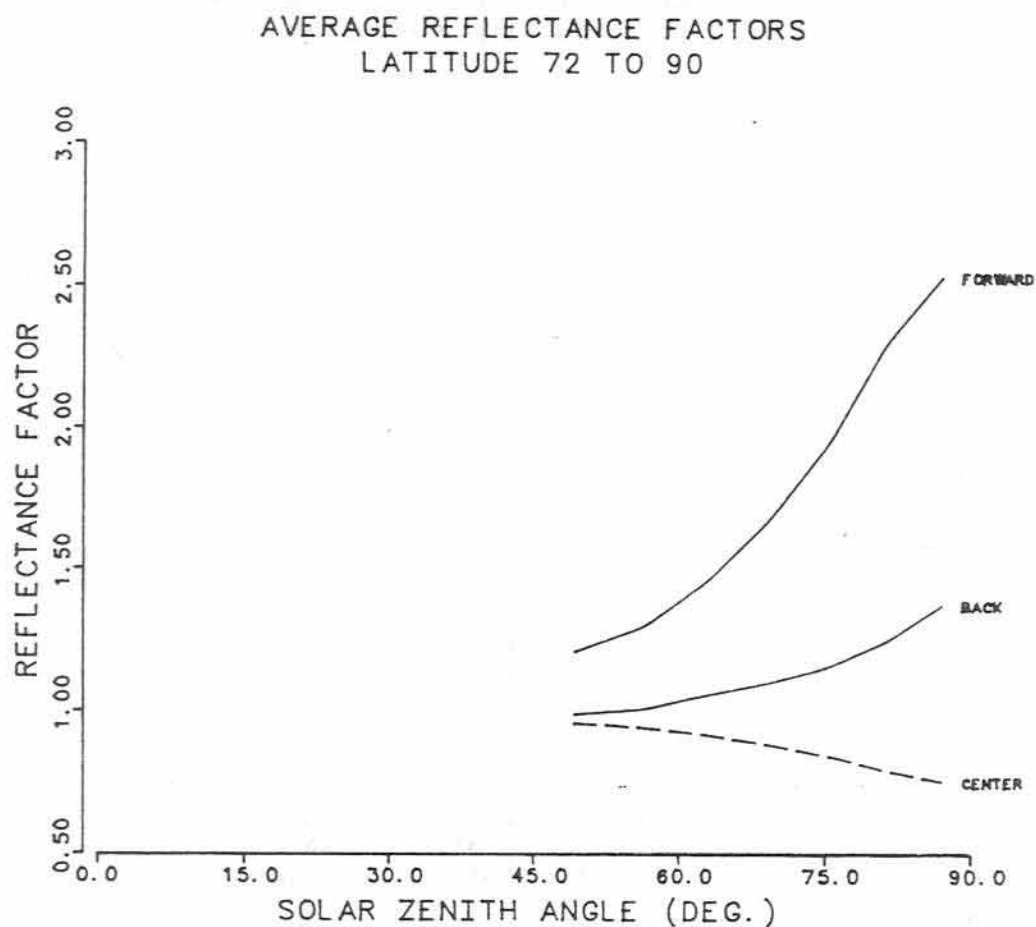


Fig. 4.8
Average Reflectance Factors for
72° to 90° North

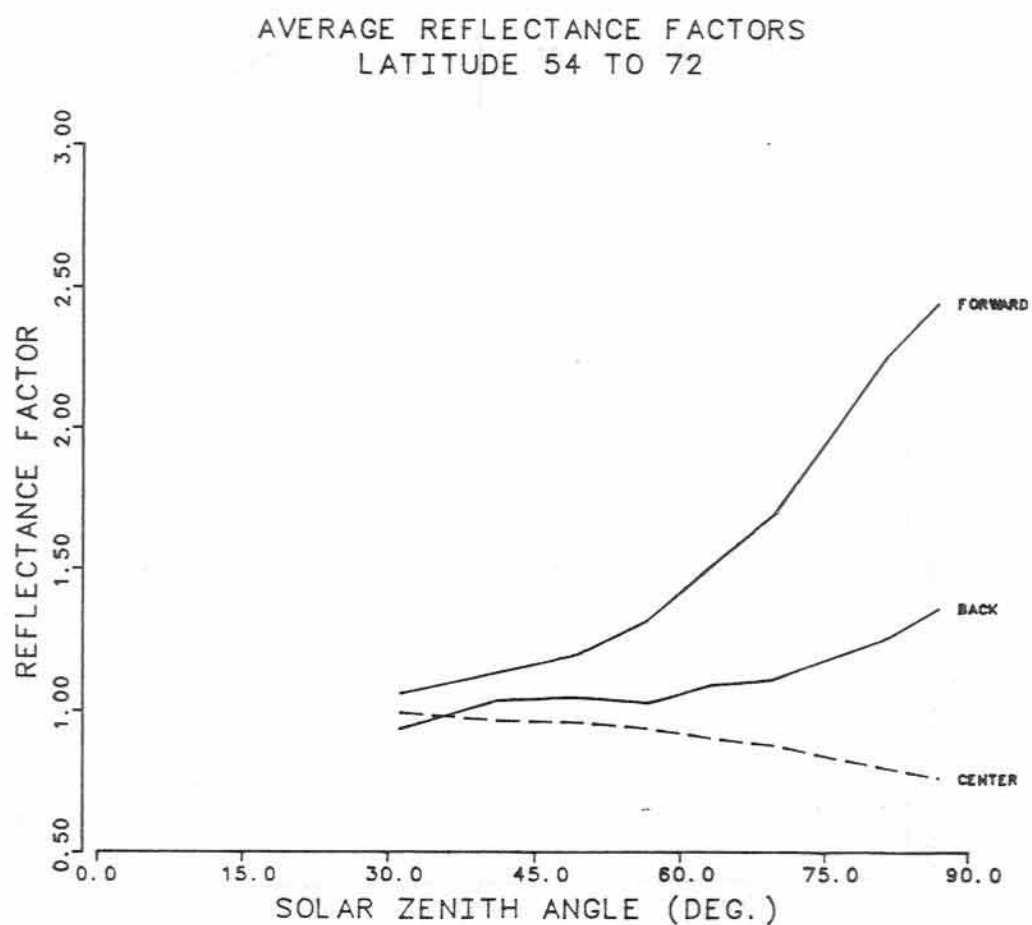


Fig. 4.9
Average Reflectance Factors for
54° to 72° North

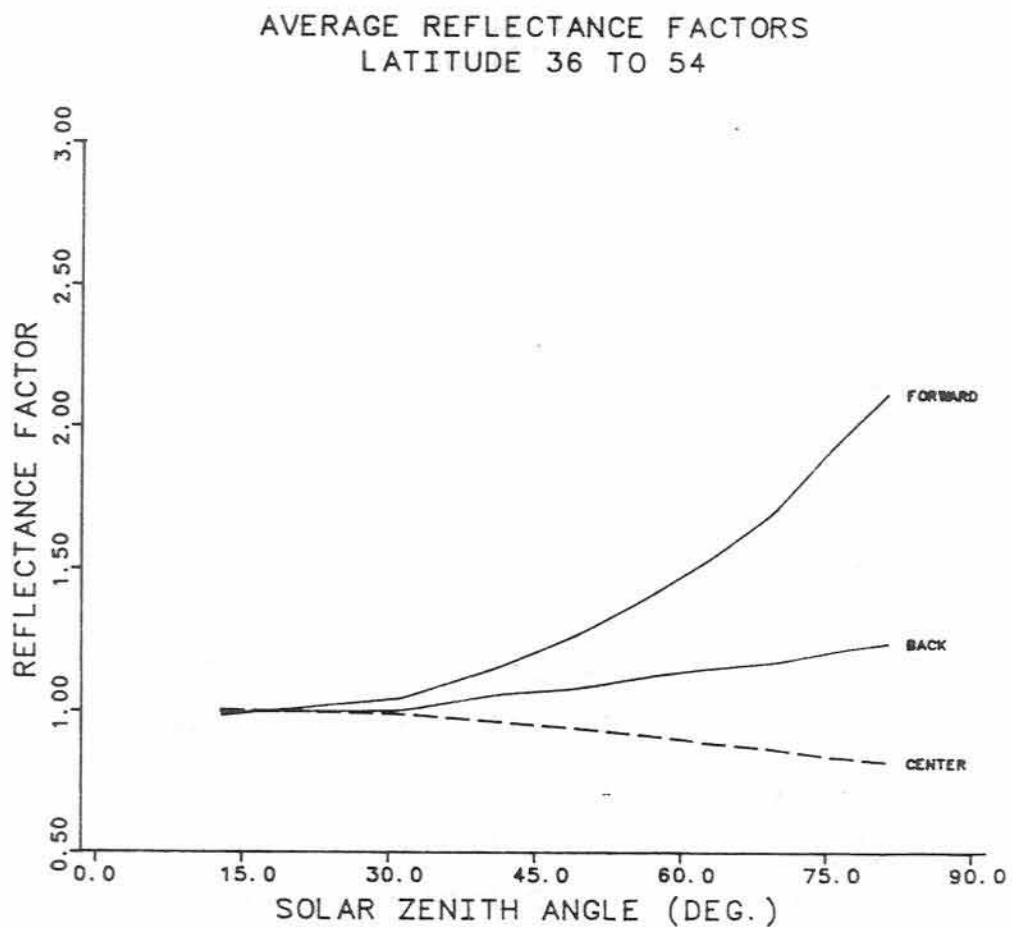


Fig. 4.10
Average Reflectance Factors for
36° to 54° North

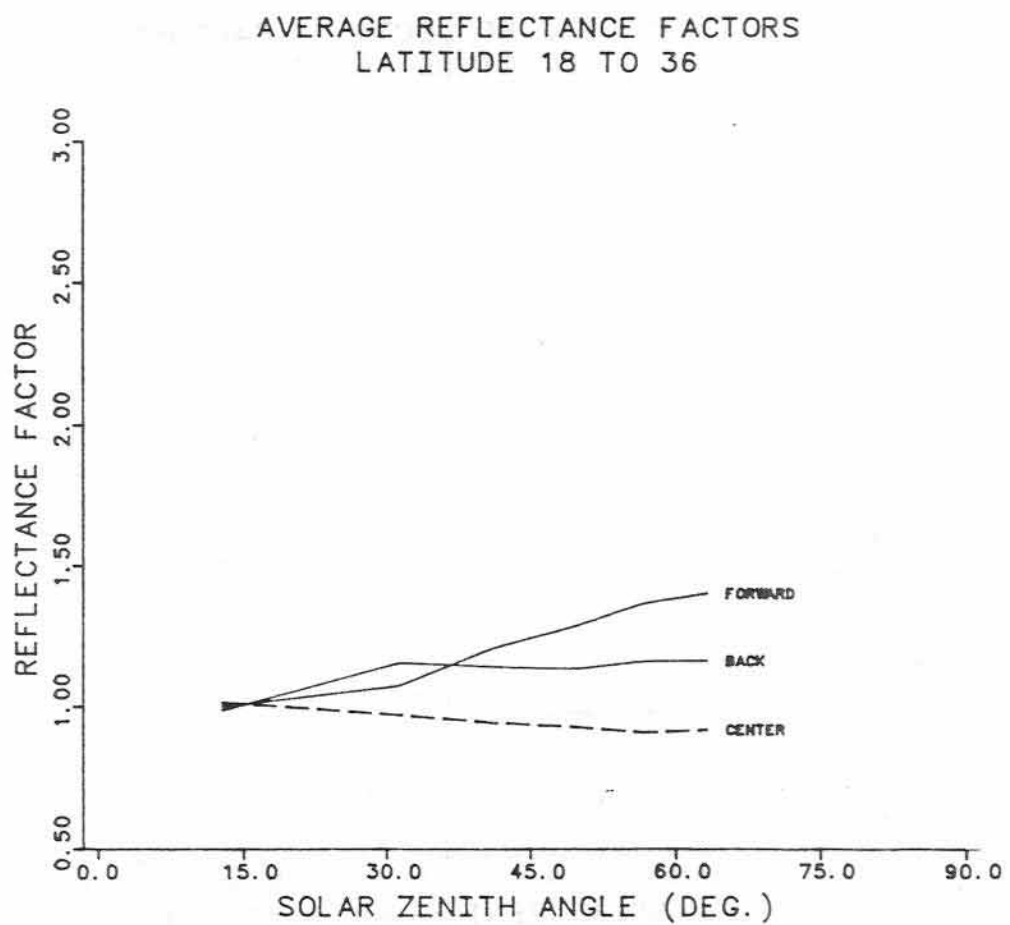


Fig. 4.11
Average Reflectance Factors for
18° to 36° North

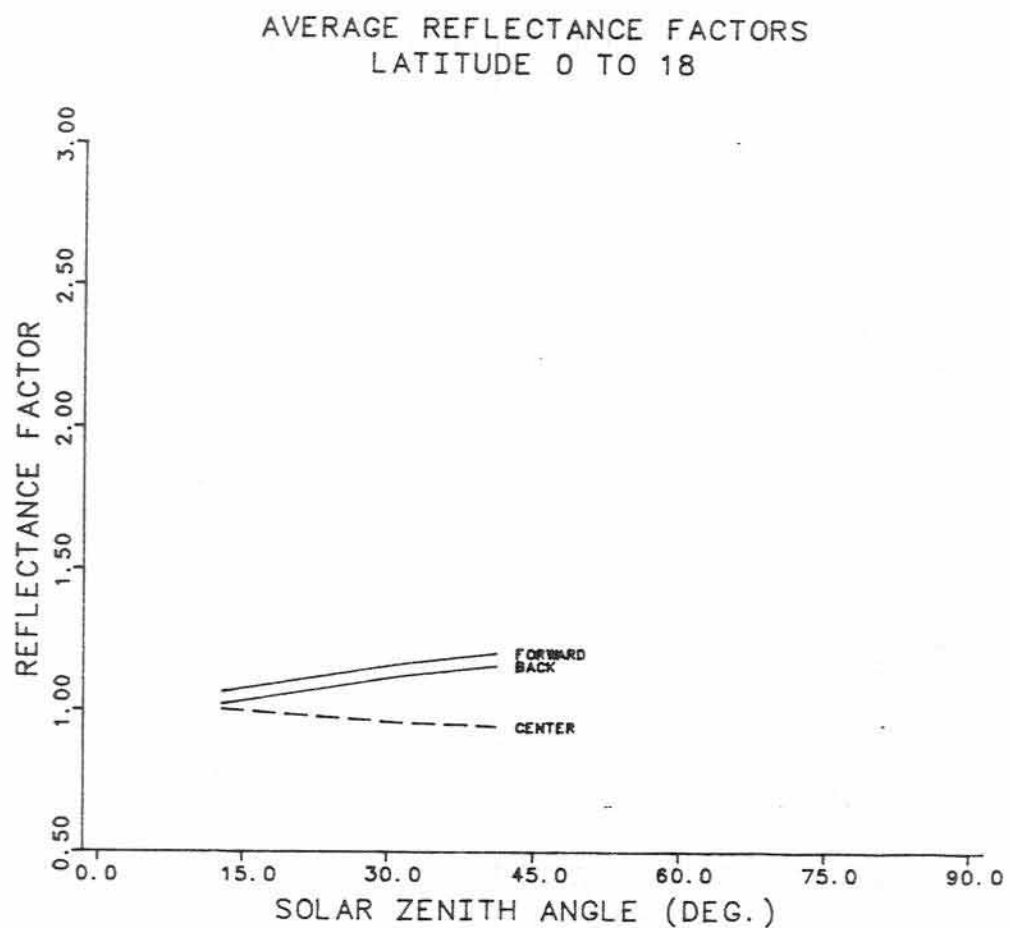


Fig. 4.12
Average Reflectance Factors for
0° to 18° North

AVERAGE REFLECTANCE FACTORS
LATITUDE -18 TO 0

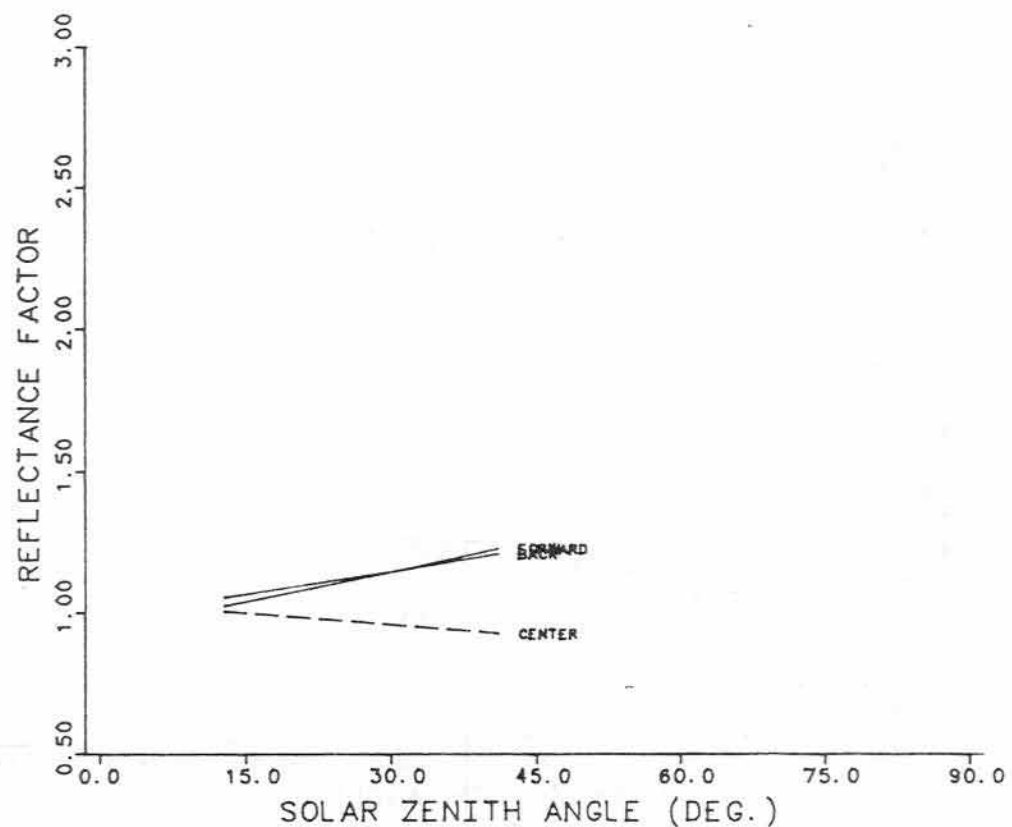


Fig. 4.13
Average Reflectance Factors for
0° to 18° South

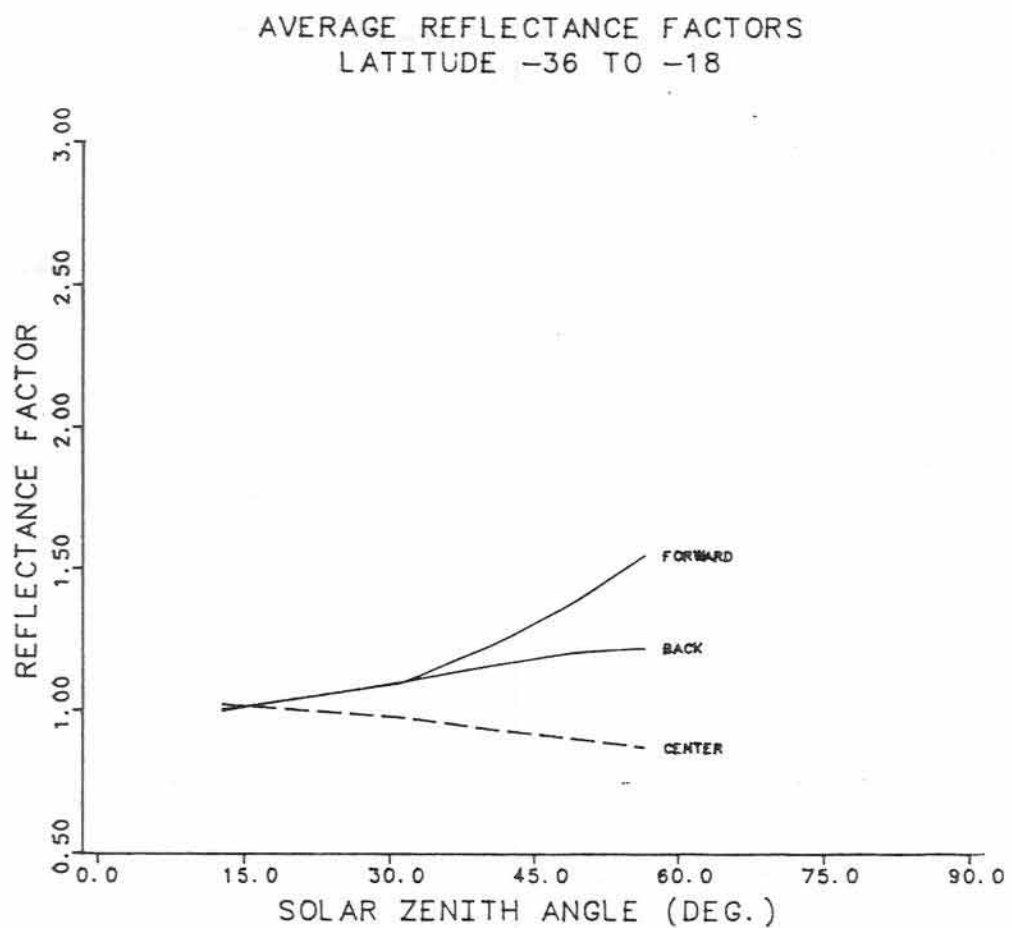


Fig. 4.14
Average Reflectance Factors for
18° to 36° South

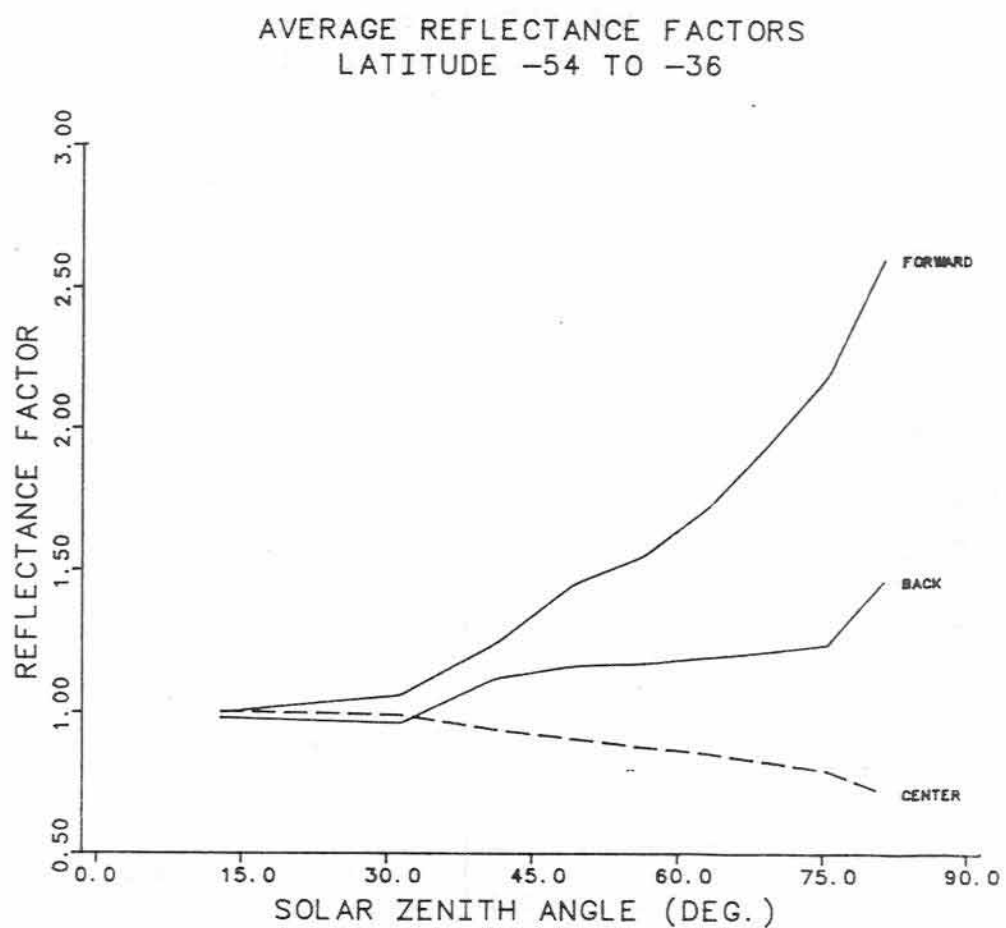


Fig. 4.15
Average Reflectance Factors for
36° to 54° South

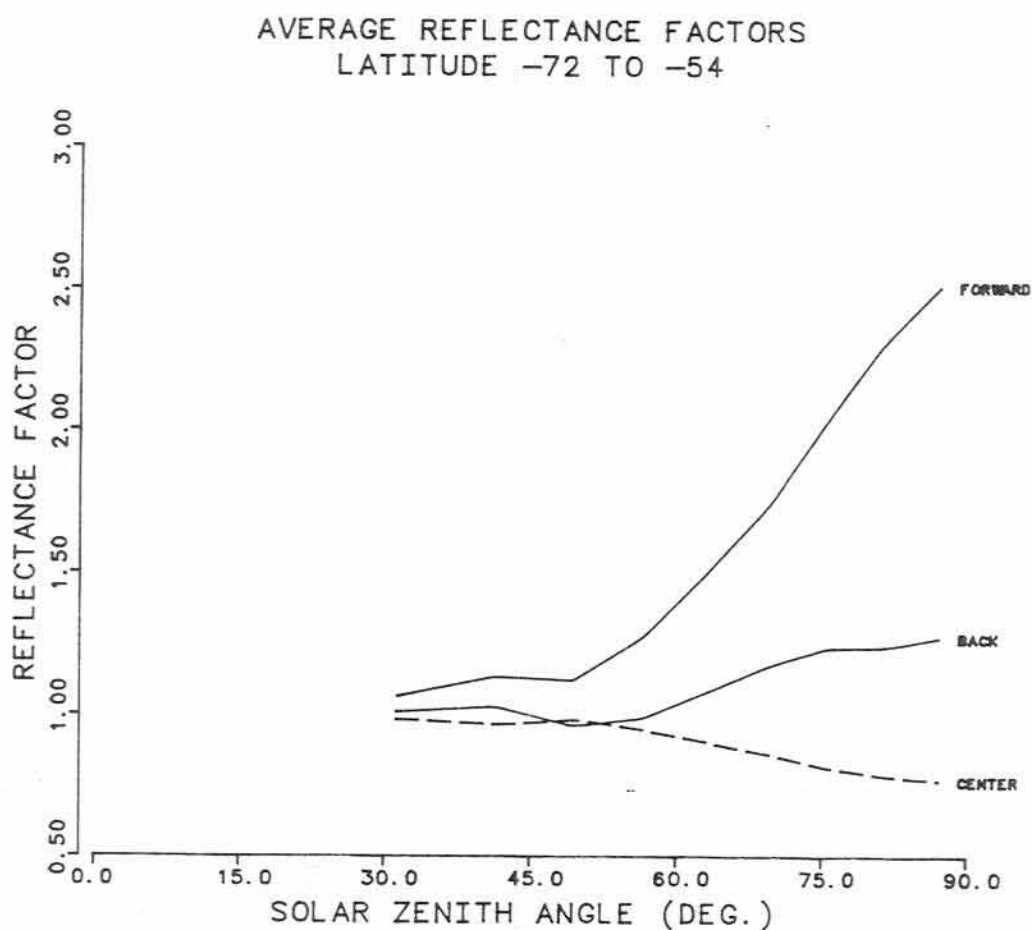


Fig. 4.16
Average Reflectance Factors for
54° to 72° South

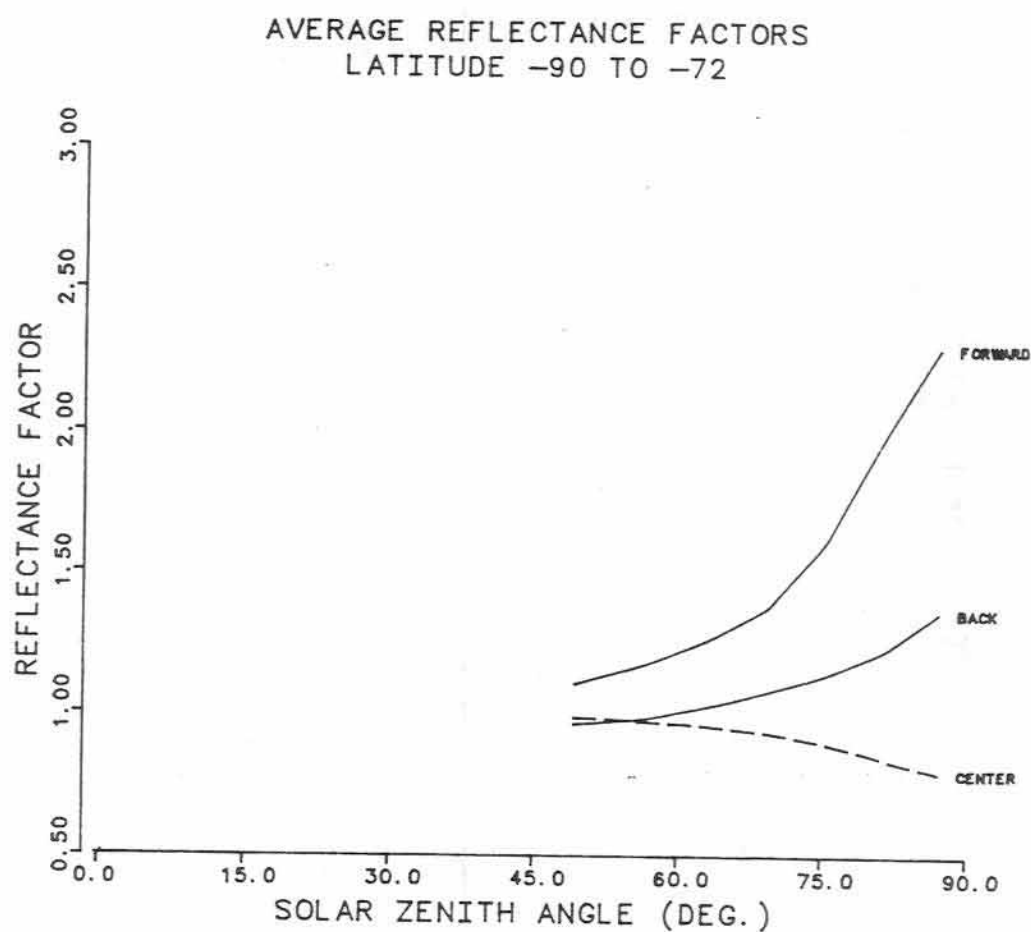


Fig. 4.17

Average Reflectance Factors for
72° to 90° South

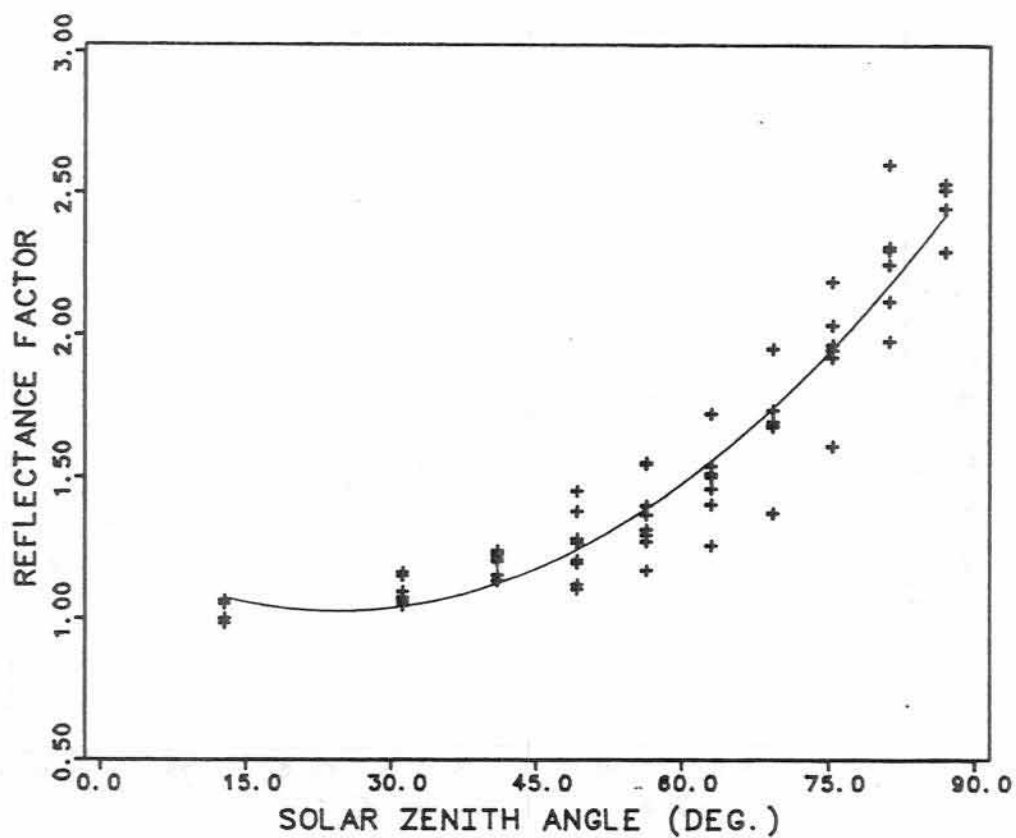


Fig. 4.18
Average Reflectance Factors (Forward)
and Best Fit Polynomial

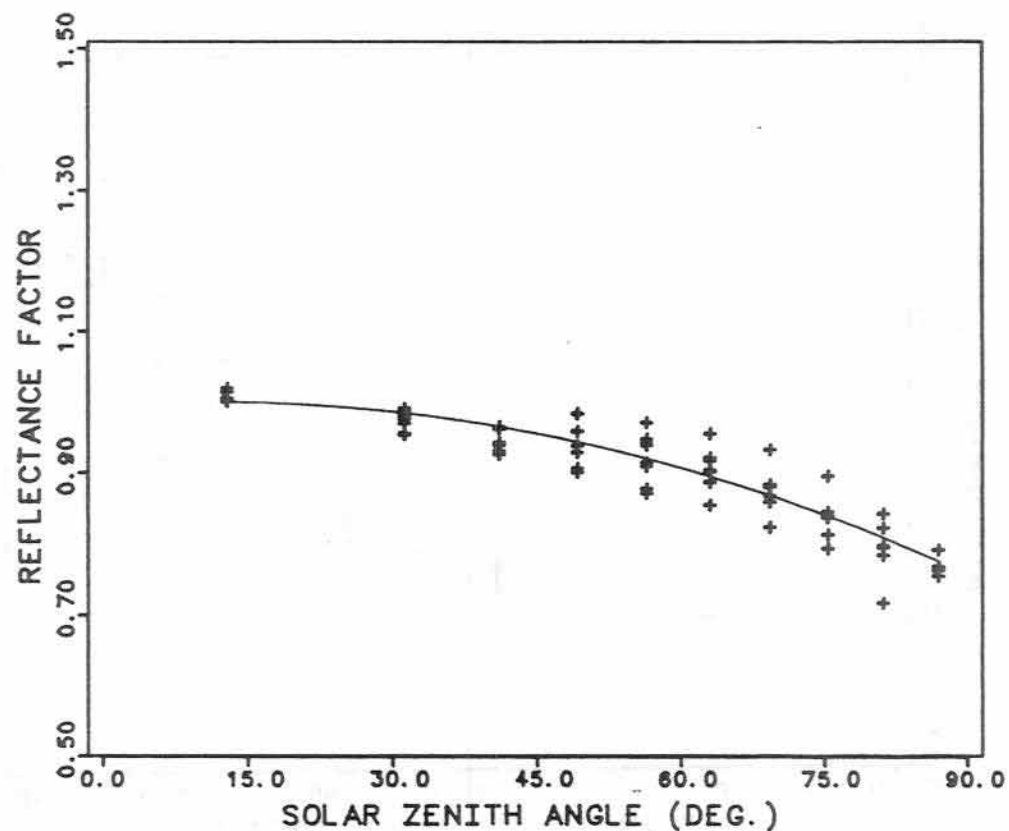


Fig. 4.19
Average Reflectance Factors (Center)
and Best Fit Polynomial

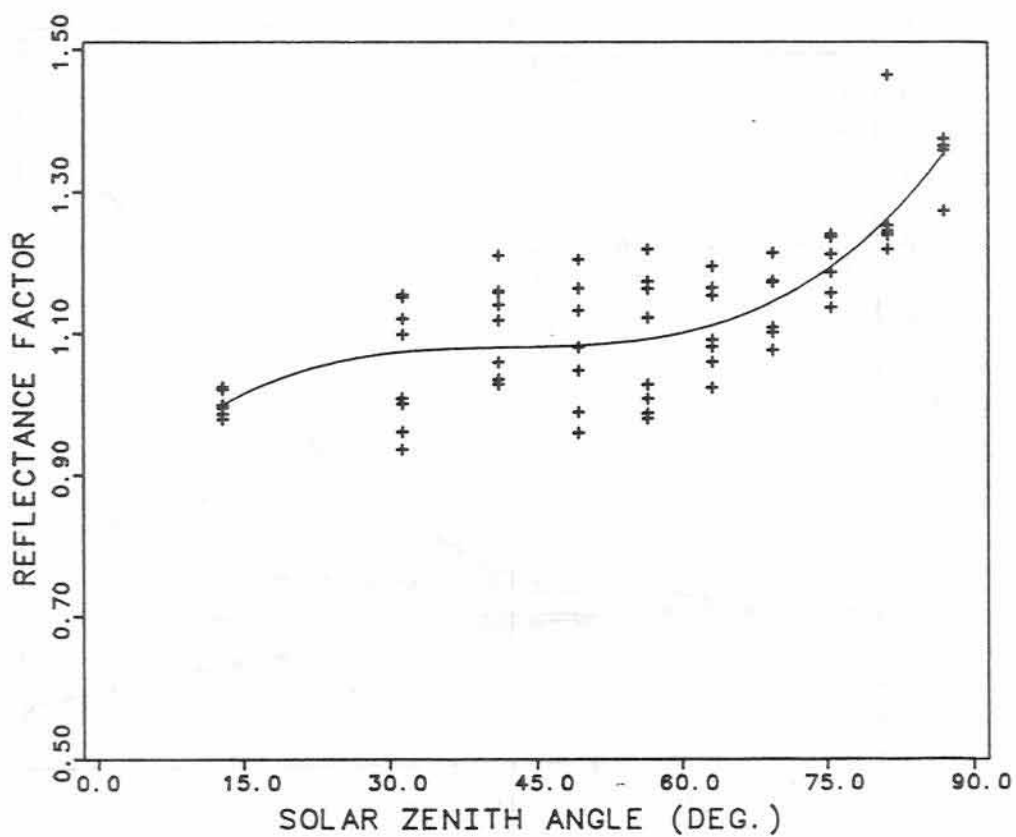


Fig. 4.20
Average Reflectance Factors (Back)
and Best Fit Cubic

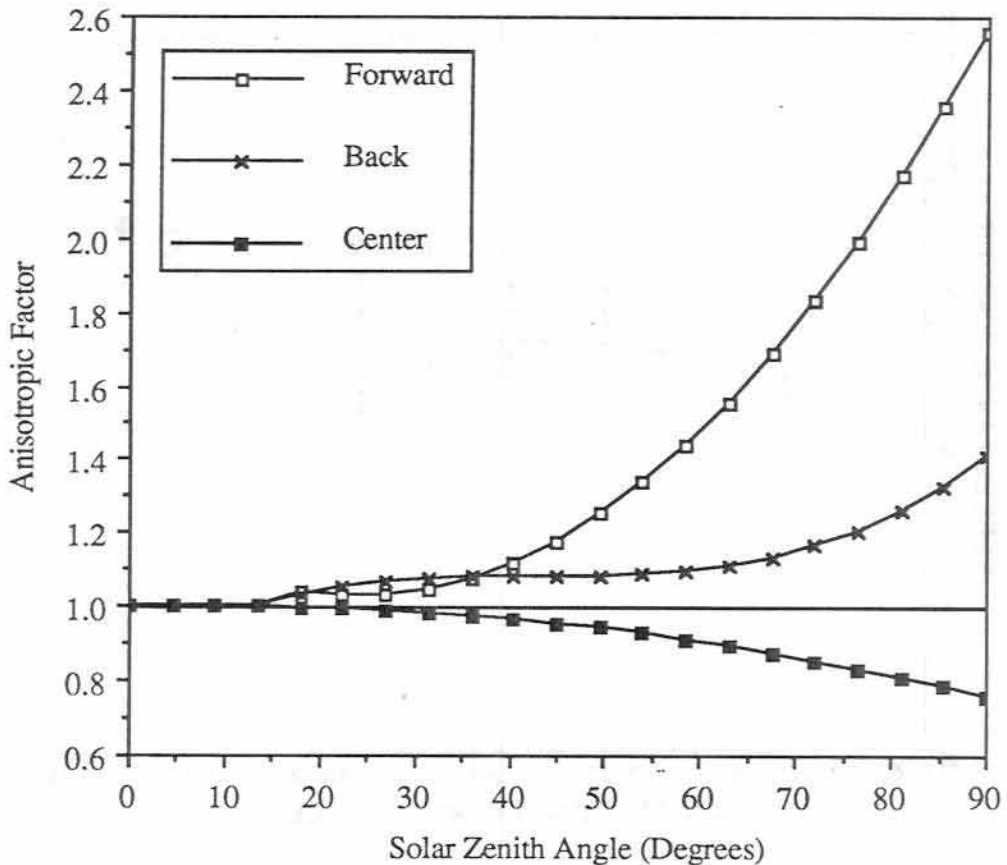


Fig. 4.21

Anisotropic Model

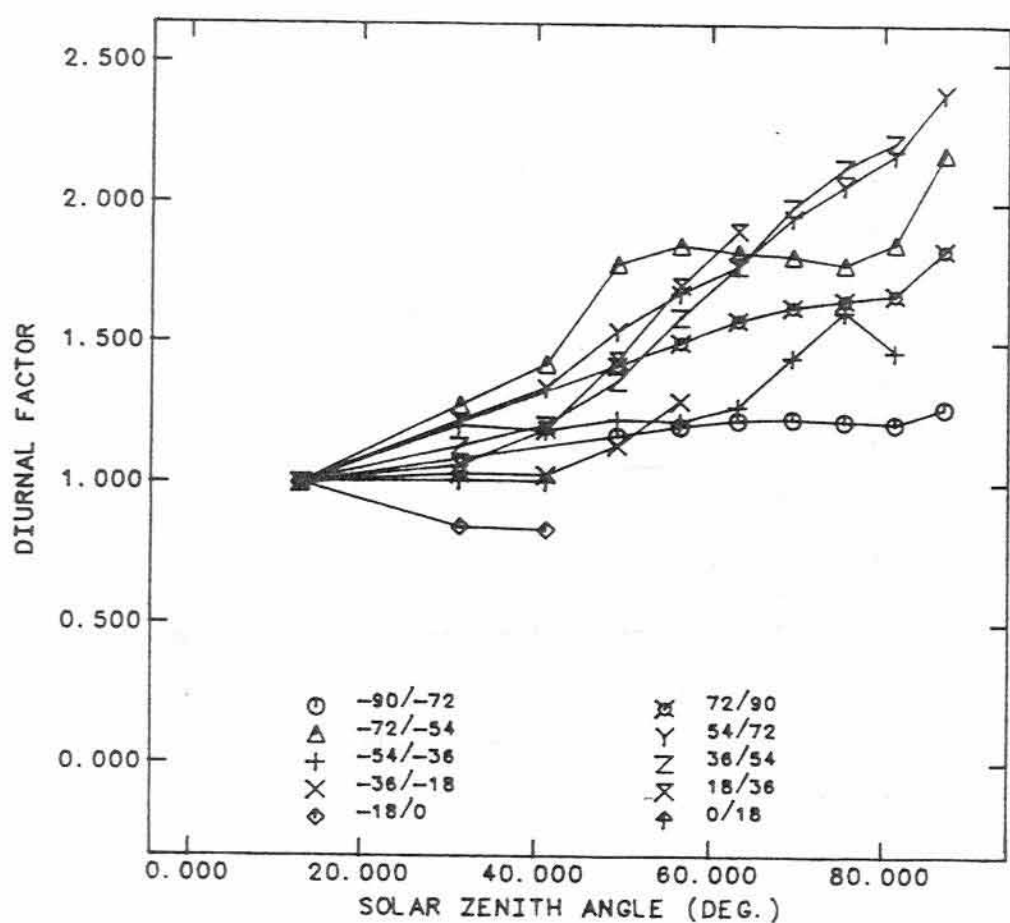


Fig. 4.22
Intermediate Diurnal Factors

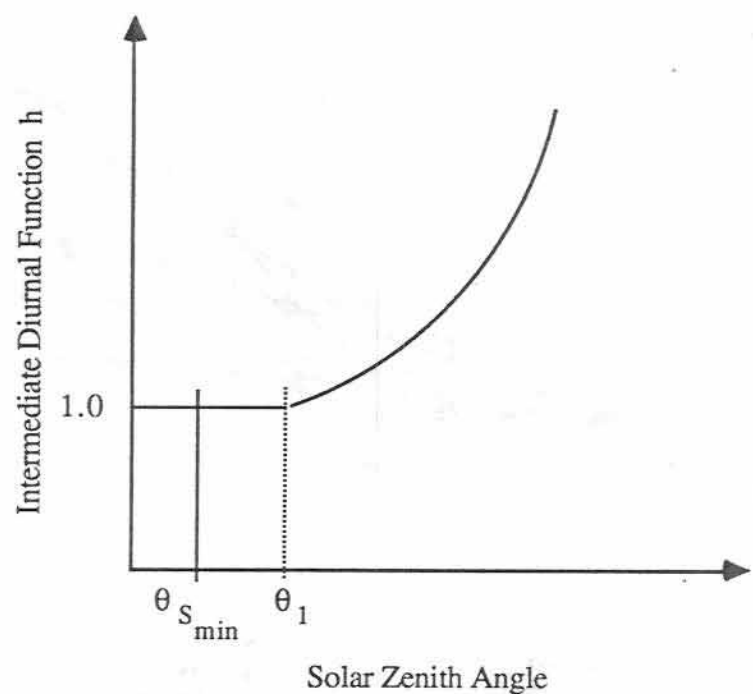


Fig. 4.23

Assumed Form of the Intermediate Diurnal Function

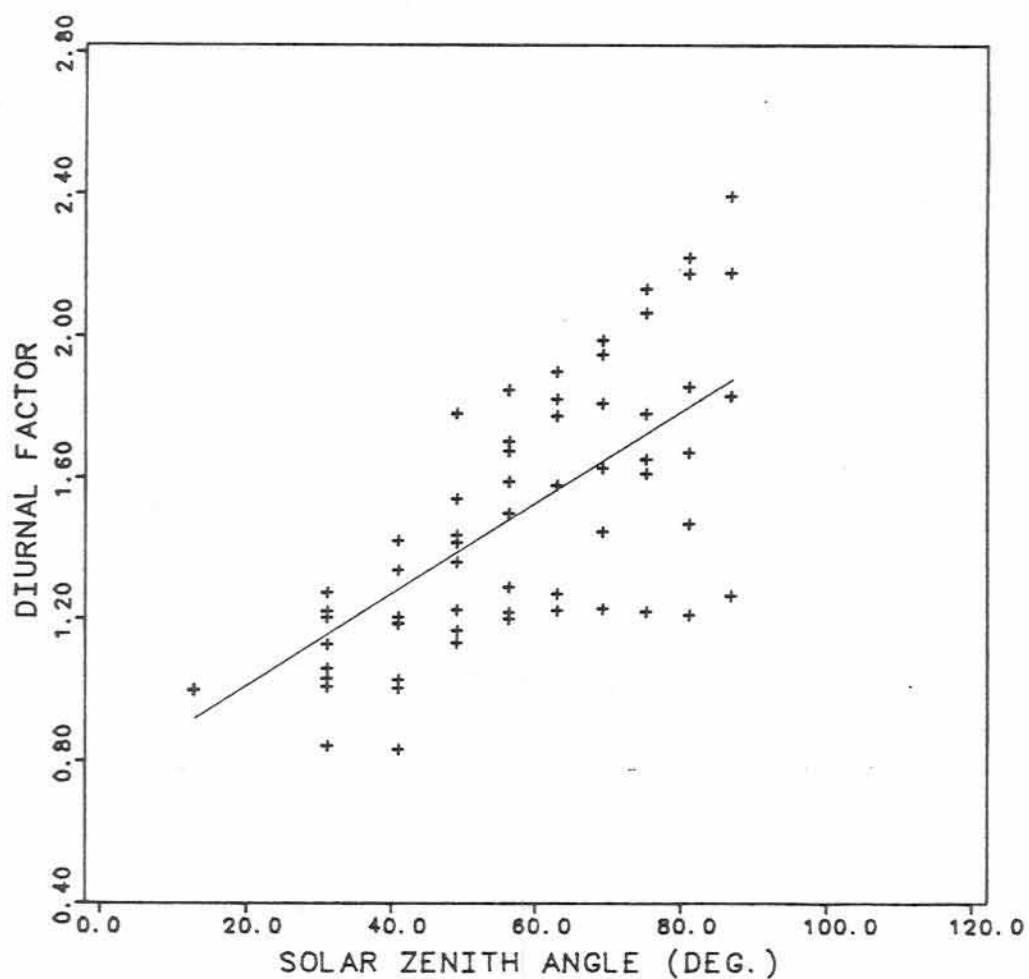


Fig. 4.24
Intermediate Diurnal Factors for all Latitude Bands
and Best Fit

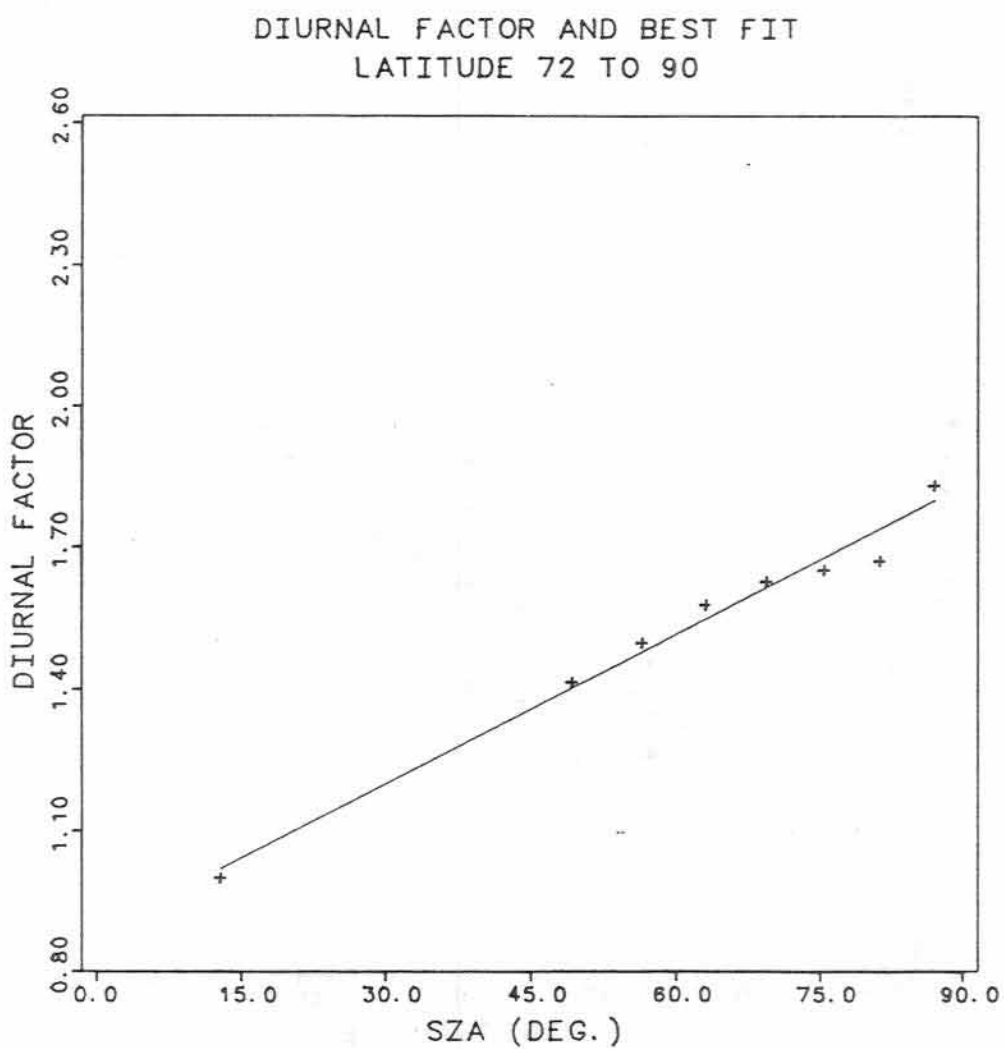


Fig. 4.25
Intermediate Diurnal Factor and Best Fit
72° to 90° North

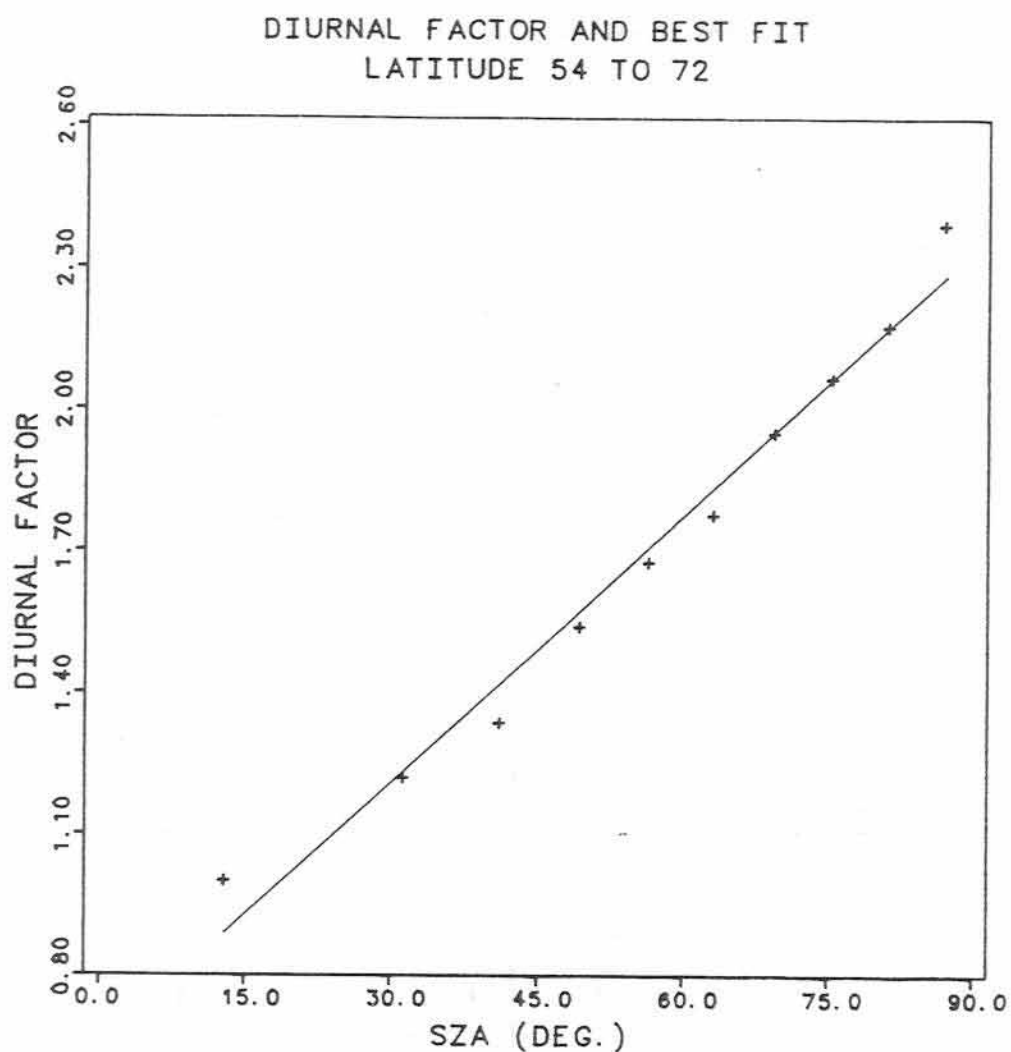


Fig. 4.26
Intermediate Diurnal Factor and Best Fit
54° to 72° North

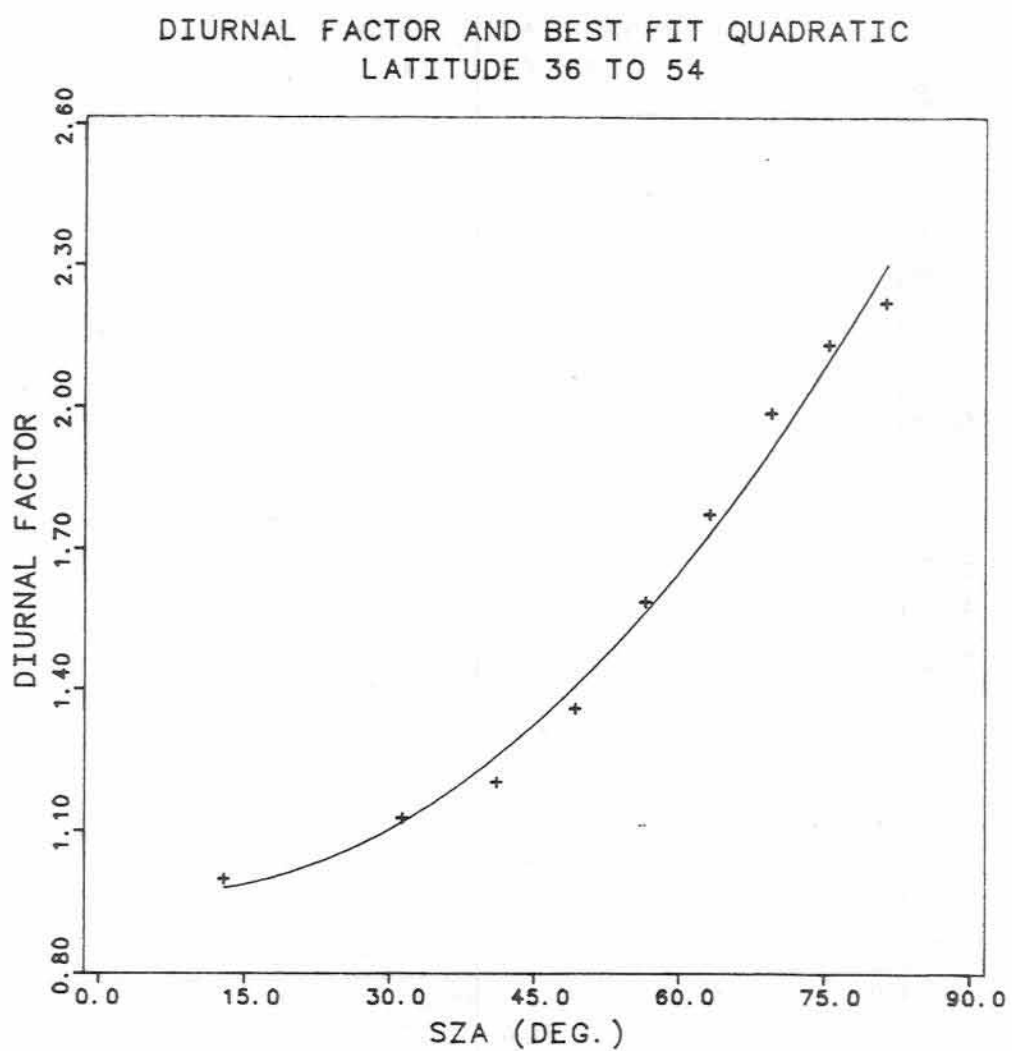


Fig. 4.27

Intermediate Diurnal Factor and Best Fit

 36° to 54° North

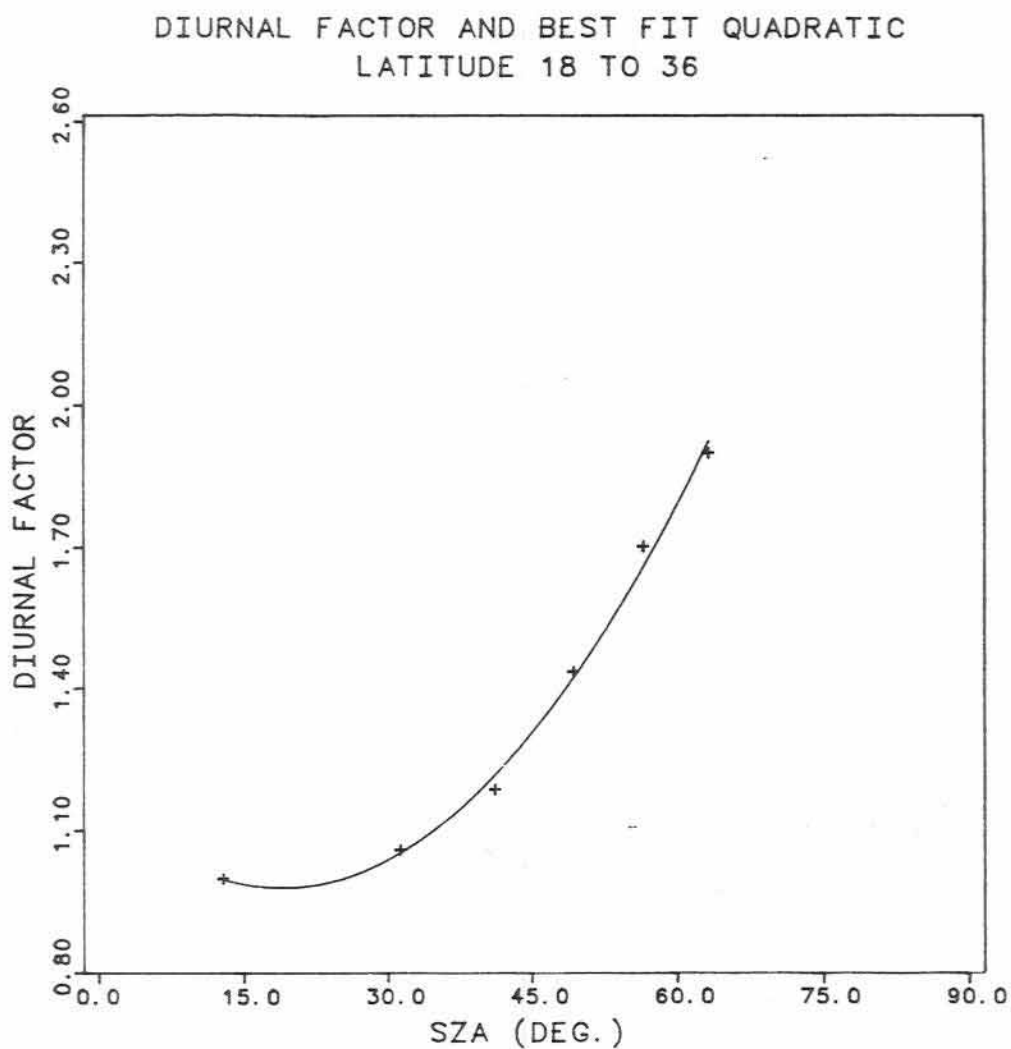


Fig. 4.28
Intermediate Diurnal Factor and Best Fit
 18° to 36° North

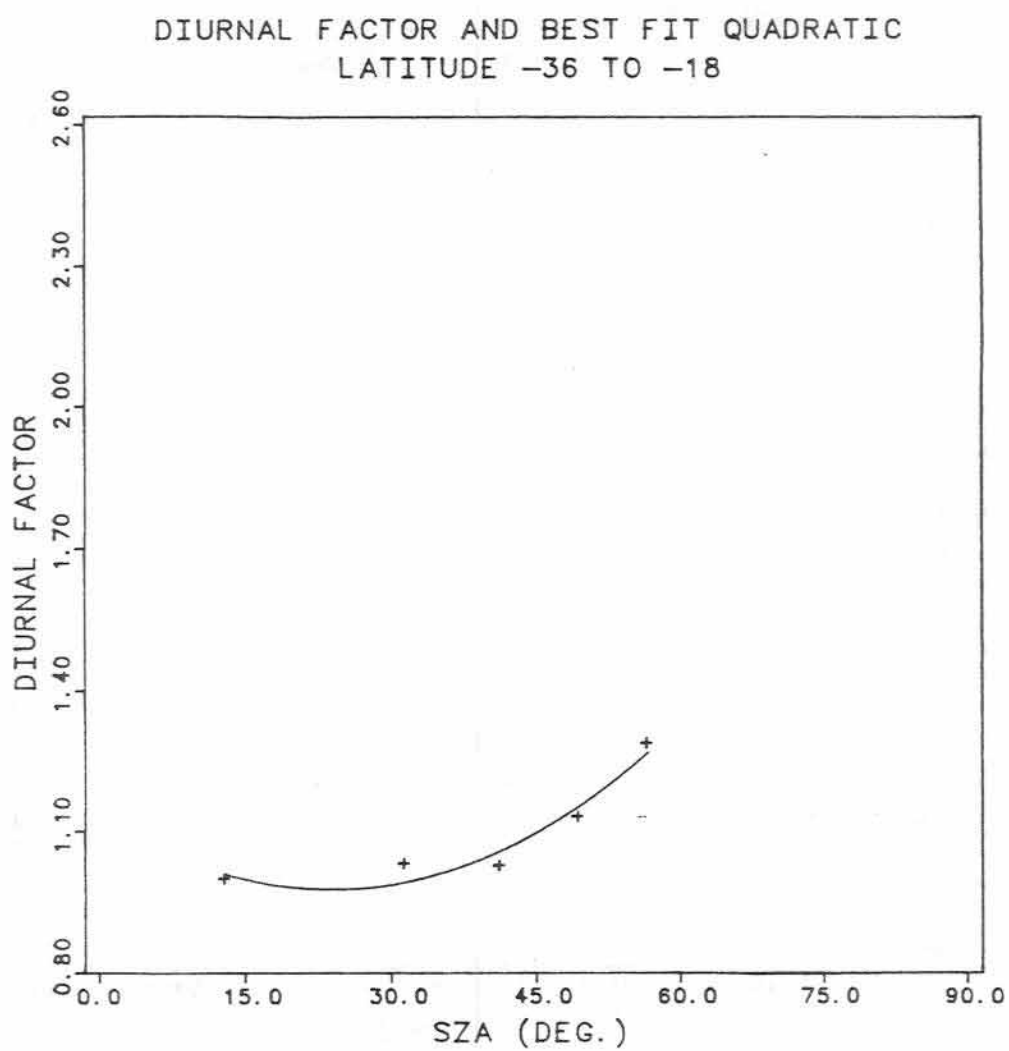


Fig. 4.29
Intermediate Diurnal Factor and Best Fit
 18° to 36° South

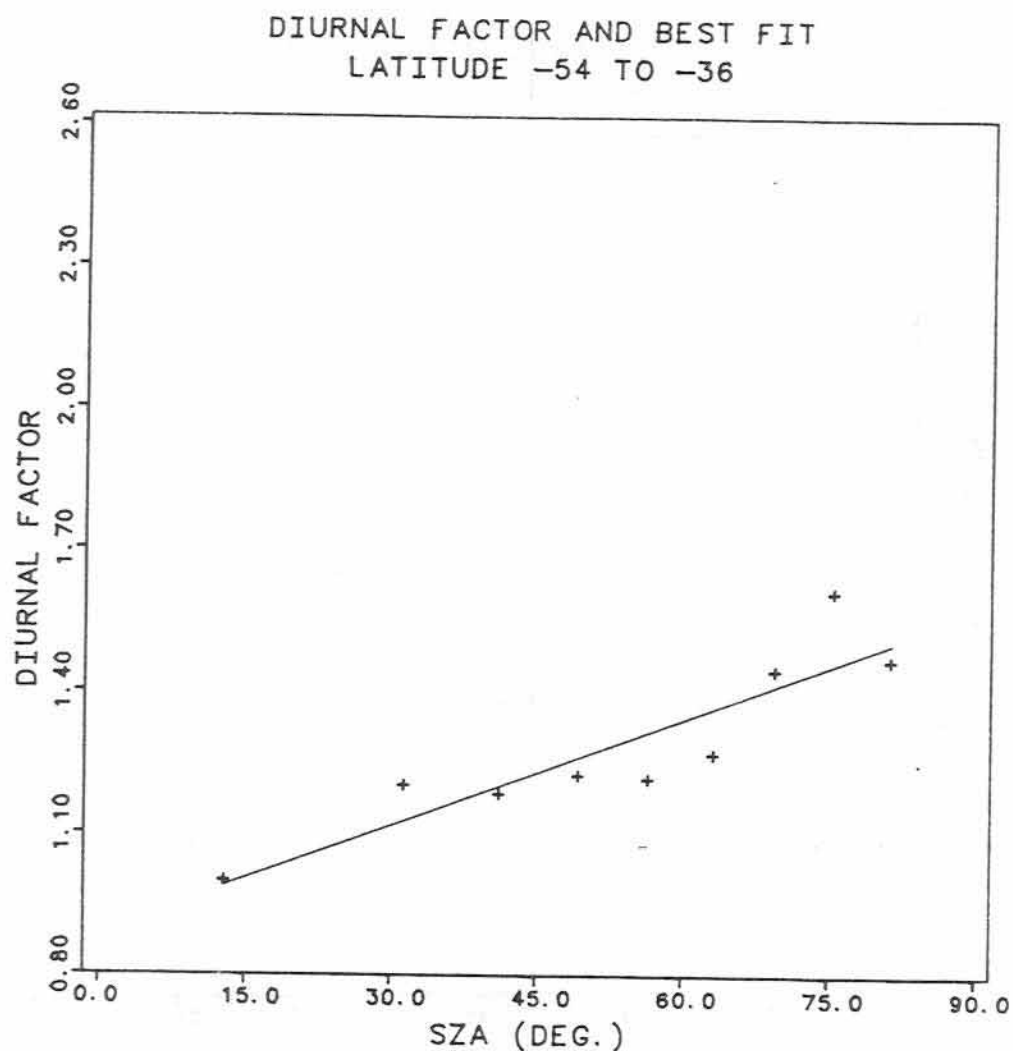


Fig. 4.30
Intermediate Diurnal Factor and Best Fit
 36° to 54° South

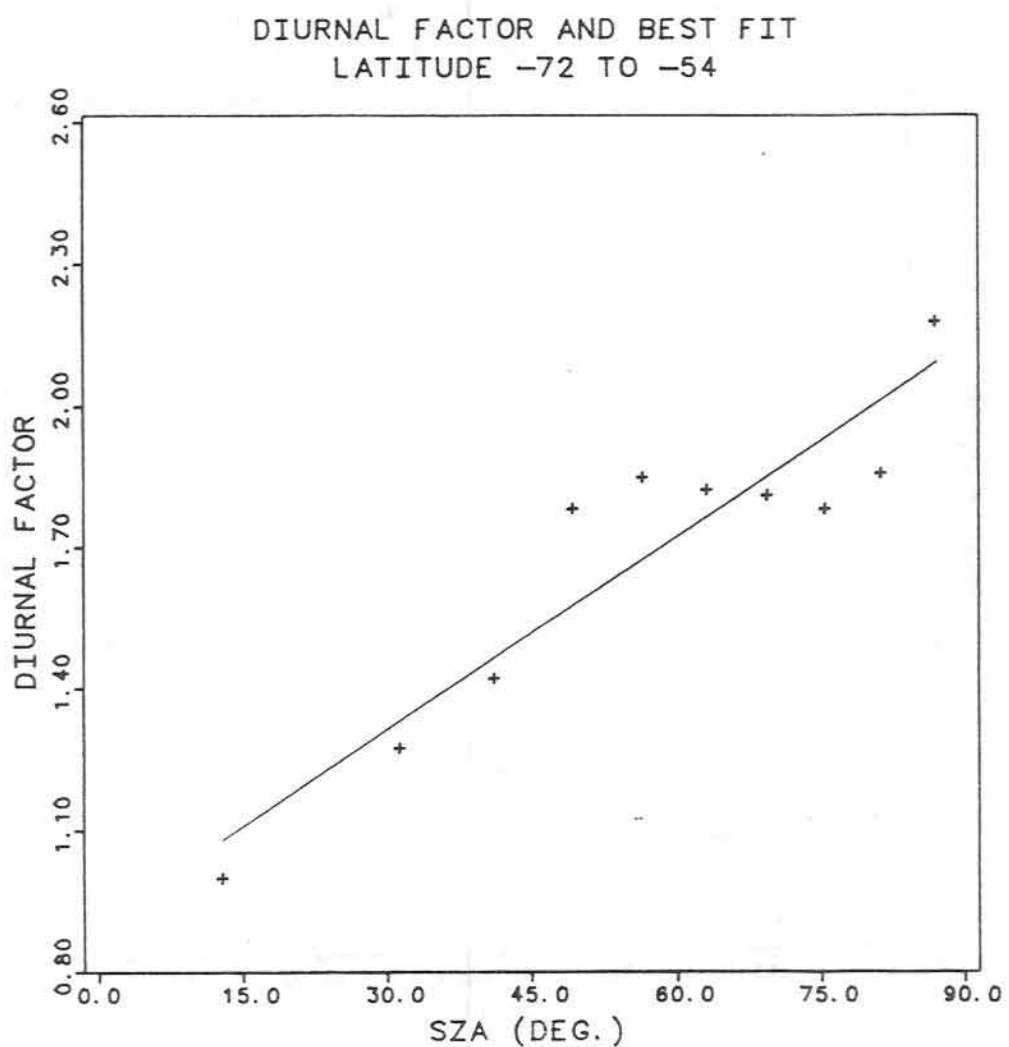


Fig. 4.31
Intermediate Diurnal Factor and Best Fit
54° to 72° South

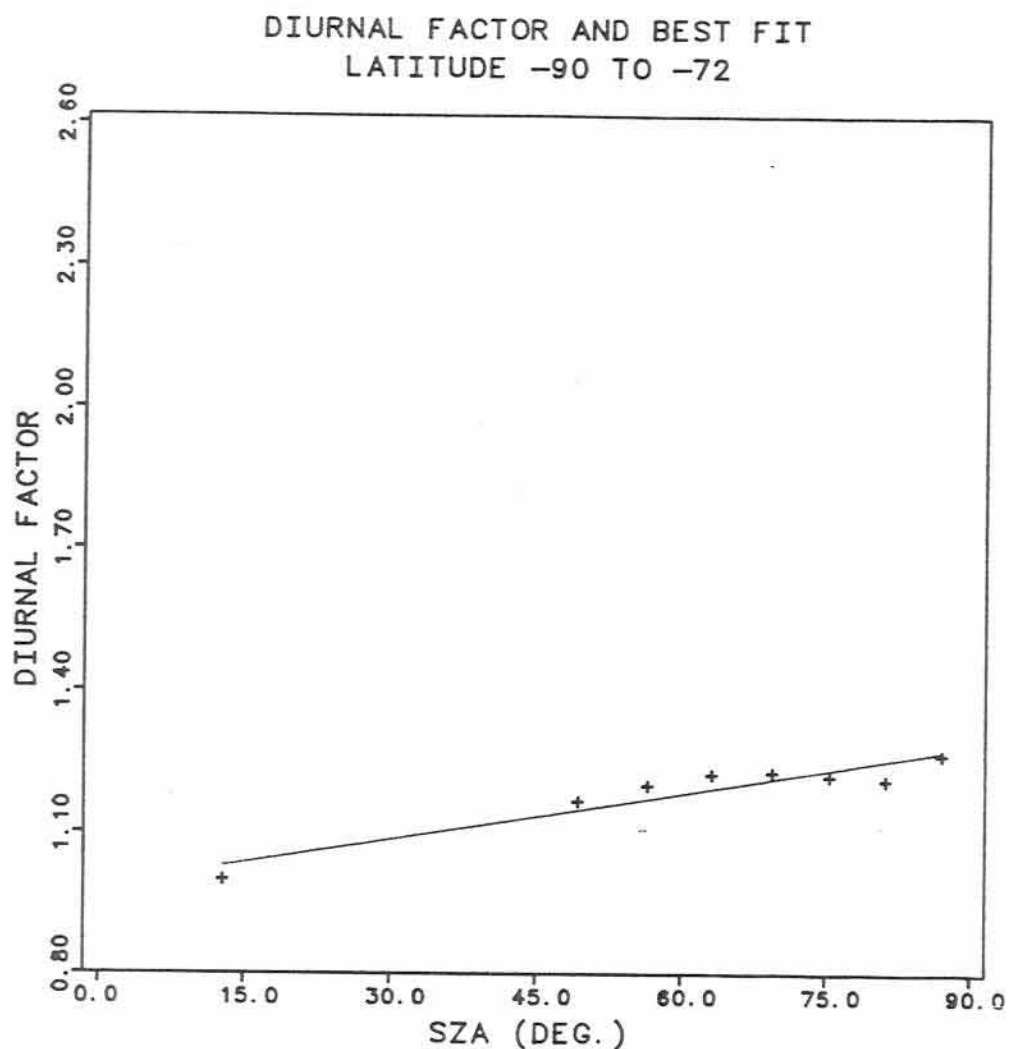


Fig. 4.32
Intermediate Diurnal Factor and Best Fit
72° to 90° South

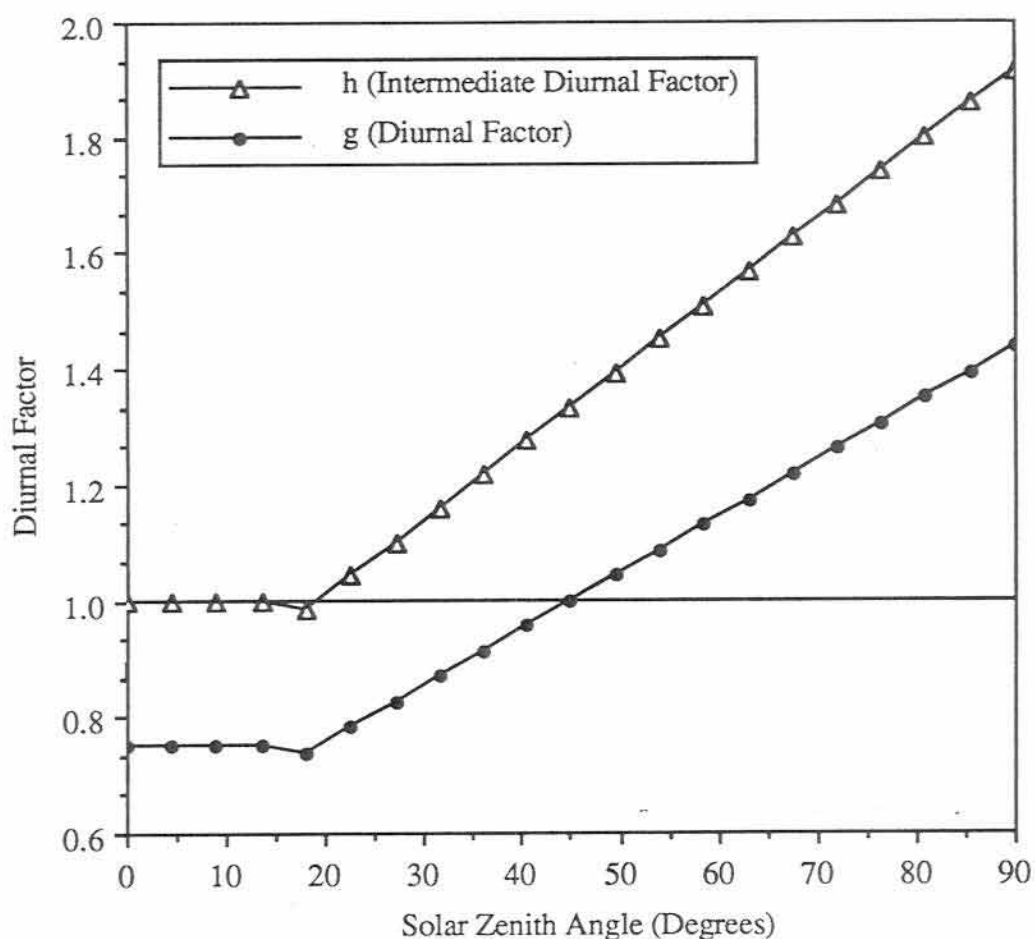


Fig. 4.33
Global Diurnal Factors

CHAPTER 5

ORBITAL EFFECTS OF ANISOTROPIC AND TIME VARIANT
SHORTWAVE EARTH RADIATION PRESSURE

5.1 *Character of Nondiffuse and Time Variant Shortwave Earth Radiation*

Pressure

5.1.1 *The Nature of an Unbiased Advanced Earth Radiation Pressure Model*

As mentioned in the previous chapter, one of the significant features of the advanced Earth radiation pressure model is its unbiased nature. Specifically, at each value of the solar zenith angle, the radiance of an Earth element, integrated over the upwelling hemisphere, results in the same value of albedo whether or not the anisotropic factors are used. Also, the diurnal model is constructed such that the mean albedo is always equal to the albedo of the nominal model. It is difficult to see how such requirements can be avoided, considering the nature and limitations of the data, the definition of the anisotropic factors, and the definition of classical albedo. Nevertheless, these requirements embody certain *de facto* assumptions of considerable importance. In particular, they assume that the nominal albedo estimates are in some sense accurate assessments of the true *mean* albedo, as expressed in Equation (2-6). In other terms, the radiometer measurements upon which the nominal albedo estimates are based are assumed to be influenced by

reflections from *all available solar zenith angles, and all available satellite view angles*. It must be acknowledged that even the best albedo estimates will fall short of this ideal to some extent. It is possible, even likely, that the radiometer measurements possess certain inherent preferences in either or both of these categories, thus resulting in a biased *mean albedo* model. The difficulty lies in determining the exact nature of any biases in the radiometer measurements.

The radiance data used in Stephens' model all come from satellites in geosynchronous or Sun-synchronous orbits. The geosynchronous satellite radiometer measurements are limited in satellite view angles, but cover the entire range of available solar zenith angles. Sun-synchronous satellites like Nimbus-7 are limited in their available ranges of solar zenith angles, for a given latitude. Also, Stephens does not use any bidirectional reflectance or diurnal corrections in the data reduction, although the need for such corrections is mentioned [Stephens *et al.*, 1981]. The result is an indeterminate picture of the possible effects of temporal variations and anisotropy in the reduction of the radiance data.

Theoretically, Taylor's latitudinally averaged radiance data are capable of producing an unbiased mean albedo model. In this context, then, the diurnal model described in Chapter 4 has been used to reduce Taylor's albedo data and obtain mean albedo values. This calculation involves considerable uncertainty, however, as the resulting values are often highly dependent on the assumed value of albedo at vertical incidence. (It should be noted that it is possible to develop a model which reasonably represents the true character and magnitude of the diurnal *variation* without necessarily knowing the vertical incident *albedo* with any great confidence.) The albedo values obtained from Taylor's data and the advanced Earth

radiation pressure model are shown in Figure 5.1. Also shown are albedos from the nominal UTOPIA albedo model, for the same season. (The STRT data appear to be slightly biased in favor of winter time intervals.) It is clear that Taylor's albedo values lie almost exclusively *above* the nominal curve. Taylor's albedo values have been fit to a second degree Legendre polynomial expansion, resulting in the experimental (EXP) model shown in the following table. Albedo coefficients for the nominal UTOPIA model are shown for the same season.

TABLE 5.1
ALBEDO COEFFICIENTS (Winter)

Coefficient	Nominal UTOPIA	EXP
a_0	0.34	0.43
a_1	0.1	0.08
a_2	0.29	0.24

Only the value for a_0 differs significantly between the EXP model and the UTOPIA model. In fact, the EXP albedo values may be simulated rather painlessly by setting $a_0 = 0.43$, and assuming the nominal values for a_1 and a_2 . The resulting model is shown in Figure 5.1.

On the basis of this exercise, one might argue that Stephens' model, for whatever reason, is underestimating the mean albedo slightly. It would be premature, however, to abandon Stephens' model for the numbers in the EXP analysis. If for no other reason than it is based on approximately 7% as much data as Stephens' model, the EXP representation must be considered inferior in the determination of mean albedo. The EXP model is included primarily as an exercise,

to indicate the types of calculations and analyses involved in the development of a truly unbiased mean albedo model. Also, the weight of evidence supporting Stephens' numbers is substantial. For example, in Chapter 3, the 4 x 4 albedo field, which was developed with the aid of a diurnal variation model, yields a value of a_0 which lies within 8% of Stephens' estimate. Also, Stephens' data set is the largest and most complete available, and his results are consistent with other assessments of the Earth radiation budget, e.g. *Jacobowitz and Tighe [1984]*. For the moment there is no compelling reason to discard Stephens' model or assume that it is significantly biased.

5.1.2 *The Flux Function*

In examining the differences and similarities between the diffuse model and the advanced Earth radiation pressure model, it is instructive to define a "flux function" Φ' which is directly proportional to the elemental flux which is intercepted by a satellite. The fluxes due to diffuse, nondiffuse, and time-variant Earth radiation pressure are all equally influenced by the angle of the incident radiation, through the cosine of the solar zenith angle. The attenuation caused by this factor has particular importance at high solar zenith angles, where anisotropy is strongest. In addition, as equation (2-19) indicates, the cosine of the satellite zenith angle α also affects the intercepted flux.

From Equation (2-19), a diffuse flux function might be defined as follows:

$$\Phi'_{\text{diff}} = \cos \theta_S \cos \bar{\alpha}, \quad (5-1)$$

where $\bar{\alpha}$ refers to the average value of the satellite zenith angle for each region of interest. For example, the average value of the satellite zenith angle for the central

scatter region is 31.5° , because the central scatter region extends from 0° to $\alpha_C = 63^\circ$. In this case, $\cos \bar{\alpha} = 0.85$. The forward and back scatter regions both use $\bar{\alpha} = 76.5^\circ$, for which $\cos \bar{\alpha} = 0.23$.

The flux function for anisotropy alone is:

$$\Phi'_{\text{anis}} = f(\theta_S) \cos \theta_S \cos \bar{\alpha},$$

where $f(\theta_S)$ is the anisotropic factor. The flux function due to diurnal variations alone is:

$$\Phi'_{\text{diurnal}} = g(\theta_S) \cos \theta_S \cos \bar{\alpha},$$

where $g(\theta_S)$ is the diurnal factor. The advanced Earth radiation pressure model, which includes both anisotropy and diurnal variations, would have the following flux function:

$$\Phi'_{\text{adv}} = f(\theta_S) g(\theta_S) \cos \theta_S \cos \bar{\alpha}. \quad (5-2)$$

These flux functions are intended as aids to comprehension. They are used solely for the purpose of visualizing the effects of anisotropy and diurnal variations, and not for computing the actual radiation pressure.

Figure 5.2 shows the anisotropic flux functions Φ'_{anis} for the forward, back, and central scatter regions, as compared with the appropriate diffuse flux functions. The back scatter region emulates the diffuse behavior quite closely, while the central scatter region shows some slight deviation from the diffuse behavior at moderate solar zenith angles. Only forward scattered reflection is strong enough to perturb the flux away from the diffuse curve, although even this discrepancy is relatively minor. The flux functions dramatically illustrate the relative importance of the anisotropic zones. Clearly the central scatter region dominates the amount of flux a satellite receives. It should be remembered, as well, that the various anisotropic

zones are of different sizes. The forward scatter region and the back scatter region each represent three-dimensional spatial surfaces which are about 40% as large as the central scatter zone. Also, the geometry of reflection off a spherical Earth is such that the forward and back scatter regions are sensed at rates even smaller than those suggested by their spatial areas. Take as an example the eclipsing LAGEOS orbit shown in Figure 3.3. During those times when the anisotropic model is active (i.e. for solar zenith angles above 15°) an Earth radiation pressure model consisting of 20 rings senses the central scatter region 80% of the time. The backscatter is sensed 13% of the time, and forward scatter only 7% of the time. All of these factors conspire to reduce the importance of anisotropic reflection in the determination of Earth radiation pressure.

Of more potential interest in the development of Earth radiation pressure models is the influence of the diurnal variation. The average global diurnal flux function is compared with the diffuse flux function in Figure 5.3. It appears that the unbiased diurnal factors indicated by the NIMBUS-7 data actually *decrease* the total time-integrated "power" of Earth radiation pressure, as indicated by the area under the curves. The behavior of these curves also indicates the likely influence of an asymmetric diurnal function, analogous to the morning/evening difference suggested by *Morgan* [1984] as an agent of LAGEOS' deceleration. Note that the diurnal curve and the diffuse curve are reasonably close at solar zenith angles above 45 degrees. It would appear that attenuation due to the cosine of the solar zenith angle is so strong that any morning/evening differences in true albedo would be of extremely limited moment.

The flux function for the advanced Earth radiation pressure model, which

combines anisotropy and latitudinally-dependent diurnal variations is plotted in Figure 5.4, and compared with the diffuse model. Interestingly, the maximum radiance levels occur at different values of the solar zenith angles, for each of the characteristic zones. Most prominent is the forward flux function, the maximum of which occurs at a solar zenith distance of approximately 55° , instead of at vertical incidence.

5.1.3 Variation Over an Orbit and the Number of Earth Segments

In the course of a satellite's orbit, it is expected that the gross variations in the radiation pressure due to "complex" (i.e. nondiffuse and diurnally varying) Earth reflection would be similar to those engendered by the diffuse model. Unlike the diffuse representation, the radiance calculated with the advanced model depends on whether the satellite is experiencing forward-scattered radiation, back-scattered radiation, or centrally reflected light. In this regard, the advanced model must use the minimum number of Earth segments which adequately simulate both the expected magnitudes of the pressure force, and the relative *occurrences* of each of the anisotropic zones. The minimum number of segments, or rings, is determined by examining the variation over an orbit of the pressure force on LAGEOS and GEOS-1.

Figure 5.5 shows the variation in the radial Earth radiation component over a single eclipsing LAGEOS orbit, using both the nominal diffuse model and the advanced model. Plots for 2 rings (19 segments) and 20 rings (1261 segments) are included. The radial component does not appear to be highly dependent on the number of rings, for either model. The transverse component, shown in Figure

5.6, displays greater sensitivity to the number of rings used. In the implementation of the advanced model, the maximum transverse acceleration clearly would be overestimated if too few segments were used.

In more general terms, it is evident that implementing the advanced model decreases the overall influence of Earth radiation pressure. The maximum radial component from the advanced model is 20% smaller than the maximum radial diffuse acceleration. The magnitude of the maximum transverse acceleration is decreased by approximately 30%.

The eclipsing June 27, 1977 GEOS-1 orbit is examined in Figures 5.7 through 5.11. The radial Earth radiation acceleration on GEOS-1 is more sensitive to the number of rings than the radial acceleration on LAGEOS, perhaps because the lower orbit of GEOS-1 subjects the spacecraft to a higher level of Earth radiation. As Figure 5.7 indicates, even the diffuse radial acceleration is slightly underestimated if too few Earth segments are utilized. The advanced model's along-track component, shown in Figure 5.8, is clearly exaggerated in magnitude if too few rings are used.

After some analysis, it has been decided that the advanced model, in order to determine accurately the character and magnitude of the Earth radiation pressure, must contain no fewer than 4 rings (61 segments). Figures 5.9 through 5.11 show radial, normal, and along-track components of the Earth radiation pressure on GEOS-1 for various numbers of rings. The four ring representation appears to model the force adequately, and in particular, removes some of the "chatter" seen in the normal component.

As mentioned earlier, it is important to determine the minimum number of

rings which permits the model to sense each anisotropic zone at the appropriate rate. For example, under some circumstances the magnitude of the advanced Earth radiation acceleration may be calculated adequately with only two rings, but if the spacecraft senses the forward scattering zone at an unrealistic rate, the estimates of the acceleration may be inaccurate for some illumination conditions. Once again, four rings seems to be an adequate compromise between computational overhead and model accuracy. Figures 5.12 and 5.13 illustrate the percentage of time a given anisotropic zone is sensed in the course of an eclipsing orbit, for GEOS-1 and LAGEOS, as a function of the number of rings. For either satellite, using only two rings causes unrealistically high estimates of the occurrences of forward or back scattered radiation. It is interesting that this criterion is equally valid for low and high orbiting satellites.

To summarize, it would appear that the basic character of the Earth radiation accelerations is largely similar, whether calculated by means of a purely diffuse model or with the added complexities of the advanced representation. The advanced model apparently requires more Earth segments in order to simulate the Earth radiation pressure properly. Finally, as expected from the analyses in Chapter 4, anisotropy and diurnal variations reduce the maximum Earth radiation flux sensed by the satellite.

5.1.4 Advanced Vs. Diffuse Models: Trajectory Comparisons

Given the basic similarities between the two models, and given the fact that their variations over an orbit are similar, it is tempting to conclude that the advanced

model may be simulated by using the diffuse representation, with slightly different values of the Earth radiation parameters. This theory is tested by means of a trajectory comparison, wherein the nominal orbit is generated with the advanced model, and the comparison trajectory is propagated with the diffuse model. GEOS-1 is used for this study because of its special sensitivity to Earth radiation pressure. Four rings (61 segments) are used in both the diffuse and advanced models.

TABLE 5.2
ADVANCED vs. DIFFUSE: TRAJECTORY COMPARISON

satellite	arc(days)	Estimated Parameters	RMS of fit (m.)
GEOS-1	30	IC	5.2
GEOS-1	30	IC, C_D , η_R	1.2
GEOS-1	30	IC, C_D , η_R , a_0 (.27)	0.5

Values in parentheses refer to the final estimates of the indicated parameters. Evidently, about half of the disparity between the models may be absorbed by decreasing the diffuse model's mean albedo by 20%. Recall from Section 5.1.3, that the anisotropic/diurnal model reduces the maximum radial component by 20%, compared with the diffuse model's maximum radial acceleration. It is clear, however, that all of the model differences do not merely disappear when a_0 is estimated. The remaining orbit error amounts to approximately 14% of the total Earth radiation "effect", as shown in Table 3.4. Attempting to adjust a_0 , a_1 , and a_2 simultaneously results in unreasonable estimates of the albedo parameters.

It remains to be seen what different signals are introduced by incorporating time variant and directional reflectance into the Earth radiation model, and how this

affects the topics discussed in previous sections, i.e. the secular decrease in LAGEOS' semimajor axis, and the along-track accelerations on high eccentricity satellites.

5.2 Orbital Effects on LAGEOS

The basic similarities, both of structure and effect, between the diffuse and advanced Earth radiation pressure models, suggest that the long period orbit perturbations of either should be comparable. The inability of diffuse Earth radiation pressure to explain the secular decrease in the semimajor axis of LAGEOS would almost certainly extend to the advanced model, which exerts a proportionately smaller influence on satellites. The orbital effects on LAGEOS engendered by the nondiffuse, time-variant model are quantified by a series of trajectory comparisons similar to those described in Chapter 3. A nominal orbit is generated with the advanced model activated, and a comparison orbit is propagated with Earth radiation pressure absent from the force model. In this and other analyses involving the advanced model, the nominal configuration uses four surface rings and 61 surface elements. (See Section 5.1.3.) Figures 5.14 through 5.18 illustrate the effect of the advanced model on the orbit elements of LAGEOS, in terms of direct trajectory comparisons. The scale of the plots are the same as those shown for the diffuse model, in Chapter 3.

The orbit perturbations on LAGEOS due to the total Earth radiation flux are similar in character for the diffuse and advanced models, although generally of smaller amplitude for the latter. The semimajor axis corrections are characterized by small, long period variations in both cases, although the periodicities in Δa depend

to some extent on the model used. Figure 5.19 shows a periodogram for the advanced model, for a 2100 day trajectory comparison. Comparing Figure 5.19 with Figure 3.13, its diffuse counterpart, reveals an interesting difference between the models. The expected periodicities at 280 days and 560 days are more clearly in evidence when using the advanced model.

Figure 5.14 reveals that a realistic anisotropic and time-variant Earth radiation pressure model is incapable of reducing the semimajor axis of LAGEOS at the rate of 1.1 mm/day. A somewhat different treatment of anisotropy is described in *Rubincam et al.* [1987], in which the Earth is divided into a diffuse northern hemisphere and an anisotropically reflecting southern hemisphere. This severe hemispherical asymmetry is posited as a limiting case, intended to explore the maximum effect of variations in the directional reflectance of the terrestrial sphere. Even this drastic model cannot affect the deceleration of LAGEOS to any significant extent. There is no evidence suggesting that Earth radiation pressure, in any form, is capable of perturbing LAGEOS' semimajor axis in the manner described by high accuracy laser range measurements.

With the exception of the node and the inclination, the remaining orbit elements are perturbed by the advanced model in largely the same fashion as the diffuse model. The amplitude of the variation in inclination is smaller in the advanced model, although generally of the same order. The perturbation in the node, however, is reduced noticeably by the utilization of the advanced model, as shown in Figure 5.18. It is clear that the torque on the orbit due to anisotropic and diurnally varying shortwave radiation is markedly different than that for diffuse Earth radiation. (See Section 3.3.2.)

The following table summarizes the trajectory comparison fits for the advanced and diffuse models for comparable one-year arcs of LAGEOS. All arcs have the same lighting conditions (7% shadow), initial epoch, and force model configurations. In order to present an accurate comparison, both the diffuse and advanced models employ four rings (61 Earth segments). Note that the inclusion of more Earth segments in the diffuse model increases the residual RMS by less than 10% over the values listed in table 3.4.

TABLE 5.3
EARTH RADIATION EFFECTS ON LAGEOS

model	Estimated Parameters	Percent Shadow	RMS of fit [m.]
diffuse, 4 rings	IC	7.	9.2
diffuse, 4 rings	IC, η_R	7.	9.2
diffuse, 4 rings	IC, C_T^* , η_R	7.	4.2
diffuse, 4 rings	IC, 1/rev C_T^* , η_R	7.	3.1
advanced, 4 rings	IC	7.	7.6
advanced, 4 rings	IC, η_R	7.	7.6
advanced, 4 rings	IC, C_T^* , η_R	7.	5.4
advanced, 4 rings	IC, 1/rev C_T^* , η_R	7.	3.8

* C_T : along track drag coefficient.

When only initial conditions are adjusted, the orbital perturbation due to advanced Earth radiation pressure is about 20% smaller than that produced by the diffuse model, as expected. However, it is clear that the advanced model produces a signal which is less "removable" by means of a single along track pseudo-drag term.

Even when a sinusoidally varying C_T is employed to simulate the effects of conventional drag, the advanced model shows a slightly higher total perturbation. This somewhat unexpected result suggests that advanced Earth radiation pressure may be more separable from other forces, drag in particular, than the diffuse model. Verification of this thesis would require the creation of converged arcs generated with the advanced model, for a number of different satellites. Given such a "library" of arcs, consider analyses and multisatellite solutions could be performed for the advanced model, just as they have been for the diffuse model.

5.3 Orbital Effects on GEOS-1

As indicated by the following table, trajectory comparisons for GEOS-1 reveal no unexpected differences in orbital perturbations between the diffuse and advanced models.

TABLE 5.4
EARTH RADIATION EFFECTS ON GEOS-1

model	Estimated Parameters	Percent Shadow	Transverse RMS [m.]
diffuse, 4 rings	IC	10.	37.0
diffuse, 4 rings	IC, C_D , η_R	10.	4.3
advanced, 4 rings	IC	10.	32.3
advanced, 4 rings	IC, C_D , η_R	10.	3.0

The effect of the advanced Earth radiation pressure model is, in all cases, less than that engendered by the diffuse representation. The estimation of a drag term does not change this conclusion, unlike the LAGEOS results.

The impact of the advanced model on real data suggests another qualitative difference between the diffuse and advanced models. In particular, there appears to be a marked change in the ability of shortwave Earth radiation pressure to alter the negative C_D values. The advanced Earth radiation pressure model *does not improve the drag coefficient estimates* during the 30 day arc examined in Section 3.3.3.1, even when a_0 is estimated. The correlation between the drag coefficients and the albedo parameters occurs only when the arc length is shortened. Analyses of the 10 day interval from 6-27-77 to 7-7-77, during which the orbit always intersects Earth's shadow at some point, reveal that the advanced and diffuse models behave similarly in their ability to drive the negative C_D estimates towards positive values. In fact, as the number of surface elements increases, the advanced model "outperforms" the diffuse model in this respect. Figure 5.20 illustrates the influence of diffuse and advanced Earth radiation pressure on the C_D estimates for increasing Earth segment numbers. The estimated values of a_0 in all cases are quite large, and, as one might expect, the use of the advanced model leads to even larger values of a_0 . Clearly, however, the same eclipse-driven Earth radiation pressure imbalance which leads to a significant along-track acceleration is present in both the diffuse and advanced models.

Given that the cause of the negative C_D 's for GEOS-1 is still uncertain, it is difficult as yet to evaluate the "unusual" behavior of the advanced model. If it is ultimately demonstrated that the negative C_D values are not due to Earth radiation

pressure, then the signal separation between drag and Earth radiation pressure could be seen as favorable. This also has implications regarding the general separability of Earth radiation pressure from other forces. Once again, a more complete analysis of this question must await the development of a number of experimental square root information matrices generated with the advanced model.

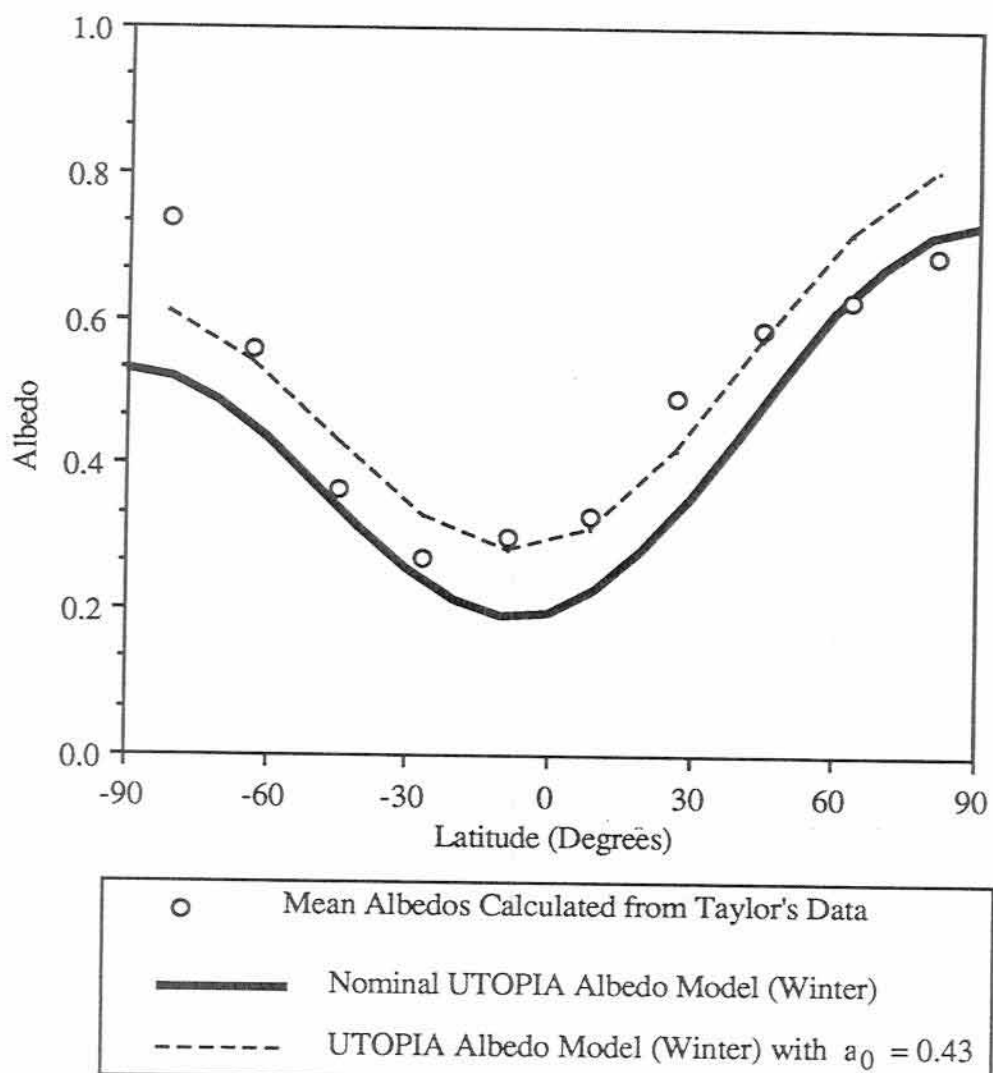


Fig. 5.1
UTOPIA Albedo Model vs. Mean Albedos from Taylor's Data

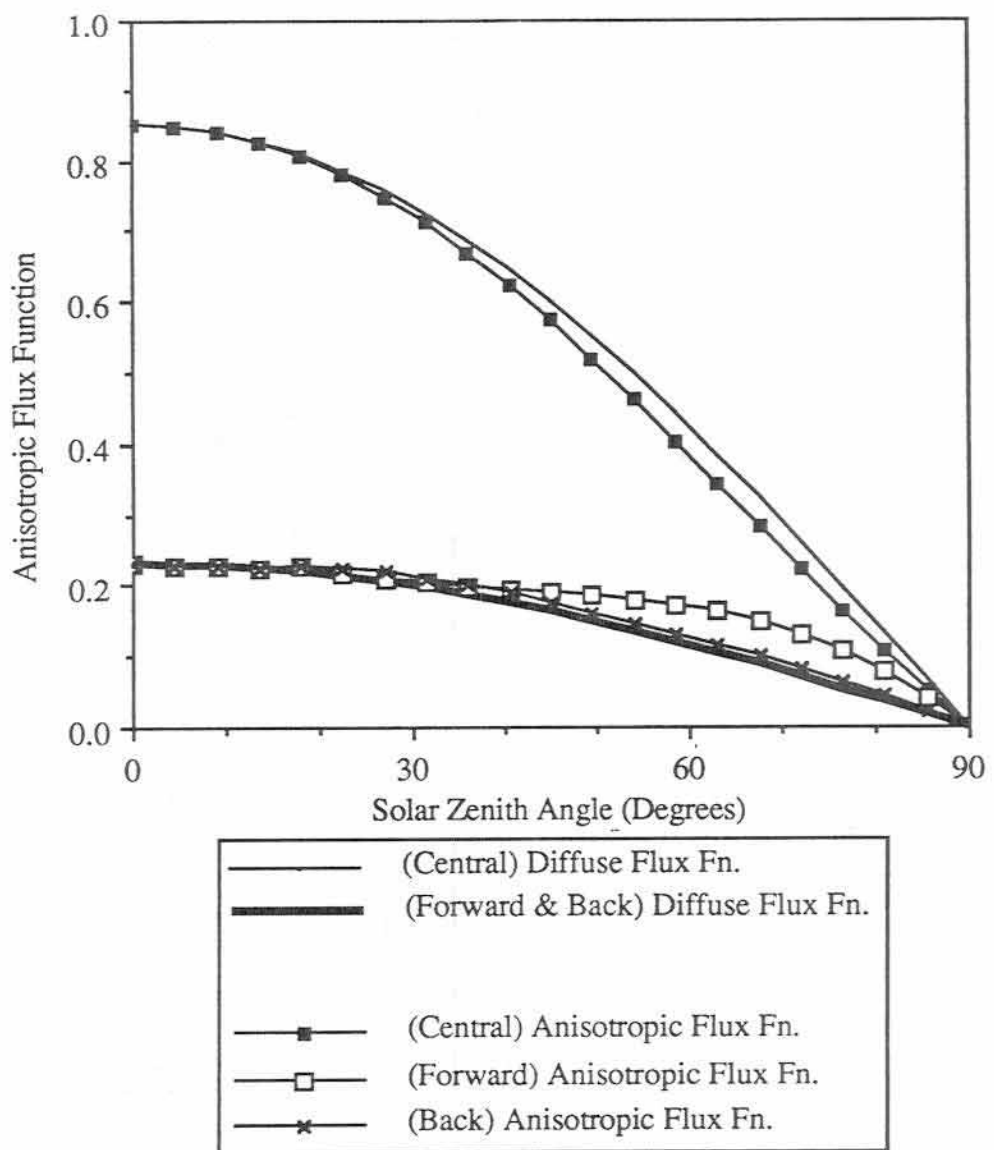


Fig. 5.2
Anisotropic Flux Functions

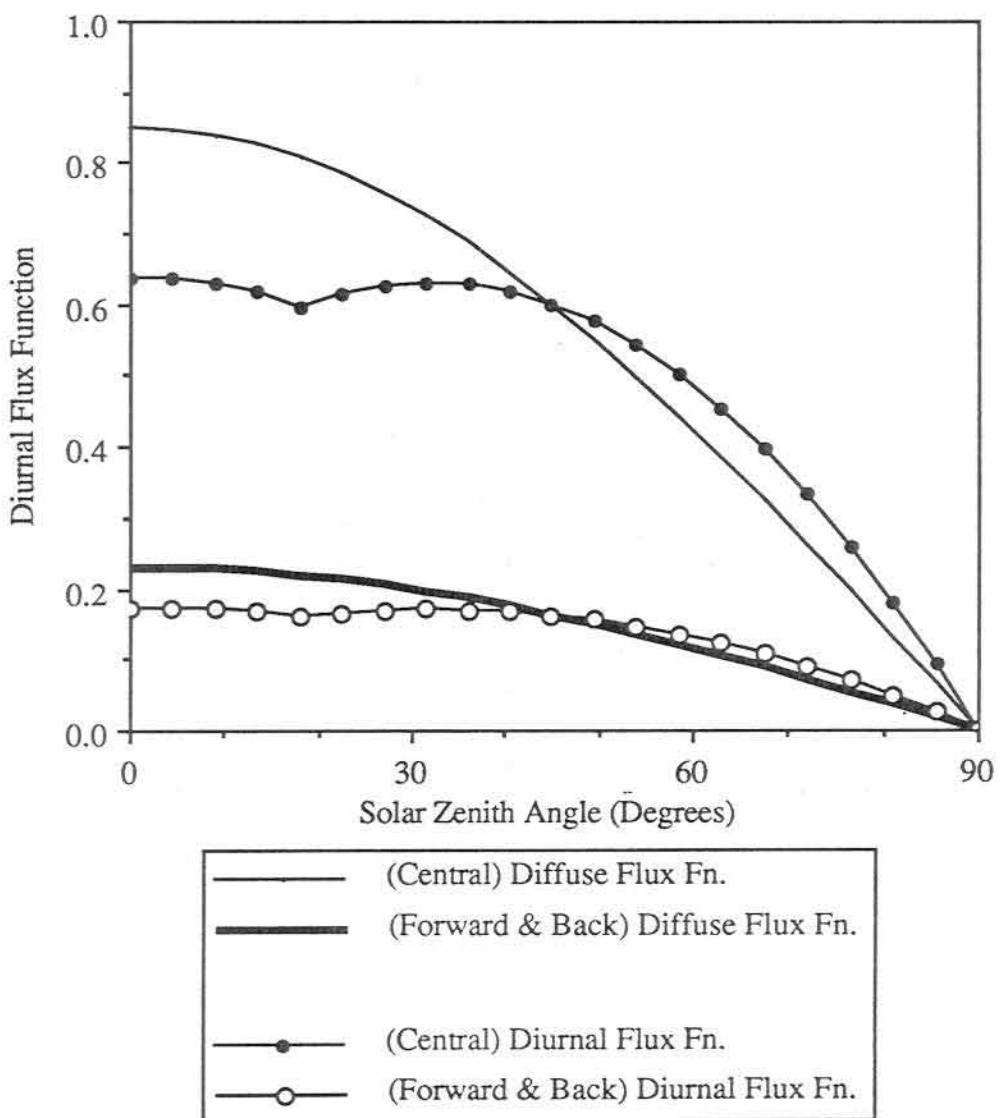


Fig. 5.3
Diurnal Flux Functions

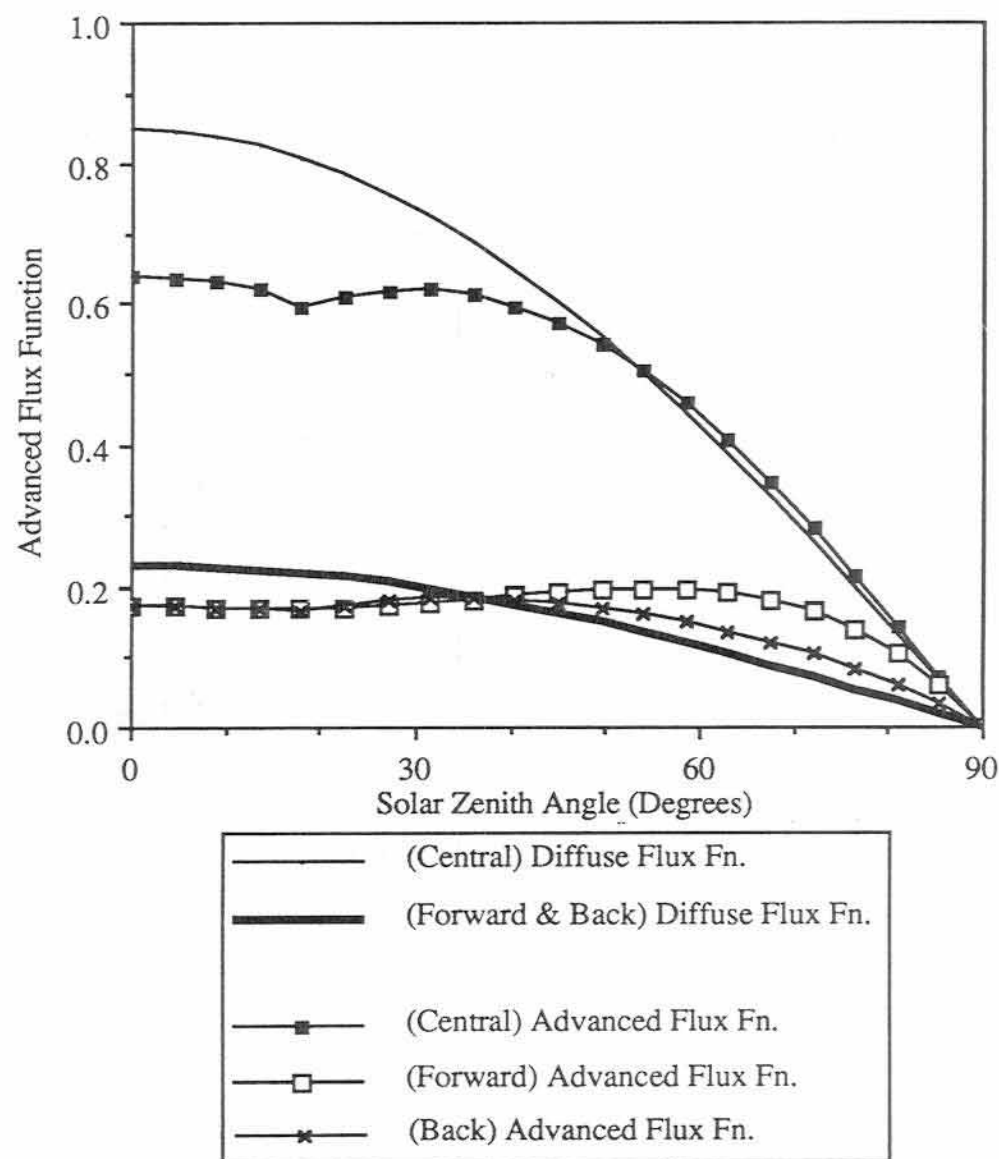


Fig. 5.4
Anisotropic / Diurnal Flux Functions

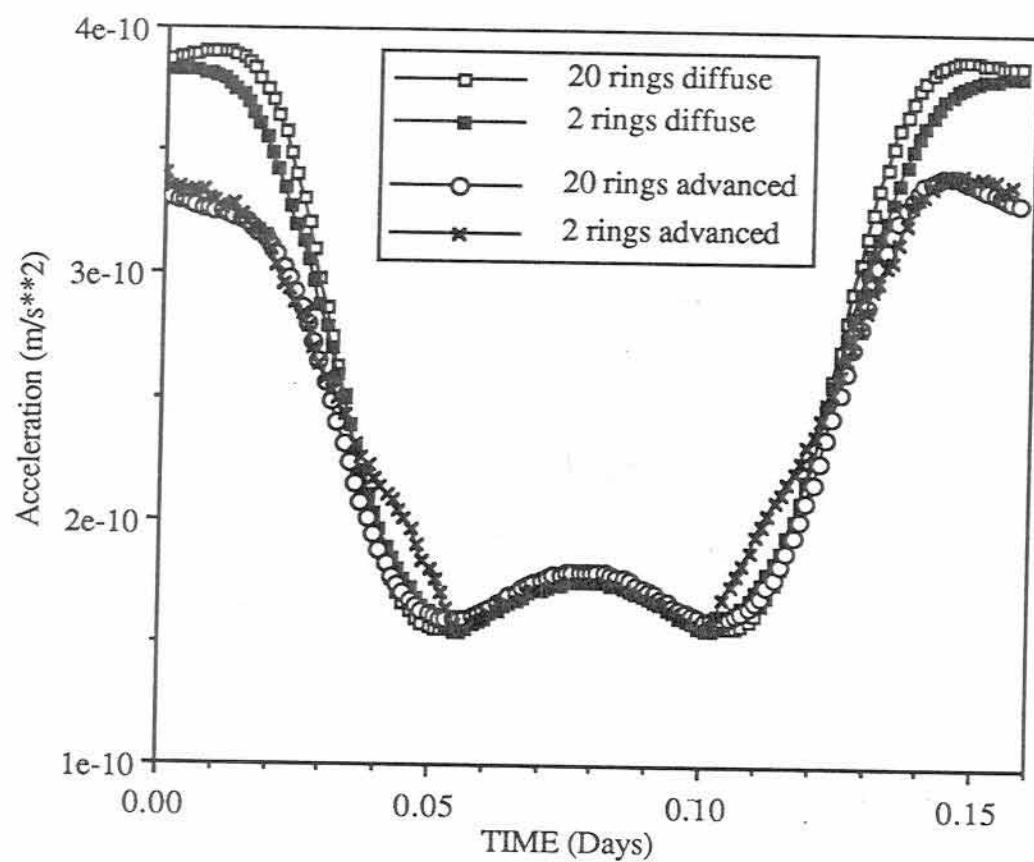


Fig. 5.5
Radial Component of Earth Radiation Acceleration on LAGEOS:
Advanced and Diffuse Models

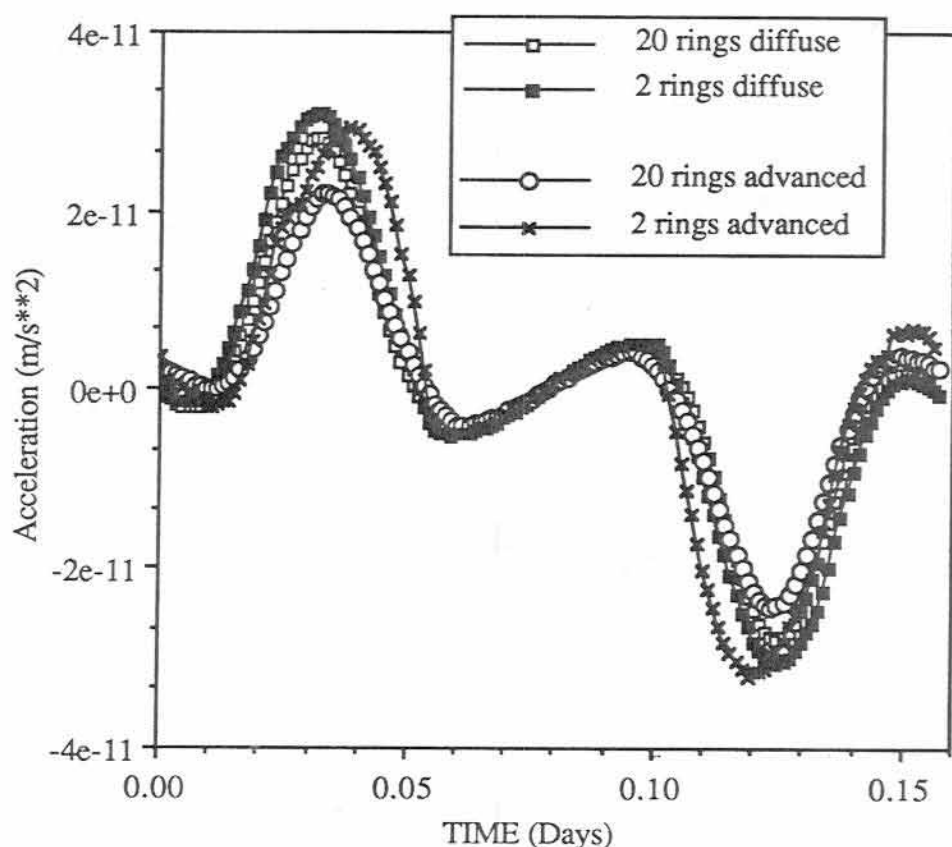


Fig. 5.6

Transverse Component of Earth Radiation Acceleration on LAGEOS:
Advanced and Diffuse Models

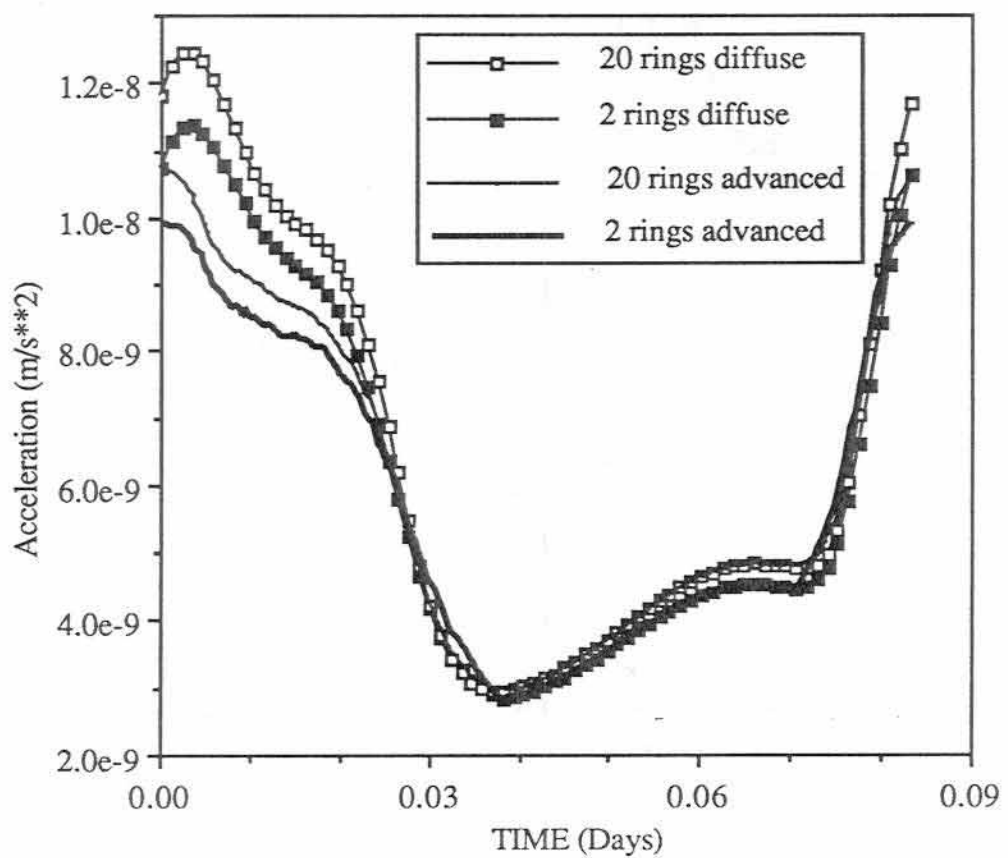


Fig. 5.7

Advanced and Diffuse Earth Radiation Acceleration: Radial Component

GEOS-1, 6-27-77

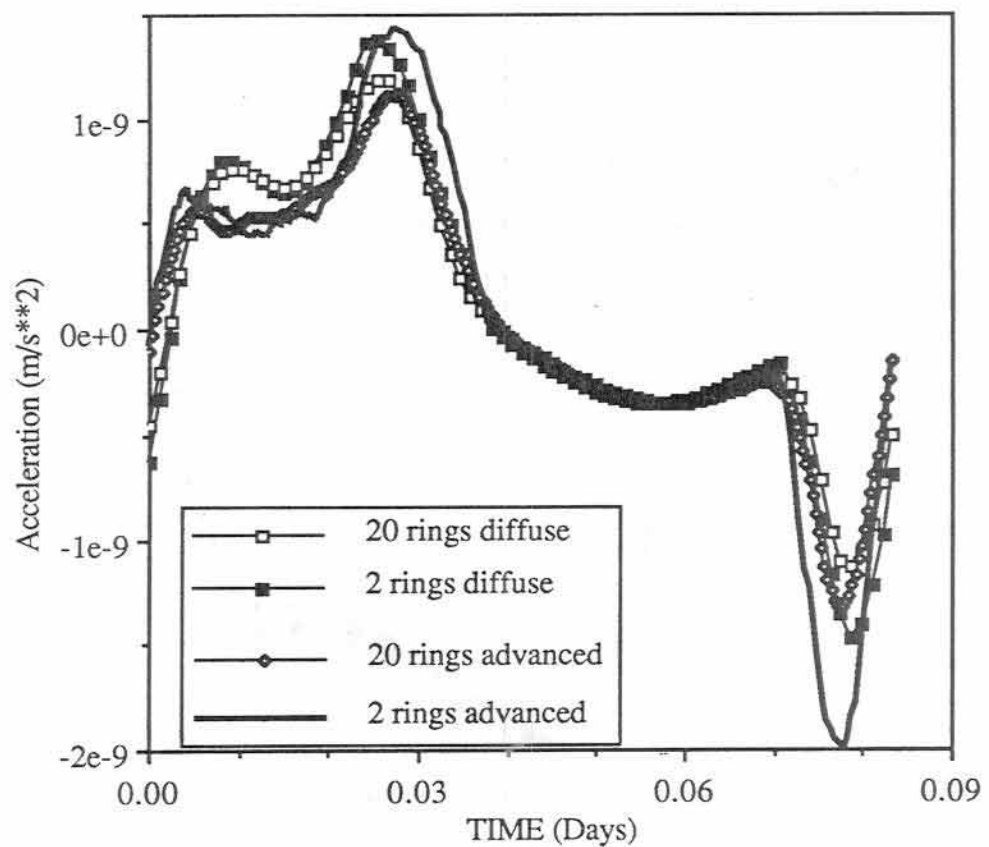


Fig. 5.8

Advanced and Diffuse Earth Radiation Acceleration: Along-Track Component

GEOS-1, 6-27-77

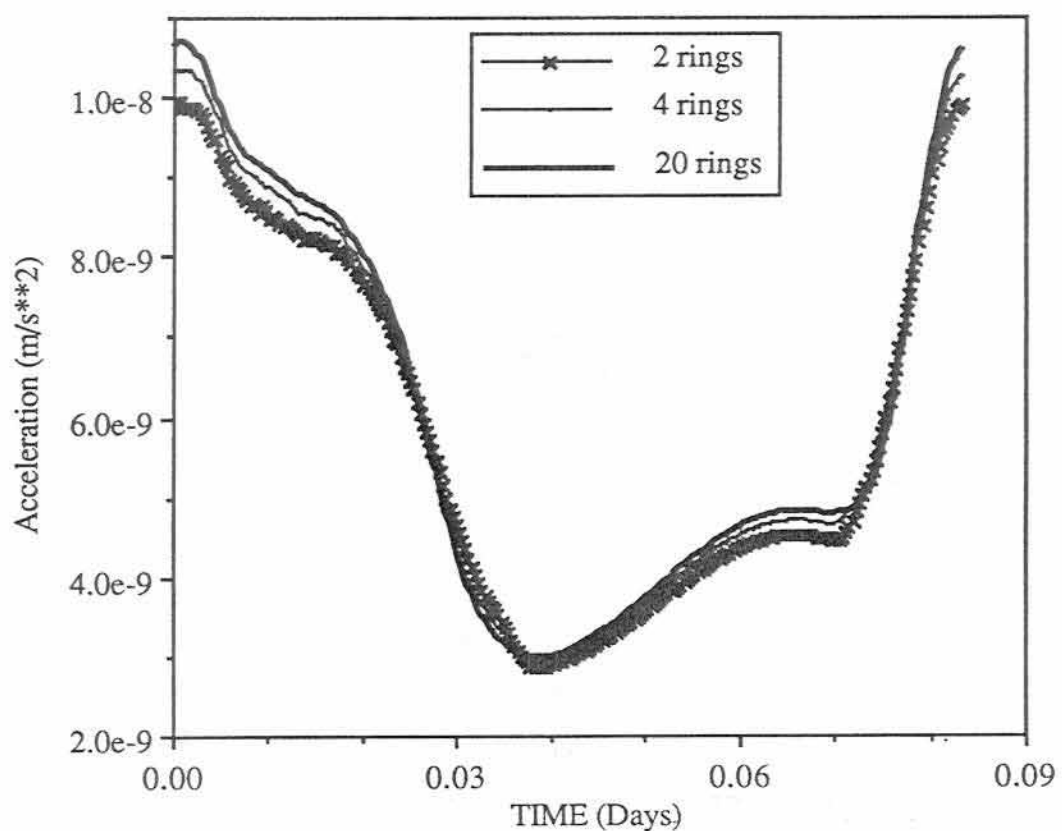


Fig. 5.9

Advanced Earth Radiation Acceleration: Radial Component

GEOS-1, 6-27-77

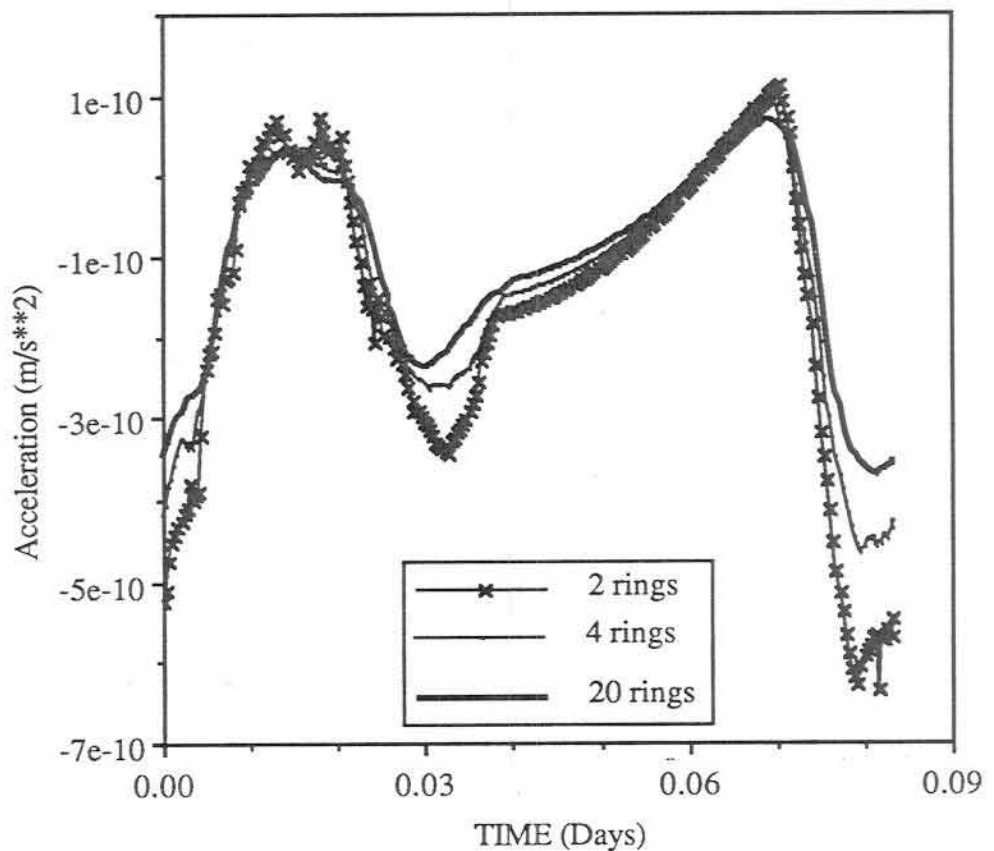


Fig. 5.10

Advanced Earth Radiation Acceleration: Normal Component

GEOS-1, 6-27-77

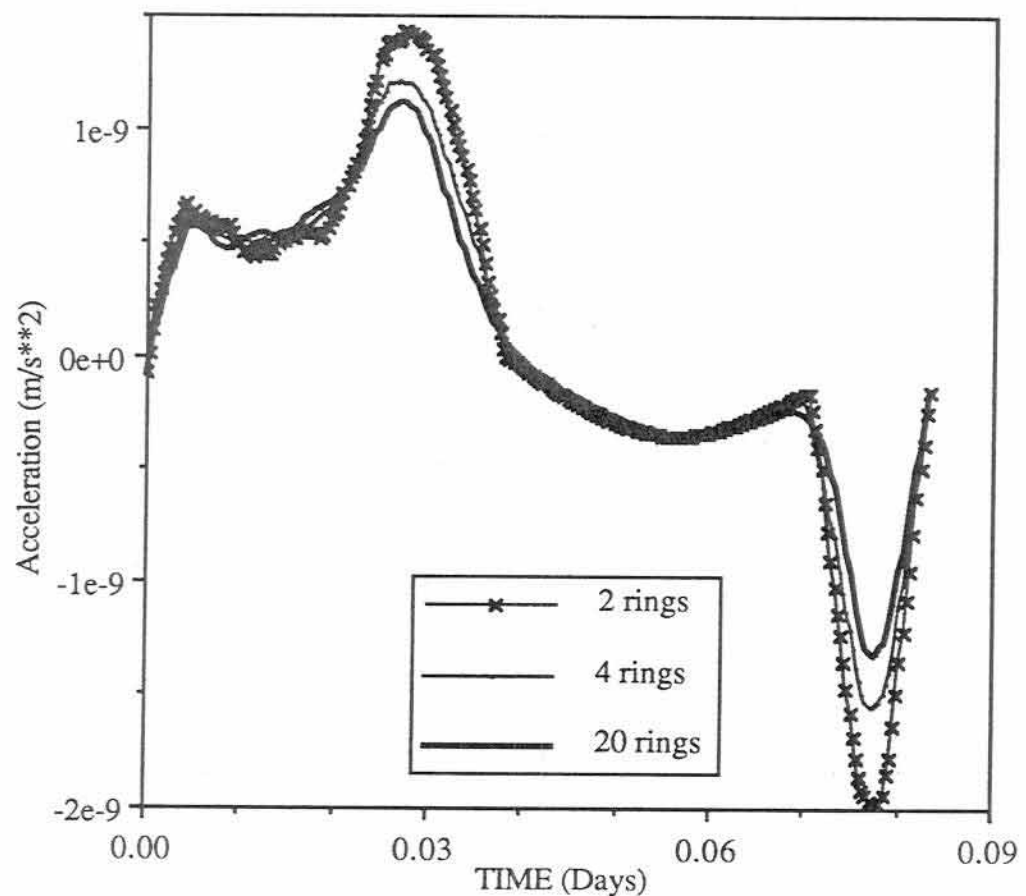


Fig. 5.11

Advanced Earth Radiation Acceleration: Along-Track Component

GEOS-1, 6-27-77

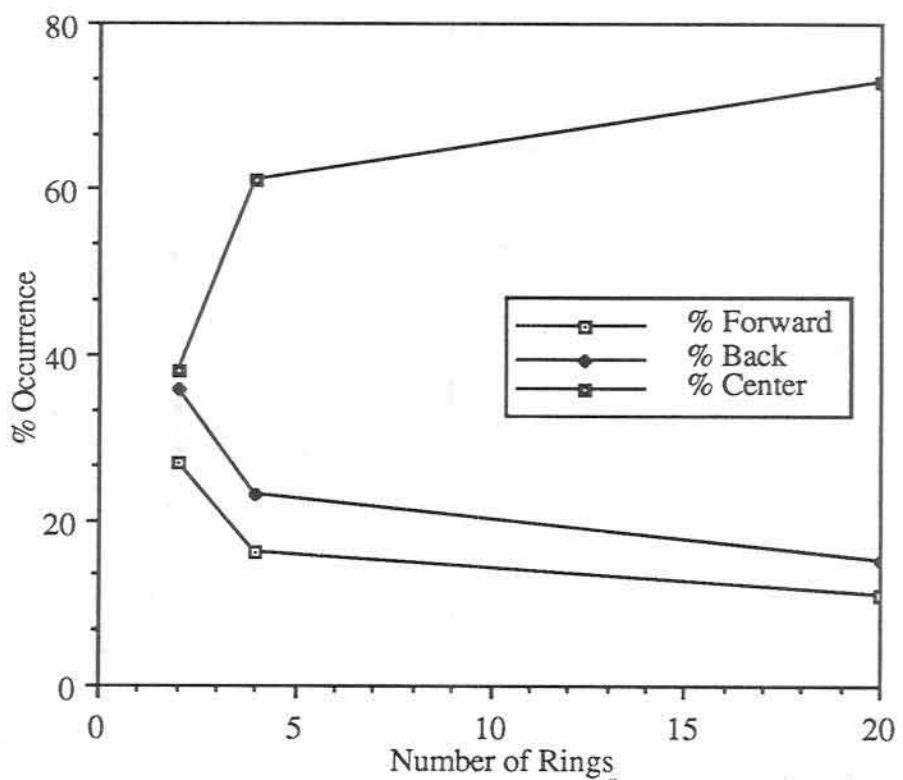


Fig. 5.12
Occurrences of Anisotropic Factors for GEOS-1
Percentage of Total vs. Number of Rings

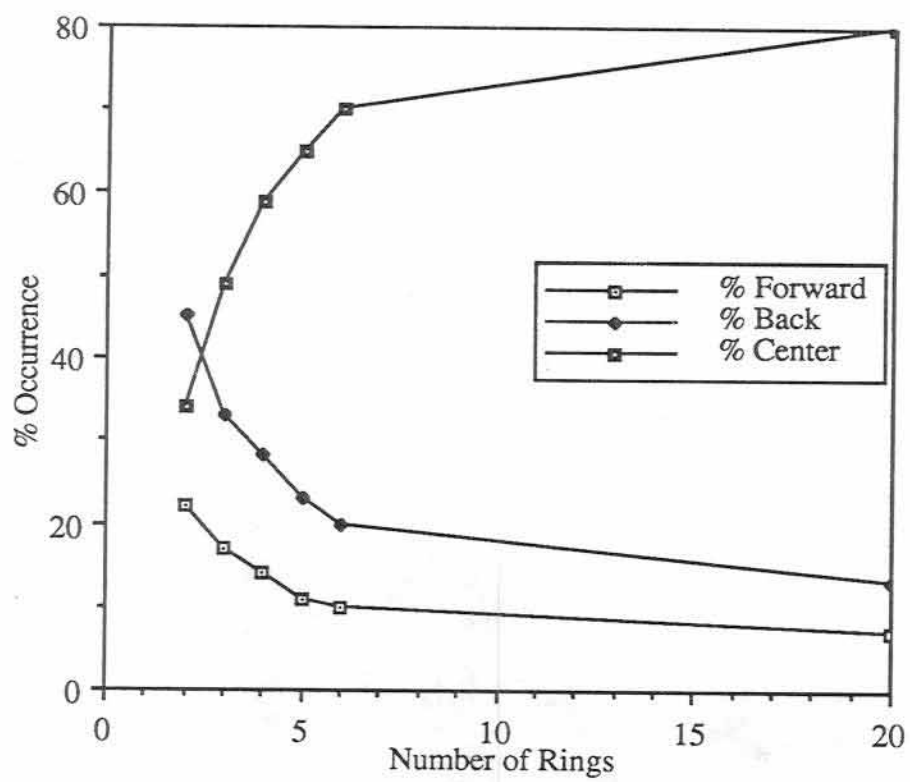


Fig. 5.13
Occurrences of Anisotropic Factors for LAGEOS
Percentage of Total vs. Number of Rings

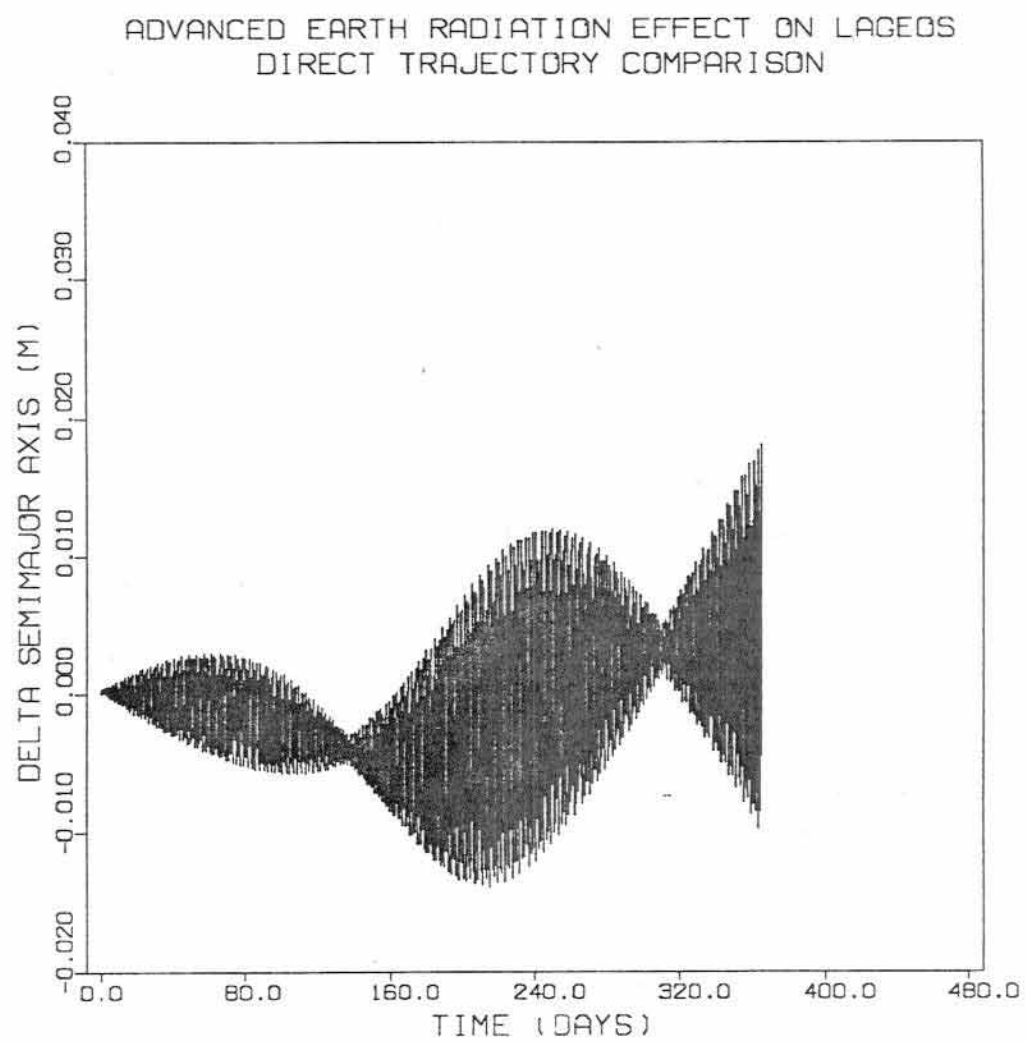


Fig. 5.14
Advanced Earth Radiation Effect on LAGEOS:
Change in the Semimajor Axis

ADVANCED EARTH RADIATION EFFECT ON LAGEOS
DIRECT TRAJECTORY COMPARISON

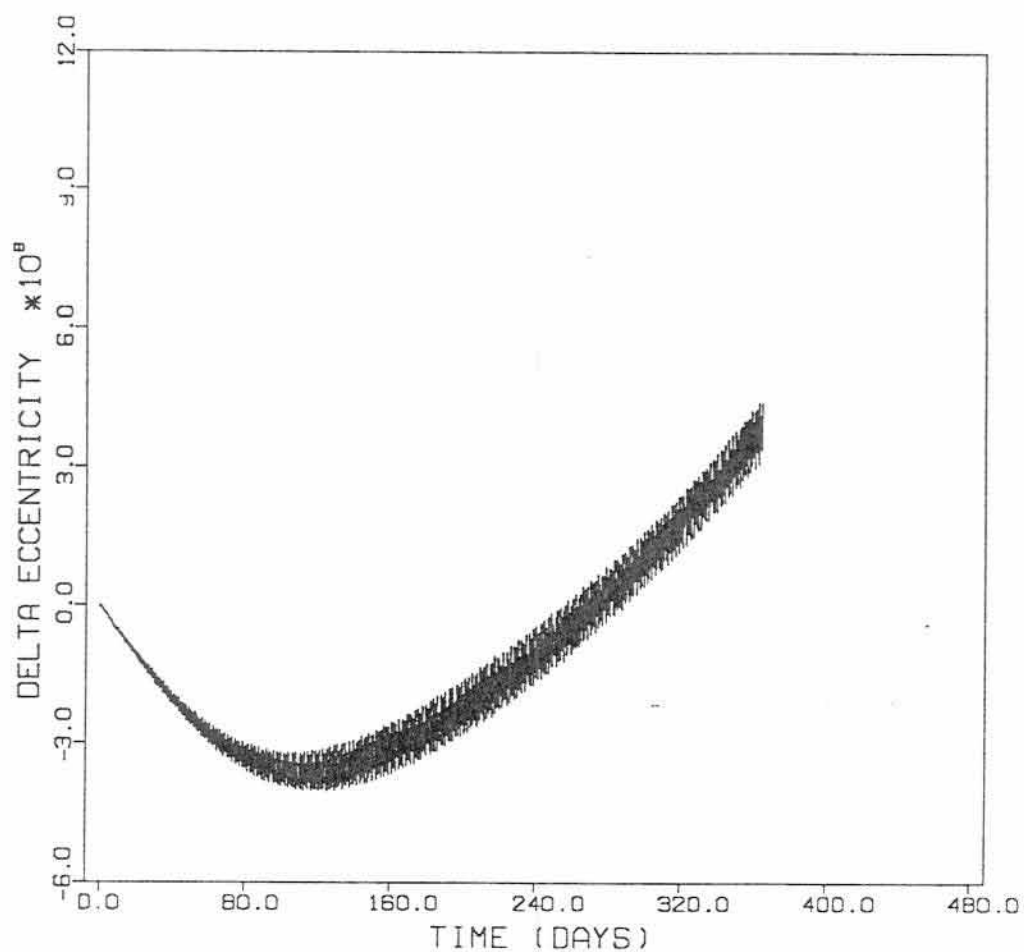


Fig. 5.15
Advanced Earth Radiation Effect on LAGEOS:
Change in the Eccentricity

ADVANCED EARTH RADIATION EFFECT ON LAGEOS
DIRECT TRAJECTORY COMPARISON

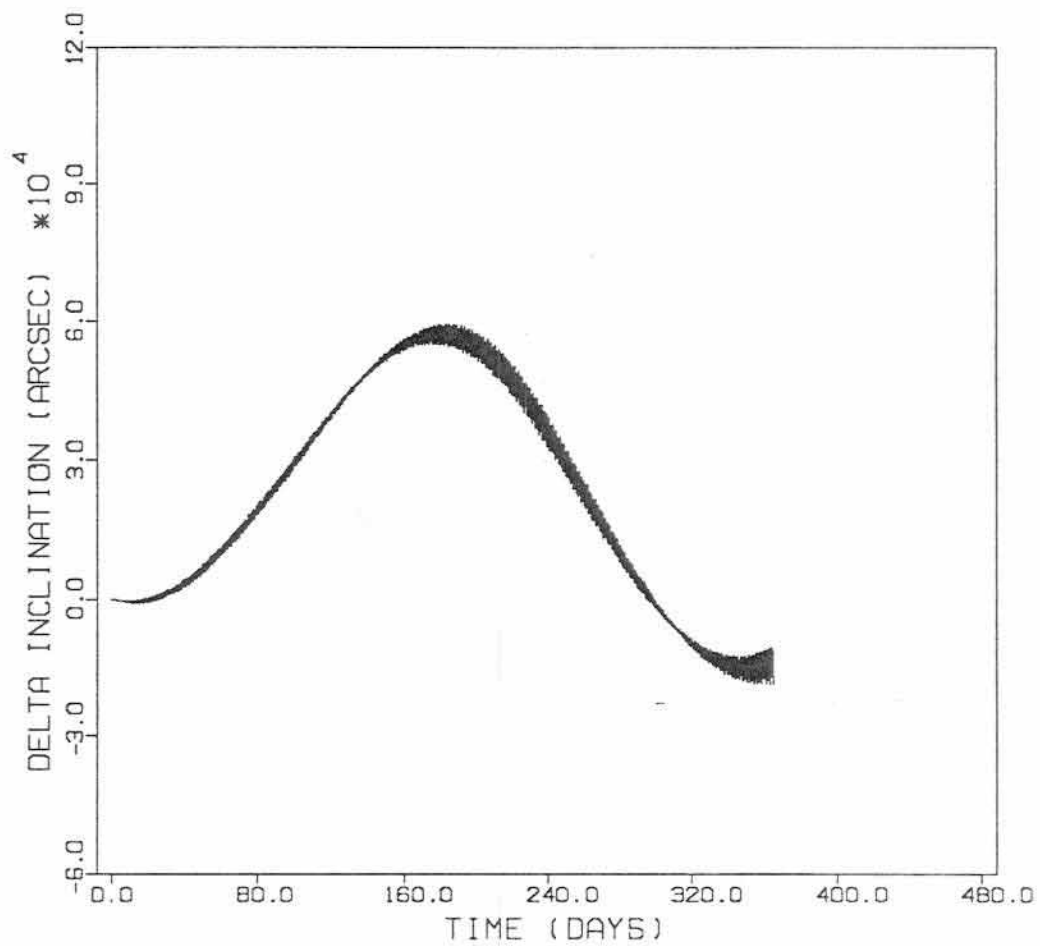


Fig. 5.16
Advanced Earth Radiation Effect on LAGEOS:
Change in the Inclination

ADVANCED EARTH RADIATION EFFECT ON LAGEOS
DIRECT TRAJECTORY COMPARISON

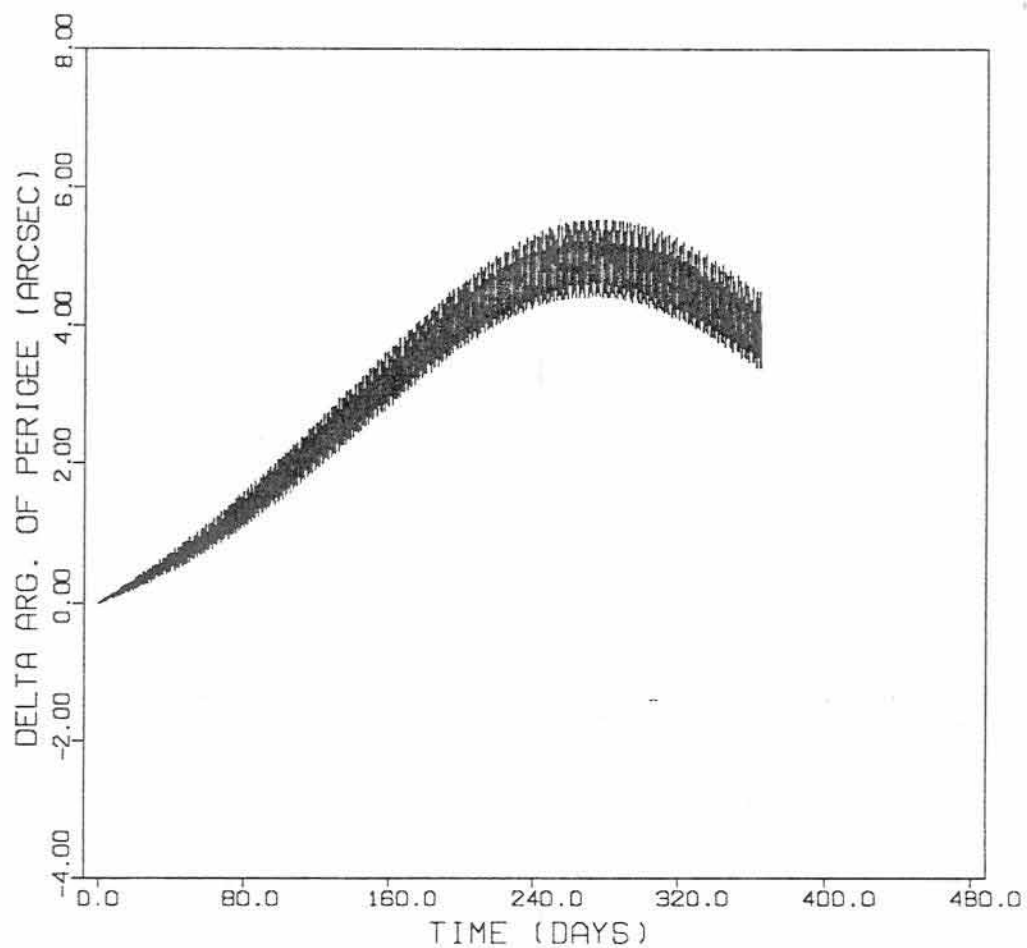


Fig. 5.17

Advanced Earth Radiation Effect on LAGEOS:
Change in the Argument of Perigee

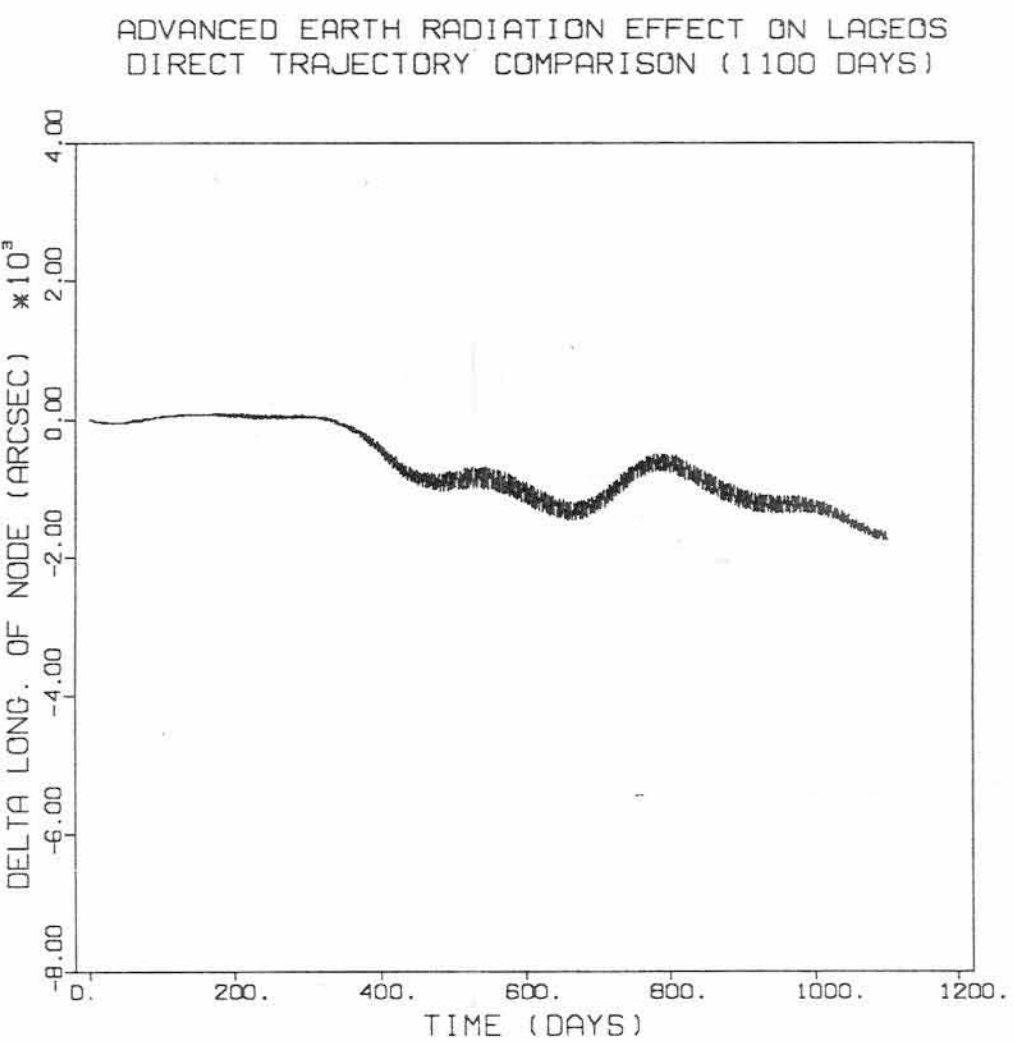


Fig. 5.18

Advanced Earth Radiation Effect on LAGEOS:
Change in the Node for a 1100 Day Arc

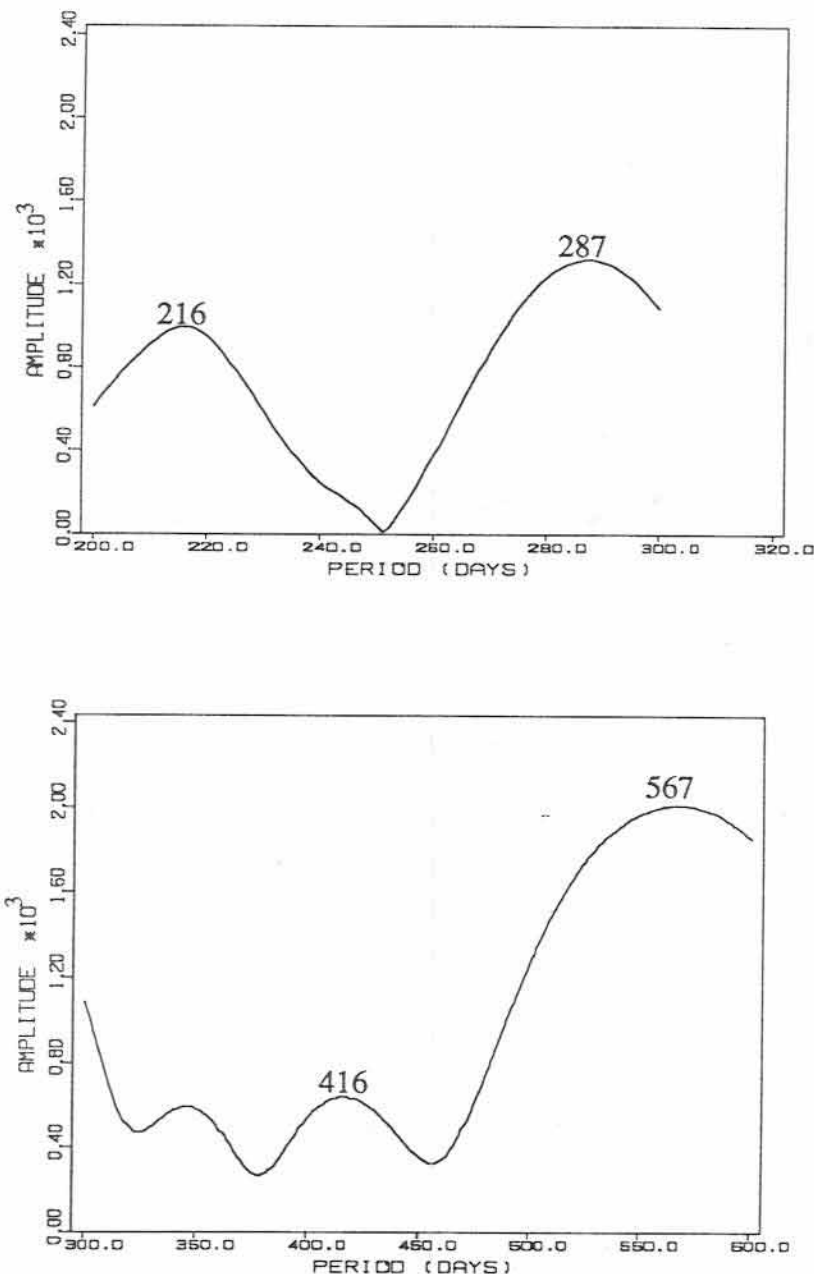


Fig. 5.19

Periodogram of Change in the Semimajor Axis of LAGEOS

2100 Day Trajectory Comparison, Advanced Model, Estimating IC, C_T, η_R

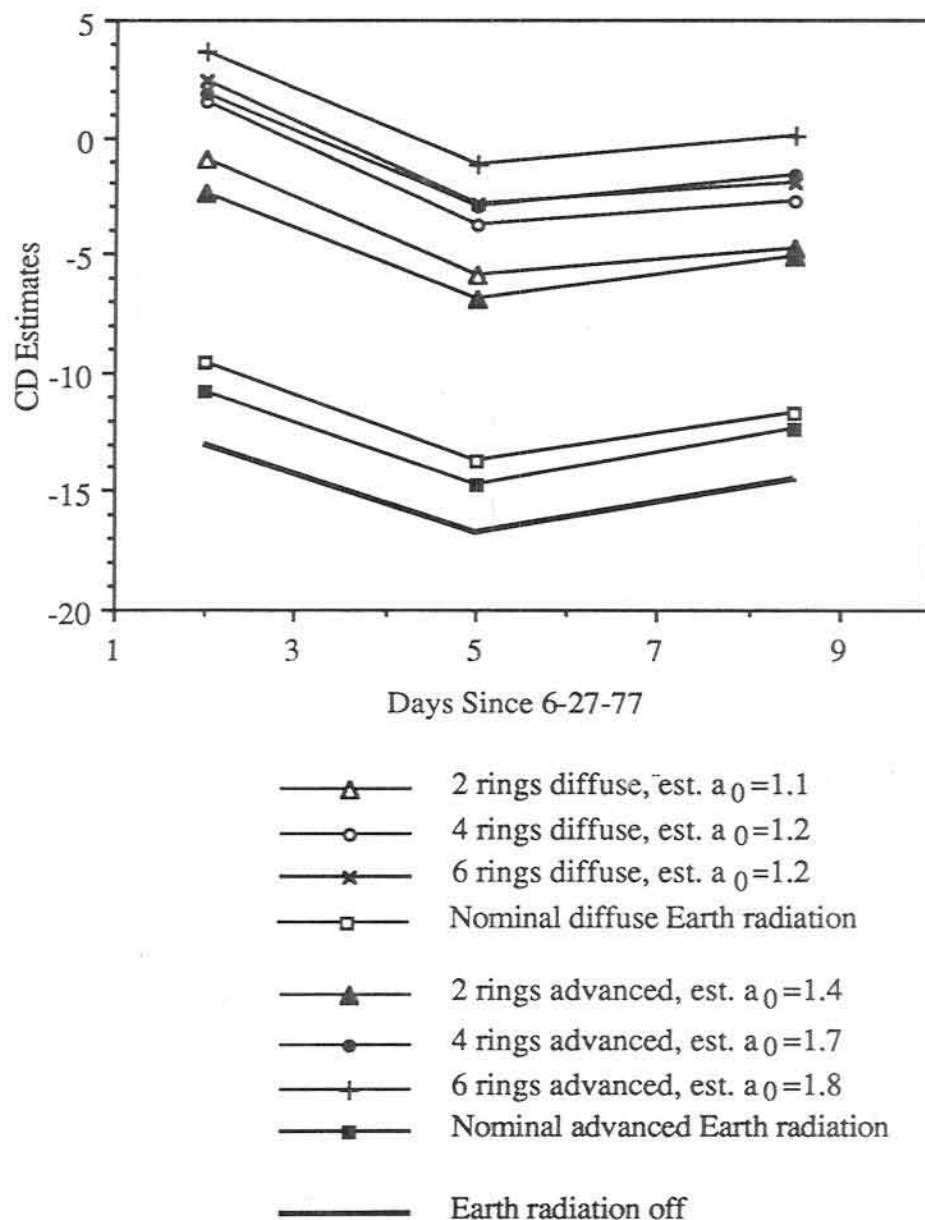


Fig. 5.20
Effects of Advanced and Diffuse Earth Radiation
on GEOS-1 C_D Estimates

CHAPTER 6

CONCLUSIONS

6.1 *Diffuse Earth Radiation Pressure*

A diffuse Earth radiation pressure model has been developed which is efficient, generally applicable, and appropriate in the context of orbit determination studies. It may be applied to any satellite, regardless of altitude, inclination, or eccentricity, and includes a seasonally varying representation of zonal emissivity and zonal albedo. It can be easily modified to embrace any albedo model which is capable of expression in terms of spherical harmonic coefficients.

Returning to the provenance of this study, it would appear that diffuse Earth radiation is unable to explain the anomalous residual behavior of LAGEOS' semimajor axis. The along track force on LAGEOS due to diffuse Earth emanations is simply too small, by at least an order of magnitude, to produce the observed secular trend in the semimajor axis, or any significant portion of the large periodic variations about this mean. Recent analyses indicate that the likely cause of the residual deceleration of LAGEOS is due, at least in part, to the "Yarkovsky effect", a variety of delayed thermal thrust described in *Rubincam* [1987] and *Rubincam* [1988].

In the broader sense, it is evident that the orbital effects of diffuse Earth radiation pressure are small but not always negligible. When the eccentricity of the

satellite's orbit is small, the orbit elements are, with the exception of the node, affected by small amplitude, long period perturbations. The longitude of the ascending node is affected by a very small secular change, which is driven to a similar degree by both the shortwave and longwave components of Earth radiation. The overall behavior is that of a uniform decrease in the node, due to longwave radiation, modulated by periodic variations induced by the shortwave radiation. The node rate is small, on the order of (10^{-3}) arcsecond per year.

High eccentricity satellites are particularly sensitive to Earth radiation pressure, especially during periods of deep eclipse. During such events, sizeable along-track accelerations or decelerations develop which do not average out in the course of an orbit. The magnitudes of drag coefficients estimated for GEOS-1 and GEOS-2 are dramatically influenced by diffuse Earth radiation pressure. The presence of diffuse Earth radiation pressure drives the drag coefficients towards a more physically reasonable level. As suggested by *Prior* [1970], this phenomenon can be of importance in the accurate determination of density estimates.

An effort has been made to estimate the albedo parameters through observations of satellite motion. The mean albedo term and the second degree albedo term are recoverable from LAGEOS data alone, if solar reflectivities are not allowed to adjust. Clearly, the estimation of solar reflectivities can adversely affect the recovery of shortwave Earth radiation parameters. The LAGEOS-only solution yields a very large value for c_0 , the term which represents the constant hemispherical offset of albedo. The inclusion of additional satellite data alters the estimates of this term, although c_0 remains difficult to estimate. This seminal attempt to estimate albedo parameters from a multisatellite solution demonstrates the

possible uses of geodetic constellations in the determination of the Earth's albedo. This analysis also indicates that the accurate recovery of the albedo terms is strongly influenced by errors in the odd degree zonals, and more weakly affected by some tide parameters. Likewise, consider analysis indicates that errors in the albedo parameters can affect the accurate estimation of the odd degree zonals and the high degree once-per day terms in the geopotential.

The extreme once per orbit variability of the shortwave component causes it to have a much greater influence on overall satellite perturbations than the nearly constant longwave radiation. Only the node appears to be strongly affected by longwave radiation, in particular the e_2 constituent.

A preliminary 4×4 albedo field has been evaluated for use with the diffuse Earth radiation pressure representation, and compared to the nominal second degree zonal model. The higher degree and order albedo field does not greatly influence the resulting orbital perturbations.

6.2 Anisotropic and Diurnally Varying Earth Radiation Pressure

An advanced Earth radiation pressure model which incorporates the known nondiffuse and diurnally variant properties of terrestrial shortwave radiation has been developed. This model is based on actual satellite radiance data, and is free of the shortcomings associated with assumed forms or theories of reflection. In addition, the model is unbiased, i.e. it introduces no concealed perturbations on the mean albedo values. In the presence of a truly unbiased estimate of mean albedo, this model realistically simulates the first order effects of directional reflectance and

short-periodic albedo variation. For anisotropy, these first order effects are: strong forward scatter, weaker back scatter, and depressed central scatter. The diurnal variation in albedo causes the hemispherical reflectivity of all Earth surface elements to increase as solar zenith angle increases.

Assuming an effectively unbiased mean albedo model, the use of an anisotropic and diurnally varying shortwave radiation model generally induces a smaller effect on the orbits of satellites than does a diffuse representation. The reason for this is the diurnal variation in albedo. When the illumination level is highest, i.e. when the solar zenith distance is at a minimum, the instantaneous albedo is less than the mean albedo. High albedo values occur only near sunrise and sunset, when the incident radiation is meager. The net result is a decrease in the maximum Earth radiation pressure exerted on a satellite. This leads to a reduction in the magnitude of the orbital perturbations, a conclusion which is born out by trajectory comparisons and analyses of real data. (In fact, a reasonable fraction of the effects of anisotropy and diurnal albedo variations can be absorbed by merely using a smaller value of the mean albedo.) The only contradiction to this general rule is the small increase in the residual RMS for LAGEOS, when a drag coefficient is estimated. This may represent a greater separability between the advanced Earth radiation pressure model and competing force effects.

The influence of anisotropy and diurnal albedo variations on the node of LAGEOS is significantly smaller than that predicted by the diffuse model. The orbital torque generated by the advanced model leads to much smaller node rates. In terms of perturbations on the semimajor axis of LAGEOS, the advanced model recovers the expected solar geometry periodicities with greater fidelity than the diffuse model.

The tendency of Earth radiation pressure to generate significant along-track accelerations on a high eccentricity spacecraft is modified somewhat by the advanced model. When anisotropy and diurnal albedo variations are included, the correlation between negative C_D values for GEOS-1 and Earth radiation parameters exists only during eclipse. When the arc is extended, the correlation disappears, again suggesting that the advanced Earth radiation pressure model may be inherently easier to separate from solar pressure and drag.

6.3 Recommendations for Further Study

Perhaps the most important single improvement in the realm of Earth radiation pressure has little to do with the calculation of the force itself. Specifically, as broadband shortwave radiometer data become more prevalent, the development of a truly unbiased mean albedo model for the Earth becomes more likely. The development of such a model is largely in the hands of remote sensing experts. It remains for force model engineers and others who require this information to express a need for specific types of data reduction, such as those performed by Rich Hucek, Philip Ardanuy, and V. Ray Taylor in support of this study. The burgeoning satellite radiometer data base also holds the hope of improving models of anisotropy and the diurnal variation in albedo. A problem with the Nimbus-7/STRT data base is its lack of coverage near the equator and its relatively short time span.

Both the diffuse and advanced models have a role in the further study of planetary radiation pressure. Quite apart from its role in advanced Earth radiation

calculations, the diffuse model is simpler and faster. It may prove useful for a wide range of studies in which the details of Earth radiation pressure are less important than computational efficiency and a rough knowledge of its effects. In addition, the diffuse model may be quite accurate enough for detailed studies of radiation pressure on non-terrestrial orbiters. The Earth's complex radiative interaction is due in large part to the presence of a transparent atmosphere. Planetary bodies with no atmosphere or opaque atmospheres offer especially promising venues for the use of the diffuse model, although *Baker* [1966] indicates that the Moon is a strong backscatterer.

The study of Venus radiation pressure may be of significance during the upcoming Magellan planetary probe. Magellan is currently targeted for a highly eccentric orbit about Venus. The known sensitivity of high eccentricity orbits to planetary radiation pressure, coupled with the large diffuse radiative flux of Venus, suggests that eclipsing trajectories of Magellan may experience along track forces similar to those sensed with GEOS-1.

Further analysis of advanced Earth radiation pressure requires a major enterprise: the development of a library of converged arcs generated with this force model. In light of the arguably small impact of Earth radiation pressure in the context of most estimation tasks, the similar behavior of the advanced and diffuse models, and the higher computational overhead required to simulate anisotropy and diurnal albedo variations, such an enterprise is not currently envisioned. Given the increasingly stringent requirements of precision orbit determination, however, such an undertaking may someday be more desirable. The advanced model may soon be necessary for both the accurate estimation of Earth radiation parameters from orbit

observations, and the accurate determination of various force effects and geophysical coefficients.

APPENDIX A

EARTH RADIATION PRESSURE ALGORITHM

The following algorithm describes the method nominally used to calculate the earth radiation pressure acceleration on a spacecraft. For the sake of comprehension, some of the actual calculations performed in UTOPIA are replaced by equivalent simplified or condensed expressions. For example, the albedo and emissivity calculations are listed explicitly in this summary. In reality, a separate subroutine is used to perform similar calculations in UTOPIA. Another simplification involves \vec{R}_{Ej} , the calculation of which is represented as a single expression, and the geometry of which is illustrated in Figure A.2. In the UTOPIA implementation, a more efficient recursive expression is utilized.

The derivation of elements of this algorithm is described in Chapter 2.

- I. Required Information:* satellite position and velocity: \vec{r}_s, \vec{v}_s
satellite parameters: η_E, A_C, m
solar position and distance: $\vec{r}_{\text{sun}}, r_{\text{sun}}, \vec{r}_{\text{EARTH}}$
number of earth surface rings: n_{ring}
- II. Calculate total number of ring elements:* $N = 1+6+12+\dots+6 n_{\text{ring}}$
- III. Calculate $\hat{r}_{\text{sun}}, \hat{r}_s, E_S/mc$, and M_B/mc*
- IV. Calculate limits of earth surface visible from satellite (see Fig. A.1):*
$$\zeta_M = \sin^{-1} (R_E / r_s)$$

$$\beta_{n_{ring}+1} = \beta_M = \pi/2 - \zeta_M$$

V. Calculate limits of central cap:

$$\zeta_1 = \cos^{-1}[(N - 1 + \cos \zeta_M)/N]$$

$$\gamma_1 = \sin^{-1} [(r_S \sin \zeta_1)/R_E]$$

$$\beta_1 = \gamma_1 - \zeta_1$$

VI. Calculate remaining ring boundaries:

Do 10 i = 2, ... n_{ring}:

$$k = k + 6 (i-1),$$

$$\cos(\zeta_i) = k \cos \zeta_1 - k + 1$$

$$\gamma_i = \sin^{-1} [(r_S \sin \zeta_i)/R_E]$$

$$10 \quad \beta_i = \gamma_i - \zeta_i$$

VII. Calculate ring centers:

Do 20 i = 2, ... n_{ring} + 1:

$$20 \quad \beta_i^* = (\beta_i + \beta_{i-1})/2$$

VIII. Calculate radiation pressure due to central cap:

$$A' = 2(1 - \cos \zeta_1)$$

$$\cos \theta_S = \hat{r}_S \cdot \hat{r}_{sun} \quad \{ \text{if } \cos \theta_S < 0, \text{ reset } \cos \theta_S = 0. \}$$

$$\phi = \sin^{-1}(\hat{Z} \cdot \hat{r}_S),$$

where \hat{Z} = normal to the earth's equator.

$$a = a_0 + a_1 P_1(\sin \phi) + a_2 P_2(\sin \phi)$$

$$e = e_0 + e_1 P_1(\sin \phi) + e_2 P_2(\sin \phi)$$

$$\text{FLUXOP} = A'(1+\eta) A_c E_S / mc$$

$$\text{FLUXIR} = A'(1+\eta) A_c M_B / mc$$

$$\vec{da} = (a * \text{FLUXOP} * \cos \theta_S + e * \text{FLUXIR}) \hat{r}_S$$

IX. Accumulate contribution from each ring:

Do 140 $i = 2, \dots n_{ring} + 1$:

$$N_{S_i} = 6(i - 1)$$

$$r = \sqrt{R_E^2 + r_S^2 - 2 R_E r_S \cos \beta_i^*}$$

Compute vector to segment center:

Do 140 $j = 1, \dots N_{S_i}$:

$$\vec{R}_{Ej} = R_E \cos \beta_i^* \hat{R} + R_E \sin \beta_i^* (\cos \lambda_j \hat{T} + \sin \lambda_j \hat{N}),$$

where $\hat{R}, \hat{T}, \hat{N}$ = radial, transverse, and normal coordinates

λ_j = relative "azimuth" of element (Figure A.2)

Transform \vec{R}_{Ej} into inertial coordinates.

$$\hat{R}_{Ej} = \vec{R}_{Ej}/R_E$$

$$\vec{r}_j = \vec{r}_S - \vec{R}_{Ej}$$

$$\hat{r}_j = \vec{r}_j / r$$

Accumulate accelerations due to this segment:

$$\phi = \sin^{-1}(\hat{Z} \cdot \hat{R}_E)$$

$$a = a_0 + a_1 P_1(\sin \phi) + a_2 P_2(\sin \phi)$$

$$e = e_0 + e_1 P_1(\sin \phi) + e_2 P_2(\sin \phi)$$

$$\cos \theta_S = \hat{R}_E \cdot \hat{r}_{sun} \quad \{ \text{if } \cos \theta_S < 0, \text{ reset } \cos \theta_S = 0. \}$$

$$\vec{da} = \vec{da} + (a * \text{FLUXOP} * \cos \theta_S + e * \text{FLUXIR}) \hat{r}_j$$

140 CONTINUE

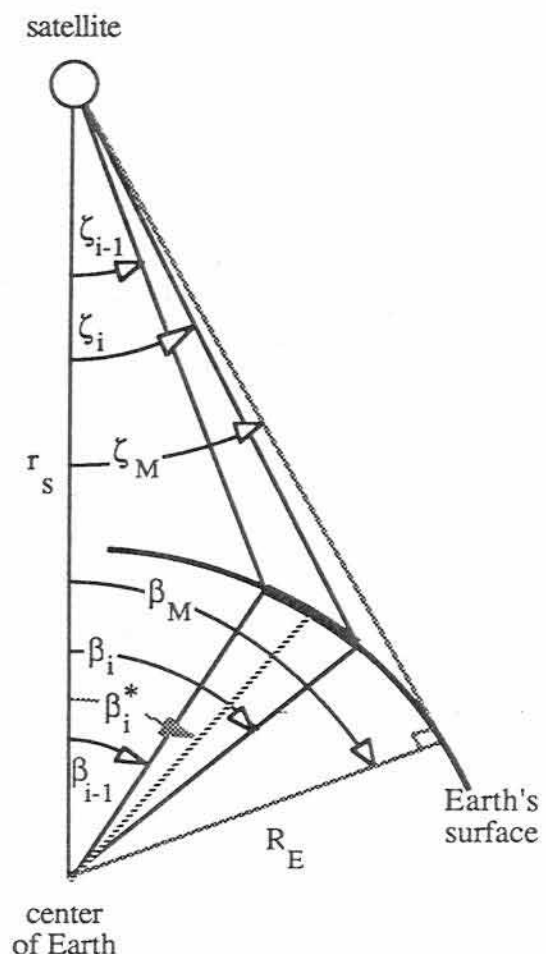


Fig. A.1
Geometry of Ring Calculations

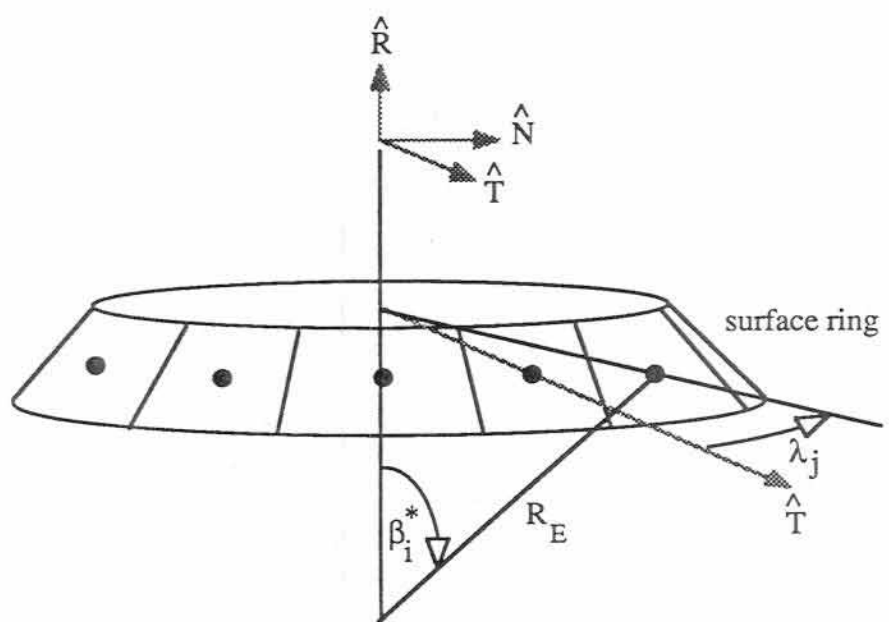


Fig. A.2
Geometry of Segment Calculations

BIBLIOGRAPHY

- Anselmo, L., P. Farinella, A. Milani, and A. M. Nobili, "Effects of the Earth-Reflected Sunlight on the Orbit of the LAGEOS Satellite," *Astronomy and Astrophysics*, 117, 3-8, 1983.
- Baker, R. M. L., Jr., "Radiation on a Satellite in the Presence of Partly Diffuse and Partly Specular Reflecting Body," in *Trajectories of Artificial Celestial Bodies*, ed. by J. Kovalevsky, Springer-Verlag, Berlin, pp. 85-150, 1966.
- Barlier, F., Y. Boudon, J. F. Falin, R. Futauly, J. P. Villain, J. J. Walch, A. M. Mainguy, and J. P. Bordet, "Preliminary Results Obtained from the Low-g Accelerometer CACTUS" *COSPAR Space Research*, Volume XVII, ed. by M. J. Rycroft, Ac. C. Stickland, Pergamon Press, Oxford, NY, 1977.
- Barlier, F., C. Pastre, A. M. Mainguy, R. Juillerat, A. Paillous, M. Romero, J. J. Walch, Y. Boudon, and A. Cazenave, "Study of Atmospheric Thermal Balance by Measurement of Radiation Pressure," *ESA Journal*, Vol. 2, pp. 27-36, 1978.
- Barlier, F., M. Carpino, P. Farinella, F. Mignard, A. Milani, A. M. Nobili, "Non-gravitational Perturbations on the Semimajor Axis of LAGEOS," *Annales Geophysicae*, 4, A, 3, pp. 193-210, 1986.
- Ciufolini, Ignazio, "Measurement of the Lense-Thirring Drag on High-Altitude, Laser-Ranged Artificial Satellites," *Physical Review Letters*, 56, No. 4, January 27, 1986.
- Dah-Ning Yuan, *Personal Communication*, Center for Space Research, the University of Texas at Austin.

Fea, K. "The Orbital Accelerations of High Balloon Satellites," in *Dynamics of Satellites* (1969), ed. by B. Morando, pp. 295-302, Springer-Verlag, New York, 1970

Garwin, L. I., "Solar Sailing - A Practical Method of Propulsion within the Solar System," *Jet Propulsion*, 28, pp. 188-190, 1958.

Gast, P.R. "Solar Irradiance," *Handbook of Geophysics and Space Environments*, Air Force Cambridge Research Laboratory, Office of Aerospace Research, USAF, pp. 16:1-9, 1965.

Hucek, R. R., H. L. Kyle, and P. E. Ardanuy, "Nimbus 7 Earth Radiation Budget Wide Field of View Climate Data Set Improvement 1. The Earth Albedo From Deconvolution of Shortwave Measurements," *Journal of Geophysical Research*, 92, D4, pp. 4107-4123, April 20, 1987.

Ardanuy, P., and R. R. Hucek, *Personal Communication*, Research and Data Systems Corporation, Lanham, Maryland.

Jacobowitz, H., and R. Tighe, "The Earth Radiation Budget Derived from the NIMBUS 7 ERB Experiment," *Journal of Geophysical Research*, 89, No. D4, pp. 4997-5010, June 30, 1984.

Kaula, William M., "Chapter 1: The Earth's Gravitational Field," *Theory of Satellite Geodesy*, Blaisdell Publ. Co., Waltham, MA, 1966.

Knocke, P. C., and J. C. Ries, "Earth Radiation Pressure Effects on Satellites," University of Texas Center for Space Research Technical Memorandum, CSR-TM-87-01, September, 1987.

Knocke, P. C., J. C. Ries, and B. D. Tapley, "Earth Radiation Pressure Effects on Satellites," Proceedings of the AIAA/AAS Astrodynamics Conference, August 15-17, 1988, pp. 577-587, paper # 88-4292-CP.

Lautmann, D. A., "Perturbations of a Close-Earth Satellite Due to Sunlight Diffusely Reflected from the Earth I: Uniform Albedo," *Celestial*

- Mechanics*, 15, pp. 387-420, 1977.
- Lautmann, D. A., "Perturbations of a Close-Earth Satellite Due to Sunlight Diffusely Reflected from the Earth II: Variable Albedo," *Celestial Mechanics*, 16, pp. 3-25, 1977.
- Levin, E., "Reflected Radiation Received by an Earth Satellite," *American Rocket Society Journal* 1328, September 1962.
- Lochry, Robert R., "The Perturbative Effects of Diffuse Radiations from the Earth and Moon on Close Satellites," Dept. of Engineering, UCLA, Ph.D. Dissertation, 1966.
- McCarthy, J. J., and T. V. Martin, "A Computer Efficient Model of Earth Albedo Satellite Effects," NASA Goddard Space Flight Center, Planetary Sciences Department Report no. 012-77, June 1977.
- Morgan, W. J., "Morning/Evening Difference in Earth's Albedo and the Deceleration of LAGEOS," *EOS*, 65, p. 855, 1984.
- Pinker, R. T., and J. A. Razgaitis, "Estimating the Solar Zenith Dependence of the Clear-Sky Planetary Albedo for Land Surfaces from the GOES Satellite," *Journal of Geophysical Research*, 88, no. C10, pp. 6007-6011, July, 1983.
- Poynting, J. H. "Radiation Pressure in the Solar System: Its Effect on Temperature and Its Pressure on Small Bodies," *Phil. Trans. A*, vol 202, pp. 525-552, June 1903.
- Prior, E. J., "Earth Albedo Effects on the Orbital Variations of Echo I and PAGEOS I," in *Dynamics of Satellites* (1969), ed. by B. Morando, pp. 295-302, Springer-Verlag, New York, 1970.
- Raschke, et al., "The Radiation Balance of the Earth-Atmosphere System from NIMBUS 3 Radiation Measurements," National Aeronautics and Space Administration, Technical Note D-7249, April, 1973.

Ries, John R., *Personal Communication*, Center for Space Research, the University of Texas at Austin.

Rubincam, David P., "On the Secular Decrease in the Semimajor Axis of LAGEOS's Orbit," National Aeronautics and Space Administration Technical Memorandum 80734, July, 1980.

Rubincam, David P., and N. R. Weiss, "Earth Albedo and the Orbit of LAGEOS," National Aeronautics and Space Administration Technical Memorandum 86210, June, 1985.

Rubincam, David P., "LAGEOS Orbit Decay Due to Infrared Radiation from Earth," National Aeronautics and Space Administration Technical Memorandum 87804, 1987.

Rubincam, David P., P. Knocke, V.R. Taylor, and S. Blackwell, "Earth Anisotropic Reflection and the Orbit of LAGEOS," *Journal of Geophysical Research*, 92, no. B11, pp. 11662-11668, October, 1987.

Rubincam, David P., "Yarkovsky Thermal Drag on LAGEOS," *Journal of Geophysical Research*, 93, no. B11, pp. 13805-13810, November 10, 1988.

Sehnal, L., "The Effect of the Re-Radiation of the Sunlight from the Earth on the Motion of Artificial Satellites," in *The Use of Artificial Satellites for Geodesy*, ed. by G. Veis, North Holland Publishing Company, Amsterdam, 1963.

Sehnal, L., "Radiation Pressure Effects in the Motion of Artificial Satellites," in *Dynamics of Satellites (1969)*, ed. by B. Morando, pp. 622-272, Springer-Verlag, New York, 1970.

Sehnal, L., "Non-Gravitational Forces in Satellite Dynamics," COSPAR-IAU-IUTAM Symposium, Sao Paolo, Brazil, June 19-21, 1974.

Sehnal, L. "The Earth Albedo Model in Spherical Harmonics," *Bull. Astron. Czechosl.*, Vol 30, No. 4, pp. 199-204, 1979.

Sehnal, L., "Effects of the Terrestrial Infrared Radiation Pressure on the Motion of an Artificial Satellite." *Celestial Mechanics*, 25, pp. 169-179, 1981.

Slabinski, Victor J., "LAGEOS Acceleration due to Intermittent Solar Heating During Eclipse Periods," Paper 3.9, The 19th Regular Meeting of the Division on Dynamical Astronomy - American Astronomical Society, Gaithersburg, Maryland, July 25-26, 1988.

Slowey, J. W., "Earth Radiation Pressure and the Determination of Density from Satellite Drag," *Space Research XIV*, Akademie-Verlag, Berlin, 1974.

Smith, D. E., "Earth-Reflected Radiation Pressure," in *Dynamics of Satellites* (1969), ed. by B. Morando, pp. 284-294, Springer-Verlag, New York, 1970.

Smith, D. E., and P. J. Dunn, "Long Term Evolution of the LAGEOS Orbit," *Geophysical Research Letters*, 7, 437-440, 1980.

Stephens, G. L, G. G. Campbell, and T. H. Vonder Haar, "Earth Radiation Budgets," *Journal of Geophysical Research*, 86, no. C10, pp. 9739-9760, October, 1981.

Stowe, L. L., and M. D. Fromm, "Nimbus-7 ERB Sub-Target Radiance Tape (STRT) Data Base," National Oceanic and Atmospheric Administration, Technical Memorandum NESDIS 3, December, 1983.

Suits, Gwynn H., "Chapter 3: The Nature of Electromagnetic Radiation," in *Manual of Remote Sensing, Vol. I*, Ed. Robert G. Reeves, American Society of Photogrammetry, Falls Church, Va., 1975.

Tapley, B. D., G. H. Born, and B. E. Schutz, "Satellite Orbit Determination: Fundamentals and Applications," from a University of Texas Short Course: Satellite Orbit Determination, June 24-28, 1985, Austin, Texas.

- Taylor, V. R., and L. L. Stowe, "Reflectance Characteristics of Uniform Earth and Cloud Surfaces Derived from NIMBUS-7 ERB," *Journal of Geophysical Research*, 89, no. D4, pp. 4987-4996, June, 1984.
- Taylor, V. R., *Personal Communication*, NOAA / National Earth Satellite Data and Information Service, Washington, D.C..
- Walch, J. J. translation of: "Choix d'un modele de rayonnement d'albedo terrestre. Calcul pratique de son effet sur la trajectoire d'un satellite," The Use of Artificial Satellites for Geodesy and Geodynamics, vol. 3, edited by G. Veis, pp. 172-182, National Technical University, Athens, 1984.
- Willson, Richard C., "Accurate Solar 'Constant' Determinations by Cavity Pyroheliometers," *Journal of Geophysical Research*, 83, no. C8, p. 4003, August, 1978.
- Willson, Richard C., and H. S. Hudson, "Solar Luminosity Variations in Solar Cycle 21," *Nature*, 332, pp. 810-812, April 28, 1988.
- Wyatt, Stanley P., "The Effect of Terrestrial Radiation Pressure on Satellite Orbits," Dynamics of Satellites Symposium, IUTAM, 28-30 May 1962, Paris, Ed. M. Roy, Academic Press, New York, 1963, pp. 180-196.
- Zerbini, S., "Direct Solar and Earth-Albedo Radiation-Pressure Effects on the Orbit os PAGEOS I", Research in Space Science, SAO Special Report No. 383, 1979.